GEOLOGICA ULTRAIECTINA

Mededelingen van de
Faculteit Aardwetenschappen der
Rijksuniversiteit te Utrecht

No. 77

Influence of deformation on the fluid transport properties of salt rocks

COLIN J. PEACH

Prof. Schmeling,

GEOLOGICA ULTRAIECTINA with best wishes

Colin J. Peach

Mededelingen van de
Faculteit Aardwetenschappen der
Rijksuniversiteit te Utrecht

No. 77

Influence of deformation on the fluid transport properties of salt rocks

Influence of deformation on the fluid transport properties of salt rocks

Invloed van deformatie op de vloeistoftransporteigenschappen van zoutgesteenten

(met een samenvatting in het Nederlands)

PROEFSCHRIFT

TER VERKRIJGING VAN DE GRAAD VAN DOCTOR AAN DE RIJKSUNIVERSITEIT TE UTRECHT, OP GEZAG VAN DE RECTOR MAGNIFICUS, PROF.DR. J.A. VAN GINKEL, INGEVOLGE HET BESLUIT VAN HET COLLEGE VAN DEKANEN IN HET OPENBAAR TE VERDEDIGEN OP WOENSDAG 10 APRIL 1991 DES NAMIDDAGS TE 12.45 UUR

DOOR

COLIN JACK PEACH

GEBOREN OP 3 MEI 1954 TE STAINES, ENGELAND

PROMOTOR: PROF.DR. H.J. ZWART
CO-PROMOTOR: DR. C.J. SPIERS

CIP-GEGEVENS KONINKLIJKE BIBLIOTHEEK, DEN HAAG

Peach, Colin Jack

Influence of deformation on the fluid transport properties of salt rocks / Colin Jack Peach. - [Utrecht: Instituut voor Aardwetenschappen der Rijksuniversiteit Utrecht]. - (Geologica Ultraiectina. ISSN 0072-1026: no. 77).
Proefschrift Utrecht. - Met lit. opg. - Met samenvatting in het Nederlands.
ISBN 90-71577-31-7.
Trefw.: zoutgesteenten; deformatie / zoutgesteenten; vloeistoftransporteigenschappen.

To my Parents

CONTENTS

ABSTRACT / SUMMARY

While the fluid transport properties of rocks are well understood under hydrostatic conditions, little is known regarding these properties in rocks undergoing crystal plastic deformation. However, such data are needed as input in the field of radioactive waste disposal in salt formations. They are also needed to understand deformation, shear zone evolution and associated fluid movement, metamorphism and mineralization in the deep crust and even upper mantle.

The present study is concerned with the development of a fundamental understanding of the influence of crystal plastic deformation on dilatancy and permeability evolution in salt rocks and salt/anhydrite rocks. It is experimentally based and seeks to explain the influence of deformation on permeability in the framework of "percolation theory", currently finding wide application in solid state physics. The results relate directly to the behaviour of salt rock in disposal systems and, viewing salt as an analogue material, provide insight into the effects of plastic deformation on the fluid transport properties of crystalline rocks in general.

Chapter 1 introduces the problems to be investigated. **Chapter 2** describes the experimental apparatus and methods used and developed during the study.

The work reported in **Chapter 3** was principally directed at the influence of crystal plastic deformation on dilatancy and permeability development in natural rocksalt (Asse Speisesalz, Germany) under repository relevant conditions. The intact starting material was found to have an extremely low permeability ($< 10^{-21}m^2$). In deformed material from gallery walls, values up to $10^{-16}m^2$ were measured. In triaxial deformation experiments performed on intact material at room temperature, minor amounts of dilatancy (< 0.2 vol%) accompanying crystal plastic deformation led to extremely rapid initial increases in permeability, suggesting critical behaviour of the type described by percolation theory. Microstructural evidence showed that dilatancy was associated with grain boundary and transgranular microcracks. Additional short-term hydrostatic experiments, performed on dry dilated material, showed deformation-induced permeability to depend on pressure in a manner best explained by an elastic microcrack closure model. Long-term hydrostatic experiments on dilated material, dry and wet, showed permeability to decrease with time. Permeability decay rates were faster in wet material presumably due to crack healing processes.

Chapter 4 documents triaxial compression experiments designed to determine the influence of plastic deformation on dilatancy and permeability development in fine grained synthetic salt rock, at room temperature, confining pressures (P_c) in the range 5 - 20 MPa and strain rates ($\dot{\varepsilon}$) of ~ 4 x $10^{-5}s^{-1}$ to total strains of ~ 15%. The samples exhibited broadly similar mechanical behaviour to the Asse salt, though they were slightly weaker and showed more dilatancy (upto 3 vol%) in the dilatant field (P_c < 18 MPa) and were slightly stronger in the non-dilatant field (P_c > 18 MPa). Microstructural observations confirmed that deformation occurred by dislocation glide with grain boundary microcracking in the dilatant field. As in the experiments on Asse material, minor amounts of dilatancy produced extremely rapid initial increases in permeability from ($\leq 10^{-21}m^2$ to ~ 2 x $10^{-16}m^2$), again suggesting critical behaviour. The minor differences observed in mechanical and dilatant behaviour between the synthetic and natural salts are explained in terms of the difference in grainsize.

Chapter 5 represents an extension of the work on synthetic salt (Chapter 4) to systematically determine the influence of controlled amounts of anhydrite added to the synthetic material as a rigid second phase. Triaxial compression experiments were carried out on synthetic salt rock samples containing 0 - 35 vol% anhydrite present in 1 of 3 grainsizes, i.e. ~ 10x, 1x, 0.1x the halite matrix grainsize of ~ 350 μm. All experiments were carried out at room temperature with $\dot{\varepsilon}$ = 4 x $10^{-5}s^{-1}$ and P_c = 20 MPa (i.e. within the non-dilatant field for pure synthetic salt) reaching total strains of ~ 15%. All samples containing ≥ 10 vol% anhydrite showed significant dilatation (up to 2.5 vol%). All types of sample also showed a tendency for flow stress and dilatancy (at constant strain) to increase with increasing anhydrite content. Dilatation of low permeability samples containing > 10-20 vol% anhydrite was initially accompanied by extremely rapid permeability development (from ≤ $10^{-21}m^2$, at low anhydrite content, to ~ 3 x $10^{-17}m^2$ in most cases), again consistent with critical behaviour. Microstructural studies showed that the salt "matrix" of all samples deformed by dislocation glide mechanisms with minor grain boundary dilatation. In contrast the anhydrite always showed extensive microfracture and/or dilatation. The tendency for flow stresses to increase with anhydrite content was inferred to be due to concentration of strain in the halite and rigid particle hardening effects similar to those seen in some metals.

In **Chapter 6** the experimental results are compared with microphysical models. First, classical Darcian flow models relating permeability to fully connected porosity are reviewed and shown to be inapplicable to the experimental data. The fundamentals of modern percolation theory are then introduced and used to develop a microcrack linkage model predicting the critical development (sudden appearance)

of permeability with dilatancy during deformation. When applied to the observed crack microstructure, this "bond percolation" model successfully explains the initial rapid growth of permeability seen in the Asse and pure synthetic salts. From detailed comparison of the model with the results for these materials, it is inferred that through going microcrack linkage (the percolation threshold) occurs at minute dilatations of < 0.05 vol% and is associated with the linkage of very thin (< 1 μm) grain boundary microcracks. Post-critical permeability saturation can be explained in terms of a broadening in crack width distribution, with non-axial cracks remaining thin and limiting the flow. The bond percolation model is not appropriate for explaining the permeability development for the salt/anhydrite rocks, since dilatancy is concentrated in the anhydrite sites. For this reason the experimental data are compared with various "site percolation" models, which essentially describe the initial growth of permeability in terms of the establishment of physical contact between the dilated and permeable anhydrite sites. These models were found to offer a satisfactory explanation of the experimental results, in particular the influence of anhydrite content on critical behaviour.

In conclusion the present work has shown that minor dilatancy during plastic deformation of salt and salt-anhydrite material can lead to very large increases in permeability. The thesis is closed, via **Chapter 7**, with a discussion of the implications of this for the fluid transport properties of salt rocks in the waste repository environment and for the fluid transport properties of regions of the Earth's crust and upper mantle undergoing plastic deformation. Suggestions for further work are included here.

CHAPTER 1

Introduction: Definition of Problems and Aims

1.1. General background and scope

The fluid transport properties of a wide range of rock materials, from porous sediments to dense, crystalline, igneous rocks have been investigated experimentally under hydrostatic test conditions (Brace et al., 1968; Brace, 1980; Sutherland and Cave 1980; Walls et al., 1982; Gangi, 1985) and are well understood (Katz and Thompson, 1986). The influence of elastic deformation and brittle failure on fluid transport properties have also been investigated for a limited number of rock types (Zoback and Byerlee, 1975; Brace, 1978; Trimmer et al., 1980; Bernabe, 1986). However, very little is known regarding the fluid transport properties of rocks undergoing ductile deformation (Fischer and Paterson, 1989) by crystal plastic or diffusional flow mechanisms, or under conditions approaching the transition from such mechanisms to deformation dominated by cataclasis, i.e. near to the so-called "brittle-ductile transition" (Duba et al., 1990; Rutter, 1986). This type of data on the influence of "ductile deformation" on fluid permeability form fundamental input in the field of radioactive-waste disposal in salt rock formations where an understanding of such effects plays an important role in assessing repository performance. Such data are also essential in understanding hydrothermal mineralization and in the elucidation of deep crustal deformation / metamorphic processes, where fluid / rock interactions can be seen to have been of great importance (White and Knipe, 1978; Cox et al., 1986; Kerrich, 1986; Touret, 1986; McCaig and Knipe, 1990; Rubie, 1990). Of particular interest here is the possible role of localized shear zones as paths of enhanced fluid permeability with coupled water weakening (Rutter and Brodie, 1985; Kronenberg et al., 1990). The latter aspect may have important consequences for the strength of the continental lithosphere and even for the lithospheric upper mantle (Brodie and Rutter, 1987; Drury et al., 1990; Hoogerduijn Strating, 1991). Recent geochemical work (Brodie, 1980, 1981; Watson and Brenan, 1987) strongly suggests that fluid transport into and through such zones requires either brittle deformation or ongoing creep-induced dilatancy.

The research work reported here in this thesis is concerned with the development of a fundamental understanding of plastic-deformation-induced dilatancy and permeability effects in salt rocks and salt/anhydrite rocks. The results are directly

relevant to the behaviour of salt rock in radioactive waste disposal and storage systems, and viewing salt as an analogue material, provide important insight into the influence of plastic deformation on the fluid transport properties of crystalline rocks in general.

1.2. Questions relating to radioactive waste disposal in salt rock

Salt formations have long been recognized as a relatively favourable medium for geological disposal of radioactive waste (Nat. Acad. of Sci. U.S., 1957). This is because of the relatively high ductility and low creep strength of rocksalt under near-ambient conditions, its high thermal conductivity, naturally low permeability ($< 10^{-22}m^2$, c.f. $10^{-16}m^2$ for a relatively tight sandstone) and self-healing capacity (Gevantman, 1981; Carter and Hansen, 1983; Peach et al., 1987). Most proposed disposal concepts focus on deep boreholes operated either from the surface or from galleries within a conventional mine (Dutch OPLA - Eindrapport Fase 1, 1989), see Figure 1.1.

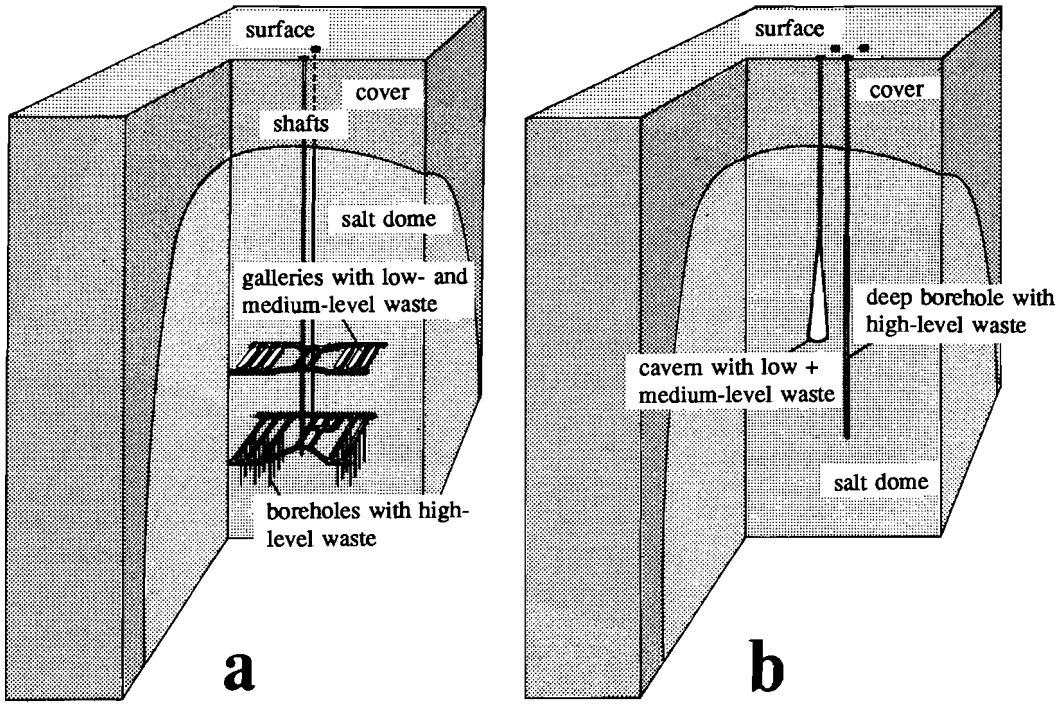

Figure 1.1a and b. Typical concepts for disposal of radioactive waste in salt domes.
a) Mine disposal concept.
b) Disposal concept with deep boreholes and caverns.
Depth scale ≈ 1 - 1.5 km in both cases.

The construction of a disposal system for high level radioactive waste (HLW) in a salt formation, whether a layer, pillow or dome, will inevitably lead to a mechanical and thermal perturbation of the entire geological system. Such perturbations are expected to be small (Rolnik, 1988). For a thorough assessment of the isolation capacity of salt structures it is nonetheless necessary to quantitatively model the long term response of the geological system and crucial parts thereof. The only real route by which radioactive material, disposed of in salt, can reach the biosphere is via fluid phase transport (transport in groundwater or migrating gas). The principal aim of long-term modelling must therefore be to determine whether or not water or gas migration can occur on a scale which might threaten the isolation capacity of a repository (Bérest and Ghoreychi, 1988).

Broadly speaking, the disposal of radioactive waste in salt bodies can be expected to lead to two types of mechanical perturbation: The first is the thermal stressing effect produced by introducing heat emitting HLW. This thermal stressing will lead to plastic deformation of the surrounding salt in a time dependent manner governed by the deformation properties of the salt and the evolution of the thermal pulse. For a thorough safety analysis, it is necessary to model how the system will respond to such effects in the long-term (Prij, 1984; Rolnik, 1988). Some of the principal questions here are:

i) How will the stress and displacement fields within the salt body evolve with time?
ii) To what extent will the plastically deforming salt remain impermeable to liquids and gases?

The second type of mechanical perturbation is caused by the construction and operation of the disposal system itself, e.g. the construction of shafts, galleries and boreholes. When the repository system is sealed, these potential transport paths will be backfilled and even dammed (e.g. Matalucci and Hunter, 1981, for the U.S. WIPP site). In view of the low creep strength of rocksalt, it is anticipated that all openings will subsequently converge and close-up under the influence of the lithostatic pressure and thermally induced stresses. However, little is known about the influence of deformation, in the region surrounding converging openings, on the fluid transport properties of salt rock.

On the basis of the above, it is apparent that a thorough safety assessment requires a detailed understanding of the rheological behaviour of salt rock. However, an understanding is also required of the influence of plastic deformation on dilatancy and permeability development of both pure salt and salt containing typical (rigid)

impurities such as anhydrite. Very little experimental data exists in this area. In addition, no previous attempts have been made to apply modern theories of permeability development by microcrack linkage (percolation theory) to the case of rocksalt deforming predominantly by crystal-plastic mechanisms.

1.3. Fluid transport properties of crystalline rocks: Salt as an analogue

As mentioned previously, almost nothing is known regarding the influence of crystal-plastic deformation processes on dilatancy and permeability development in crystalline rocks such as silicates. A limited number of experiments have been performed on single phase materials such as marble, limestone and sodium chloride under conditions favouring ductile deformation predominantly by crystal plasticity (Edmond and Paterson, 1972; Fischer and Paterson, 1989). These have shown dilatancy development, though no data appear to have been published relating permeability to deformation. At the same time, microstructures from monomineralic rocks which have undergone crystal plastic deformation in the lower crust and upper mantle often show clear evidence for healed microcracks and grain boundary fluid inclusion arrays (White and White, 1981), also suggesting significant dilatancy. In addition, plastically deformed polyphase rocks often show evidence for substantial microfracturing of the rigid phases, e.g. feldspars in plastically deformed quartzites and pyroxenes in plastically deformed olivine peridotites (Drury et al., 1990). In order to gain quantitative insight into dilatancy and permeability development in such materials, well controlled experiments are needed. For the case of silicates, however, the very high temperatures and pressures required present extreme practical difficulties for measurement of permeability and small volume changes related to dilatancy. Bearing this in mind, pure rocksalt offers a very attractive analogue material for monomineralic crystalline rocks, since it is easily deformable by crystal plastic mechanisms at near-ambient conditions. Synthetic salt/anhydrite rocks also offer an analogue for silicate rocks containing a rigid second phase.

In order to gain insight into the behaviour of crystalline rocks in general, from experimental results obtained from such analogues, appropriate microphysical models of permeability development during plastic deformation are needed. Here, the modern theory of critical microcrack linkage (percolation theory) offers a suitable starting point.

1.4. Aims of the present study

The aims of the thesis can now be specified as follows:

1) To determine the influence of crystal plastic deformation on dilatancy and permeability development in natural rocksalt under low pressure and temperature (disposal/storage relevant) conditions.

2) To determine the influence of crystal plastic deformation on dilatancy and permeability development in synthetic salt rock, and to go on to systematically determine the influence of controlled amounts of anhydrite as a rigid second phase.

3) To compare the experimental results with microphysical models relating dilatancy and permeability induced during plastic deformation, with special emphasis on critical microcrack linkage models (percolation theory).

4) To thus develop a quantitative, mechanism-based understanding of permeability development during dilatant plastic deformation of salt and salt/anhydrite rocks.

5) To consider the implications for radioactive waste disposal and storage in salt formations, and for permeability development during (localized) deformation of silicate rocks in the lower crust and upper mantle.

In order to achieve these aims it was necessary to develop apparatus with the capability of measuring not only conventional rheological parameters but also extremely small volume changes and permeability during deformation. The present experiments on salt were carried out under room temperature conditions at relatively rapid strain rates ($\sim 10^{-5}s^{-1}$). Under these conditions, it is well established that pure polycrystalline salt deforms essentially by a dislocation glide mechanism (Heard, 1972; Frost and Ashby, 1982; Skrotzki and Haasen, 1988). For orientation, a deformation mechanism map is provided in Figure 1.2.

Those aspects of the present thesis pertaining to the behaviour of natural salt rock were conducted in the framework of waste disposal research programmes funded by the European Community and the Dutch government.

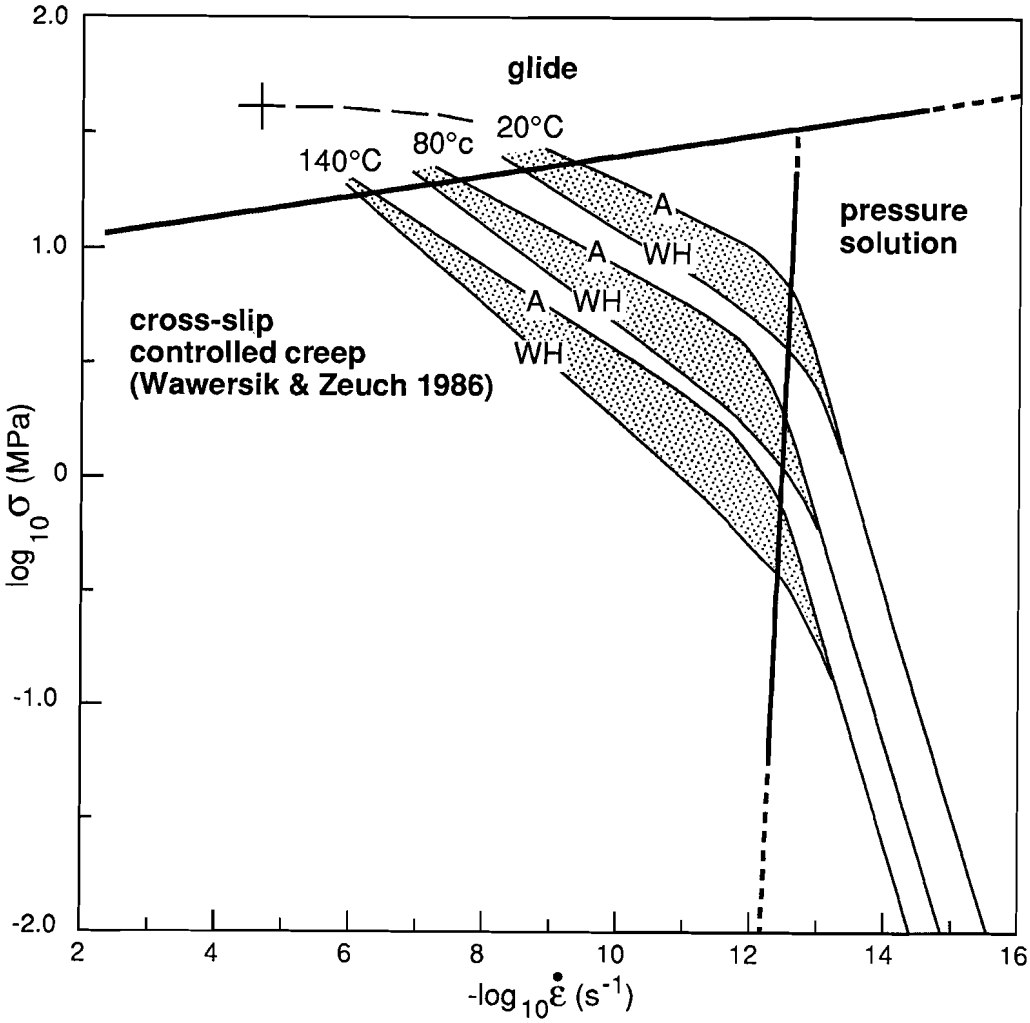

Figure 1.2. Deformation mechanism map drawn for polycrystalline salt rock with a grainsize of 10 mm, covering the temperature range 20-140°C (after Spiers et al., 1990). Note that the conditions of the experiments reported in this thesis (room temperature, strain rate ~ $10^{-5}s^{-1}$) fall in the glide or plasticity field. The detailed rate controlling mechanism in the "dislocation creep" field at the temperatures indicated remains unclear. However, the isotherms represented here are drawn for the cross-slip model of Wawersik and Zeuch (1986), applied for the extremes of Asse (A) and West Hackberry (WH) salts. N.B. σ = flow stress, $\dot{\varepsilon}$ = strain rate.

CHAPTER 2

Experimental Apparatus and Methods

2.1. Introduction

The experimental programme reported in this thesis required development of apparatus and methods for combined deformation, dilatometry and permeametry. The programme was based around a motor driven, triaxial deformation apparatus designed originally by the late H. Heard (Lawrence Livermore National Labs., CA, USA), with the capability of measuring conventional rheological parameters (stress, σ; strain, ε; strain rate, $\dot{\varepsilon}$) plus volume change under different values of confining pressure, temperature and pore fluid pressure. This apparatus will be referred to as the "Heard Apparatus".

To suit the needs of the present programme, this apparatus had to be substantially modified to allow very small volume changes occurring during ductile deformation to be measured. In addition, systems and methods had to be developed to allow measurement of sample permeability to both gases and liquids during deformation.

2.2. Deformation apparatus

As mentioned above, all experiments reported in this thesis were carried out using the Heard triaxial machine, modified to allow accurate volume change measurements to be made during testing. The apparatus is described here together with information regarding calibration and the methods used in data acquisition and processing. The description updates that given by Spiers et al. (1986) for the original configuration, and includes all developments, modifications and refinements added during the period 1985 - 1990.

2.2.1. General aspects

The Heard apparatus consists of an externally heated, silicone fluid medium, triaxial testing machine (see Figures 2.1 and 2.2) linked to an electronics and pressure control system. The testing machine is situated inside a high pressure testing bunker

(in the HPT Laboratory at Utrecht), with the electronics and pressure control unit situated outside (see Figure 2.1).

The testing machine itself consists of a furnace-clad main pressure vessel containing the sample, an auxilliary pressure vessel, and a yoke/piston loading system driven by a motor/gear-train/ball-screw arrangement (omitted from Figure 2.2 but visible in Figure 2.1). Note that the main and auxilliary pressure vessels are connected together via a link of wide-bore, high pressure tubing. The whole apparatus is designed such that when the yoke/piston assembly is advanced to load the sample, confining fluid is displaced from the main vessel into the auxilliary vessel, the volume and pressure of the system remaining constant (that is, independently of sample volume change, apparatus distortion, and temperature changes in the moving fluid). Sample volume change is measured (applying corrections for the other volumetric effects) using a linear potentiometer to record the piston displacement of a servo-controlled volumometer pump which maintains constant pressure in the confining pressure system during deformation. Viton fluoroelastomer 'O'-rings ensure leak-proof operation of all the dynamic and static seals. Axial load on the sample is measured using a conventional semi-internal, LVDT-based load cell situated at the top of the main vessel, and displacement is measured at the yoke using a high precision LVDT (linear variable differential transformer). Pressures are measured using strain-gauge type pressure transducers in addition to conventional pressure gauges. Pore fluid pressure is introduced into the jacket-sealed sample assembly by means of independent pipes connected, via ports in the load cell block, to inlets in the upper and lower end-pieces of the assembly. Sample temperature is measured at the jacket outer surface using two chromel/alumel thermocouples also brought in through a port in the load cell block. Temperature is controlled using a 3-term PID (proportional/integral/derivative) process controller. The confining pressure for the whole system is generated using a compressed-air driven pump located in the control unit. The liquid pressure system for the two pore fluid lines is described in Section 2.4. Note that all components of the pore fluid system are constructed from AISI 316 quality stainless steel. A dry gas pore fluid system in the form of a transient step permeameter may alternatively be connected and is described in Section 2.5.

The apparatus is designed for axi-symmetric compression testing of cylindrical samples (up to 10 cm diameter by 25 cm length) at confining pressures up to 100 MPa, and temperatures up to 400°C, at constant strain rate (10^{-4} to $10^{-9}s^{-1}$) or at constant stress (creep tests). Stress relaxation and stepping tests are also possible. Modifications to the drive system have also enabled strain rate stepping tests to be performed. Controlled strain (displacement) rate tests are carried out using a

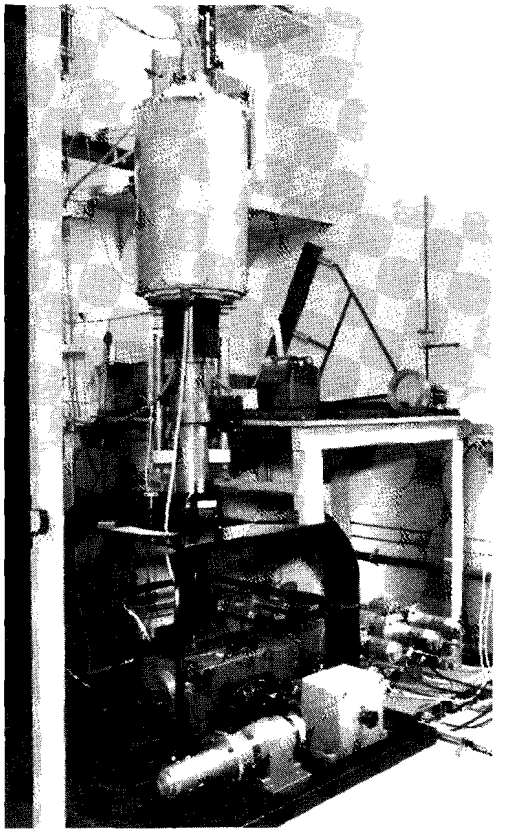

Figure 2.1. Photograph showing the Heard deformation apparatus as situated inside a bunker in the High Pressure - Temperature Laboratory at the Institute for Earth Sciences, Utrecht. Note the gear-box / ball-screw drive system situated within the base frame at the foot of the apparatus. Apparatus height = 2.4 m.

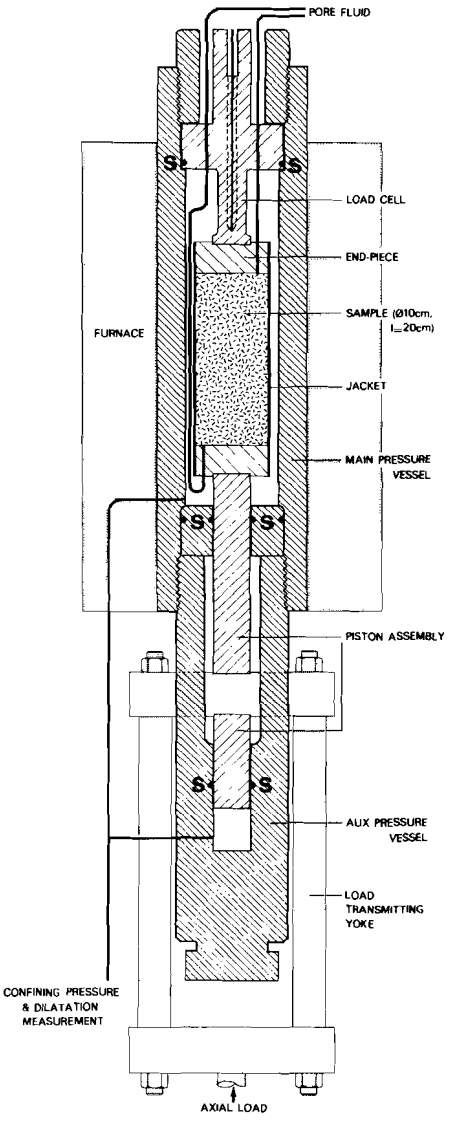

Figure 2.2. Semi-schematic diagram illustrating a section through the Heard deformation apparatus. Note that the motor /gear-train / ball-screw system that drives the yoke / piston assembly has been omitted from this diagram for simplicity. S = seals ('O'-ring packing assemblies).

constant speed drive motor (in conjunction with a multi-ratio gearbox). Pore fluid can be introduced into the sample at fixed pressure (up to 50 MPa) or in through-flowing mode. The main specifications of the apparatus are summarized in Table 2.1. During any given experiment, it is possible to measure axial load (stress), displacement (strain), displacement (strain) rate, sample temperature, confining pressure, pore fluid pressure (at each end of the sample), and sample volume change (hence dilatancy). Output signals are recorded using a 6-channel chart recorder linked to a digital data logging system.

Parameter	Operational Range of Machine	Measurement Resolution	Max. Control Drift
Stress	100 MPa (i.e. 400 kN on 70 mm ϕ sample)	~ 0.02 MPa	0.02 MPa
Displacement	~ 10 cm	10.0 μm	
Volume Change	10 ml (stroke reset-able)	~ 0.05 ml	
Confining Pressure	100 MPa	0.01 MPa	0.005 MPa
Pore Pressure	50 MPa	0.01 MPa	0.005 MPa
Temperature	400°C	0.1 °C	0.2 °C

Table 2.1. Summary of main specifications of Heard Apparatus, as modified at Utrecht.

2.2.2. Sample assembly

Cylindrical samples up to 100 mm in diameter by 250 mm in length can be tested in the Heard apparatus. However, the experiments documented in this thesis were performed using either samples of 70 mm diameter by ~ 150 mm length, or 50 mm by ~ 125 mm length. The sample assembly used is illustrated in Figure 2.3. This is

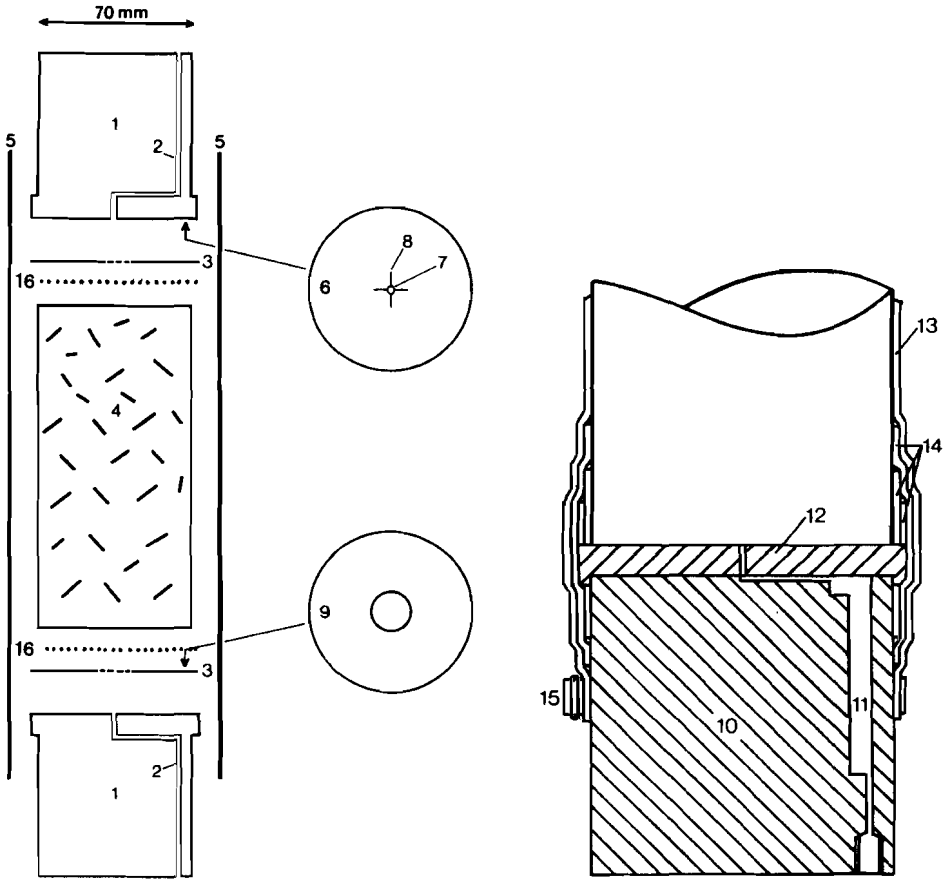

A) Expanded Diagram Illustrating Sample Assembly.

B) Detail of End-Piece Configuration and Jacketing Arrangement.

Figure 2.3. Semi-schematic diagram illustrating A) the 70 mm sample assembly, and B) detail of the end-piece configuration and jacketing arrangement currently in use. Key overleaf.

Key to Figure 2.3. (see previous page)

1. Piston end-pieces.
2. Pore fluid inlets.
3. Teflon end-sheets (to minimize friction at the sample/end-piece interfaces).
4. Salt rock sample.
5. Rubber jacket.
6. Piston end-piece, face view.
7. Pore fluid inlet bore.
8. Fine (0.2 mm) slots to distribute pore fluid (N.B. these slots are cut radially in order to minimize friction effects at the sample/end-piece interface. They are restricted to the central region of the end-piece faces for the same reason).
9. Teflon end-sheet, face view (N.B. the central cut-out is to prevent sealing of the pore fluid inlet slots).
10. End-piece (detailed).
11. Detailed design of pore fluid inlet with salt chamber (see text).
12. Removable end-cap (for filling salt chamber).
13. Rubber jacket (e.g. Viton).
14. Viton collars to protect the jacket from damage at the stepped end-piece/sample interface.
15. Ratchet clamp.
16. Glass fibre tissue end sheets which act as gas spreaders.

N.B. All metallic components are constructed from 316 stainless steel.

inserted into the main vessel (via the upper closure) by means of the composite insertion assembly shown in Figure 2.4.

The configuration of the end-pieces constitutes an important feature of the 70 mm sample assembly (refer Figure 2.3). In particular, the pore fluid inlets have been modified (for work at high temperatures and with pore fluid) to incorporate a chamber filled (before each test) with finely-powdered salt (Figure 2.3b). This powdered salt is intended to pre-saturate brine flowing into the heated sample from the cold external pore fluid (brine) system). This design ensures that dissolution of the sample by entrant pore fluid is minimized.

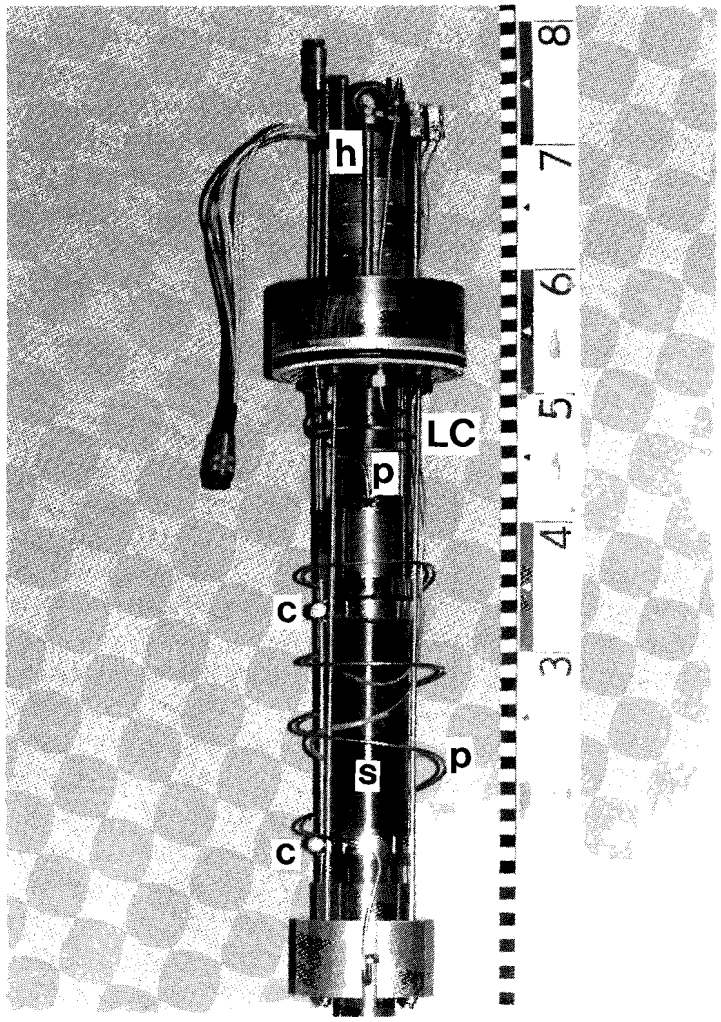

Figure 2.4. Photograph illustrating the 50 mm sample assembly in position in the sample / load-cell insertion assembly. Note the sample (s) jacket sealing clamps (c), load cell column (LC), LVDT housing (h) and the upper and lower pore fluid access pipes (p).

2.2.3. Calibration

The following characteristics of the Heard apparatus must be and were determined (calibrated) empirically, before each series of tests:

a) The force vs. output (mV) characteristics of the load cell.
b) The compliance characteristics of the loading frame (required for correcting displacement measurements for apparatus distortion).
c) The dependence of the internal apparatus volume on axial load (required for correcting volume change measurements for apparatus distortion).

Calibration (a) was realized with the aid of specially machined brass test specimens of well defined yield stress value determined, before and after deformation in the Heard apparatus, using a 100 kN INSTRON-1362 materials testing machine with certificated load cell. A steel dummy of known elastic properties was used in calibrations (b) and (c).

2.2.4. Data acquisition and processing

The Heard apparatus produces the following DC low level output signals:

a) Load cell output.
b) Displacement transducer (LVDT) output.
c) Volumometer output.
d) External force from strain gauges on yoke (includes seal friction).
e) Confining pressure transducer output.
f) Sample thermocouple outputs (2 thermocouples, top and bottom of sample).

As mentioned in Section 2.2.1., these raw data signals are recorded as a function of time using a 6-channel chart recorder, the pen positions of which are logged by an EPSON QX-16 microcomputer using a 12 bit A/D converter. The computer programme CHARTLOG supervises the logging. A data recovery option allows the backup chart record to be retraced and digitized using the recorder's chart drive under computer control. This option is only required in the rare event of a failure in the normal, magnetic disk based, digital recording system. The required rheological and volume change data (e.g. stress and volume change vs. strain data, or strain and volume change vs. time data) are obtained from the raw data by computing the stress, strain, volume change, strain rate, confining pressure, pore pressure, and temperature (etc.) as a function of time. This procedure involves the application of a

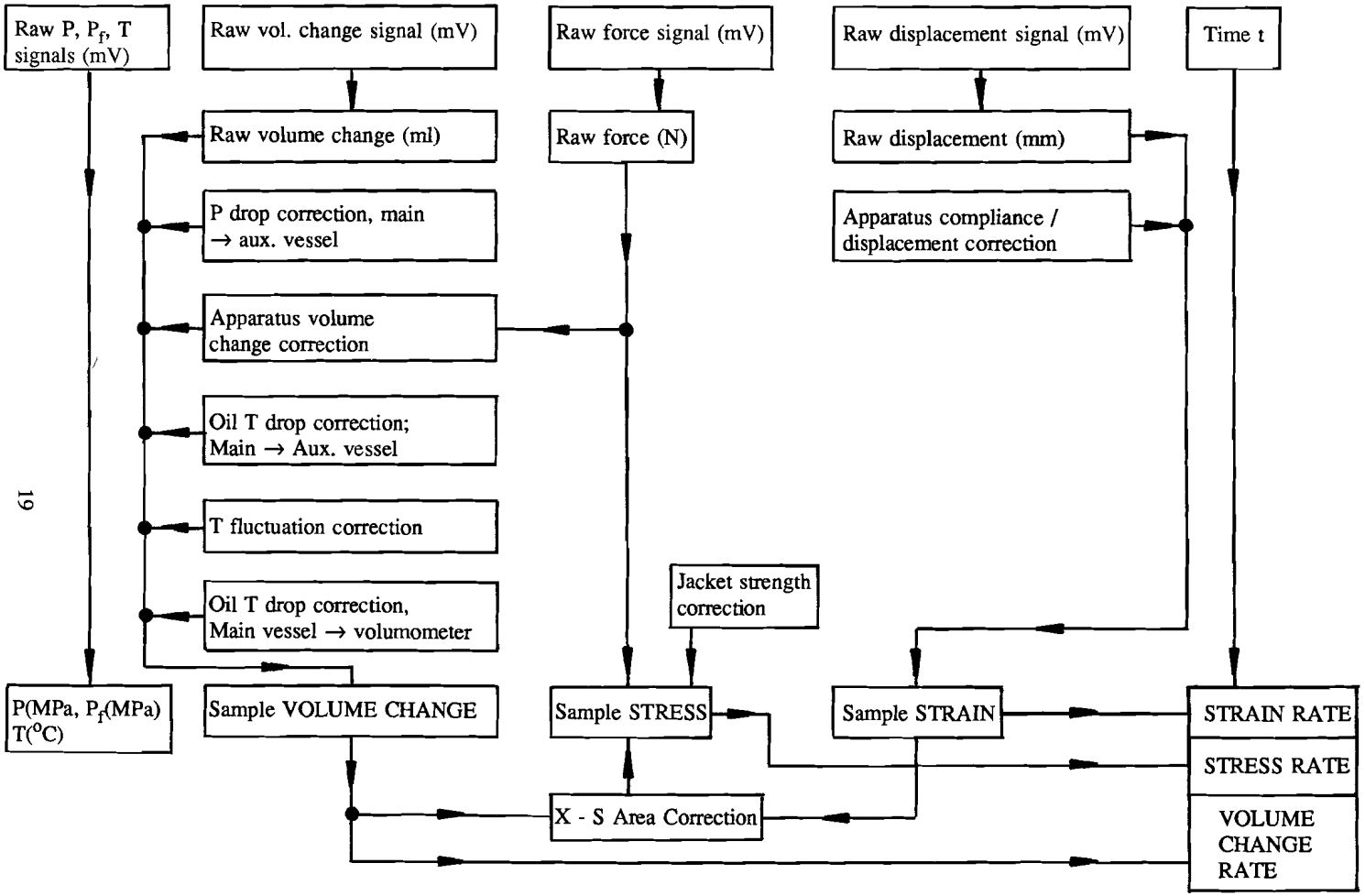

Figure 2.5. Correction scheme for processing data from the Heard apparatus. Diagram shows the macroscopic relationship between the raw data and the output parameters at any time t after start of test. P = pressure, T = temperature, X - S = cross sectional, P_f = pore fluid pressure.

considerable number of corrections based upon the empirically determined apparatus calibration data. The complete set of corrections necessary is illustrated in Figure 2.5. A sophisticated data processing algorithm has been developed following the correction scheme. It forms the basis of a highly generalized data processing package. This package, originally written in FORTRAN IV by C.J. Spiers, has been translated to Microsoft ® FORTRAN 77 for use on microcomputers. Together with a number of dedicated support programmes written by the author, the package is suitable for processing the data from almost every conceivable type of axi-symmetric deformation test, namely:

1) Constant strain rate tests.
2) Strain rate stepping tests.
3) Constant stress (load) tests.
4) Stress (load) stepping tests.
5) Stress relaxation tests.
6) Constant stress rate tests.
7) Stress rate stepping tests.

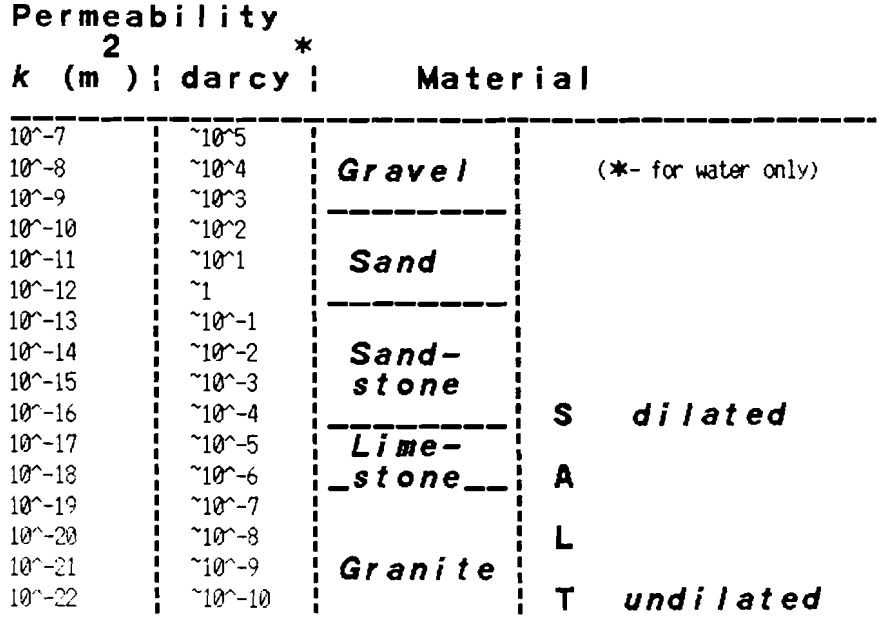

Figure 2.6. Permeability magnitude familiarization chart.

2.3. Methods of permeametry

Henri Darcy's empirical law (1856) for purely viscous fluid flow in a consolidated porous medium can be written for one-dimensional flow as

$$Q = \frac{-\kappa}{\mu} \cdot A \cdot \frac{\Delta P}{\Delta L} \qquad (2.1)$$

Q = volume flow rate (m^2s^{-1})
A = specimen cross sectional area (m^2)
μ = dynamic viscosity of the fluid (Pa.s)
$\Delta P/\Delta L$ = macroscopic fluid pressure gradient ($Pa.m^{-1}$)
κ = permeability (m^2)

The volume transfer rate Q of fluid is proportional to ΔP, the pressure potential difference driving the flow across an element of the porous medium of length ΔL. The permeability, κ, is a material property of the porous medium that is independent of the fluid used. The permeability has units of area (m^2), although the "darcy" (units = cm^2.cp/s.atm and 1 darcy $\approx 9.8697 \times 10^{-13} m^2$, for water) is more commonly used in the oil and chemical engineering, industries. The S.I. unit (m^2) will be employed throughout this thesis. (See Figure 2.6 for orientation towards permeability magnitudes and units).

One of the principal goals of this thesis was to measure changes in fluid permeability (κ) occurring during deformation, i.e. to carry out permeametry during deformation tests in the Heard apparatus. Permeametry on porous materials can in principle be carried out in at least 4 different ways:

i) Steady state "DC" permeametry;
this entails measurement of volumetric flow-through rate under a constant fluid pressure gradient, or conversely by the measurement of the pressure gradient developed as a result of a controlled (constant) through-flow rate.

ii) "Transient Step" permeametry;
this entails measurement of the pressure gradient decay due to flow-through following the sudden application of a fluid pressure transient.

iii) Steady state "AC" permeametry;
this entails measurement of the frequency dependent fluid pressure attenuation caused by an alternating flow-through of fluid.

iv) "Streaming Potential" permeametry;
this entails measurement of electrical potential differences developed due to the electroviscous interaction or "electrokinetic effect" accompanying fluid flow-through under an imposed fluid pressure gradient (DC, AC or transient).

In the present study, methods (i), (ii) and (iii) above were developed, though (iii) was not fully implemented.

The specific variants of the methods implemented in this study will be described in greater detail along with the necessary apparatus and practice in Sections 2.4 and 2.5. There first follows a general description of features inherent to non-DC methods and factors affecting the various methods of wet permeametry.

2.3.1. Aspects inherent to non-DC methods: Electrical analogy and time dependent effects

The terms "DC" (direct current) and "AC" (alternating current) permeametry both originate from a useful analogy with electrical circuits. The familiar Ohm's law

$$I = \frac{E}{R} \tag{2.2}$$

for DC electrical conduction is just one of many transport equations where

$$\textit{rate of transfer process} = \frac{\textit{driving force}}{\textit{resistance}} \tag{2.3}$$

In Ohm's law (Equation 2.2) the rate of charge transfer (or current, I) equates to the electromotive force (or voltage, E) divided by the resistance (R). Ohm's law is thus analogous to Darcy's law of Equation 2.1. Both describe steady state DC processes.

Transient and AC permeametry methods introduce the possibility of lower permeability determination but require a knowledge of the interrelation between fluid storage (capacity) within the specimen (due to fluid compression in pores coupled with the changes in porosity due to bulk rock/matrix compressibilities) and the purely resistive fluid permeability. To continue the analogy with electrical circuits, non-DC permeametry is thus similar to the determination of impedance in electrical networks containing resistive, capacitative and inductive (R, C, L) components. Time dependent information, such as phase and frequency dependence between flow and driving potential, is necessary to separate the resistive and reactive components of the total impedance. In non-DC permeametry, such

knowledge of the frequency response enables the connected porosity and pore structure (reactive) effects to be separated from the value of the purely resistive DC permeability.

Frequency dependent flow is the subject of a large amount of current research into the low frequency propagation of sound in wet sediments where sound is strongly attenuated by viscous fluid flow in the sediment pores (Yamamoto and Turgut 1988). The nomenclature "dynamic permeability" (Johnson et al. 1987) is used to describe frequency dependent apparent permeability $\kappa(\omega)$ measured by such sonic probe methods. A great deal of information regarding pore structure can potentially be extracted by such methods (Sheng and Zhou 1988), and with development may become the basis of future permeameters - see Charlaix et al. (1988) for a description of an experimental attempt.

2.3.2. Fluid rock interactions affecting permeametry

2.3.2.1. Electroviscous interaction and the electrokinetic effect

The streaming potential produced by the flow of ions in an electrically conductive fluid flowing past a charged solid interface is known as the "electrokinetic effect". Quartz/water systems exhibit such effects due to the electrochemical double layer thought to exist at solid-liquid interfaces (e.g. pores of a sandstone). The double layer consists of a negatively charged adsorbed layer and an adjacent positive layer of immobile counterions (Stern layer). A shear plane defines the interface between this immobile layer of cations and the mobile diffuse layer of fluid with its associated net positive charge. It is the motion of this diffuse layer, induced by a pressure differential along the interface, that produces the streaming current and the electrical streaming potential across the specimen. The double layer is characterized by the Zeta potential (ζ), the potential at the shear plane with respect to the bulk fluid and the streaming potential is given (see Bockris and Reddy, 1970 - Section 7.9),

$$\Delta\Psi = \frac{\varepsilon\ \zeta\ \Delta P}{4\pi\ \mu\ \sigma} \qquad \underline{\text{or}} \qquad \text{(C.G.S. Units)} \quad (2.4)$$

$$\Delta\Psi = \frac{\varepsilon_0\ \varepsilon\ \zeta\ \Delta P}{\mu\ \sigma} \qquad \text{(S.I. Units)} \quad (2.5)$$

where for the present purposes

$\Delta\Psi$ = streaming potential difference
ε = fluid dielectric constant
σ = fluid electrical conductivity
ζ = zeta potential
μ = fluid viscosity
ΔP = fluid pressure difference
ε_0 = permittivity of free space

Since Darcy's Law states

$$Q = \frac{\kappa A \Delta P}{\mu L} \qquad ((2.1))$$

then,

$$\Delta\Psi = \frac{\varepsilon_0 \varepsilon \zeta Q L}{\sigma \kappa A} \qquad (2.6)$$

Thus, the streaming potential is directly proportional to flow rate and inversely proportional to the permeability.

This relation forms the basis of the streaming potential permeametry method (Chandler, 1981). In practice Chandler used the voltage developed across a sample in response to a transient step in fluid pressure, together with a suitable analysis, to obtain a good linear relation with the DC permeability (determined by steady state flow through) covering a 3 order of magnitude range in permeability.

The effect of the electroviscous interaction is to produce drag and, if significant, it may lead to an underestimate of the true permeability if not taken into account during permeametry. The effect is greatest in low permeability materials.

2.3.2.2. Further fluid/rock interactions affecting permeametry

Perhaps the most important consideration in the choice of permeametry method is the volume and chemical reactivity of fluid which is transmitted through the sample during the test. In theory (Peach et al., 1987; Spiers et al., 1990), the flow due to the presence of a gradient in fluid pressure can cause modification to the pore structure by dissolution and precipitation reactions, thus affecting the permeability.

This problem with non-inert fluids can be minimized by the use of transient and AC methods which minimize fluid and hence mass transport. For low permeability the steady state AC sinusoidal method (Fischer, 1987; Kranz et al., 1990; Fischer and Paterson, 1991 - in prep.) has the least net flow of fluid through the sample and therefore the least physico-chemical interaction; an important factor when considering permeametry/dilatometry at elevated pressure and temperature in chemically active systems. In this study, fluid/rock interaction was avoided as required, by the use of inert dry argon gas for permeametry.

2.4. Steady-state DC flow-through permeametry and its application to this study

2.4.1. Principles

The so-called steady state "DC" methods of permeametry are well described in the American Petroleum Institute's code of practice on permeability determination (API-RP27, 1956). Well established low pressure methods such as the "constant head" and slow "falling head", (see also Verruijt, 1982 and Dullien, 1979), and the servo-driven, flow-through method employed in the present experiments, at higher fluid pressures, all have the advantage that they are a simple, direct application of Darcy's Law (see Equation 2.1) provided the fluid used is incompressible. In these methods the fluid flow is purely resistive by viscous dissipation. Capacitance or storage effects of the fluid in the pores (due to fluid and/or rock compressibility) play no role once steady state has been achieved. The methods are most appropriate when the fluid is stiff. Compressible fluids such as gases can be used but appropriate corections, usually assuming the pressure x velocity product is constant, must be made.

The present steady-state method, in which the volume flow rate of liquid is measured directly, has a lower limit of applicability due to the practical difficulty of low volume flow measurement on a reasonable time scale. This limit is around 5 x $10^{-18}m^2$ (see Figure 2.6 for orientation with respect to permeability magnitudes). The volume flow rate is measured by the displacement of the upstream and downstream fluid pressure control pumps which maintain a constant fluid pressure difference across the test specimen. Thus knowing the specimen cross sectional area perpendicular to flow (A), its length (L) the dynamic viscosity of the fluid (μ), and the pressure difference maintained across the sample (ΔP), the permeability (κ) may be determined simply by measuring the volume flow rate (Q). The method assumes that there is no interaction between the fluid and the rock. Electroviscous drag

effects (see electrokinetic effect, Section 2.3.2.1) and chemical interaction may affect permeametry on samples of low permeability. Flow rates should be low enough that laminar flow is maintained, i.e. no turbulence may occur to produce non-darcian behaviour.

2.4.2. Apparatus

The liquid pore fluid system used here is attached to the sample, under confining pressure within the Heard apparatus as illustrated in Figures 2.2, 2.4 and 2.7. The layout of pipework is designed for relatively high pressures (50 MPa) and is constructed where possible from AISI 316 stainless steel for corrosion resistance (see Figure 2.7). Two reservoirs (~ 1 litre internal volume) that may be isolated or linked, one to each half of the system, are housed outside the concrete cell containing the Heard apparatus. Two Bourdon gauges 0-140 MPa give visual indication of the pore fluid pressures in each system half. More accurate measurement of the pressure changes for control purposes are made by use of two 0-50 MPa Jensen type PE500 transducers with a non-linearity of 0.5%. A differential pressure transducer (± 0-22 MPa differential, 85 MPa background pressure - Validyne type P365D) is available for use with the transient pulse method. This is placed between the upstream and downstream fluid lines (across the sample) when in use.

Fluid flow through the sample under test is driven using two servo-controlled pump units. These enable steady-state flow-through experiments to be carried out, and are essentially identical to the volumometer system used successfully for the Heard apparatus oil pressure-controller/volumometer. This volumometer pump and the two for liquid permeametry are visible in Figures 2.8 and 2.9. A servo-controlled motor, attached to a reduction gear box, drives the piston in and out of the pump body to maintain constant pressure in the pore fluid system. The pressure signal used for control is derived from a transducer attached to a fluid line. Each controller unit (see Figure 2.10) has tuneable P.I.D. characteristics, to achieve optimum response, and will control to ~ 0.02% of the transducer full scale input. Signal conditioning and display are provided in each unit. The displacement of each pump is transmitted using a linear potentiometer (Midori, Green Pot LP-200F, non-linearity ± 0.5%) and provides the means of measuring volume changes in the fluid system to which the pump is attached. Each pump has an internal volume of about 10 ml and each turn represents a displaced volume of 0.13 ml. The conditioned output from the linear potentiometer is displayed on a chart recorder with a full stroke of the pump equivalent to 1V. Fluid pressures can likewise be displayed on chart record.

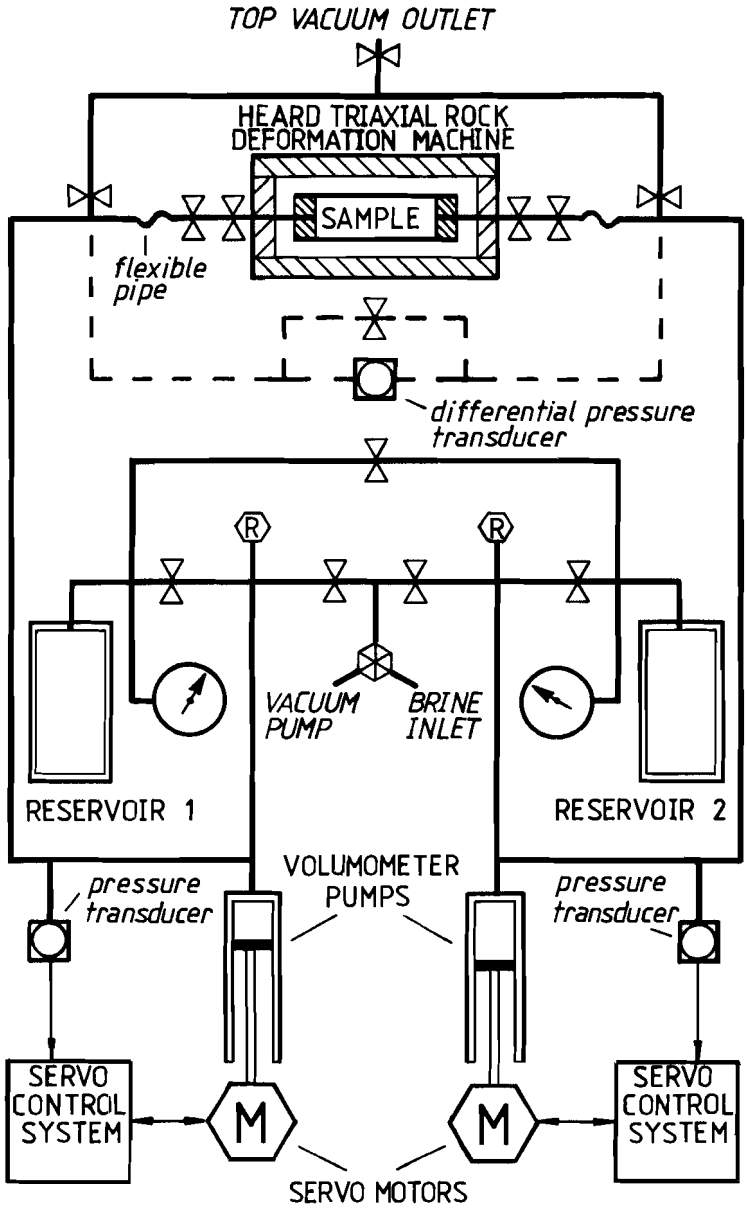

Figure 2.7. Schematic diagram of the liquid (brine) permeability system used in the present study.

Temperatures of the sample and reservoir are also recorded using Cr.Al. thermocouples in conjunction with Analogic digital thermometers that have conditioned analogue outputs for the purpose of chart recording.

2.4.3. Practice (steady-state flow method)

Permeability determination using the steady method in conjunction with a long term flow-through experiment is a relatively simple operation. The jacketed sample is first inserted into the Heard apparatus pressure vessel. Glass fibre and teflon are used against the piston end pieces as shown in Figure 2.3. In the experiments reported in this thesis, all liquid permeability measurements were done using saturated brine.

The fully saturated brine for the pore fluid is prepared by dissolving excess salt, from the same batch as the samples, in distilled water. The brine system and pumps are filled to the level of the highest valves before the flexible sample connectors, after evacuating, from the lower vacuum point. The reservoirs are filled in a similar way after evacuating them first through their bleed connectors. The full system is degassed by further evacuation from the top vacuum connection via a gas wash bottle containing some saturated brine. This also eliminates undersaturation of the system brine, due to evaporation under vacuum and slight precipitation of salt in the system pipes. When bubbles of gas no longer appear from the system into the wash bottle, the fluid is allowed to suck back into the pipework from the bottle completely filling the system.

The flexible connecting pipes are attached to the sample at the taps above the Heard apparatus after disconnecting the gas system (if used). This section is evacuated along with the sample from the top vacuum point via a wash bottle with saturated brine. The section is filled by removing the vacuum and allowing the brine to suck back into the sample.

The fluid system is now ready for use in steady-state flow determination and the sample taps are shut while the servo systems are switched on and the pumps adjusted. The reservoirs are pressurized by stroking the pumps, shutting the reservoir valves whilst restroking, to accumulate brine under pressure. When the required pressures in each reservoir are obtained, the two halves of the system are isolated by closing the link valve. The pumps are then adjusted to the required pressures with the upstream pump (higher pressure) full and the downstream pump (lower pressure) empty. The servo systems are checked for stable control and then

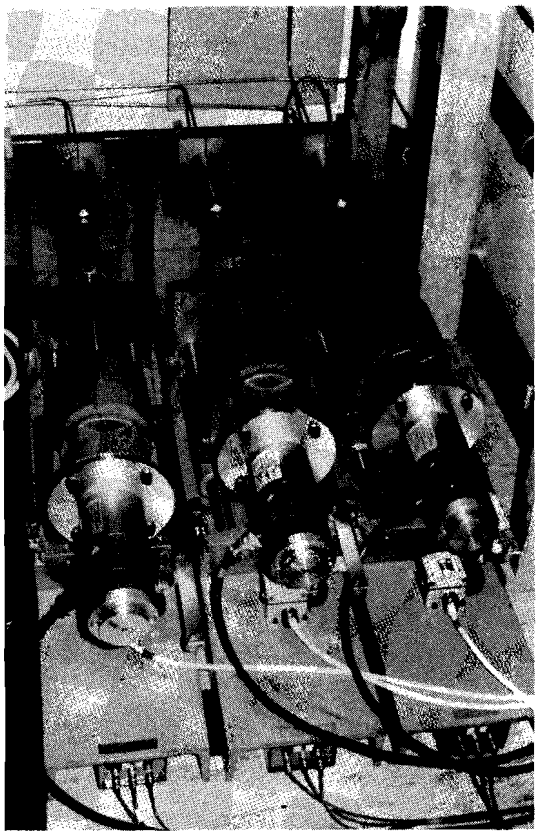

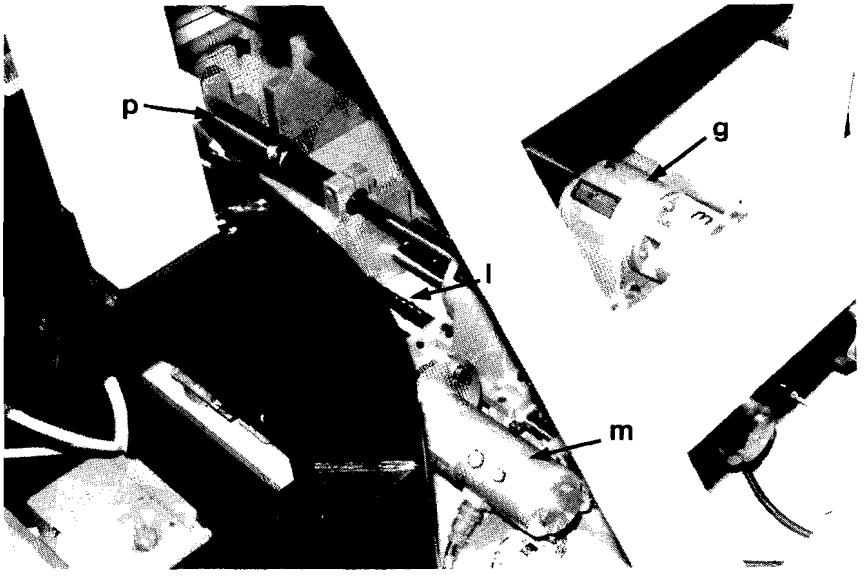

Figures 2.8 and 2.9. Two views of the servo-controlled fluid pressure / volumometer pump units (m = motor, g = gear box, p = pump body and l = linear potentiometer).

the sample taps are opened to allow flow-through. The two pumps will follow each other in compensation as the system is of constant volume when steady-state is reached. The displacement of both pumps are recorded since their opposing displacements may be used to cancel effects of temperatures on the system volume in the data reduction process. The slope of the pump displacement vs. time record is used to determine the volume flow rate through the sample and hence the permeability (using Equation 2.1 - Darcy's law). The rock sample may also be deformed simultaneously and/or subjected to various confining pressures with the brine fluid system still in operation, recording internal pore volume change and changes in permeability.

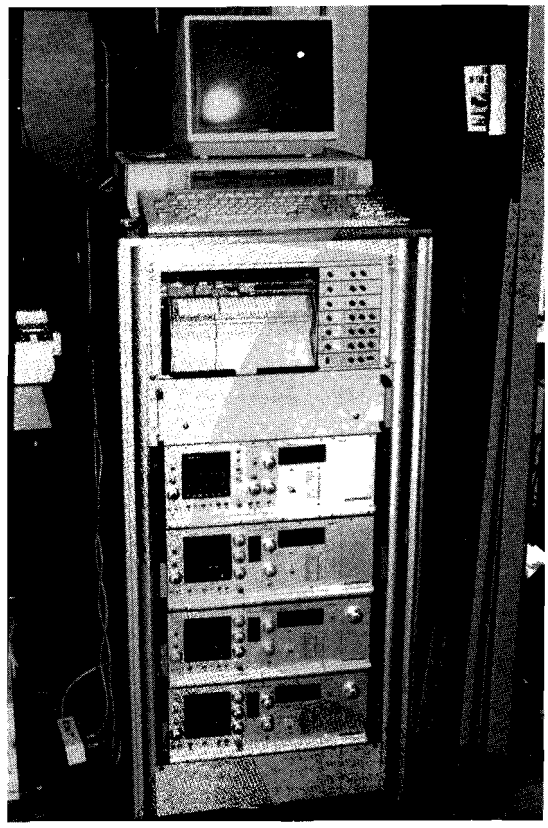

Figure 2.10. View of the electronics cabinet housing the motor drive and 3 volumometer servo-controller units (lower half) and chart recorder (upper half). The EPSON QX-16 microcomputer above was used to log the deformation experimental data.

2.5. Transient step permeametry and its application in this study

The transient step method was used in the present study to measure permeability to argon gas. The general principles of the method are first described, followed by a description of the argon apparatus used here.

2.5.1. Principles

The transient step permeability method was introduced by Brace (Brace et al., 1968) and has been developed and used by numerous experimentalists (see Sanyal et al., 1972; Zoback and Byerlee, 1975; Trimmer et al., 1980; Sutherland and Cave, 1980; Neuzil et al., 1981; Walls et al., 1982 and Bernabe, 1987). The method which entails the sudden application of a fluid pressure difference or step across a fluid saturated specimen and the monitoring of the decay with time of that pressure difference is a highly convenient and suitable method for use with salt rock. The disadvantage of the transient step test is that it is a polychromatic experiment with respect to frequency spectral content of the pore pressure transient. Hence the extraction of effective porosity data and separation of their phase lag effects at low permeability make it difficult to use on low permeability, high porosity rocks like some chalks and claystones. Ultra low permeability measurements have been made successfully to $10^{-23}m^2$ on fractured, low porosity, crystalline rocks (Trimmer, 1982).

The duration of the transient step test depends strongly, for a given permeability, upon the choice of fluid. The more incompressible and less viscous the fluid the shorter the necessary duration. As the test requires the measurement of fluid pressure in up- and down-stream reservoirs, it is actually the fluid compressibility that is most important in converting the flow to that pressure change and is therefore the most important duration-controlling factor. Figure 2.11 shows a computer simulation of how low viscosity argon gas can take longer to decay a given ΔP than more viscous, but much less compressible, liquid brine under otherwise identical conditions.

Various analyses of the transient flow problem assuming a variety of boundary conditions have been presented (see Brace et al., 1968; Hsieh et al., 1981; Lin, 1982 by numerical methods; Walls et al., 1982 and Walder and Nur, 1986). Of these Hsieh et al. produced the most general solution. They consider effects of fluid storage within the specimen porosity, and include bulk rock and matrix compressibilities as well as the effects of reservoir volume up and downstream, for

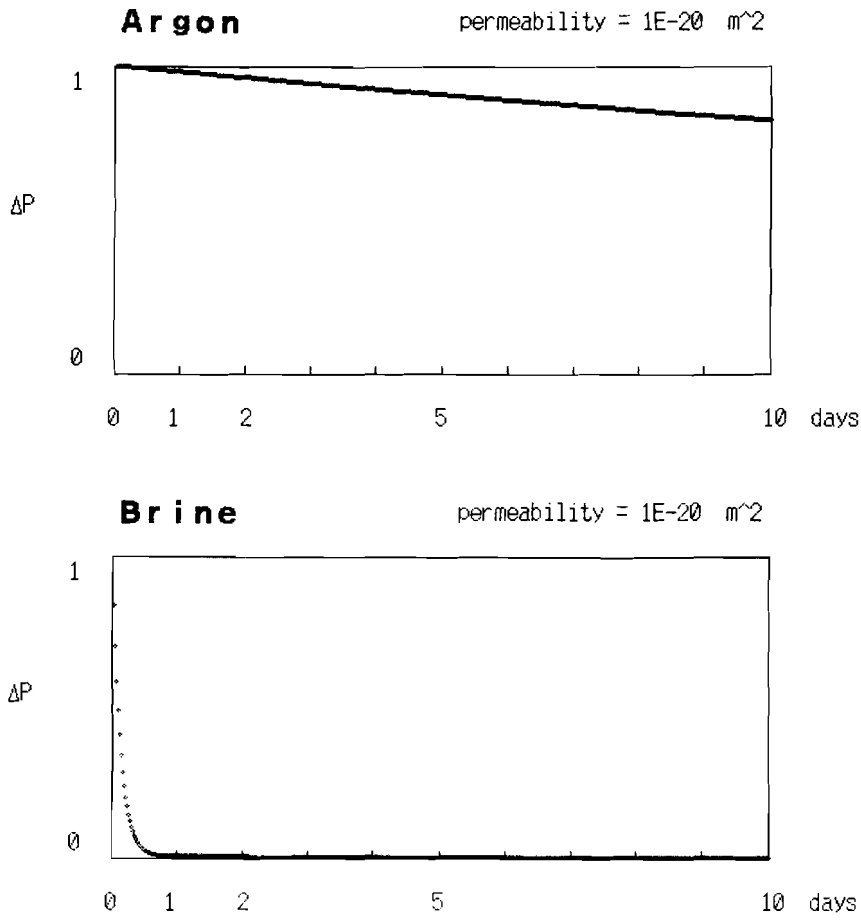

Figure 2.11. Computer simulations showing the effect of fluid type on the duration of a transient pulse decay. Normalized pressure decay versus time in days. Note that, although argon gas is less viscous, the lower compressibility of brine produces the faster decay rate and makes a permeability determination possible within a few hours rather than days (at $10^{-20}m^2$).

long and short times. For the authors' application to salt rock, however, with low porosity and simple connectivity (few occluded pores) a more simple analysis given by Sutherland and Cave (1980) was used. The results confirmed that this approach was entirely appropriate. Sutherland and Cave's analysis and method is now presented here as used by this study.

Essentially, the method involves measurement of the decay with time of a rapidly induced fluid pressure difference, applied across a specimen of known dimensions, using reservoirs (at each end of the sample) of known volume. Integrating Darcy's law, it follows that for a succession of steady-states the decay of pressure difference with time is exponential and has the form:-

$$\Delta P_t = \Delta P_o \, e^{-\alpha t} \tag{2.7}$$

where

ΔP_o = fluid pressure difference across sample at time t = 0 (the instant the pressure step is applied)
ΔP_t = fluid pressure difference across sample after an elapsed time t

$$\alpha = \frac{\kappa.A}{\mu.\beta.L} \cdot \left[\frac{V_1+V_2}{V_1.V_2}\right] \tag{2.8}$$

with

κ = permeability (m^2)
A = specimen cross sectioned area (m^2)
L = specimen length (m)
V_1 = volume of reservoir 1 (m^3)
V_2 = volume of reservoir 2 (m^3)
μ = dynamic viscosity (Argon) (Pa.S)
ß = isothermal compressibility (Argon) (Pa^{-1})

Rearrangement and application of logarithms to Equation (2.7) gives:

$$\log_e \left[\frac{\Delta P_o}{\Delta P_t}\right] = -\alpha t \tag{2.9}$$

Differentiation with respect to time then yields:

$$d/dt\ (\log_e \Delta P_o - \log_e \Delta P_t) = -\alpha \qquad (2.10)$$

Hence from a graphical plot of $\log_e(\Delta P_t)$ vs. time (t), the numerical value of the slope of the resultant line will be α. Using Equation 2.8 for α and known values of A, L, ß, μ, V_1 and V_2, the permeability (κ) may thus be obtained.

Several assumptions are inherent in the method:

i) Darcy's law for laminar flow through porous media is obeyed at all times, i.e. the flow rate is proportional to the pressure difference across the specimen and inversely proportional to the viscosity of the fluid.
ii) No boundary layer slip occurs between the fluid and the pore walls (see section on Klinkenberg effect).
iii) Pore space volume should be small relative to reservoirs.
iv) The volume of the system (pore space, reservoirs, connecting pipes, etc.) must remain constant, i.e. the compressibility of the system must be small so that the pressure changes during the experiment do not alter the system volume.
v) There should be no interaction between the fluid and the rock, i.e. no chemical reaction or electrokinetic drag effects.
vi) Temperature should remain constant.
vii) The physical properties of the fluid (viscosity, compressibility) should be independent of pressure within the range of the applied pressure step.
viii) There should be no leaks from the system or around the specimen.
ix) The sample should be in a state of equilibrium before applying the pressure step.

The conditions i, ii, v, vii outlined above are well satisfied using the noble gas Argon, as the fluid. Argon was used in all of the transient step work reported in this thesis. Its physical properties are well characterized by virial equations of state published in Cook (1961). These equations (the M.I.T. set) allow the isothermal compressibility and viscosity to be accurately calculated for the exact pressure-temperature conditions of each test.

2.5.2. Apparatus

As described in Section 2.2, the Heard triaxial deformation apparatus has the facility to allow access of fluid to the sample assembly via pipes which pass through the main vessel top closure. In principle, this allows permeability

determinations to be carried out on samples subjected to elevated confining pressure, temperature and differential stress. A gas permeability apparatus was designed and built for this purpose. This apparatus, designed for the transient step technique (Trimmer, 1982) is described below. The essential details of the apparatus are schematically illustrated in Figure 2.12. The cabinet housing the main components may be seen in the accompanying photograph, Figure 2.13.

Within the cabinet, a symmetrical arrangement of pipes and valves allows isolation of the system into two halves, each with access to one end of the sample (see Figure 2.12). The two halves may be linked for pressure equilibration purposes by a centrally located, link valve. Two reservoirs each with a volume of 2.8 l may be incorporated to provide a larger system volume when determining high permeabilities > $10^{-15}m^2$, and alternatively serve as reservoirs to aid system filling and pressure adjustment. The system may be evacuated via a vacuum pump attached to one of the vent valves. Argon (99.9% pure) is supplied from a nearby bottle and regulator. All fittings are gas tight within the limits of detection of a mass spectrometer based, helium leak detector. Any leaks were therefore inferred to represent an equivalent system permeability of < $10^{-22}m^2$. The background leak rate and the time necessary for measurement by the transient pulse technique limit the apparatus to a useful working range of ~ $10^{-12}m^2$. This adequately covers the present range of interest.

Visual indication of the gas pressure within the external part of the system (useful for filling and adjustment) is provided by two Bourdon tube gauges mounted on the front panel. Accurate measurement of pressures during the transient pulse test is achieved using two 0-2.0 MPa, bonded strain gauge type, diaphragm pressure transducers (Jensen type PE20 GL) with a non-linearity of 0.3%. The conditioning and display of the transducer signals takes place in the electronics module at the top of the cabinet. Conditioned pressure signals are monitored externally by an EPSON QX-10 microcomputer via a 12 bit resolution A/D converter, see Figure 2.14. During any given test, the computer logs the pressure at regular time intervals. It then reduces, stores and plots the data, and finally calculates the permeability.

The sample assembly is similar to that used in a normal deformation test (see Spiers et al., 1986). A sample of rock machined to a right cylinder, ~ 150 mm long and 70 mm in diameter, in the case of natural salt and 125 x 50 mm for artificial material, is jacketed in neoprene or viton sleeves, after location between steel end-pieces which act as pistons during a deformation test. The end-pieces have polished end-caps with a central hole (1 mm diameter - see Spiers et al., 1986) drilled through them to allow gas into the sample from the external circuit leading to the gas

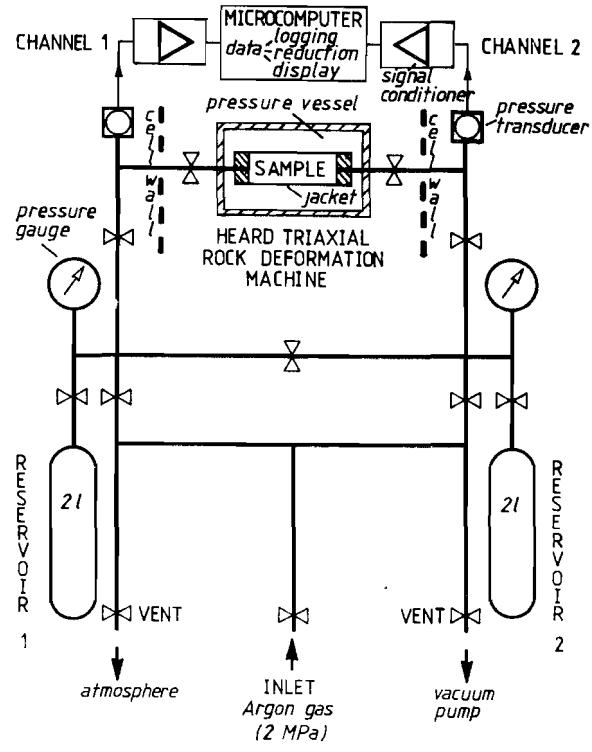

Figure 2.12. Schematic diagram of the transient step gas permeability apparatus used in this study.

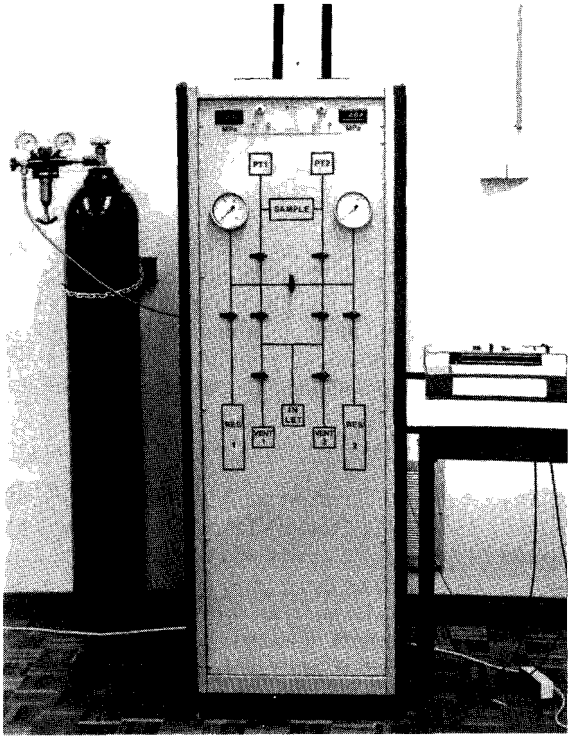

Figure 2.13. Photograph of the gas permeability apparatus.

permeability apparatus (see Figure 2.3). To facilitate free flow of gas into the ends of the sample, two sheets of glass fibre tissue are placed between the salt and a perforated "Teflon" (P.T.F.E.) sheet covering each end-cap. During deformation, the teflon sheets lower the end friction on the sample, and the glass fibre breaks apart as the sample spreads laterally. This maintains a relatively free passage for gas flowing to and from the sample. The performance of this gas distribution assembly was compared with an assembly using rigid, highly porous, sintered glass plates in the determination of permeability of a salt sample with $\kappa \approx 5 \times 10^{-16} m^2$. Both assemblies gave similar values of permeability, thus showing the flow resistance of the glass-fibre/teflon assembly to be negligible. The glass fibre/teflon assembly is preferred because of its lower sample/piston friction properties. These prevent barrelling of the salt sample during deformation. A barrelled sample will have anomalous permeability in the region of the end-caps, since the end zones may remain undilated thus preventing flow of gas into the bulk of the sample, and lowering the apparent bulk permeability value considerably.

2.5.3. Practice

The transient step method of permeability measurement is easily applied to salt rock using the apparatus described in Section 2.5.2. Once a specimen has been inserted into the Heard apparatus pressure vessel, it can be subjected to repeated permeability determinations before, during and after triaxial deformation. The usual procedure for permeametry is as follows.

Firstly, a vacuum purge of the system and specimen is carried out before filling the system with 99.9% pure Argon gas. The system is then re-purged and filled once more. This ensures the system and specimen contain only Argon gas.

The next step is to select appropriate reservoir volumes. Several reservoir volumes are available depending on which valves are utilized to close the external parts of the apparatus. The minimum volumes (V_1 = 81.2 ml, V_2 = 78.4 ml), that is only containing the pressure transducer and sample connection pipes, are normally used. These are sufficiently large to be greater than the pore volume, yet small enough to give reasonable pressure changes for the small gas influx rates encountered with low permeabilities. The volumes of the various system sections were determined using a technique based on the PVT properties of Argon and introducing an accurately known volume change to the system whilst measuring the associated pressure changes at constant temperature.

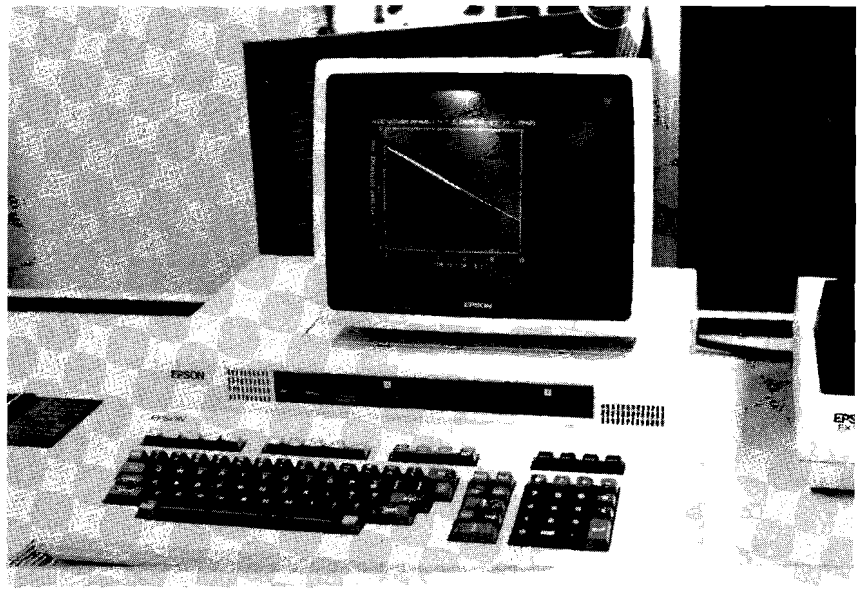

Figure 2.14. Photograph of the EPSON QX-10 microcomputer used to log and process the transient step permeametry data.

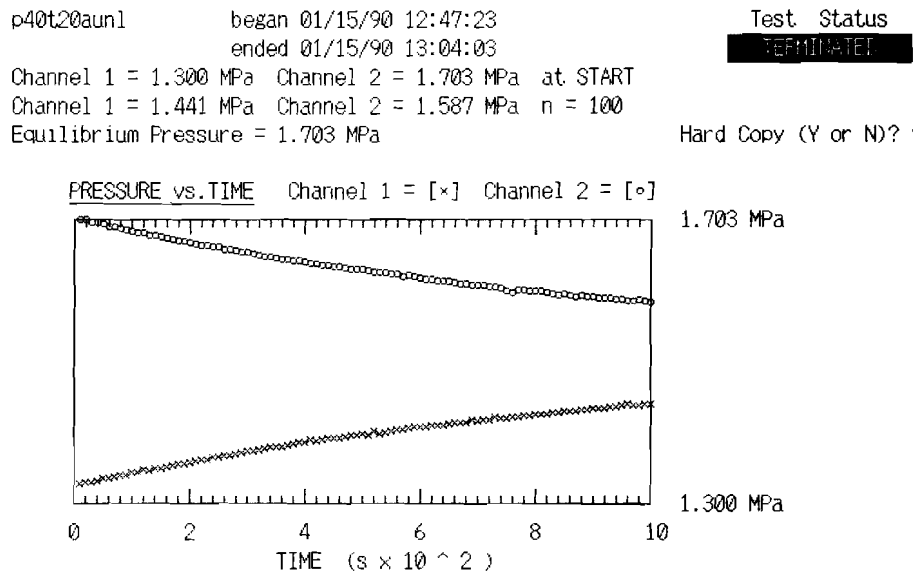

Figure 2.15. Output from the computer program PERMALOG for a synthetic rocksalt sample (P40T20) of permeability $\kappa = 2.64 \times 10^{-17} m^2$. See Figure 2.16 for test conditions.

Before any individual permeability determination, samples are allowed to equilibrate with an internal Argon gas pressure of 17.5 MPa. This is facilitated by the link tap between the two halves of the permeability system. Equilibrium is assumed when the upstream and downstream pressure transducers remain constant, after re-isolation of the apparatus halves, for at least 5 minutes. Once equilibrated, the specimen is isolated from the reservoirs by taps closest to the sample, then the pressure is adjusted in one half of the permeability system, ready for the step. The automatic data logging programme (PERMALOG) in the microcomputer is then started, and the pressure pulse is applied to the specimen by reopening the two taps. The sudden pressure change initiates the logging sequence, and the differential pressure vs. time history is recorded systematically onto floppy disk, by the microcomputer. The data is subsequently processed by a second programme (PERMAFIT), to compute the permeability. Examples of output from PERMALOG and PERMAFIT are given in Figures 2.15 and 2.16. PERMAFIT makes use of the virial equations of state for argon to calculate the appropriate compressibility and viscosity (see Section 2.5.1).

N.B. In carrying out a permeability test, an effective confining pressure of at least 0.8 MPa is generally maintained to ensure sealing of the jacket against the rock sample. A value of 0.35 MPa was found quite adequate by Sutherland and Cave (1980).

2.5.4. Klinkenberg effect

Flow of compressible gases in narrow conduits (fine pores, capillaries) is known to exhibit non-Darcian behaviour under conditions of low mean gas pressure. The flow rate is then dependent not only on the applied pressure difference (Darcy's law) but also on the mean pressure of the gas, with the result that gas permeametry of finely porous material often yields significantly higher permeability values than those obtained from liquid permeametry. These observations have been explained, using the kinetic theory of gases, by the mechanism of "slip". The mean velocity of gas molecules at the conduit wall boundary becomes non-zero when slip occurs, and an additional downstream component of flow results as the bulk of the flowing gas slips along the conduit boundary. (N.B. Pure Darcian flow behaviour requires linear viscous, laminar flow parallel to the walls of the conduit where the mean velocity at the wall boundary is zero). In extremely narrow capillaries at very low pressures (near vacuum), the passage of gas may be entirely by molecular streaming - an extreme case of slip which is a non-viscous, diffusive process called Knudsen flow (Dullien, 1979).

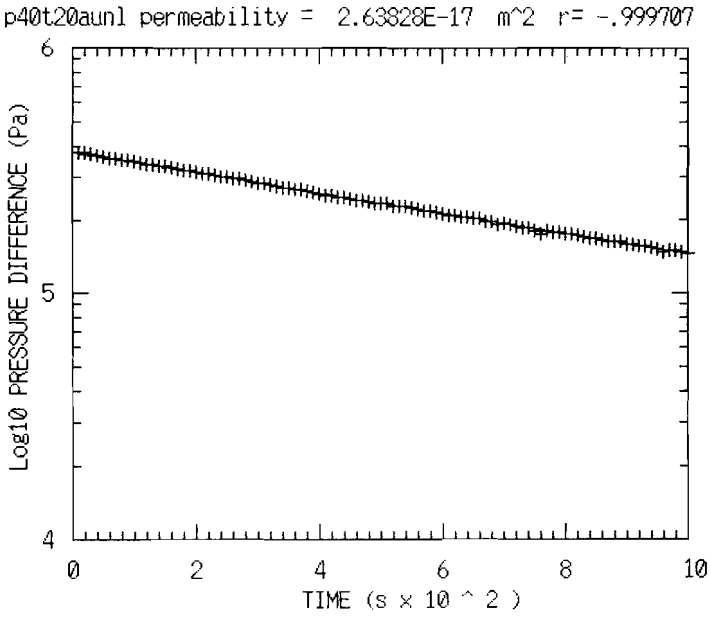

test temperature = 20 celsius
argon equilibrium pressure = 1.70313E+06 Pa
argon compressibility = 6.25411E-07 Pa^-1 at mean pressure = 1.51432E+06 Pa
gauge zero = 101325 Pa (above are gauge pressures)
argon viscosity = 2.25504E-05 Pa.s
pressure pulse =-379958 Pa
reservoir volumes : v1 = 7.17189E-05 m^3 , v2 = 7.04075E-05 m^3
number of data points = 100
test began 01/15/90 12:47:23
test ended 01/15/90 13:04:03

Figure 2.16. Output from the computer program PERMAFIT for a synthetic rocksalt sample (P40T20) of permeability $\kappa = 2.64 \times 10^{-17} m^2$. The permeability was determined at a confining pressure of 10 MPa and mean (argon gas) pore fluid pressure of 1.5 MPa, using a 0.2 MPa step for the argon gas pressure transient. The determination was made immediately after a shortening deformation at a constant axial strain rate of $\sim 4 \times 10^{-5} s^{-1}$ to 9.2% axial strain and 0.5% dilatant volume change at the same confining pressure. The axial load was removed before the start of the permeability test.

The phenomenon of slip (investigated by Klinkenberg; 1941) is related to the mean free path of the flowing gas molecules and contributes most to the flow when the conduit diameter is smaller than the mean free path, and when the gas pressure is low and the mean free path relatively large. Argon gas at the typical temperature and pressures used in these tests (20°C, 1.5 MPa) has a mean free path of the order of 5 nm. Low permeability rock salt samples with narrow pathways of this magnitude will and do show some slight effects of slip.

The effect of slip was investigated in the present study using the recommended approach outlined by Klinkenberg (Klinkenberg, 1941) and the American Petroleum Institute code of practice (A.P.I. RP27, 1956). This involves determination of the apparent permeability to gas of a sample, at constant pore structure, at different mean gas pressures. The pressure dependence of gas permeability, due to slip, will show a linear relationship between apparent permeability (κ_A) and the reciprocal of the mean gas pressure (P_m), of the form

$$\kappa_A = \kappa (1 + b/P_m)$$

where b is the Klinkenberg constant.

The true (inert liquid) permeability (κ) may be obtained from extrapolation of the linear trend to infinite pressure ($1/P_m = 0$).

As the gas permeameter was intended for use with salt rock in this study, two samples representing the likely range of permeabilities to be encountered were tested to check for the possible presence of the Klinkenberg effect. A salt rock sample (SP143) with a low permeability ($10^{-19}m^2$), and most likely to show slip phenomena, was subjected to gas permeametry at several mean gas pressures. The mean pressure dependence was small - see Figure 2.17, lower plot. The line (least squares best fit) is drawn through the solid circles which represent determinations made at constant effective confining pressure and presumed constant pore structure. The apparent permeability at the gas pressures normally used differed by less than 8% from the liquid permeability, and therefore slip, although present, does not significantly affect the permeability measurements down to $10^{-19}m^2$. The alteration of pore structure due to changes in effective confining pressure can also be seen in Figure 2.17 (open circles).

A similar set of permeability determinations carried out with constant external confining pressure on a salt rock sample (SP107) of much higher permeability (~ $10^{-16}m^2$), (Figure 2.17 upper plot), showed no apparent effects of slip, but did show

considerable variation in permeability due to alternations in pore structure as a result of changes in effective stress. Despite the scatter, the extrapolated liquid permeability value differs by less than 5% from values determined at normal test pressures.

The effect of slip at the limit of the transient step apparatus resolution ($\equiv 10^{-21}m^2$) has not been checked due to lack of available time (each permeability tests lasts tens of days). Therefore, determinations of gas permeability $< 10^{-20}m^2$ must be viewed as upper bounds (probably slight overestimates) on the true, inert liquid permeabilities.

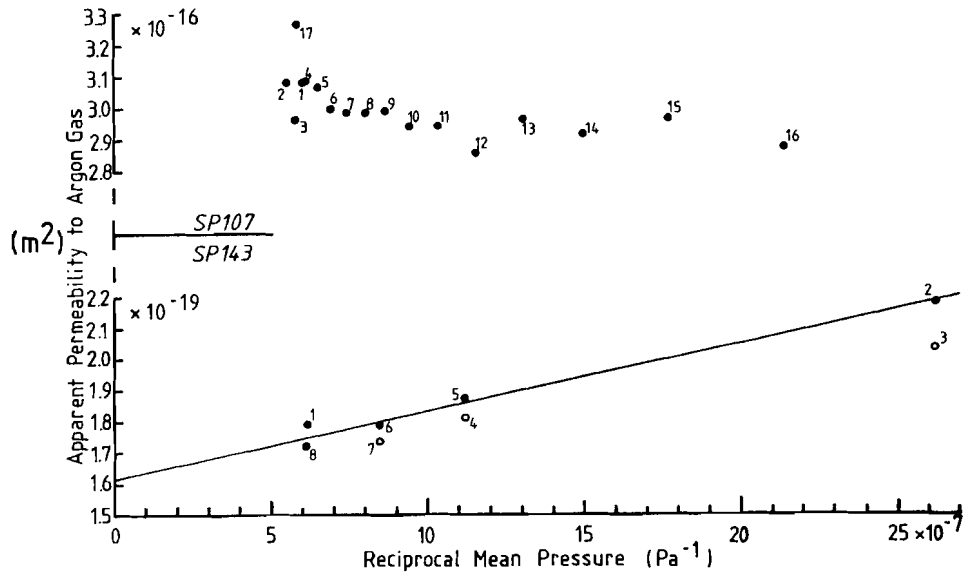

Figure 2.17. The results of two sequences of permeability determinations for two Asse salt rock specimens SP107 and SP143 (see Peach et al., 1987) of substantially different permeability carried out with various mean argon gas pressures, to determine the Klinkenberg effect.

CHAPTER 3

Experiments on Natural Salt Rock

3.1. Introduction

As described in Chapter 1, the brine/gas transport properties of salt rock, and the influence of deformation and microstructural change upon these properties, are of fundamental importance in determining the performance of radioactive waste repositories and storage caverns sited in salt formations. While it is well-established that the permeability of undisturbed natural salt rock is very low (Gloyna and Reynolds, 1961; Sutherland and Cave, 1980 and Baes et al., 1983), little quantitative information exists regarding the influence of deformation and complex stress histories on the permeability of natural salt. The present chapter documents permeability measurements performed on natural salt rock from the Asse mine, Germany, and on experimentally deformed samples of this material. Firstly, the natural starting material is characterized with respect to microstructure and initial permeability. A series of experiments designed to investigate permeability development during plastic deformation (dislocation glide field - Skrotzki and Haasen, 1988), under conditions allowing minor dilatancy, is then described. Lastly, hydrostatic experiments intended to assess the permeability persistence/decay characteristics of dilated Asse salt are reported.

3.2. Natural starting material: characterization

3.2.1. Source and handling

The salt rock used in the present experiments was obtained, courtesy of Prof. H. Gies, from the Asse II Mine, Remlingen, Germany. The material was taken from the Speisesalz (Na2Sp) formation of the Staßfurt Halite evaporite series (Zechstein Z2 cycle of the late Permian). It was extracted, by the Asse Mine staff, from the 800 m level of the mine, in the form of 110 mm diameter cores drilled horizontally into the gallery wall. The cores were drilled dry and handled with extreme care. The source position of each length of core recovered was accurately recorded by the mine staff, paying particular attention to depths with respect to the gallery wall. After transport to Utrecht, the cores were stored in a low humidity room (RH $\leq$

15%) and were subsequently machined into cylindrical samples (70 mm diameter by 157 mm length) suitable for testing.

3.2.2. Composition and microstructure

A detailed description of the Asse Speisesalz used here can be found in Spiers et al. (1986) or Spiers et al. (1988). For this reason, only a brief description is now given with a number of relevant additions.

The material is a colourless, almost pure halite rock (> 98% NaCl) as the name "Speisesalz" might suggest. It has an average grainsize in the range 3-10 mm and possesses a slight grain-shape fabric (see Figure 3.1). The main impurity phase (~ 1%) is polyhalite ($K_2SO_4.MgSO_4.2CaSO_4.2H_2O$) which occurs as small (0.05 - 1.0 mm) euhedral crystals, often twinned, and frequently concentrated near halite grain boundaries (Figure 3.1). Minor amounts of anhydrite are also present. The halite grains exhibit a range of morphologies from equiaxed/sub-idiomorphic to irregular, lobate and coarsely serrated or bulged. Nonetheless, many triple point grain boundary junctions approach equilibrium (120°) configuration. Grain boundaries are often filled with fluid inclusions containing both brine and gas. In addition, fluid inclusion trails can often be seen traversing individual grains. The total water content is small (0.05 - 1 wt% - Spiers et al., 1986) and over half can be attributed to the water of crystallization of the polyhalite. The remainder is present as brine in the inclusions and in fluid films in grain boundaries and triple junctions. Very few cracks are present in the virgin material taken from depth > 3 m from the gallery wall. Etched and polished sections of this material, prepared using the techniques described by Urai et al. (1987), reveal very little internal dislocation structure and indicate low dislocation densities. High internal strain features such as slip bands and kink bands (indicative of dislocation glide mechanisms - Carter and Hansen, 1983) are almost entirely absent. Roughly half of the grains exhibit a well developed subgrain structure with a mean subgrainsize of ~ 200 μm (see Figure 3.2). Subgrain structure is often concentrated around stress intensifiers such as polyhalite grains. Substructure-free grains are often seen to have replaced grains containing substructure, thus implying recrystallization. Material taken from near the

---

Figure 3.2. Reflection optical micrograph showing subgrain structure typically developed in the Asse Speisesalz. Note substructure free grains (g) also, and grain boundary fluid inclusions (arrowed).

Figure 3.1. Dark field optical micrograph showing the general microstructural nature and grain shape fabric of the Asse Speisesalz. Note the polyhalite lathes (p) occurring at grain boundaries.

10 mm

Figure 3.2.

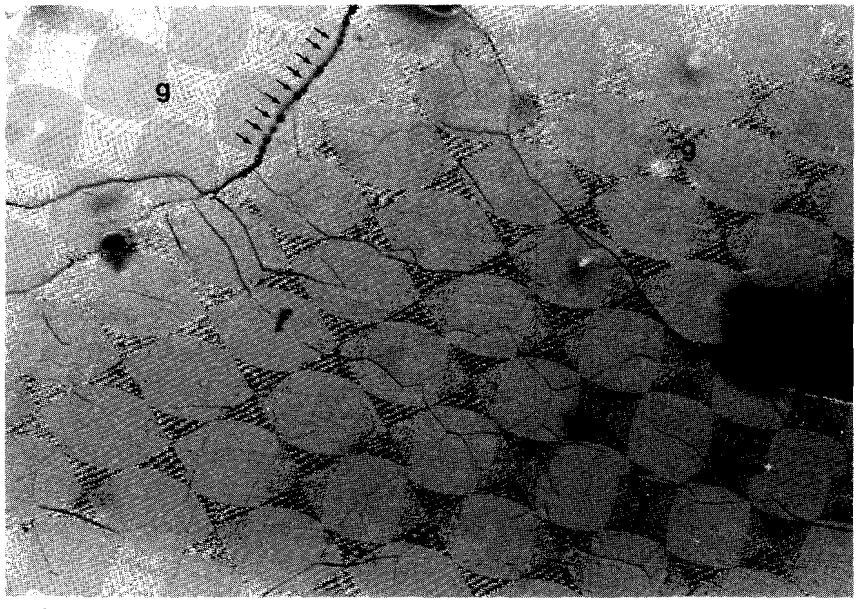

200 μm

gallery wall is essentially similar but shows high internal strain dislocation etch features and some microcracking presumably related to gallery convergence under higher deviatoric stress, within the "dislocation glide" deformation mechanism field (see Figure 1.2).

On the basis of the above, the microstructure of Asse II Speisesalz in the undisturbed condition is interpreted by Urai et al. (1987) to be a dynamically recrystallized microstructure that may have resulted from brine assisted grain boundary migration operating in combination with dislocation creep and perhaps pressure solution under relatively low flow stresses (0.5 - 1.5 MPa, see Spiers et al., 1986; Urai et al., 1987 and Spiers et al., 1990).

Constant strain rate triaxial tests performed on the Speisesalz material by the present author (a detailed account of which is beyond the scope of this thesis - see Spiers et al., 1989) have shown that at elevated temperatures (150°C), low strain rates ($3.5 \times 10^{-7} s^{-1}$) and relatively high confining pressure (> 6.5 MPa), steady state creep is achieved as a result of glide and recovery by dynamic recrystallization. The dynamically recrystallized microstructure shows fluid-assisted grain boundary migration, coupled with dislocation glide/creep substructures and is very similar to the microstructure of the natural material. This strongly supports the interpretation that the natural microstructure is dynamically rather than statically recrystallized (a point of controversy in recent literature).

3.2.3. Permeability measurement

Argon gas transient step permeametry was performed on "Viton ®" fluoroelastomer jacketed samples under confining pressures in the range 2.5 - 7.5 MPa at room temperature. The Heard triaxial apparatus plus permeameter described in Chapter 2 were used. A mean argon gas pressure of 1.5 MPa and a step of 0.2 MPa was generally used for the permeametry. Matted glass fibre/tissue gas spreaders and perforated 0.05 mm thick "teflon ®" (P.T.F.E.) end sheets were employed to minimize specimen/piston boundary effects. All permeability determinations were made in the direction of the original cores, which is also the direction of maximum shortening in subsequent deformation experiments. No permeability anisotropy effects could therefore be detected.

A single sample (SP143) of undeformed material with low permeability was used to check for the Klinkenberg effect in making the present measurements (see Chapter 2). Under the assumption that the pore structure of the test material is constant at

constant conventional effective pressure, this effect was found to be negligible (< 8% at $10^{-19}m^2$) for the purposes of practical permeametry. Justification for this assumption emerges from Section 3.2.5. In the present context, conventional effective pressure P_e^* is defined as $P_e^* = P_c - P_f$ where P_c is confining pressure and P_f is the pore fluid pressure.

3.2.4. Permeability data and preliminary discussion

Despite great care in core handling, a considerable scatter in gas permeability values was recorded in the starting material - see Figure 3.3 and Table 3.1. Assuming the cores themselves have not been greatly damaged, this scatter reflects two trends:-

i) Firstly the magnitude of the permeability is strongly dependent on the effective conventional confining pressure to which the machined cores were subjected, during permeametry. The variation in measured permeability, to argon gas, of a single sample (SP136) with three different confining pressures may be seen in Figure 3.3 (data sets k, l, m). The trend indicated shows a decreasing sensitivity of measured permeability to confining pressure, above 10 MPa. Extrapolation of this trend to the lithostatic pressure expected for undisturbed Asse salt at 800 m depth (≈ 18 MPa) suggests an "in-situ" permeability value of 3 x $10^{-21}m^2$ for this particular sample. The measured decrease of permeability with increasing confining pressure is interpreted as being mainly due to the elastic closure of cracks and voids. This interpretation is based on the observation (in short term tests) that the permeability is recoverable during hydrostatic unloading in the pressure range 0 - 10 MPa. The cracks and voids were probably produced by unloading or damage during exhumation of the core samples from the mine, and/or by dilational creep (in samples near gallery walls).

   N.B. The dependence of measured permeability upon confining pressure reported here demonstrates that it is only meaningful to compare permeabilities of different samples at similar combinations of P_c and P_f.

ii) Secondly, the position of core material relative to the mine gallery wall also appears to affect the magnitude of the gas permeability in a systematic way. The highest permeabilities for cores under a given confining pressure correlate with cores known to have been extracted from near the gallery wall and which have certainly undergone dilational creep. The lowest permeabilities correlate with cores deeper in the bore hole sequences, and represent less disturbed salt rock. In Figure 3.3 determinations a, b and e are examples of wall rock material,

Table 3.1. Asse Speisesalz starting material: Permeability to argon gas (see accompanying Figure 3.3).

Core	Specimen No.	Distance from Gallery Wall (cm)	Mean Argon Gas Pressure (MPa)	Confining Pressure (MPa)	Permeability (m^2)
B3/2	BGR6 (a)	21 - 50	1.537	2.5	4.654×10^{-19}
B3/2	BGR6 (a)	21 - 50	1.532	2.5	4.316×10^{-19}
B3/1	BGR5 (b)	0 - 21	1.563	2.5	3.376×10^{-18}
B3/1	BGR5 (b)	0 - 21	1.530	2.5	3.754×10^{-18}
B3/3B	BGR4 (c)	63 - 96	1.536	2.5	8.006×10^{-21}
B3/3B	BGR4 (c)	63 - 96	1.523	2.5	1.944×10^{-20}
B4/6B	BGR3 (d)	195 - 236	1.542	2.5	9.935×10^{-21}
B4/6B	BGR3 (d)	195 - 236	1.531	2.5	2.006×10^{-20}
B4/1A	SP143 (e)	0 - 37	1.533	5.0	1.789×10^{-19} #1
B4/1A	SP143	0 - 37	0.281	3.8	2.172×10^{-19} #2
B4/1A	SP143	0 - 37	0.281	5.0	2.025×10^{-19} #3
B4/1A	SP143	0 - 37	0.778	5.0	1.807×10^{-19} #4
B4/1A	SP143	0 - 37	0.778	4.2	1.870×10^{-19} #5
B4/1A	SP143	0 - 37	1.079	4.6	1.784×10^{-19} #6
B4/1A	SP143	0 - 37	1.078	5.0	1.732×10^{-19} #7
B4/1A	SP143 (e)	0 - 37	1.535	5.0	1.720×10^{-19} #8
B4/1A	SP143	0 - 37	1.535	20.0	2.296×10^{-20} #9
B2/7A	SP142 (f)	269 - 316	1.534	5.0	2.504×10^{-21}
B4/5A	SP141 (g)	155 - 195	1.533	5.0	1.245×10^{-21}
B4/4A	SP140 (h)	109 - 155	1.532	5.0	2.733×10^{-21}
B4/3A	SP139 (i)	77 - 109	1.535	5.0	1.923×10^{-21}
B4/2A	SP138 (j)	37 - 77	1.533	5.0	2.241×10^{-21}
B2/5A	SP137	179 - 224	1.531	5.0	2.280×10^{-23}*
B1/1	SP136 (k)	0 - 45	1.542	2.5	7.688×10^{-20}
B1/1	SP136 (k)	0 - 45	1.527	2.5	8.970×10^{-20}
B1/1	SP136 (l)	0 - 45	1.530	5.0	1.044×10^{-20}
B1/1	SP136 (l)	0 - 45	1.520	5.0	1.405×10^{-20}
B1/1	SP136 (m)	0 - 45	1.534	7.5	8.726×10^{-21}
B1/1	SP136 (m)	0 - 45	1.520	7.5	9.399×10^{-21}
B1/1	SP136 (m)	0 - 45	1.532	7.5	4.195×10^{-21}

* below resolution of apparatus, certainly $< 1 \times 10^{-21} m^2$.

N.B. a) Points a, b, c, d and e in Figure 3.3 are mean values of data so marked here.
b) All pressures are gauge pressures; zero = 1 atmosphere (101325 Pa).
c) Permeabilities are not corrected for the Klinkenberg effect.
d) #1 - #9 refer also to Figures 3.9 and 3.10.

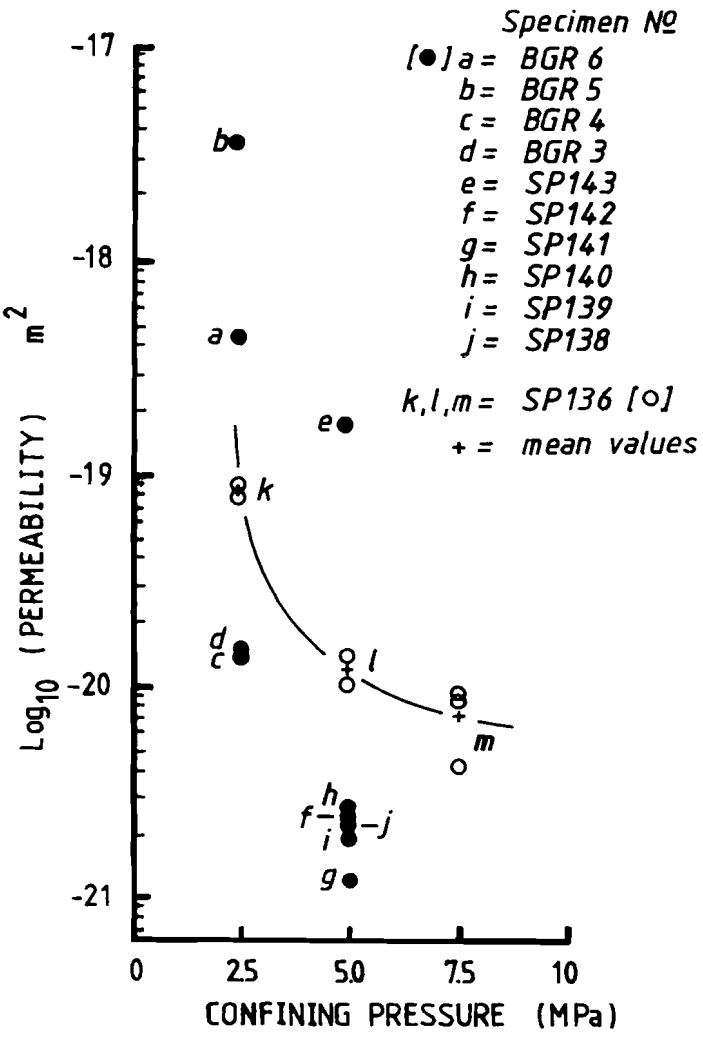

Figure 3.3. Permeability determinations for Asse Speisesalz starting material showing sample variation and influence of confining pressure.

determinations f, g, h, i and j are examples of deeper material. A detailed comparison of argon gas permeabilities at two confining pressures, for cores of known position, has been carried out using the available drilling records. This data is shown in Figure 3.4 using the original core numbers, for four closely spaced cores (B1 - B4) drilled horizontally into the gallery wall at the Asse

mine. Open rectangles represent determinations at confining pressures of 2.5 MPa (1.0 MPa effective), and black rectangles represent those at 5.0 MPa (3.5 MPa effective). Determination B2/5A, marked with an asterisk, lies beyond the resolution of the apparatus (i.e. less than $10^{-22}m^2$) and is therefore not reliable, though it may be assumed with certainty to be below $10^{-21}m^2$. The rapid decrease in permeability with depth, inwards from the gallery wall, is clear and is indicated by the trend lines.

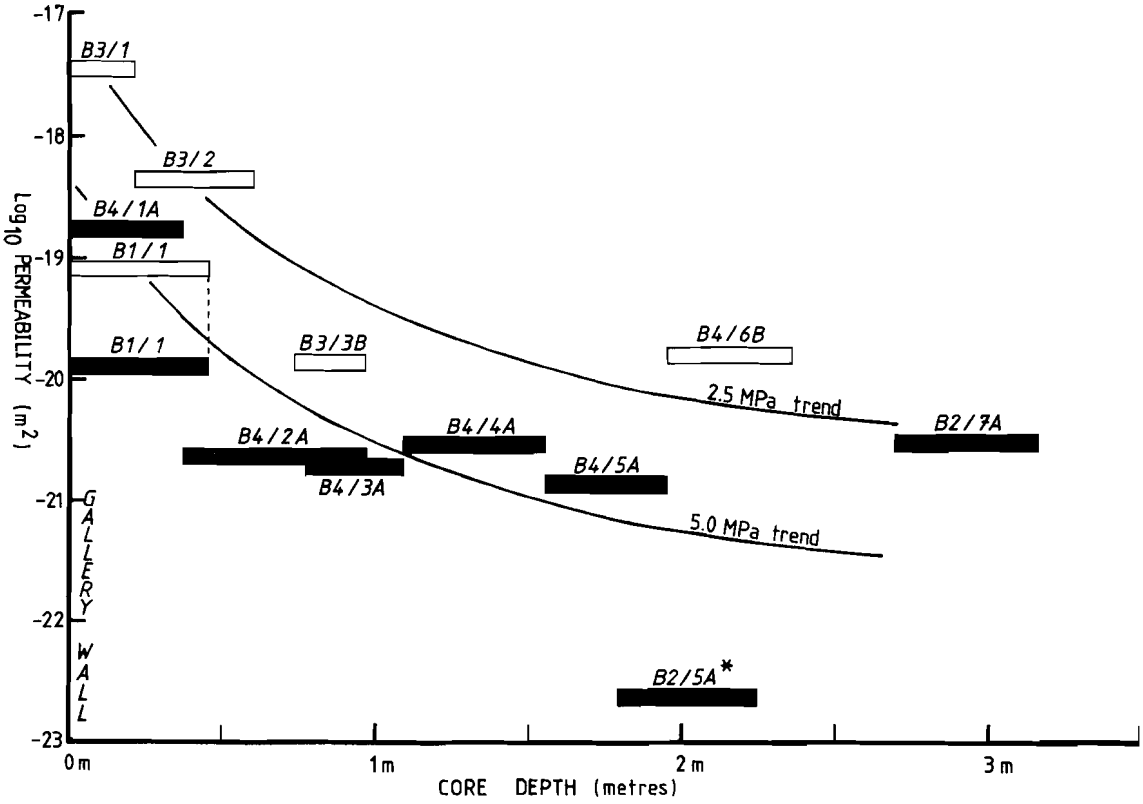

Figure 3.4. Argon gas permeability, determined in the laboratory versus core extraction depth measured horizontally from the gallery wall at the Asse Mine 800 m level (Speisesalz Formation).

3.2.5. Further analysis

A more detailed analysis of the permeability dependence upon confining pressure (P_c) and pore fluid pressure (P_f) seen in the tests on near wall material (Asse samples SP136 and SP143) will now be attempted. This analysis is based on comparison of the results with the model developed by Walsh (1981) relating permeability change in a cracked (elastic) medium to generalized effective pressure change.

Conventional effective pressure (P_e*) used to describe the pressure dependence of some physical property (e.g. porosity, microcrack dilatancy, or, as in this case, permeability), in a fluid filled porous medium is simply defined as

$$P_e^* = P_c - P_f \tag{3.1}$$

(see Brace, 1972, for review). The more generalized effective pressure (P_e) is defined as

$$P_e = P_c - s \, . \, P_f \tag{3.2}$$

(see Nur and Byerlee, 1971) where s is a factor depending upon the physical property in question. When a property does not vary linearly with P_c or P_f then effective pressure does not in general have any simple analytic expression (Robin, 1973).

In the Walsh model, permeability change occurs essentially as a result of crack aperture variation, this being determined by an assumed Hertzian response of loaded asperities on crack walls. Walsh derives an expression for the variation in fluid conductance for a single fracture. This may be simply extended to describe the variation in macroscopic permeability of a body containing many linked fractures assumed to be uniformly distributed in a macroscopically non-tortuous network. Walsh's relation for the average permeability change of such an ideal body's response to changes in effective stress is given

$$\frac{\langle \kappa \rangle}{\langle \kappa_o \rangle} = \left[1 - \frac{\sqrt{2}\,h}{a_o} \log_e \left(\frac{P_e}{P_{e_o}} \right) \right]^3 \left[\frac{1 - b(P_e - P_{e_o})}{1 + b(P_e - P_{e_o})} \right] \tag{3.3}$$

where κ is the macroscopic permeability at a generalized effective pressure, P_e. Permeability, κ_o, and effective pressure, P_{e_o}, describe a reference state where the

average fracture half aperture is $\langle a_o \rangle$, b is a constant and h is the rugosity or fracture roughness, see Figure 3.5 for definition. The two bracketed terms on the right hand side of this relation describe the pressure dependence of aperture related parameters [1st bracket] and crack surface tortuosity parameters [2nd bracket]. The model embodies a cubic relation ($\kappa \propto d^3$) between the permeability and the crack aperture or crack width (d) due to the incorporation of a parallel plate flow model. Such a parallel plate model was tested by Brown (1987) by computer simulation of fracture flow behaviour between randomly generated rough (fractal) surfaces in contact and found to be applicable to within a factor of 2. The Walsh model also embodies a linear relation between fracture asperity contact area fraction (α) and effective pressure ($d\alpha/dP_e$ = constant), and also an inverse logarithmic relation between fracture aperture (a) and effective pressure ($da/dP_e = -\sqrt{2}h/P_e$). Both relations arise from a Hertzian contact model for the interaction between opposing fracture surfaces in contact under load (Walsh and Grosenbaugh, 1979).

Now for reasonable rugosity amplitudes (h) and surface correlation "wavelengths" and for the pressures of present interest, it is easily shown (see Walsh 1981) that the tortuosity term in Equation 3.3 is approximately equal to 1, i.e. the crack face tortuosity does not change significantly with effective pressure. Thus Equation 3.3 can be rewritten

$$\left(\frac{\langle \kappa \rangle}{\langle \kappa_o \rangle}\right)^{\frac{1}{3}} = [B] - [A]\,[B]\,\log_e\left(\frac{P_e}{P_{e_o}}\right) \tag{3.4}$$

where $[A] = \sqrt{2}h/\langle a_o \rangle$ and $[B] \approx 1$.

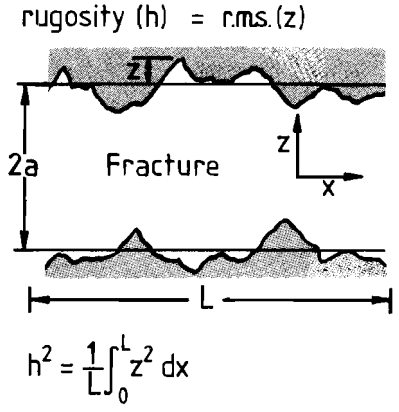

Figure 3.5. Definitions used to describe fracture aperture (a) and rugosity (h).

In principle, the applicability of this model to the pressure dependent permeability behaviour seen in the Asse samples SP136 and SP143 can now be assessed by plotting the κ and $P_e = (P_c - s \, . \, P_f)$ data obtained for these samples in a diagram of $(\langle\kappa\rangle/\langle\kappa_o\rangle)^{1/3}$ vs. $\log_e(P_e/P_{e_o})$. Since an effective stress relation for the samples is not known, this plotting exercise is first carried out taking $P_e = P_c - P_f$, i.e. with s = 1. The results obtained are shown in Figures 3.6 and 3.7. In both cases, reasonable straight lines were obtained and a linear best fit was constructed. The tortuosity terms (intercept) thus determined were both close to unity, consistent with the model (Equation 3.4), see Table 3.2.

Table 3.2. Results of fitting the Walsh model (Equation 3.4) to permeability vs. effective pressure data from Asse salt samples SP136 and SP143 assuming an effective pressure law of the form $P_e = P_c - s.P_f$. Best fit lines of form $y = c - m\log_{10}x$ where $y = (\kappa/\kappa_o)^{1/3}$, $x = (P_e/P_{e_o})$, $c = [B]$, $m = [A][B]$, $[A] = \sqrt{2}\, h/\langle a_o\rangle$ and $[B] =$ ("tortuosity term")$^{1/3}$, see Equation 3.4.

Specimen	s	[A]	[B]	$h/\langle a_o\rangle$	$\langle\kappa_o\rangle$ m^2	P_e MPa
SP136	1	0.5338	1.1054	0.377	1.2245×10^{-20}	3.48
SP143	1	0.2939	1.0409	0.208	1.7585×10^{-19}	3.47
SP143	0.5	0.3248	1.0151	0.230	1.7585×10^{-19}	4.28
SP143	0	0.3513	0.9950	0.248	1.7585×10^{-19}	5.10
SP143 *	1	0.3558	1.0195	0.252	1.6257×10^{-19}	3.47
SP143 *	0.5	0.3889	0.9877	0.275	1.6257×10^{-19}	4.28
SP143 *	0	0.4159	0.9638	0.294	1.6257×10^{-19}	5.10

* Klinkenberg corrected, i.e. κ_o is the interpolated "ideal liquid" permeability.

The results presented above suggest that the Walsh model offers a reasonable description of the experimental data for samples SP136 and SP143, assuming that $s \approx 1$ in the relation $P_e = P_c - s \, . \, P_f$ and not correcting for the Klinkenberg effect. This assumption is equivalent to assuming that the pore structure is constant at constant conventional effective pressure, $P_e = P_c - P_f$. It is supported by the fact that the κ vs. $1/P_f$ data obtained for SP143 and constant P_e (s = 1, $P_e^* = 3.5$ MPa) are closely consistent with the linear relation predicted by the Klinkenberg theory (see Chapter 2 and Figure 3.8), which itself assumes constant pore structure.

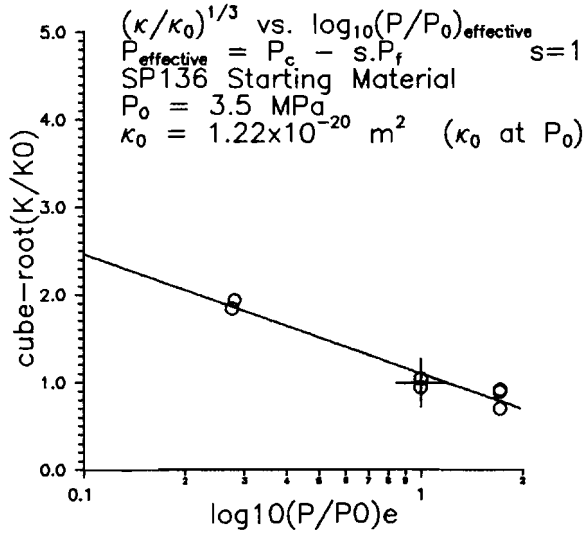

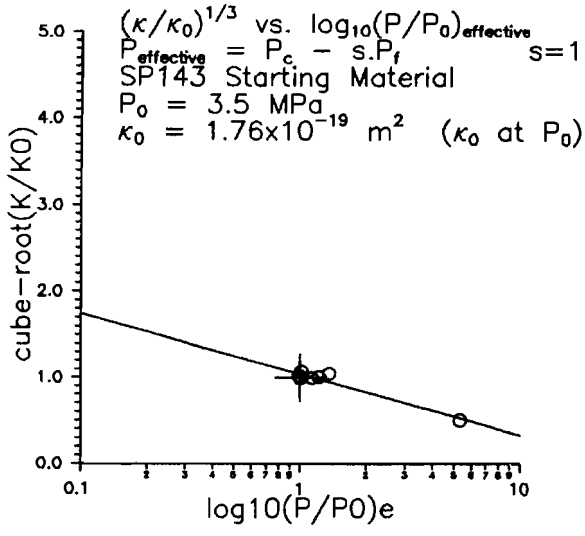

Figures 3.6. and 3.7. Plots of permeability change versus conventional effective pressure change relative to reference states κ_0 and P_0 (marked with +) for Asse starting material. $(\kappa/\kappa_0)^{1/3}$ is plotted against $\log(P/P_0)$ in accordance with the Walsh model. Figure 3.6 shows data for sample SP136 and Figure 3.7 shows data for SP143.

Furthermore, if the Walsh model (Equation 3.3) is applied to predict the κ vs. P_f behaviour of SP143, assuming no Klinkenberg effect and taking $s < 1$, $\kappa_o = 1.7585 \times 10^{-19} m^2$ at $P_e^* = 3.466$ MPa (conventional effective pressure, $s = 1$) and calculating the equivalent P_e for $s < 1$ knowing P_c and P_f, highly non-linear curves for fixed values of s (0, 0.5, 1) are predicted (see Figures 3.8 and 3.9) with the limiting straight line $\kappa = \kappa_o$ being approached only when $s \approx 1$ (see Figures 3.8, 3.9).

The implication is that the observed linear κ vs. $1/P_f$ behaviour at constant P_e^* can be explained only by the combined requirement that $s \approx 1$ and that a minor Klinkenberg effect occurs, with a positive coefficient $b = 0.1297$ (MPa), (see Figures 3.8 and 3.9). If the Walsh model was to apply exclusively, then changing κ_o at constant P_e would not shift the predicted curves as it does between Figures 3.8 and 3.9.

The inferred Klinkenberg effect for SP143 is clearly very small (~ + 8.6% error in κ at $1 \times 10^{-19} m^2$ and 1.5 MPa mean argon gas pressure; based on mean free path ($\langle\lambda\rangle$) calculations for argon gas at these conditions ($\langle\lambda\rangle \approx 5$ nm) and "cubic law" of permeability variation with aperture ($\kappa \propto d^3$) this error could rise to ~ + 47% relative to a much lower permeability, $\kappa = 1 \times 10^{-21} m^2$). For most practical purposes of κ measurement in natural salt rock ($\kappa > 10^{-20} m^2$), it is therefore justifiable to neglect the effect. Notably, the true liquid permeability value (κ_L, shown in Figures 3.8 and 3.9) obtained for SP143 at $P_c - P_f = 3.5$ MPa (by extrapolation of the κ vs. $1/P_f$ line to $1/P_f = 0$, see Chapter 2) was $1.62 \times 10^{-19} m^2$.

Removing the Klinkenberg effect from the experimental data and replotting the corrected values in a similar manner to Figures 3.6 and 3.7 (see Figure 3.10 and Table 3.2), yields only minor changes in the fitted parameters [A] and [B] in the Walsh model applied for $s = 1$. Notably [B] remains ≈ 1. The natural salt data are therefore consistent with the Walsh fracture aperture variation model following a conventional effective stress law ($s \approx 1$) and a small, practically negligible, Klinkenberg effect for permeabilities at or near $10^{-19} m^2$ to $10^{-20} m^2$.

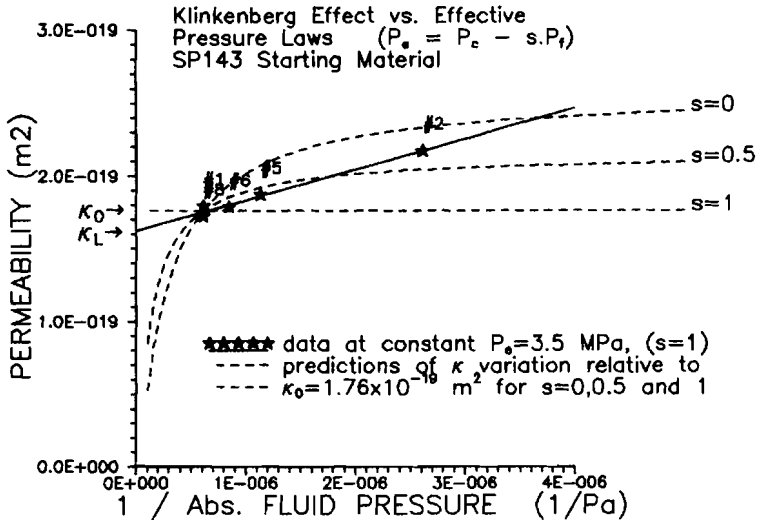

Figure 3.8. Comparison of Klinkenberg effect with choice of Effective Pressure Law. Reference permeability κ_0 = 1.76 x 10^{-19}m^2 (c.f. Figure 3.9). Data follow a straight line typical of the Klinkenberg effect.

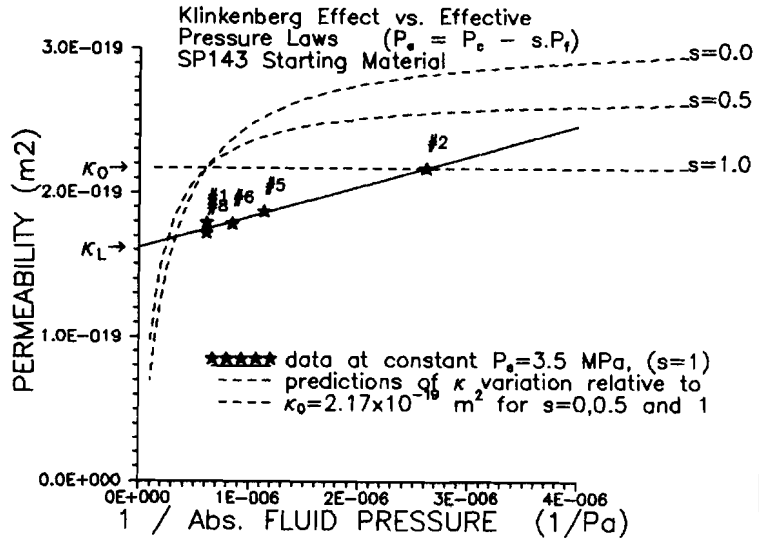

Figure 3.9.

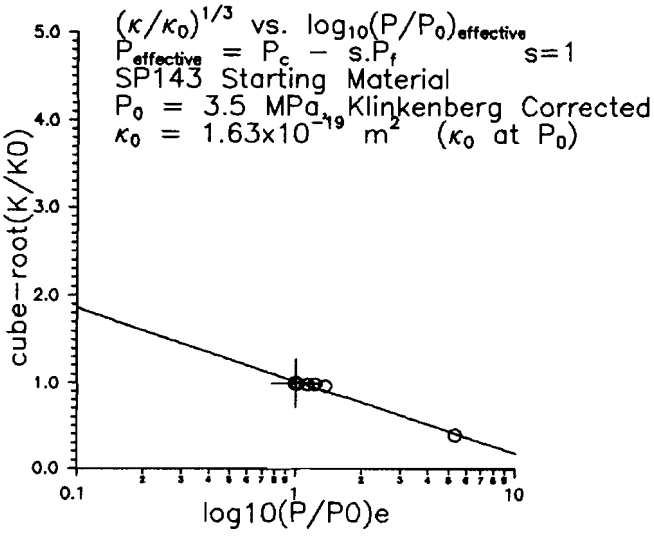

Figure 3.10. Replotted data of Figure 3.7, with effects of gas slippage (Klinkenberg effect) removed.

3.2.6. Summary of findings for the Asse starting material

The main findings and conclusions drawn for the Asse Speisesalz starting material can now be detailed as follows:

i) Natural undisturbed Asse salt rock situated at depths equivalent to confining pressures > 10 MPa can be assumed to have inert fluid permeabilities (see Section 3.2.4) of $\leq 1 \times 10^{-21} m^2$.

Figure 3.9. Comparison of Klinkenberg effect with choice of Effective Pressure Law. Reference permeability shifted to $\kappa_0 = 2.17 \times 10^{-19} m^2$, P_0 same as for Figure 3.8. In the absence of a Klinkenberg effect, with shift in κ_0 the data should remain a close fit to some characteristic curve. Clearly comparing with Figure 3.8 this is <u>not</u> so and therefore data <u>are</u> subject to an additional effect not described by the Walsh model.

ii) Salt rock material extracted from near gallery walls may exhibit substantially higher, creep-induced, permeabilities reaching values of the order of 1 x $10^{-17}m^2$ (or higher if badly disturbed), as deduced from gas permeametry under hydrostatic confinement. However, this value falls to almost undisturbed values within 1-2 m of the wall, at least in the case of the 800 m gallery at Asse.

iii) With respect to permeability, and using the terminology of Walsh (1981) and Bernabe (1986), the disturbed/dilated Asse salt rock material, from near gallery walls, appears to obey an effective stress law of the form $P_e = P_c - s \, . \, P_f$ where $s \approx 1$. In other words, the permeability and pore structure of the material remains roughly constant at constant conventional effective stress, with dry argon gas as pore fluid.

iv) In dilated gallery wall material, permeability appears to be related to the effective pressure (hydrostatic case) via the Walsh (1981) model. The model relates elastically recoverable fracture aperture changes, determined by Hertzian contact between asperities at the fracture microscale, to applied changes in effective pressure. It also describes the resulting permeability change using a cubic relation with fracture aperture, $\kappa \propto a^3$, taking into account the variable flow blocking effects of the asperity contacts themselves. Thus in accordance with the Walsh model (applied assuming that fracture plane tortuosity changes are negligible), the permeability is related to the conventional effective pressure, P_e, by the relation

$$\frac{\langle \kappa \rangle}{\langle \kappa_o \rangle} = \left[1 - \sqrt{2} \left(\frac{h}{\langle a_o \rangle} \right) \log_e \left(\frac{P}{P_o} \right)_e \right]^3$$

v) Low permeability disturbed Asse salt rock material ($\kappa < 10^{-19}m^2$) exhibits a small Klinkenberg (gas slippage) effect for low gas pressures ($P_f < 0.5$ MPa). At the gas pressures normally used in the permeability determinations ($\langle P_f \rangle$ = 1.5 MPa) the relative error due to slippage at ~$10^{-19}m^2$ is about + 8% w.r.t. the liquid permeability. The relative error has been estimated to rise to + 47% at $10^{-21}m^2$, a smaller absolute error than at $10^{-19}m^2$. For most practical purposes, the Klinkenberg effect may be ignored.

3.3. Influence of controlled deformation on dilatancy and permeability development

Having characterized the Asse Speisesalz starting material, experiments designed to investigate the influence of axi-symmetric deformation on dilatancy and permeability development in this material are reported.

Experimental conditions of high strain rate, high stress and low confining pressure were chosen to favour deformation by dislocation glide controlled mechanisms, (see Figure 1.2 for deformation mechanism map), with minor dilatation (see previous reports by Spiers et al., 1986). These conditions can be viewed as representing the worst case (i.e. most dilatant) to be expected in a waste repository environment, for example in the converging walls of open or backfilled galleries and boreholes. The criteria for dilatancy, namely $\sigma_1 - \sigma_3 \geq 20.7$ MPa, $\sigma_2 = \sigma_3 < 3.5$ MPa from Wawersik and Hannum (1980), and $\sigma_1 - \sigma_3 \geq (2.74)\ P_c + (6.4 \pm 2.8)$ MPa where P_c = confining pressure ($\sigma_2 = \sigma_3$) from Spiers et al., 1989, excludes the bulk of the repository away from gallery walls (see finite element analysis of repository stress conditions in Prij, 1983, 1984; Pudewills, 1988; Rolnik, 1988).

The experiments are thus of direct relevance to assessing the influence of creep phenomena on the near field performance of salt-based repository and storage systems. They are also relevant to fluid transport processes occurring during halokinesis, evaporite dewatering and metamorphism.

3.3.1. Method

Five Asse Speisesalz salt rock samples (SP138, 139, 140, 141, 142, see Table 3.1) with initial permeabilities in the range 1 x $10^{-21}m^2$ to 3 x $10^{-21}m^2$ (at P_e = 3.5 MPa), were deformed using the Heard triaxial apparatus at strain rates of ~ 3 x $10^{-5}s^{-1}$, at room temperature and at 5 MPa confining pressure. The samples were tested in their natural condition (i.e. without added brine) using the standard 70 mm sample assembly described in Chapter 2. Glass fibre tissue gas-spreaders and perforated Teflon end sheets (0.05 mm thick) were used to minimize specimen/piston permeametry and friction boundary effects respectively. The samples were deformed in stages using the Heard triaxial apparatus, with argon gas permeability determinations being made at each stage. Permeametry was carried out using the transient step technique at 1.5 MPa mean gas pressure. The volumometer system attached to the Heard apparatus was used to measure specimen volume change during deformation. In every experiment the deformation was halted, by

arresting the loading piston at 2% permanent strain, and also at 10%, to determine the sample permeability (in the loaded state). In one case (SP142), the deformation was also halted at the 4%, 6% and 8% stages in order to more completely map the relationship between strain and permeability. Since full computerized logging had not been implemented on the deformation apparatus when the above experiments were performed, the raw mechanical data were recorded using a 6-channel chart recorder. The chart records were subsequently digitized and processed following the methods outlined previously (Chapter 2).

3.3.2. Results

The stress vs. strain and volume change vs. strain curves obtained in the present experiments are presented in Figures 3.11 - 3.15. Note that in these figures, axial strain (ε) and volume change ($\Delta V/V_0$) have been corrected for purely elastic deformation of the sample, using elastic moduli for fully dense NaCl rock. V_0 is taken as the initial unloaded specimen volume. The relative magnitude of these corrections in ε and $\Delta V/V_0$ is of the order of 1% at full load. Note the excellent reproducibility of the curves. The stress vs. strain curves show strong, near-parabolic work hardening. In each case the sample volume decreases in the first ~ 1% strain, then increasing such that the quantity $\Delta V/V_0$ is almost linearly related to strain above 3% strain.

The permeability measurements obtained are given in Table 3.3. Permeability versus strain data are plotted in Figure 3.16. As can be seen from this graph the spread in permeability values for the different specimens remains very small throughout deformation and all samples can therefore be assumed to have followed a permeability vs. strain trend similar to that shown by the more detailed data set obtained for SP142 (Figure 3.16). For this sample, the permeability increases more or less exponentially during the first 4% of strain (linear portion in Figure 3.16) then assymptotically approaching an apparent limiting value of around $3 \times 10^{-16} m^2$, reached at about 10% strain. This permeability saturation value is at least two orders of magnitude within the upper resolution limit of the permeameter and therefore is not an artefact produced by the apparatus.

The permeability versus volume change data obtained for the entire suite of samples tested is plotted in Figures 3.17a and b. Here the initial rapid increase in permeability appears even more dramatic, with κ rising roughly exponentially through 5 orders of magnitude in the first 0.2% dilatant volume change. Note that in Figure 3.17b positive volume change is measured from the minimum of each

Table 3.3. Deformed Speisesalz material: values of permeability versus strain and volume change. Test conditions: P_c = 5.0 MPa, P_f = 1.5 MPa (argon gas), dry, room temperature, $\dot{\varepsilon} \sim 3 \times 10^{-5} s^{-1}$ during loading.

Sample	ε %	$\sigma_1 - \sigma_3$ MPa	$\Delta V/V_o$ %	$[(\Delta V/V_o)-(\Delta V/V_o)_{min}]$ %	κ m^2
SP138	0	0	0	0.07	2.241×10^{-21}
	2.48	30.99	- 0.029	0.041	3.471×10^{-19}
	9.2	44.42	0.766	0.836	1.936×10^{-16}
	~ 9.2	0	~ 0.766	~ 0.836	2.955×10^{-16}
SP139	0	0	0	0.085	1.923×10^{-21}
	2.46	31.92	- 0.036	0.049	3.506×10^{-19}
	10.35	44.61	0.947	1.032	2.727×10^{-16}
	~ 10.44	0	~ 0.947	~ 1.032	4.150×10^{-16}
SP140	0	0	0	0.049	2.733×10^{-21}
	2.395	30.91	- 0.009	0.040	7.690×10^{-20}
	10.33	44.02	1.106	1.057	2.743×10^{-16}
	~ 10.41	0	~ 1.106	~ 1.057	4.395×10^{-16}
SP141	0	0	0	0.093	1.245×10^{-21}
	2.31	31.08	- 0.061	0.032	5.454×10^{-20}
	9.81	44.9	0.934	1.027	6.332×10^{-16}
	~ 9.81	0	~ 0.934	~ 1.027	8.955×10^{-16}
SP142	0	0	0	0.058	2.504×10^{-21}
	2.368	30.54	- 0.016	0.042	2.303×10^{-19}
	4.346	35.34	0.14	0.198	3.283×10^{-17}
	6.344	38.7	0.399	0.457	2.028×10^{-16}
	8.394	40.73	0.665	0.723	3.382×10^{-16}
	10.342	44.29	0.961	1.019	3.529×10^{-16}
	~ 10.342	0	~ 0.961	~ 1.019	5.108×10^{-16}

volume change data curve (Figures 3.11 - 3.15), this minimum being interpreted as the beginning of bulk dilatation following minor compaction of the sample. The onset of local dilatation (presumably by microcracking) is not apparent from bulk $\Delta V/V$ data.

In addition to the log-linear plots of Figures 3.17a and b, a graph of $\log_{10}\kappa$ vs. $\log_{10}$ (volume change) is presented in Figure 3.18, to assess the applicability of a power law relation of the form $\kappa \propto (\Delta V/V)^n$ to the present data. Obviously no single exponent (n) can describe the data. Initially n decreases from ~ 4 to < 1 after 0.8 volume change.

Figure 3.11. SP138

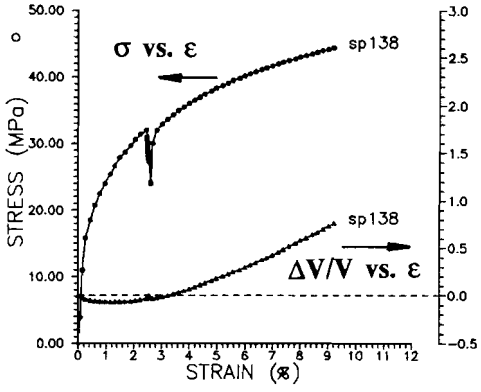

Figure 3.12. SP139

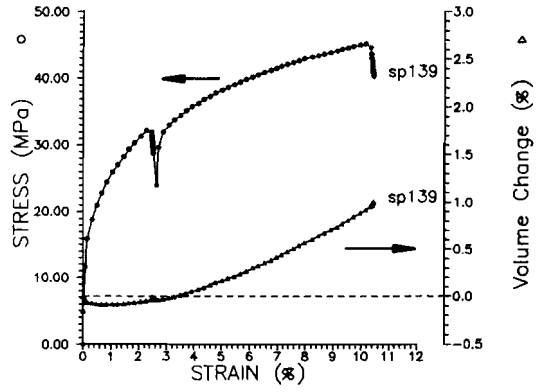

Figure 3.13. SP140

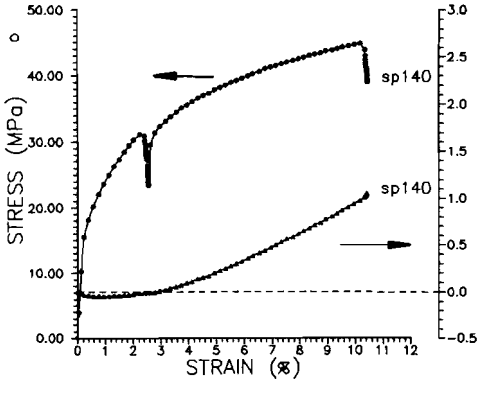

Figure 3.14. SP141

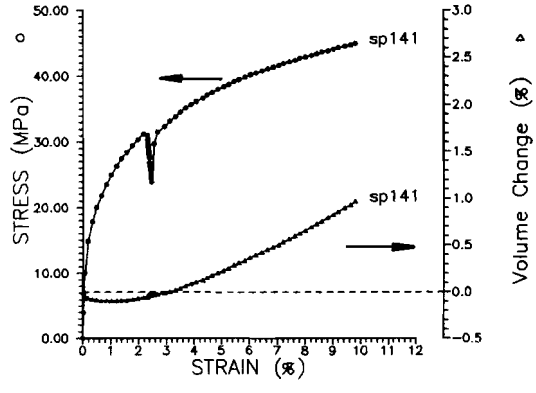

Figures 3.11 - 3.14. Stress and volume change ($\Delta V/V_0$) versus strain data for tests SP138, 139, 140 and 141 (V_0 = initial volume of undeformed sample). The break in the loading curves at ~ 2% strain was to allow an overnight permeability determination. Test conditions: P_c = 5.0 MPa, P_f = 1.5 MPa (argon gas), dry, room temperature $\dot{\varepsilon} \approx 3 \times 10^{-5} s^{-1}$ during loading.

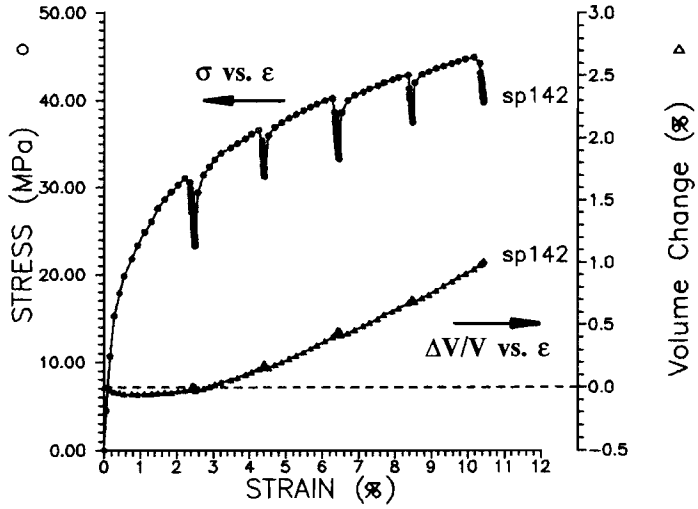

Figure 3.15. Stress and volume change ($\Delta V/V_0$) versus strain data for test SP142 (V_0 = initial volume of undeformed sample). The breaks in the loading curves at ~ 2, 4, 6, 8% strain were to allow permeability determinations. Test conditions as for Figures 3.11 - 3.14.

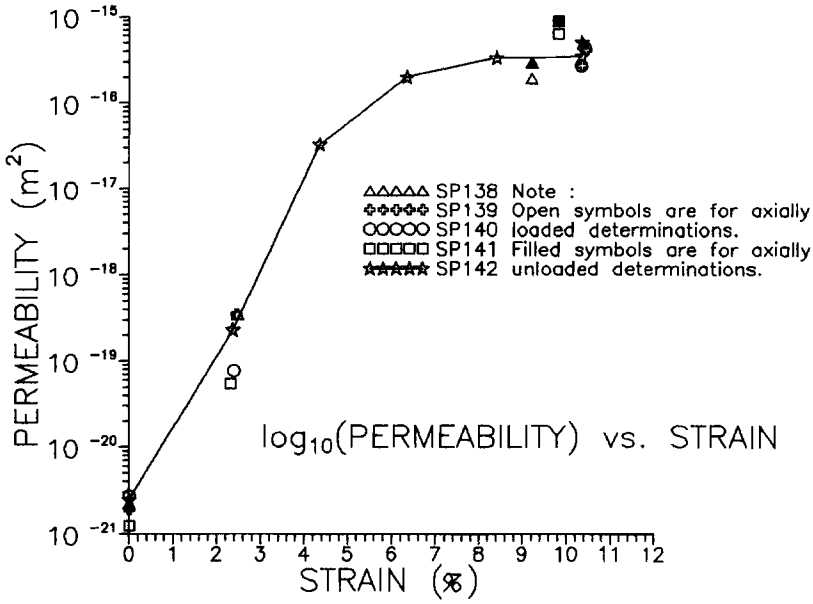

Figure 3.16. Plot of $\log_{10}$(permeability) versus strain for samples SP138 - SP142. Data points at maximum strain, for each data set, show effect of axially unloading the specimen (see legend).

Figure 3.17a.

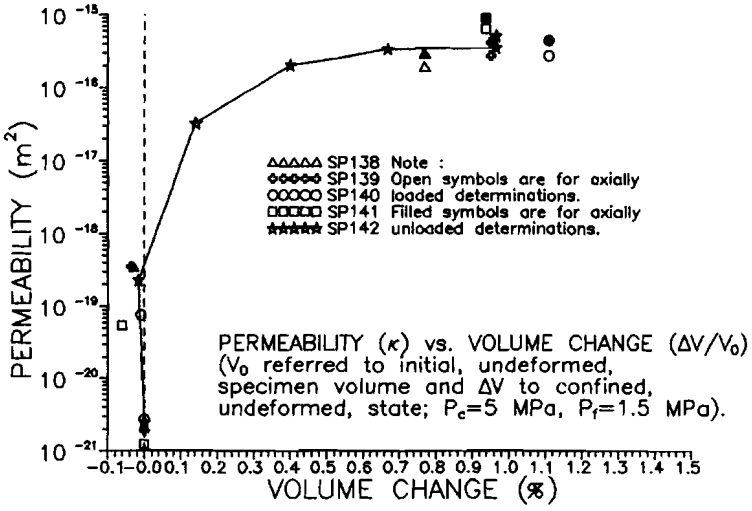

Figure 3.17b.

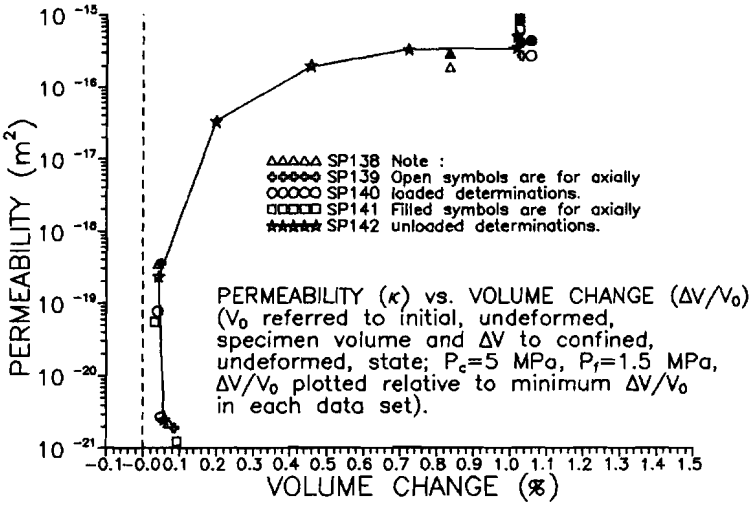

Figure 3.17a, b. Plots of $\log_{10}$(permeability) versus volume change (dilatation is shown positive). In Figure 3.17a $\Delta V/V_0$ = zero at start of test whereas in Figure 3.17b $\Delta V/V_0$ is taken to be zero at the minimum value of volume change obtained for each test, making all volume changes positive (see legend).

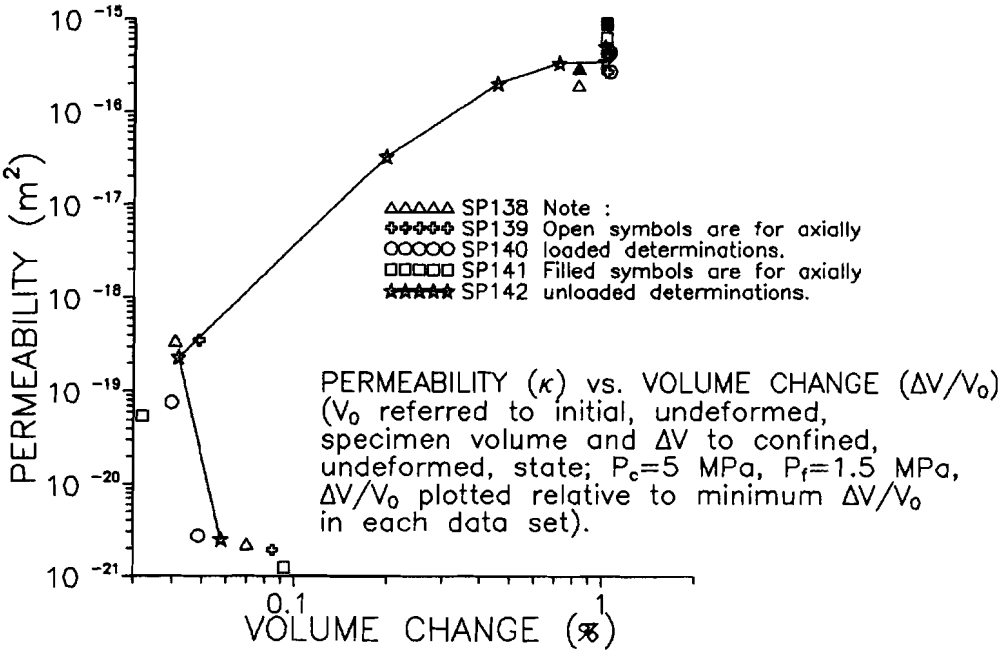

Figure 3.18. Plot of $\log_{10}$(permeability) versus $\log_{10}$(volume change). Data as for 3.17b, all recorded volume changes are therefore positive; see legend.

3.3.3. Microstructural observations

3.3.3.1. Specimen scale observations

Externally the deformed specimens SP138 - SP142 showed only slight barrelling (cylindrical to within 1.2%) reflecting minimal end effects. All specimens showed cracking on the grain scale and radially disposed, wide (up to 0.2 mm) axially oriented cracks on the cylindrical outer surfaces. Some of these followed grain boundaries others were transgranular. Polished slabs cut parallel and perpendicular to the specimens cylindrical axis revealed that the density of axial cracks dropped radially towards the centre of the specimen. Photographs of acetate peels from such polished slabs are shown in Figure 3.19.

Figure 3.19a.

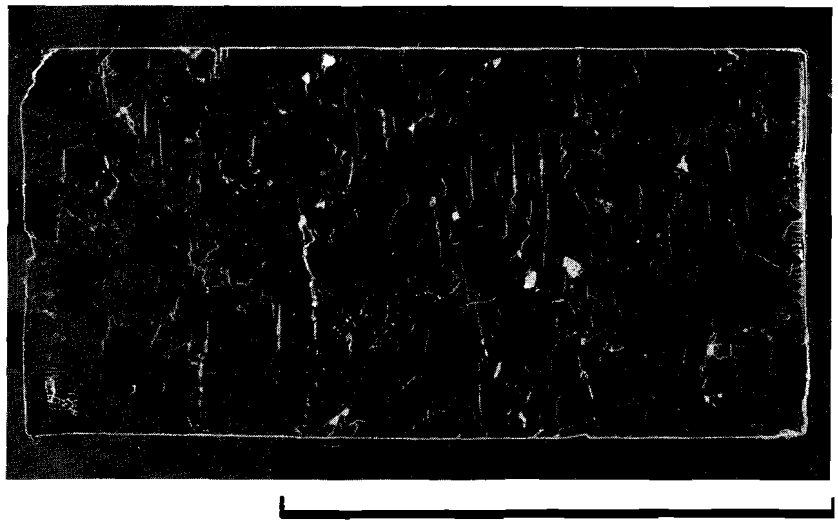

Figure 3.19b.

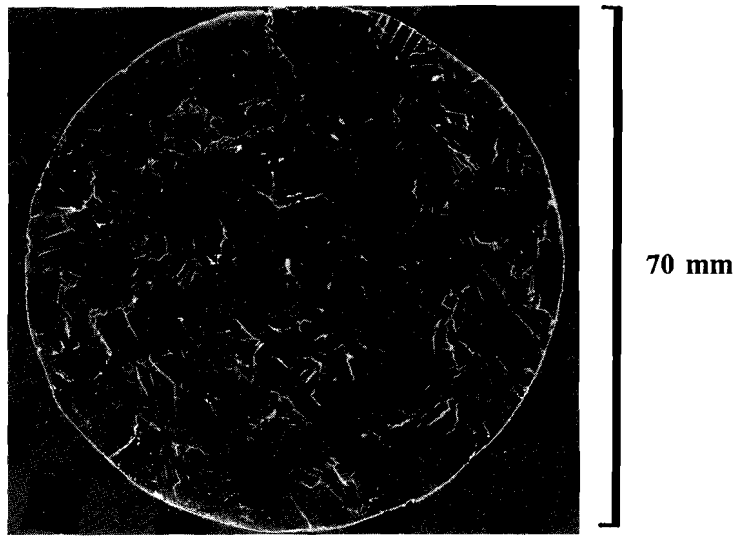

Figure 3.19a and b. Photographs of acetate peels taken from polished slabs of sample SP142. The major fractures are visible and the dilated grain boundaries are also apparent. Figure 3.19a shows a section cut parallel to the compression axis (here vertical). Figure 3.19b is oriented perpendicular to compression.

3.3.3.2. Observations in thin section.

The overall grain structure is similar to the starting material with respect to grain sizes and shapes, with some grain flattening in the maximum shortening direction. Most grain boundaries are dilated and can be regarded as intergranular cracks. Intragranular cracking is also evident with cracks sometimes following cleavage planes in a zig-zag fashion. Cracks oriented parallel to the specimen cylindrical axis (hence compression direction) are widest and often wedge shaped with some evidence of accommodation by grain boundary sliding (see Figure 3.20a).

Polished and etched thin sections reveal densely developed dislocation microstructures, such as slip band patterns, in heterogenous domains within grains. Slip bands are often seen spreading from stress concentrators such as neighbouring grain corners (see Figure 3.20b) and inclusions such as polyhalite crystals. The cellular dislocation etch patterns and subgrains typically seen in the starting material are overprinted with dense dislocation etch features. Fluid inclusions in grain boundaries show disruption with micro-crystallite growths around them due to evaporation of their leaked brine. Intact grain boundaries are rare.

A more quantitative description of the crack distribution was obtained by measurement of grain boundary and crack (grain boundary and transgranular) intercepts along oriented traverses on sections of deformed specimen, SP142 - see Figure 3.21 accompanying Table 3.4 for orientation and results. Essentially the crack spacing (grain boundary and transgranular, together) differs little from the grain boundary spacing (cracked or intact) in all orientations. Some variation in grainsize is evident between the horizontal and vertical sections, reflecting some inhomogeneity of grainsize on the specimen scale and not an orientation effect. The crack spacing follows this variation relatively closely and remains similar to the average grain diameter throughout the specimen. Horizontally oriented cracks, sub-perpendicular to the specimen shortening axis, are much narrower in aperture than vertical, axially oriented cracks.

Crack connectivity is not clearly apparent in 2D sections, but viewing a polished block impregnated with in 3D blue resin, by virtue of the rock's transparency, showed the larger axial cracks to be more or less isolated from each other. Connectivity between the larger cracks appears to be via the narrower sub-horizontal grain boundary cracks.

Figure 3.20a.

Figure 3.20a and b. Microstructural features seen in sample SP142 deformed at room temperature, and strain rate of $3 \times 10^{-5} s^{-1}$.
a) Optical micrograph showing wedge-shaped grain boundary and trans-granular cracks with evidence of accommodation by grain boundary displacement. b) Reflection optical micrograph showing dislocation etch features.

Figure 3.20b.

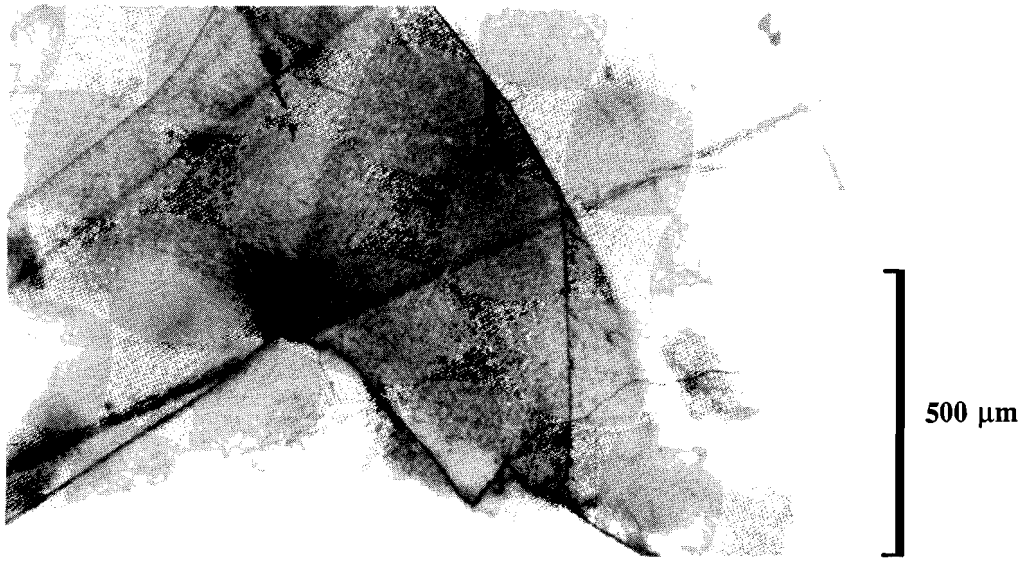

Table 3.4. Results of stereological measurements on grain boundaries and cracks in deformed specimen SP142 (see Figure 3.21 for orientation).

Crack or Grain Boundary Spacing Statistics

L_3 = mean intercept, σ_{n-1} = sample standard deviation.

Traverse Direction	Grain Boundaries (Cracked or Intact)	Cracks (Grain Boundary and Transgranular)	Total Length
	L_3 (σ_{n-1}) mm	L_3 (σ_{n-1}) mm	mm
V_z	3.48 (0.75)	4.67 (1.12)	477.02
V_y	4.46 (1.03)	4.70 (0.66)	300.50
H_y	1.47 (0.20)	2.03 (0.47)	237.51
H_x	1.97 (0.06)	1.87 (0.40)	475.32

Average deformed grainsize	1.5	- 4.5	mm	
Average crack spacing	1.9	- 4.7	mm	
Average crack length	~ 1.5	- 4.5	mm	(controlled by grainsize)
Average crack density	0.15	- 0.01	mm^{-3}	
Crack widths range from	0.00	- 0.2	mm	

Average crack widths were calculated, assuming penny shaped cracks, from the specimen dilatation, average crack density and length. Results were found to lie in the range 0.02 - 0.03 mm.

Figure 3.21. Orientations of sections and traverse directions for Table 3.4.

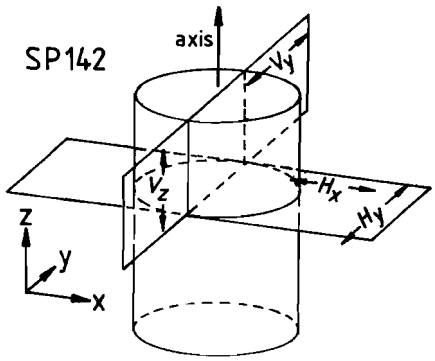

3.3.4. Summary and discussion

The present experiments were performed on intact Asse Speisesalz under room temperature and high strain rate conditions known, from previous data (Spiers et al. 1986, Wawersik and Hannum 1980), to favour deformation by dislocation plasticity (glide) with minor dilatation. The chosen conditions can be viewed as representing the worst case (i.e. most dilatant) to be expected in a waste repository environment, i.e. broadly comparable with conditions near (within 3 m of) converging gallery walls.

All aspects of mechanical behaviour observed in the experiments were closely reproducible, with the permeability of the samples increasing very rapidly from $10^{-21}m^2$ to $10^{-16}m^2$ in the first 4% strain (0.2% dilatancy) asymptotically approaching a more or less constant value of ~ 5 x $10^{-16}m^2$ by 10% axial shortening (1.0% dilatancy). In accordance with the previous data, microstructural work has shown that the samples deformed by a coupled process of dislocation plasticity plus microcracking. Intensive grain boundary microcracking predominates over transgranular cracking with crack lengths and spacing determined by the grainsize. The microcracking is seen together with grain boundary sliding, as accommodation to widespread crystal plasticity on a limited number of slip systems (i.e. less than the 5 independent slip systems required for homogeneous plastic deformation in polycrystals - "Von Misès ductility criterion", see Nicolas and Poirier, 1976 and Paterson, 1969). Most of the dilatant volume change is concentrated in wide (up to 0.2 mm) radially disposed axial cracks connected by axially sub-perpendicular grain boundary cracks of much narrower aperture. These narrower cracks would most probably control the fluid transport properties (permeability) over the moderate range of strain (0 - 10%) studied here. A calculation based on the elastic crack closure model of Walsh 1981 (see Section 3.2.5 and Equation 3.4) using data reported in Section 3.4 (SP107, see Figure 3.28) suggests that the average crack apertures in the loaded condition (P_c = 5.0 MPa and P_f = 1.5 MPa, argon) would be only a factor of 1.5 narrower than that seen in the unloaded specimen thin sections at ambient conditions. On the basis of the general microstructure, the mechanism of micro-fracture seems to have been similar to the "Cleavage 3" or "Brittle Intergranular Fracture 3" (BIF 3) mechanism of Gandhi and Ashby (1979). This is reasonably consistent with their fracture mechanism map for NaCl (see Figure 3.22) though it is important to note that this is drawn for uniaxial tensile loading of NaCl with a smaller grainsize (100 μm).

Returning to the question of permeability development during deformation, attention is now focussed on the significance of the highly non-linear relations between

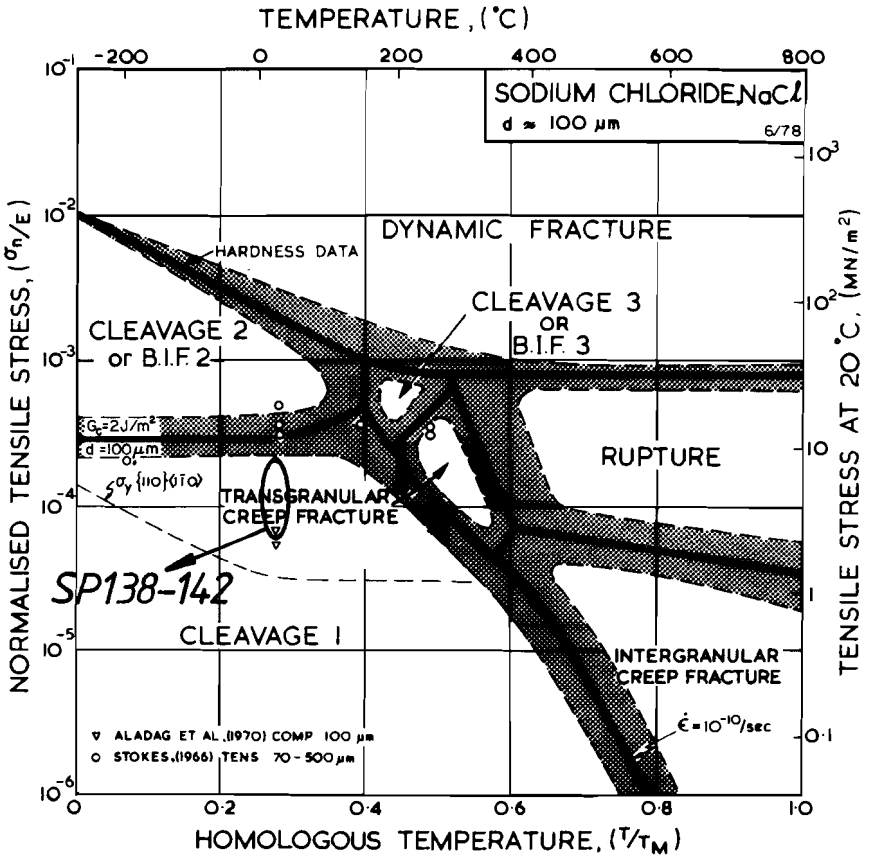

Figure 3.22. Fracture mechanism map for NaCl taken from Ghandi and Ashby (1979). Note this is drawn for tensile loading and a grain size of 100 μm. The stress level required to propagate a cleavage crack in compression is 8-15 times higher than for tension. The range of compressional flow stresses (30 - 50 MPa) for samples SP138 - SP142 have been divided by 8 in accordance with Ghandi and Ashby (1979) and plotted on the diagram for T/T_m = 0.29 (room temperature). Since the stress to propagate grain scale cracks is inversely proportional to grain size the effect of the coarser grain size of Asse salt will be to shift the "cleavage 2" and "3" mechanism fields to lower stresses, to almost certainly include the data. It should also be noted that the map is for the predominant fracture mechanism at failure, which was not reached in these experiments.

permeability and dilatancy (or strain) seen in the present tests. Remarkably the sample permeability was found to increase by some 4-5 orders of magnitude (10^{-21} - $10^{-16}m^2$) in the first 0.2% of positive-going dilatative behaviour, increasing by only one further order (to 5 x $10^{-16}m^2$) in the following 1% dilatation. Expressed in terms of a power law of the form $\kappa \propto (\Delta V/V_0)^n$, this type of behaviour was shown to correspond to a change in n from $n > 4$, at dilatation < 0.2%, to $n < 1$ at higher volumetric strains. This is entirely inconsistent with permeability vs. porosity (ϕ) relations for well-connected porous media of essentially constant structural nature. Such relations, often referred to as Carman-Kozeny type, are of the form $\kappa \propto \phi^m$ where m is a constant (often ~ 3) over a wide range of ϕ (Dullien 1979). It is inferred that the present behaviour probably reflects early critical behaviour in which crack connectivity is established giving a sudden "appearance" of permeability, this being followed by less significant increase in connectivity, crack density and aperture. On this basis, and taking into account the chosen "worst case" conditions explained above, it is inferred (from the asymptotic behaviour seen in the κ vs. $\Delta V/V_0$ data, Figure 3.17a and b) that the maximum value for plastic-deformation-induced permeability in homogeneous dry salt rock, under waste repository conditions is probably around 5 x $10^{-16}m^2$.

Clearly, an appropriate microphysical model that includes the above mentioned critical threshold of connectivity-growth behaviour is needed for purposes of comparison with the present κ vs. $\Delta V/V_0$ data. Such a model based on the principles of percolation theory (Broadbent and Hammersly, 1957; Stauffer, 1985; Gueguen and Dienes, 1989), is developed in Chapter 6 and yields good agreement with the data presented here.

3.4. Permeability decay characteristics of dry, dilated salt rock

These experiments were designed to monitor the decay or "healing" of permeability (to gas) with time in dry, dilated rocksalt under hydrostatic loading conditions. The aim was to provide insight into the rate of change of deformation-induced permeability to gas under the low temperature hydrostatic conditions expected to prevail in waste repositories (and in naturally evolving salt deposits) in the long term.

3.4.1. Method

An extensive series of argon gas permeability determinations was made on a single sample (SP107) of dry dilated Asse Speisesalz previously deformed in the Heard apparatus to 10% plastic strain at a strain rate of 4.5 x $10^{-5}s^{-1}$ and at 5.1 MPa confining pressure. The sample exhibited a final volume increase of 1.3%. These permeability determinations were carried out at regular intervals of time, under selected confining pressures, i.e. at 3, 10, 15 MPa and at room temperature, with the entire test lasting around 2 months. The argon gas permeametry was executed using the apparatus and transient step method described in Chapter 2 of this thesis (see also Peach et al., 1987). The mean argon gas pressure used in all of the permeability tests was 1.5 MPa. This gas pressure and the use of a 0.5 MPa transient step created conditions such that the "Klinkenberg effect" was insignificant (< 5%) and could therefore be ignored (see Chapter 2, Section 2.4 and Section 3.2.6).

3.4.2. Results

The results obtained for specimen SP107 are given in Table 3.5 and as a linear plot of permeability versus time in Figure 3.23. Note that 3 main periods of data collection, referred to as "runs", are distinguished, corresponding to the three confining pressures (P_c = 3, 10, 15 MPa) used during these periods. Three plots, one for each run, are also presented (Figures 3.24, 3.25, 3.26) showing linear permeability versus $\log_{10}$ (time). Time for each plotted run is measured from the application of each confining pressure increment. The conventional effective pressures for these runs were 1.5, 8.5 and 13.5 MPa respectively. Permeability values at 1.5 MPa effective confining pressure are shown at the end of each run, for comparison. Note that no permeability reduction occurs at the lowest pressure investigated (P_e = 1.5 MPa). However, permeability reduction did occur at higher pressures.

Extrapolation of these data down to permeabilities of $10^{-21}m^2$ along linear and logarithmic trend lines (calculated by linear regression of data points indicated in Table 3.5) are also shown on Figures 3.25 and 3.26. These trends provide some constraint on the time necessary for the permeability to decay to the level of natural, non-dilated salt rock ($10^{-21}m^2$, see Section 3.2).

A separate plot of permeability versus conventional effective confining pressure ($P_e = P_c - P_f$) for determination numbers 26-29, 46-52 and 62-65 (which correspond to

pressure stepping sequences performed at the end of each main run), shows the short-term or time-independent pressure dependence, see Figure 3.27. Determinations 62-65, which cover a cycle in effective confining pressure from 13.5 MPa to 1.5 MPa and back, show the short term recoverability of the permeability to be total. Earlier permeability determinations (numbers 1-17) on the same specimen under lower effective confining pressures (used as a check for the Klinkenberg effect, See Chapter 2, Section 2.4.4) are also plotted as additional relevant data. Trend lines are drawn by visual fit only and serve simply to link each data set.

3.4.3. Recoverable permeability data: comparison with the Walsh model

The totally recoverable permeability seen in the short-term pressure-stepping/cycling sequences reported above indicates that the instantaneous response of the sample was entirely elastic. It is therefore appropriate to compare the results with the elastic crack closure model of Walsh (1981) discussed previously (Section 3.2.5). This model predicts the κ vs. P_e relation given in Equation 3.3. In order to check its applicability, the short-term κ vs. P_e data presented in Figure 3.27 are replotted in the $(\kappa/\kappa_o)^{1/3}$ vs. $\log_{10}(P/P_o)_e)$ diagram of Figure 3.28 assuming an effective stress law of the form $P_e = P_c - s.P_f$ with $s = 1$. In this diagram, a reasonably linear plot is obtained for the pressure cycling sequence corresponding to determinations 46 to 52, and the data obtained from the remaining stepping sequences exhibit a closely similar trend. The parameters obtained by fitting the three data sets to the Walsh model are given in Table 3.6. Notably, the value of [B] obtained for all data sets is very close to 1, as predicted by the theory (Equation 3.4). Furthermore, the ratios of crack rugosity (h) to half aperture (a_o) show a systematic increase in the later test sequences, consistent with time dependent crack closure during the intervening runs.

On the basis of the above, and taking into account (1) the fact that s was found to be ~ 1 in the experiments on the starting material, and (2) that the Klinkenberg effect has been shown to be negligible, it is suggested that the Walsh model offers a roughly valid description of the instantaneous κ vs. P_e behaviour seen in the present tests. To fully confirm this, however, more data are needed.

Table 3.5. Results of the three consecutive, dry, hydrostatic runs on dilated Asse salt rock - Specimen SP107. Permeability evolution data at room temperature and three different effective confining pressures.

Test Number	Elapsed time (s)	Permeability (m^2)	
Confining Pressure 3.0 MPa (1.5 MPa effective)			RUN 1
20	52	2.803×10^{-16}	
21	3724	2.787×10^{-16}	
22	5400	2.799×10^{-16}	
23	9671	2.797×10^{-16}	
24	84453	2.750×10^{-16}	
25	93352	2.761×10^{-16}	
26	329395	2.821×10^{-16}	
27	330932	2.832×10^{-16}	
Confining Pressure 10.0 MPa (8.5 MPa effective) (Pressure applied at 331754 s total elapsed time)			RUN 2
28	331950 - 331754	1.806×10^{-16}	
29	332470 - 331754	1.764×10^{-16}	
30	333025 - 331754	1.822×10^{-16}	
31	334888 - 331754	1.756×10^{-16}	
32	336172 - 331754	1.754×10^{-16}	
33	338360 - 331754	1.753×10^{-16}	
34	340543 - 331754	1.749×10^{-16}	
35	344701 - 331754	1.733×10^{-16}	
36	351173 - 331754	1.736×10^{-16}	
* 37	358545 - 331754	1.731×10^{-16}	
* 38	418864 - 331754	1.682×10^{-16}	
* 39	432325 - 331754	1.672×10^{-16}	
* 40	448189 - 331754	1.633×10^{-16}	
* 41	504118 - 331754	1.633×10^{-16}	
* 42	528147 - 331754	1.626×10^{-16}	
* 43	594931 - 331754	1.580×10^{-16}	
# * 44	620525 - 331754	1.582×10^{-16}	
# * 45	677604 - 331754	1.546×10^{-16}	
# * 46	703024 - 331754	1.531×10^{-16}	
# * 47	849769 - 331754	1.498×10^{-16}	
Confining Pressure 3 MPa (1.5 MPa effective)			
48	851070 - 331754	2.345×10^{-16}	
49	852862 - 331754	2.365×10^{-16}	
Confining Pressure 15 MPa (13.5 MPa effective) (Pressure applied at 854251 s total elapsed time)			RUN 3
50	aborted	----	

51	855272 - 854251	1.177×10^{-16}
52	856405 - 854251	1.164×10^{-16}
53	858959 - 854251	1.155×10^{-16}
54	867993 - 854251	1.136×10^{-16}
55	876832 - 854251	1.119×10^{-16}
* 56	935545 - 854251	1.069×10^{-16}
* 57	945384 - 854251	1.063×10^{-16}
* 58	964567 - 854251	1.049×10^{-16}
# * 59	1022430 - 854251	1.020×10^{-16}
# * 60	1048276 - 854251	1.017×10^{-16}
# * 61	1114217 - 854251	9.907×10^{-17}
# * 62	1196952 - 854251	9.666×10^{-17}

Confining Pressure 3 MPa (1.5 MPa effective)

63	1200125 - 854251	2.077×10^{-16}
64	1200874 - 854251	2.087×10^{-16}

Confining Pressure 15 MPa (13.5 MPa effective pressure)

65	1202018 - 854251	9.729×10^{-17}

* indicates data used in linear regression, straight line fit of type $\kappa = a + bt$, where κ = permeability (m^2), t = time (s), a = intercept at t = 0, and b = permeability decay rate.
The results of the linear regression for runs 2 and 3 are:

RUN 2	$a = 1.8524 \times 10^{-16} m^2$
	$b = -4.3239 \times 10^{-23} m^2 s^{-1}$
Correlation coefficient	$r = -0.9865$
RUN 3	$a = 1.4273 \times 10^{-16} m^2$
	$b = -3.8956 \times 10^{-23} m^2 s^{-1}$
Correlation coefficient	$r = -0.9894$

# indicates data used in logarithmic regression, straight line fit of type $\kappa = a + b \log_{10}(t)$, where κ = permeability (m^2), t = time (s), a = intercept at t = 1, and b = logarithmic permeability decay rate.
The results of the logarithmic regression for runs 2 and 3 are:

RUN 2	$a = 3.2280 \times 10^{-16} m^2$
	$b = -3.0332 \times 10^{-17} m^2 (\log_{10} s)^{-1}$
Correlation coefficient	$r = -0.9803$
RUN 3	$a = 1.9667 \times 10^{-16} m^2$
	$b = -1.8045 \times 10^{-17} m^2 (\log_{10} s)^{-1}$
Correlation coefficient	$r = -0.9902$

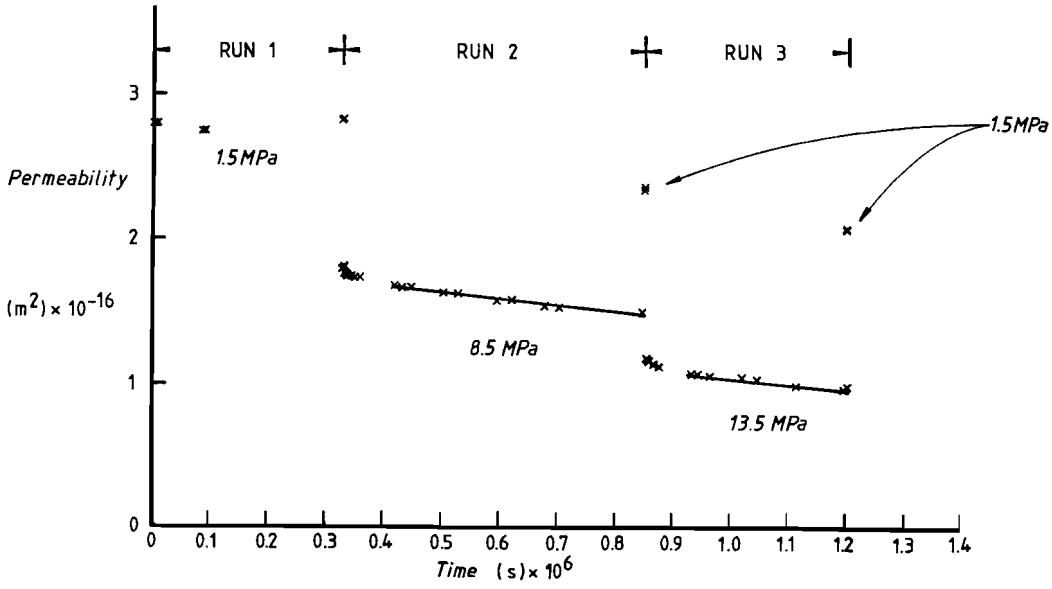

Figure 3.23. Permeability decay data for SP107. Linear permeability versus time plot for gas permeability determinations during three consecutive hydrostatic runs at 1.5, 8.5 and 13.5 MPa conventional effective confining pressure.

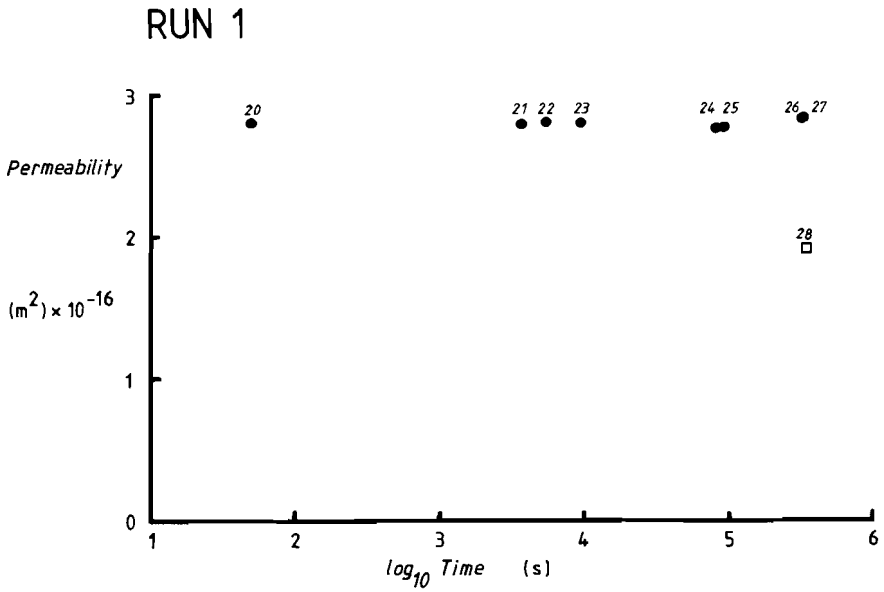

Figure 3.24. Permeability decay data for SP107. Linear permeability versus $\log_{10}$(time) plot for RUN 1 (Figure 3.23) at 1.5 MPa conventional effective confining pressure. (Data point number 28 is from RUN 2 for comparison).

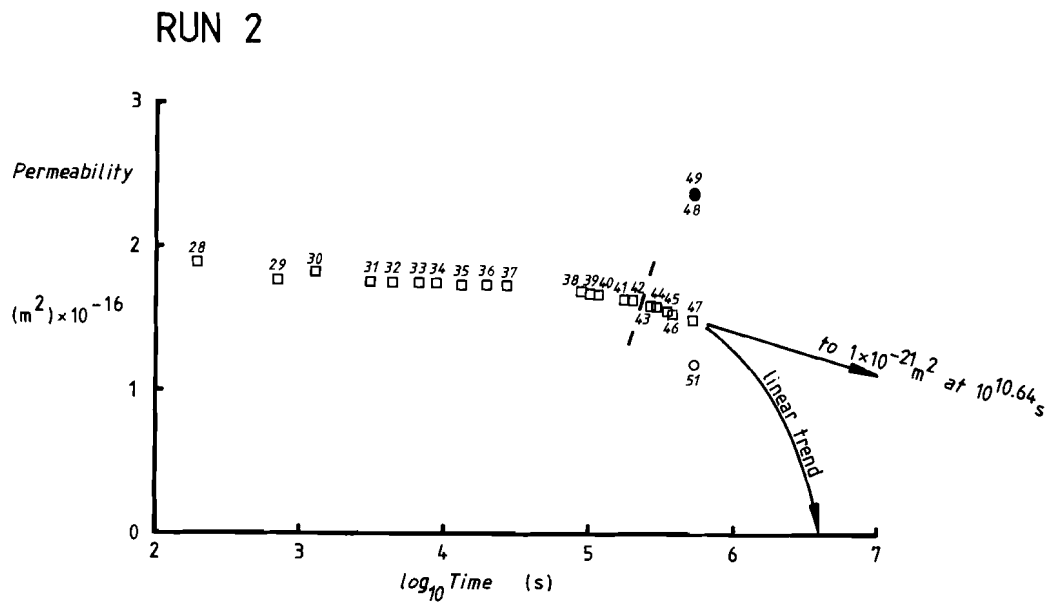

Figure 3.25. Permeability decay data for SP107. Linear permeability versus $\log_{10}$(time) plot for RUN2 at 8.5 MPa conventional effective confining pressure. (Data point number 51 is from RUN 3 and numbers 48 and 49 are determinations at 1.5 MPa conventional effective confining pressure, for comparison).

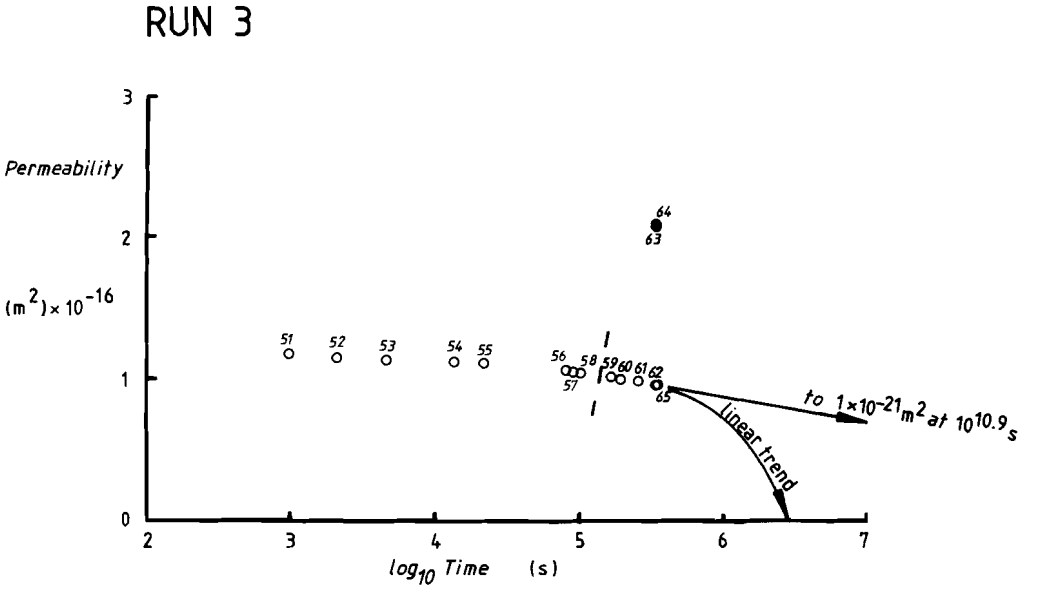

Figure 3.26. Permeability decay data for SP107. Linear permeability versus $\log_{10}$(time) plot for RUN 3 at 13.5 MPa conventional effective confining pressure. (Data points 63 and 64 are determinations made at 1.5 MPa, for comparison).

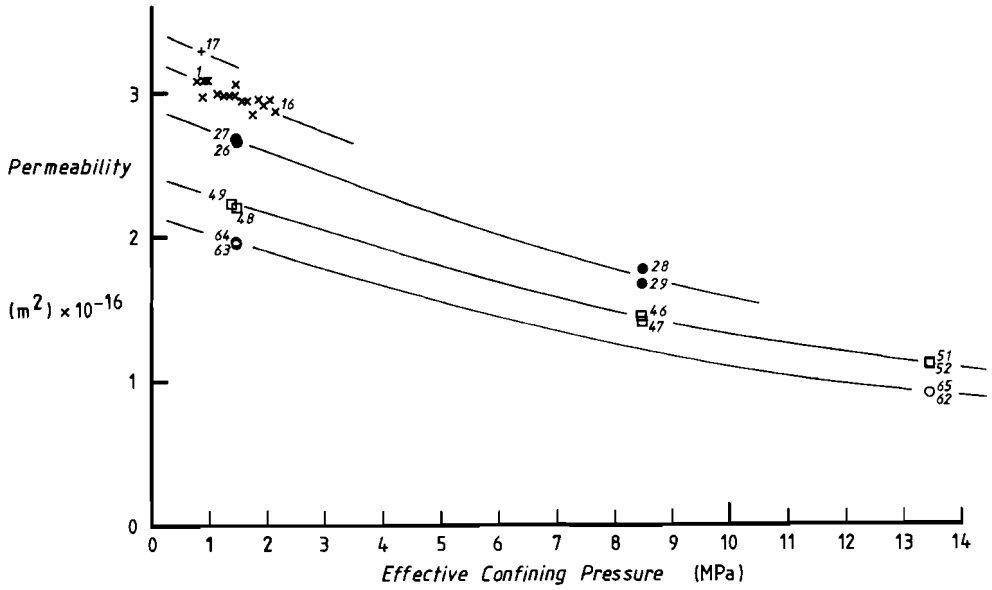

Figure 3.27. Time-independent permeability vs. effective pressure data for SP107. Graph shows linear permeability versus linear conventional effective confining pressure, for end member data points in each run. Data can be viewed as showing the instantaneous change in permeability due to changes in effective confining pressure. (Data points 1 to 17 are from an earlier test sequence on the same specimen (SP107)).

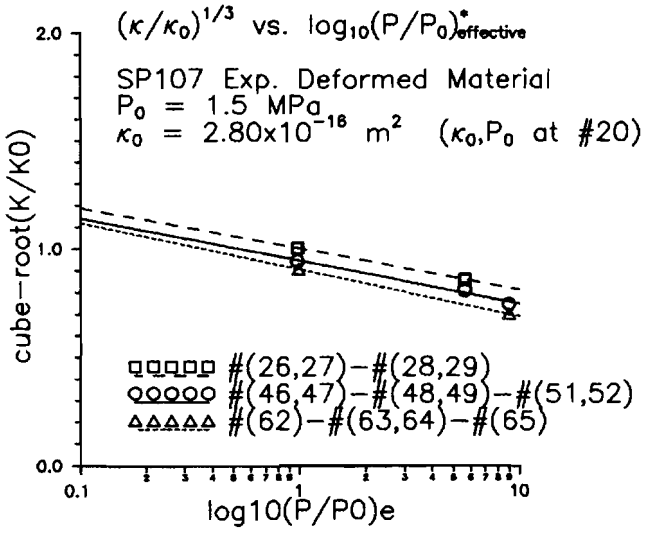

Figure 3.28. Recoverable permeability data from short-term pressure-stepping/cycling of specimen SP107, plotted in terms of the Walsh model of elastic crack closure. Conventional effective stress is assumed, and changes are referred to the permeability (κ_0) and effective pressure (P_0) at determination number 20.

Table 3.6. Fits to the Walsh Model of the recoverable permeability data from short term pressure cycling on sample SP107 (see Figure 3.28 and Equation 3.4). [A] = $\sqrt{2}h/\langle a_o \rangle$

Step Sequence	[B]	- [A].[B]	$h/\langle a_o \rangle$
(26,27) - (28,29)	1.00127	- 0.08111	0.0573
(46,47) - (48,49) - (51,52)	0.94520	- 0.08443	0.0632
(62,63) - (64,65)	0.90509	- 0.09250	0.0723

3.4.4. Summary and discussion

In the single, long term (2 months) hydrostatic test described in this section, dry deformed (1.3% dilated) Asse salt rock with a permeability of ~ $10^{-16}m^2$ underwent permeability reduction at effective confining pressures in the range 8.5 - 13.5 MPa, with permeability reduction rates of around 4 x $10^{-23}m^2s^{-1}$. The same material does not appear to lose permeability on the laboratory time scale under the lower effective confining pressure of 1.5 MPa. This suggests that time dependent changes in pore/microcrack structure were unimportant at 1.5 MPa, and that the reductions observed at the higher stress were caused by compaction creep phenomena. The absence of permeability reduction by compaction creep at the lowest pressure probably reflects the high degree of work hardening in the specimen, which was previously deformed to 10% total plastic strain under a confining pressure of 5.1 MPa reaching a final differential stress of 45 MPa. It seems likely that the compaction creep effects observed at the higher pressures were probably brought about by dislocation plastic mechanisms, since the absence of continuous brine fluid films in this highly dilated salt would prevent recrystallization and creep due to diffusive mass transfer mechanisms (see Spiers et al. 1986). Though probably related to crack closure by dislocation plastic processes, the mechanism of time dependent permeability reduction are as yet insufficiently understood to model, hence no theoretical relation can be constructed describing the permeability decay process. As a result, reliable long term extrapolation of the closure data obtained at 8.5 and 13.5 MPa effective confining pressure is problematic, i.e. unconstrained regarding the form of the permeability vs. time relation chosen. However, in the logarithmic plots, there is no indication of a decelaration of the permeability

reduction rates. The fastest likely closure times can be estimated by assuming that the linear permeability reduction trends to continue. Slower estimates can be derived from extrapolation of the slope of the logarithmic plots for the final stages of each run, assuming that the decay rate decelerates logarithmically from there on. The times to reach a natural (non-dilated) saltrock permeability of $10^{-21}m^2$ from a deformation enhanced starting permeability, given by back extrapolation of the linear best fit to time zero (start of RUN 1), are then as given in Table 3.7.

Table 3.7. Interpolation and extrapolation of the dry hydrostatic closure data (RUNS 1-3).

Conventional effective confining pressure (MPa)	Permeability at time zero (m^2)	Linear closure rate ($m^2\ s^{-1}$)	Linear Trend. Extrapolated time to $1x10^{-21}m^2$ (s)	Logarithmic Trend. Extrapolated time to $1x10^{-21}m^2$ (s)
1.5	$2.803x10^{-16}$	zero	unable to extrapolate	unable to extrapolate
8.5	$1.852x10^{-16}$	$4.324x10^{-23}$	4284072 (49.6 days)	$4.387x10^{10}$ (1390 years)
13.5	$1.427x10^{-16}$	$3.896x10^{-23}$	3663852 (42.4 days)	$7.937x10^{10}$ (2515 years)

Longer term tests and a suitable theory are clearly needed to extrapolate the present data to assess gas phase transport in repository performance studies.

In view of the fact that the dilated specimen investigated here was highly work hardened and was subjected to low confining pressures (i.e. low relative to the flow stresses during initial deformation) the observed crack closure rates at room temperatures are likely to be slow relative to naturally deformed salt. The test conditions must be seen as a worst case in relation to the waste-disposal containment situation where stresses and temperatures are likely to be higher and "dry sealing rates" faster as a result.

Aside from the time dependent behaviour seen in the present experiment, rapid changes in effective confining pressure resulted in instantaneous changes in permeability. These are due to purely elastic changes in connected porosity, such as cracks. As the magnitude of the effective confining pressure increases there is a diminished response in permeability to small changes in confining pressure (see curvature of the trend lines in Figure 3.27). This is thought to be due to the progressive elastic closure of the porosity towards some, short term, limiting value. Broadly speaking, the observed κ vs. P_e behaviour is consistent with the elastic crack closure model of Walsh (1981) and with an effective stress law for permeability of the form $P_e = P_c - s.P_f$ where $s \approx 1$.

3.5. Permeability decay experiments on wet, dilated salt rock

These experiments were performed for the purpose of assessing the time dependent permeability characteristics (i.e. permeability decay characteristics) of dilated salt rock, under hydrostatic loading conditions, with brine as the pore fluid (c.f. previous section).

3.5.1. Method

The experiments were performed in the Heard apparatus using a single sample of Asse Speisesalz (SP137). The sample was initially deformed to 9.8% strain at room temperature, 6.0 MPa effective confining pressure, and at a strain rate of around 3 x $10^{-5}s^{-1}$. This heavily dilated sample (~ 1.5%) was first subjected to gas permeametry (dry, effective pressure = 8.5 MPa), and then to brine permeametry (under steady-state flow-through conditions), using the method described in Section 2.4. The brine permeability measurements were performed under two effective confining pressures, namely 8.5 MPa (first 17 days) and 18.5 MPa (following 13 days), these being held constant between individual determinations. The corresponding testing sequences will be referred to henceforth as RUN A (8.5 MPa) and RUN B (18.5 MPa). In both runs, brine permeametry was performed using an upstream fluid pressure of 2.0 MPa, a downstream fluid pressure of 1.0 MPa, and hence a mean fluid pressure of 1.5 MPa. The confining pressures used in RUNS A and B were thus 10 MPA and 20 MPa.

3.5.2. Results and discussion

The argon gas permeametry performed on sample SP137, at 8.5 MPa effective confining pressure yielded a value (based upon four successive determinations) of 7.303 x $10^{-17}m^2$ (sample std. deviation = 3.173 x $10^{-19}m^2$). This value is only a factor of 2.2 greater than the first brine value determined under comparable conditions (RUN A) and may have been closer if decay had already taken place. The closeness of the two independent determinations suggests that electroviscous drag and chemical interaction effects are not important, in the short term, when determining permeabilities to brine at ~ $10^{-17}m^2$.

The results of the flow-through brine permeametry performed at an effective confining pressure of 8.5 MPa (i.e. RUN A) are given in Table 3.8. These results are plotted as permeability versus time in Figure 3.29 and as $\log_{10}$(permeability) vs. $\log_{10}$(time) in Figure 3.30. In Figure 3.29, the temperature of the sample is also plotted, and flow/no-flow periods are indicated. Periods of no flow were necessary (when permeability was high) because the volumometer pump capacities were too low to maintain continuous flow during overnight periods. During these periods of no-flow, the pore fluid pressure was maintained at 1.5 MPa, and both ends of the sample were linked externally. Changes in the direction of flow are indicated by the "+" and "x" symbols used to plot the data in Figure 3.29. It is clear from this figure, that the permeability changed most during periods of flow, and changed least during periods of no flow. This shows as a stepped trend in the data. The direction of flow does <u>not</u> appear to affect the decay of permeability. However, the overall decay of permeability clearly becomes decreasingly rapid with time.

As it is clear that the permeability decay behaviour is dependent on the flow rate and/or the fluid pressure gradient, the data in Figure 3.30 have been plotted with and without periods of no-flow removed. Times for both data sets were plotted relative to the start of the flow-through experiment. Since the data plotted in the linear permeability versus linear time diagram of Figure 3.29 are highly non-linear, extrapolation is problematic. No theoretical basis yet exists to aid extrapolation, as the mechanisms of permeability reduction are insufficiently understood to model. Note that the unexpected effect of flow rate (flow/no-flow) appears to be very important. However, the no-flow-corrected data when plotted in $\log_{10}$(permeability) versus $\log_{10}$(time) space (Figure 3.30 square data points) does give a fairly good straight line trend during the latter stages of the experiment, implying a decay of the type $\kappa = at^b$ when $b < 0$. The line gives some estimate of the time (~ 10^{13}s) for the permeability (κ) to reach values for natural undisturbed salt rock (~ $10^{-21}m^2$) under the imposed conditions, although its validity remains uncertain.

Table 3.8. Brine flow-through experiment RUN A, dilated Sample SP137.

10 MPa confining pressure, 8.5 MPa effective confining pressure.
Upstream fluid pressure = 2.0 MPa
Downstream fluid pressure = 1.0 MPa

Elapsed time (s)		Permeability ($m^2 \times 10^{-17}$)	Direction F/R
START	0	7.3034 (argon gas)	
	5700	3.286	F
	60420	3.378	F
	(12000)		
	(56160)		
	67320	2.956	F
	79620	2.839	R
	(83520)		
	(143526)		
	148716	2.117	R
	155916	1.963	R
	(163446)		
	(163600)		
	166716	2.094	F
	(170316)		
	(231516)		
	237096	1.905	R
	244296	1.738	R
	251496	1.586	R
	(256896)		
	(318120)		
	322716	1.570	F
	329916	1.478	F
	337116	1.429	F
	(341976)		
	(406200)		
	410886	1.246	R
	418086	1.203	R
	425286	1.115	R
	(430488)		
	(573600)		
	578040	1.090	F
	585240	1.068	F
	592440	1.062	F
	598740	1.027	F
	(601440)		
	(661800)		
	666900	1.015	R
	672900	0.9503	R
	678900	0.9374	R
	(685500)		

	(757200)		
	762624	0.9517	F
	772224	0.9233	F
	(777720)		
	(838200)		
	843840	0.9213	R
	854040	0.8672	R
	(859800)		
	(921900)		
	928884	0.8630	F
	(935199)		
	(1109400)		
	1116300	0.8545	R
	(1122300)		
	(1270200)		
	1276620	0.7799	F
	1288620	0.7618	F
	(1294800)		
	(1353000)		
	1361820	0.7837	R
	1373820	0.7380	R
	(1380000)		
	(1440600)		
	1448700	0.7528	F
	1460700	0.7050	F
FINISH	(1467000)		

F = forward flow
R = reverse flow
Bracketed times indicate start and finish of no-flow periods.

A similar set of results is given in Table 3.9 and Figures 3.31 and 3.32, for the same specimen with the effective confining pressure raised to 18.5 MPa (RUN B). The linear permeability versus time plot for this decay experiment (Figure 3.31) also shows the flow/no-flow periods, but as the permeability was lower, the periods of flow were larger and virtually continuous throughout the experiment. A similar treatment of the results shows the data with no-flow periods removed to have a steeper trend on a $\log_{10}$(permeability) versus $\log_{10}$(time) plot (Figure 3.32) than seen in RUN A. The two best fit trends obtained for the later data shown in the log/log plots for the runs A and B (no-flow removed) are specified in Table 3.10.

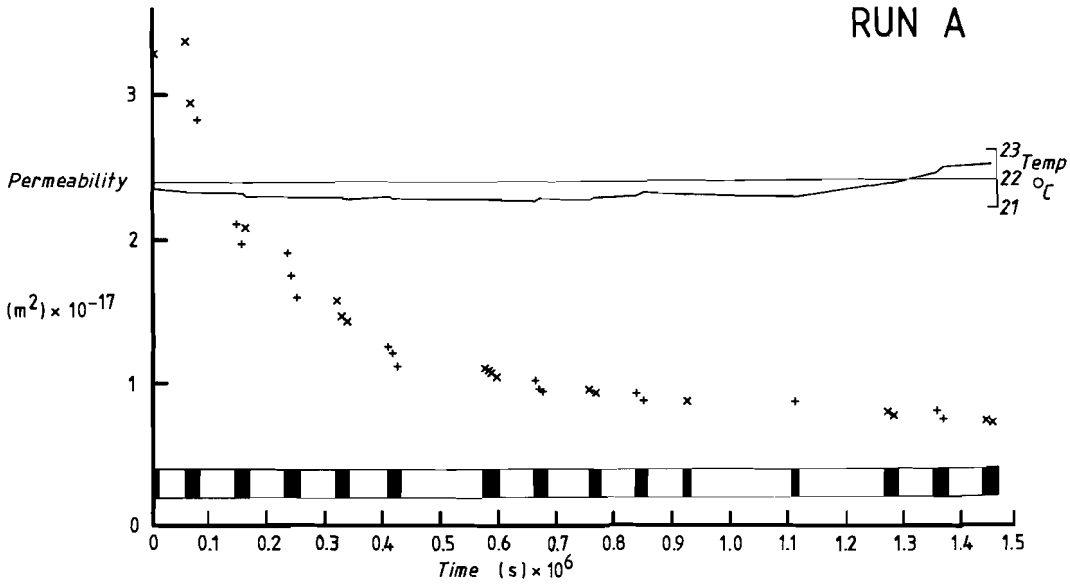

Figure 3.29. Permeability decay data for SP137, wet, RUN A. Linear permeability versus linear time plot for the brine flow through experiment at 8.5 MPa conventional effective confining pressure. Periods of flow are indicated by black bands. Data points marked by "x" indicate forward flow and points marked by "+" indicate reverse flow. The specimen temperature is also plotted for reference.

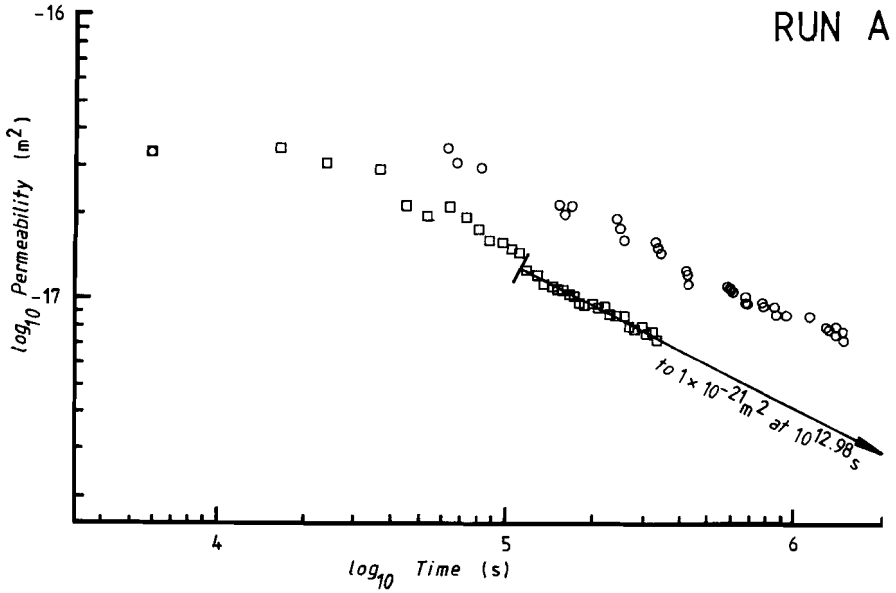

Figure 3.30. Permeability decay data for SP137, wet, run A. Log_{10}(permeability) versus log_{10}(time) plot for the brine flow through experiment at 8.5 MPa conventional effective confining pressure. Data are plotted in two ways; including periods of no-flow ("o" symbols) and by removal of periods of no-flow ("□" symbols).

Table 3.9. Brine flow-through experiment RUN B, Sample SP137

20 MPa confining pressure, 18,5 MPa effective confining pressure.
Upstream fluid pressure = 2.0 MPa
Downstream fluid pressure = 1.0 MPa

	Elapsed time (s)	Permeability (m^2 x 10^{-18})	Direction F/R
START	0		
	6360	4.565	R
	12360	4.153	R
	18360	3.838	R
	(25140)		
	(86640)		
	93624	2.933	F
	99624	2.894	F
	105624	2.787	F
	111624	2.702	F
	(120180)		
	(121440)		
	150360	2.536	F
	174360	2.369	F
	198360	2.194	F
	222360	1.969	F
	(253920)		
	(255540)		
	282540	1.795	F
	306540	1.668	F
	330540	1.518	F
	354540	1.391	F
	378540	1.268	F
	402540	1.124	F
	426540	1.018	F
	450540	0.9563	F
	474540	0.8923	F
	498540	0.8915	F
	(523740)		
	(524340)		
	584340	0.7404	F
	704340	0.6236	F
	824340	0.5570	F
	944340	0.4757	F
	1064340	0.4174	F
FINISH	(1132440)		
	(1132440)	confining pressure dropped to 10 MPa, 8.5 MPa (effective)	
	1137600	3.988	

F = forward flow
R = reverse flow
Bracketed times indicate start and finish of no-flow periods.

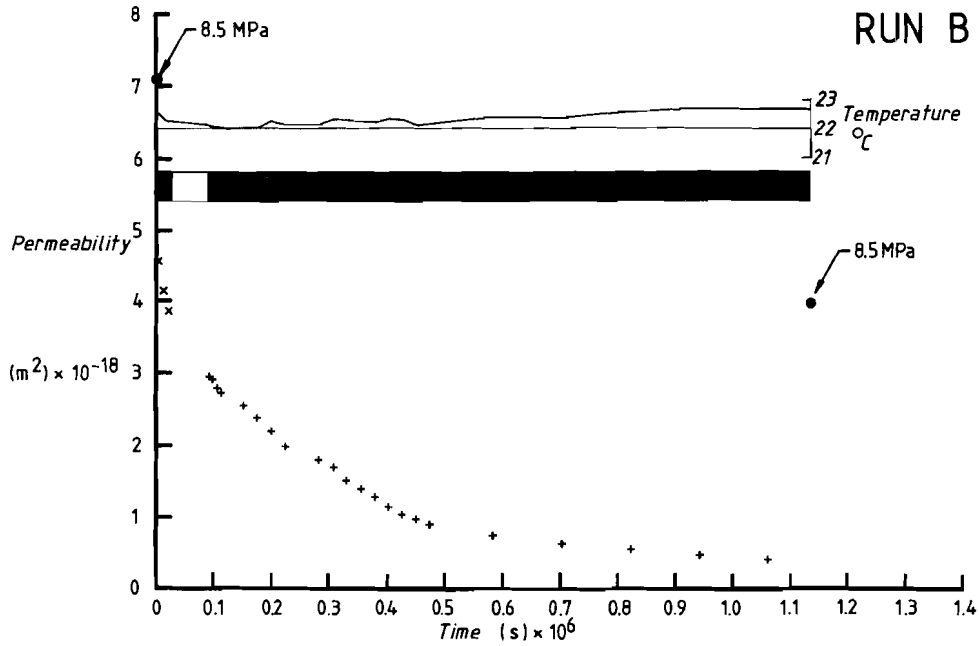

Figure 3.31. Permeability decay data for SP137, wet, RUN B. Linear Permeability versus time plot for the brine flow-through experiment at 18.5 MPa conventional effective confining pressure. Periods of flow are indicated by black bands. Data points marked by "x" indicate forward flow and points marked by "+" indicate reverse flow. The specimen temperature and two determinations at 8.5 MPa conventional effective confining pressure are plotted for reference.

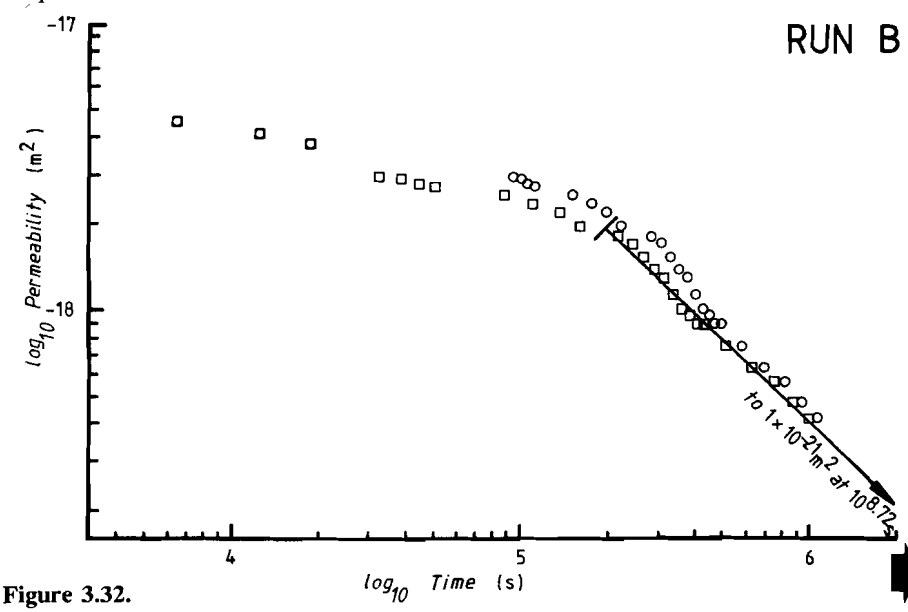

Figure 3.32.

Table 3.10. Linear regression results for $\log_{10}$(permeability) versus $\log_{10}$(time) data from brine flow-through Runs A and B, Sample SP137.

RUN A	RUN B
8.5 MPa effective confining pressure	18.5 MPa effective confining pressure
a = - 14.2899	a = - 12.6362
b = - 0.5171	b = - 0.9588
c = - 0.9894	c = - 0.9957

where: a = $\log_{10}$(permeability) at time t = 1 s.
b = slope of the $\log_{10}$(permeability) versus $\log_{10}$(time) plot.
c = correlation coefficient giving degree of fit to straight line by linear regression.
κ = at^b and $\log_{10}a + b.\log_{10}t$.

At the beginning and the end of the 18.5 MPa run (RUN B), the permeability was determined at 8.5 MPA for comparison. These values are plotted in Figure 3.31 and show recoverable and non-recoverable parts of the permeability loss due to flow-through at the increased effective confining pressure of 18.5 MPa. The permanent change in permeability (measured from a starting permeability of 7.05 x $10^{-18}m^2$ at 8.5 MPa effective confining pressure) was 3.06 x $10^{-18}m^2$ after a period of ~ 1 x 10^6s at 18.5 MPa. Elastic closure of the porosity probably accounts for the 3.58 x $10^{-18}m^2$ recoverable permeability as a result of the removal of the 10 MPa excess confining pressure.

A fluorescent dye which was allowed to flow into the specimen in the final stage of the experiment, showed an even distribution of colour throughout the entire specimen when this was later sectioned. This indicated a homogeneous distribution of fluid pathways throughout the sample. Microstructural examination of a gamma-irradiated portion of the sample (following the method of Urai et al. 1987) revealed that it had recrystallized by about 60-70% during the entire sequence of brine permeability determinations (by fluid-assisted grain boundary migration).

Figure 3.32. Permeability decay data for SP137, wet, RUN B. Log_{10}(permeability) versus $\log_{10}$(time) plot for the brine flow-through experiment at 18.5 MPa conventional effective confining pressure. Data are plotted in two ways; including periods of no-flow ("o" symbols) and by removal of periods of no-flow ("□" symbols).

Finally a comparison of the permeability decay rates between wet and dry Asse salt rock is attempted. This is possible because the sample (SP107) used in the dry decay tests and the sample (SP137) used in the wet tests, were both deformed under similar conditions. The permeability decay rate for the wet case, for a permeability of 1 x $10^{-17}m^2$ at 8.5 MPa effective confining pressure and ΔP_f = 2 MPa, can be determined directly from the data. The corresponding decay rate for the same permeability and effective confining pressure for the dry case relies on extrapolation as discussed in Section 3.4.2. Extrapolation of the linear and logarithmic trends for the dry (SP107) data yield two widely differing decay rates at 1 x $10^{-17}m^2$. These wet and dry decay rates for a permeability of 1 x $10^{-17}m^2$ at 8.5 MPa conventional effective confining pressure are:

WET (direct	3.27 x $10^{-23}m^2s^{-1}$
DRY (linear extrapolation)	4.324 x $10^{-23}m^2s^{-1}$
DRY (logarithmic extrapolation)	6.41 x $10^{-23}m^2s^{-1}$

Clearly, permeability reduction was faster in the wet test. This is inferred to be due to the operation of processes such as crack closure by pressure solution (Spiers and Schutjens, 1990) and microstructural modification by fluid-assisted recrystallization (as observed).

3.5.3. Summary

For experimentally deformed (dilated) Asse salt rock under worst case conditions, prevailing for example in mine gallery wall rock, the following may be concluded from the saturated brine flow through experiments.

The permeability to brine is very close (within a factor of 2) to the permeability to argon gas, under the same effective confining pressure. This suggests that electroviscous drag effects do not affect permeability determination with brine for permeabilities of the order of $10^{-17}m^2$. At a given permeability and effective confining pressure, wet dilated Asse salt rock undergoes a more rapid decay of permeability during a saturated brine flow-through experiment, than the equivalent dry material.

Permeability decay rate depends upon brine flow rate and/or fluid pressure gradient, not just the presence of brine in the pores. This effect was unexpected but is apparently very important. It severely limits the interpretation of the results and extrapolation from this single long term test. Nonetheless, the results show that the

permeability decay is strongly dependent upon the effective confining pressure range chosen. A doubling in effective confining pressure causes a doubling of the long term permeability decay rate (expressed as $d(\log_{10}\kappa)/d(\log_{10}t)$) when flow of saturated brine takes place under constant pressure gradient. The permeability decay under brine flow-through appears to obey a power law of the form $\kappa = at^b$ where b = - 0.5 for 8.5 MPa conventional effective confining pressure and b = -1 for 18.5 MPa, under a fluid pressure gradient of 7 MPa per metre in both cases.

3.6. General conclusions

The following general conclusions are drawn for this chapter. In situ natural Asse Speisesalz, away from the creeping free surfaces of mined cavities (gallery walls, shafts and boreholes) is impermeable ($< 10^{-21}m^2$) and crack free, with a recrystallized grain structure and tight grain boundaries. Around galleries, shafts and boreholes high deviatoric stresses, with low hydrostatic components, cause rapid creep of the rocksalt through crystal plasticity accompanied by dilatation, mainly by intergranular fracture. These dilated grain boundaries induce a considerable permeability increase near the cavity walls. Laboratory permeability measurements, traversing this boundary region using cores of known position, showed that the permeability increases systematically from a low "undisturbed value of $< 10^{-21}m^2$, $\geq$ 3 m in from the mine gallery wall, to a maximum value of $\sim 10^{-17}m^2$ at the wall surface. Triaxial deformation experiments, aimed at investigating this dilatancy induced permeability, showed similar changes in permeability to occur during rapid flow by crystal plastic mechanisms (glide) accompanied by dilatation. The rate of increase of permeability with strain and, in particular, dilatation was surprising, with 5 orders of magnitude increase in 4% strain and just 0.2% dilational volume change. Clearly a model very different from the established-porosity/permeability relations of the Carman-Kozeny type (see Chapter 6) is required to describe this critical threshold behaviour, which presumably involves rapid evolution of connectivity rather than a steady change in conductivity of pre-existing pathways. This problem is addressed in Chapter 6, where a microcrack linkage model is developed based on percolation theory and found to agree favourably with the data of these experiments on natural salt rock.

The permeability of dry, dilated Asse material responds to short term changes in effective confining pressure in a recoverable manner, and is described well by the Walsh (1981) elastic crack closure model. This model embodies an inverse logarithmic relation between fracture aperture (a) and effective confining pressure (P_e), i.e. $a \propto - \log_e (P_e)$, and a cubic relation between permeability (κ) and fracture

aperture ($\kappa \propto a^3$) i.e. $\kappa^{1/3} \propto - \log_e (P_e)$. Application of this model to naturally dilated wall rock material and experimentally deformed and dilated, deeper, material showed that, with respect to permeability, dilated salt rock obeyed an effective stress law of the type $P_e = P_c - s \, . \, P_f$ where $s \approx 1$, i.e. a conventional effective stress law $P_e = P_c - P_f$. In addition, for argon gas permeabilities less than $10^{-19}m^2$, a Klinkenberg gas slippage effect was also evident causing an error of + 8% at $10^{-19}m^2$ possibly rising to 47% of the measured value at $10^{-21}m^2$, at the mean argon gas fluid pressure used (1.5 MPa). Permeabilities to brine were found to be within a factor of 2 lower than for argon gas under equivalent conditions indicating that electroviscous drag effects affecting brine permeametry must also be small for such close agreement.

The longer term aspects of permeability change with effective pressure relevant to the closure of a storage cavity in salt rock were examined by a 2 month duration hydrostatic test on dry experimentally deformed and dilated Asse Speisesalz material using argon gas permeametry. A similar duration test, using brine as pore fluid and steady state flow-through permeametry, was performed to study the wet behaviour. In both cases the duration was not long enough to allow reliable extrapolation of the times of decay to natural background levels of permeability (~ $10^{-21}m^2$). It was clear, however, that wet decay rates were much greater than dry at a given effective confining pressure. The wet decay rates were also enhanced at higher effective pressures and by the presence of a fluid pressure gradient and/or through flow of brine though the magnitude of the gradient was admittedly rather high (7 MPa/metre). The absence of a theoretical model which should encompass dislocation creep effects, pressure solution, the influence of fluid pressure gradient, and recrystallization of the deformed salt rock by fluid-assisted grain boundary migration, constituent mechanisms makes long term prediction of the permeability decay in wet material very difficult. More information on the individual mechanisms is needed first and indeed advances are being made into quantitative descriptions, especially in the field of pressure solution (Spiers and Schutjens, 1990). Dry material exhibited a resistance to creep closure due to work hardening, where the applied effective pressure during the permeability decay test was much less than the stress required to deform the material to 10% strain before the test began. The stored energy due to work hardening is consumed in the wet decay tests by fluid-assisted recrystallization that was observed to have taken place throughout the majority (60-70%) of the specimen. No recrystallization took place in the dry specimen.

In naturally deformed rocks of other less soluble materials (silicates etc.) it may be expected that similar processes will occur during metamorphism involving fluid

transport. It is interesting to speculate that since such small volume changes (0.2%) are required for a change of 5 orders of magnitude in permeability, through microcracking as an accommodation to restricted crystal-plastic flow, then fluid flow may be expected well into the plastic fields of macroscopic mechanical behaviour (where, minor dilatancy might not be recognized but inhomogeneous plastic deformation and grain scale intergranular microcracking is possible). These questions are addressed in Chapter 7.

CHAPTER 4

Experiments on Synthetic Fine-Grained Salt Rock

4.1. Introduction

The experiments reported in Chapter 3 showed that plastic deformation of natural salt rock (Asse Speisesalz) under conditions allowing minor dilatancy (≤ 0.1%) can lead to very large increases in permeability. The observed dilatancy and permeability development was attributed to grain-scale microcracking caused by the existence of insufficient easy slip systems (i.e. < 5 independent ones) to allow strain compatibility to be maintained from grain to grain. Taking this into account, the development of dilatancy and permeability in salt rock might be expected to depend on grainsize and initial microstructure. It could also depend upon the content of rigid impurity phases (such as anhydrite), since rigid inclusions create their own grain-scale strain compatibility problems (Ashby, 1970). Thus the effects of grainsize, initial microstructure, and impurity content might have important implications for the behaviour of salt rock both in the radioactive waste disposal environment and as a silicate rock analogue.

The present chapter is concerned with determining the influence of crystal plastic deformation on dilatancy and permeability development in a fine-grained, synthetic equivalent of pure natural salt rock. The underlying aims were

a) to compare the observed behaviour with that of the Asse Speisesalz, thus assessing the effects of grainsize and microstructure, and
b) to develop an understanding of the behaviour of a well-defined, pure, synthetic salt rock system as a basis for investigating the effect of controlled fractions of anhydrite added as a second (rigid) phase (see Chapter 5).

4.2. Experimental approach and methods

The present approach involved combined triaxial deformation plus permeametry experiments performed on synthetic salt rock samples, at room temperature and at relatively rapid strain rates (~ $10^{-5}s^{-1}$). Two sets of tests were carried out. The first series was performed at systematically varied confining pressures in an attempt to

locate the transition from dilatant to non-dilatant behaviour (i.e. the dilatancy transition). The second set was carried out, within the dilatant field, to monitor the development of permeability with dilatancy under similar conditions to the tests on Asse salt (Chapter 3). The synthetic test material used was specially prepared for the purpose and consisted of recrystallized material of fine grainsize (300 - 350 μm) but otherwise (broadly) comparable to natural salt in microstructure, density and initial permeability.

4.2.1. Sample preparation

Great difficulty was encountered in finding a suitable method of reproducibly preparing samples with the required density and microstructure. After numerous trials, only the method described here proved successful, and it should therefore be regarded as critical.

Starting Material - The samples were prepared by cold pressing and annealing granular sodium chloride starting material. This consisted of unsieved, analytical grade sodium chloride powder (Merck) with an average initial grainsize in the range 200 - 400 μm. The grains were predominantly well-developed cubic crystals, containing occasional brine-filled fluid inclusions. Since no special precautions were taken in handling the material, it also contained a small amount of adsorbed atmospheric water. In all, the total water content of the starting material is estimated to have been < 0.1 wt%.

Cold Pressing Apparatus - The granular salt starting material was cold pressed using a piston and cylinder compaction apparatus specially constructed from a high strength stainless steel (DIN werkstoff nr. 4122). This apparatus consisted of a cylindrical pressure vessel (50 mm internal diameter by 120 mm outside diameter by 200 mm length) with loose-fitting stainless steel pistons sealing in the polished bore of the vessel with the aid of 'Buna-N' 'O'-rings located in grooves around the pistons. Each piston also possessed a sealable axial port to allow evacuation of the salt prior to pressing.

Pressing Procedure - Before each cold pressing run, the bore of the vessel had to be treated to lower the salt/vessel friction during pressing. To achieve this, the bore was coated with P.T.F.E. ('teflon') from an aerosol spray (Dow Corning G.M.B.H., München) and fine graphite powder was generously applied whilst the spray dried. The P.T.F.E. and graphite did contaminate the surface of the pressed samples slightly, but no visible penetration or internal discoloration resulted at any stage of

preparation or testing. Once the bore had been prepared, the lower piston was inserted into the vessel and a glass-fibre tissue disc placed above it to aid subsequent sample/piston separation. A fixed quantity of salt powder (~ 530 g) was then funnelled into the vessel, a second glass-fibre tissue disc was placed above it, and the upper piston was inserted. The sample was then evacuated and the two piston ports sealed to maintain vacuum during the pressing. Pressing was carried out using a 400 kN hydraulic press to apply an axial stress of ~ 200 MPa for 20 minutes. At this stage, the compacted sample could not easily be removed from the vessel without damage. This problem was overcome by cooling the vessel plus contents to -20°C in a refrigerator. The different thermal contractions of the steel (~ 1 x 10^{-5}/°C) and salt (~ 4 x 10^{-5}/°C) then allowed the salt sample to be easily pressed out with a low capacity laboratory press (whilst cold). The cold sample was subsequently removed to a dry room (R.H. < 15%) to warm up to room temperature, thus avoiding condensation of atmospheric moisture onto the sample. When at room temperature, the 50 mm diameter cylindrical samples thus produced were wiped free of excess graphite and P.T.F.E. They were then machined in a lathe to the desired length. The sample density at this stage was 98.7 ± 0.3% of the theoretical density of NaCl.

Annealing Stage - The machined samples were next placed between 1 cm thick by 50 mm diameter stainless steel end-blocks (A.I.S.I. 316 quality) separated by 0.05 mm thick 'teflon' sheets, and jacketed in 'viton' sleeves. The sleeves were then sealed against the blocks under vacuum using wire closures. The samples were subsequently annealed at 150°C and 100 MPa confining pressure for one week in an externally heated, large capacity, silicone oil filled pressure vessel. The final results were translucent, recrystallized, synthetic salt rock samples (125 mm long by 50 mm diameter) with few visible defects and a permeability lower than could be resolved in tests of 1 day duration by the argon gas transient step method (i.e. < $10^{-21}m^2$). The final density was > 99.5%. The samples were stored before and after deformation in a dry room (RH ≤ 15%).

4.2.2. Apparatus and experimental procedure

The present deformation/permeametry experiments were performed using the dilatometric triaxial apparatus (i.e. the Heard apparatus) and transient step argon permeametry system described in Chapter 2. The procedures followed and techniques used were essentially identical to those described for the experiments on natural salt rock in Chapter 3 (see also Chapter 2). This included the use of perforated 'teflon' end-sheets and glass fibre gas spreaders to minimize specimen

barrelling, through piston boundary effects, and to maximize gas access throughout deformation (see Chapter 2). The raw signals from the Heard apparatus (i.e. force, displacement, volume change and temperature) were logged directly by means of a micro computer (EPSON QX-16) and reduced to give stress vs. strain and volume change vs. strain data using the programs described in Chapter 2.

To investigate the influence of confining pressure and the location of the dilatancy transition, a series of 6 samples (P40T-11, 19, 20, 21, 23 and 25) was first deformed at strain rates of ~ 4 x $10^{-5}s^{-1}$ and at room temperature, using constant confining pressures in the range 5 to 20 MPa. The samples were each deformed to total strains of ~ 10%. Their permeability to argon gas was determined both before and after deformation at a reference confining pressure of 5 MPa. This was done using the transient step method operating at 1.5 MPa mean pressure with an initial step of ~ 0.2 MPa.

In the second series of tests, two samples (P40T24 and P40T48) were used to investigate the detailed development of permeability with dilatancy under conditions identical to the natural salt experiments (c.f. Section 3.3), i.e. under room temperature conditions at 5 MPa confining pressure and 1.5 MPa mean argon pressure. The specimens were deformed incrementally at a strain rate of 4 x $10^{-5}s^{-1}$, in steps of ~ 2% strain, arresting the loading piston after each increment and allowing stress relaxation. Argon gas permeametry was carried out during and between each increment (using the transient step technique with 0.2 MPa steps) to allow a dynamic and static evaluation of the permeability throughout the deformation.

On removal from the apparatus the specimens were stored in a dry room and later sectioned for microstructural analysis as described in Section 4.4. A deeply blue-coloured epoxy resin was impregnated into the sectioned material under vacuum. By filling all accessible porosity connected to the plane of the section, this clearly highlighted the dilatant regions and permeable networks.

4.3. Results

The set of 6 experiments performed to investigate the influence of confining pressure and the location of the dilatancy transition is listed in the first block of Table 4.1, together with the experimental conditions and data on the initial and final state of the samples. The two tests performed to monitor the development of permeability with dilatancy are similarly listed in the second block of Table 4.1.

Recall that all samples were deformed at a strain rate of ~ 4 x $10^{-5}s^{-1}$ with a (pore fluid) pressure of 1.5 MPa argon gas.

4.3.1. Mechanical data: Effect of confining pressure

The stress vs. strain curves and volume change vs. strain curves, obtained from the first 6 tests listed in Table 4.1, are shown in Figures 4.1a-f in order of descending confining pressure. The curves exhibit similar stress vs. strain behaviour with a progressive drop in flow stress towards the lower confining pressures. This trend is explicitly illustrated in Figure 4.2, where the flow stresses supported at fixed strains are plotted against confining pressure for all samples tested. In addition, the volume change data of Figure 4.1 show a clear progression from non-dilatant behaviour ($\Delta V/V_0 \leq 0$), at 20 MPa confining pressure, to strongly dilatant ($\Delta V/V_0 > 0$) behaviour at 5 MPa. This effect may be clearly seen from a plot of volume change against confining pressure, at constant strain (see Figure 4.3). Where developed, dilatancy appears to be approximately linearly related to strain (see Figure 4.1).

4.3.2. Permeability development

It is clearly apparent from Table 4.1 that the final permeability of the present samples increases dramatically with the dilatancy produced at progressively lower confining pressures. As described previously, detailed monitoring of permeability development during deformation was provided by experiments P40T24 and P40T48 (Block 2, Table 4.1). These were deformed at a confining pressure of 5 MPa in steps of ~ 2% strain (rate ≈ 4 x $10^{-5}s^{-1}$), with argon gas permeametry being performed during and between each step.

The stress vs. strain and volume change vs. strain data obtained for P40T24 and P40T48 are given in Figures 4.4a and b. Note the close reproducibility of the data, also in comparison with sample P40T11 (Figure 4.1f) which was tested in a single step (6.7% strain) under otherwise identical conditions. The jumps in the volume trace on specimen P40T24 (Figure 4.4a) were due to minor volumometer control plus thermal drift problems. The twin test, P40T48 (Figure 4.4b), was free from these problems.

The permeability vs. strain and volume change data for samples P40T24 and P40T48 are presented in Table 4.2 and also in Figures 4.5 (permeability vs. strain) and 4.6 (permeability vs. volume change). In all cases, the limited permeability data

obtained (dynamically) during test P40T11 are also included. Clearly, taking into account the initial permeabilities (Table 4.1), a very rapid development of permeability occurs with respect to strain (see Figure 4.5). The development of permeability is even more rapid with respect to dilatant volume change (see Tables 4.1, 4.2 and Figure 4.6). These data show that a dilatant volume change of only 0.25% causes a permeability increase of at least 4 orders of magnitude (to values of ~ 2 x $10^{-17}m^2$) before saturating more gradually to permeabilities of ~ 2 x $10^{-16}m^2$ by 1% volume change. Beyond this, the permeabilities remain more or less constant, to volume changes up to ~ 3% (P40T48). Broadly speaking, the initial and final permeability vs. volume change data obtained, for the remaining samples in Table 4.1 which showed dilatancy, are entirely consistent with the detailed data given here. Lastly, it is interesting to note that a small permeability increase was recorded when the axial load was removed from samples P40T24, P40T48 and P40T11 at the end of each deformation run - see Figures 4.5 and 4.6 (solid symbols).

Table 4.1. Deformation experiments on fine-grained synthetic salt deformation experiments a strain rates of ~ 4 x $10^{-5}s^{-1}$.

Specimen Number	Initial Density (Pure NaCl = 100%)	Initial Permeability	Confining Pressure	Total Strain	Total Volume Change	Final Permeability
P40T25	99.68%	1.05x$10^{-21}m^2$	20.0 MPa	15.8%	- 0.07%	< $10^{-21}m^2$
P40T19	99.54%	< $10^{-21}m^2$	20.0 MPa	9.6%	- 0.19%	< $10^{-21}m^2$
P40T23	99.66%	< $10^{-21}m^2$	17.5 MPa	9.2%	+ 0.00%	< $10^{-21}m^2$
P40T21	99.58%	< $10^{-21}m^2$	15.0 MPa	9.4%	+ 0.23%	< $10^{-21}m^2$
P40T20	99.64%	< $10^{-21}m^2$	10.0 MPa	9.2%	+ 0.50%	3.3x$10^{-17}m^2$
P40T11	98.23%**	< $10^{-21}m^2$	5.0 MPa	6.7%	+ 1.10%	3.6x$10^{-16}m^2$
P40T24*	98.85%	< $10^{-21}m^2$	5.0 MPa	11.8%	+ 2.50%	1.76x$10^{-16}m^2$
P40T48*	99.78%	< $10^{-21}m^2$	5.0 MPa	13.1%	+ 3.10%	3.26x$10^{-16}m^2$

* stepped tests
** relative density before annealing

Permeabilities measured at 5 MPa confining pressure (1.5 MPa mean argon gas pressure). Positive volume changes are dilatant. Effective pressures were up to 1.5 MPa less than the listed confining pressures, dependent upon permeability (argon pore fluid).

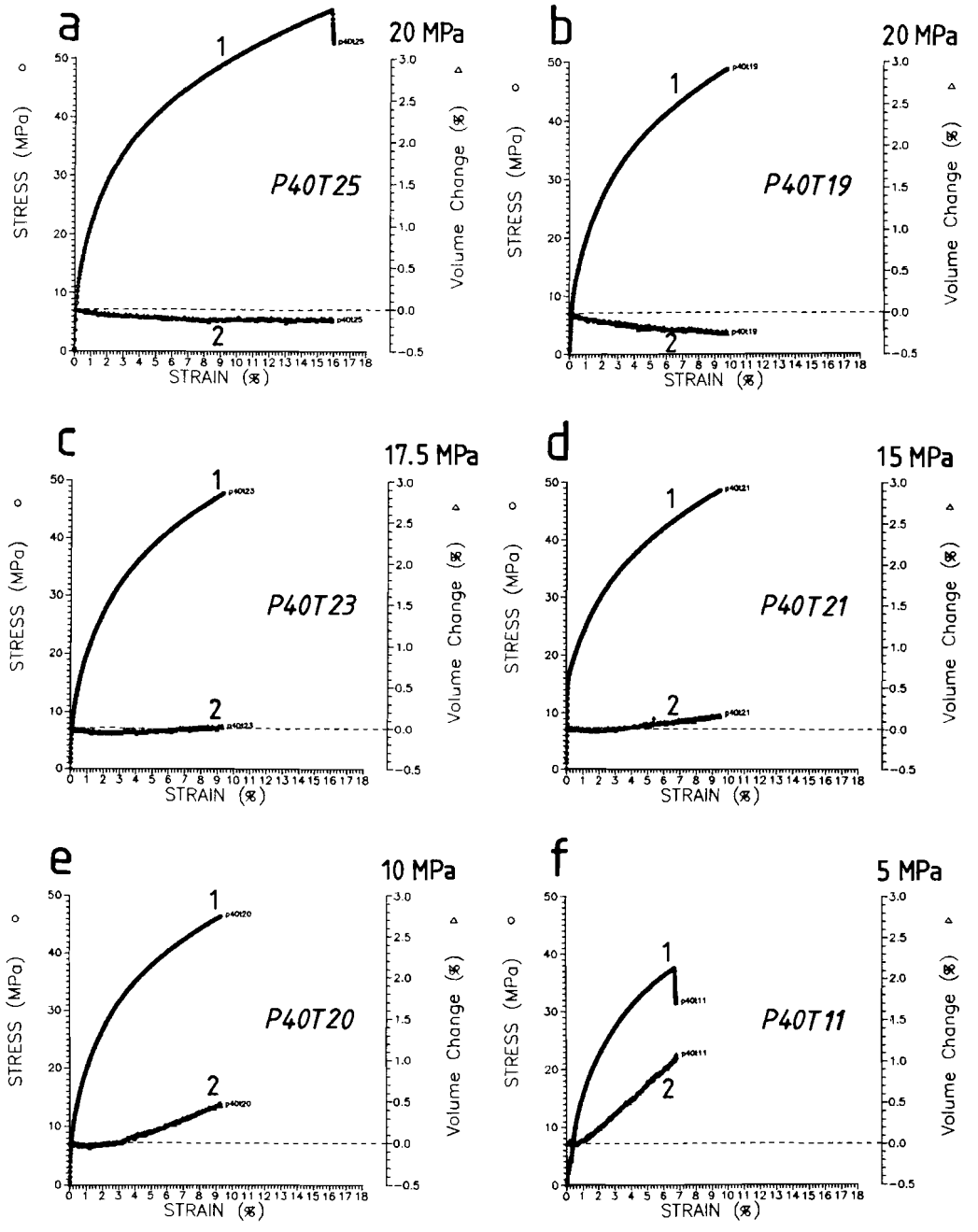

Figure 4.1a-f. Stress vs. strain (1) and volume change vs. strain (2) curves for the pure synthetic salt material deformed at ~ 4 x $10^{-5}s^{-1}$ under the confining pressures indicated. Volume change is expressed in terms of the volumetric strain $\Delta V/V_0$ x 100%, where ΔV is total volume change (expansion positive) and V_0 is initial sample volume.

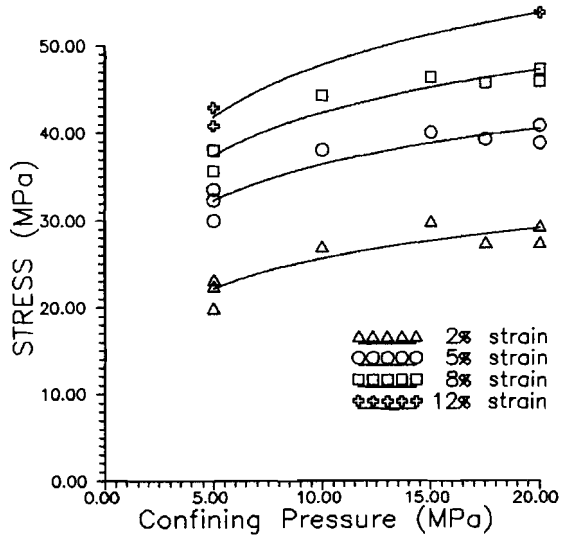

Figure 4.2. Flow stress supported at fixed strains, plotted against confining pressure for the entire suite of synthetic salt samples tested.

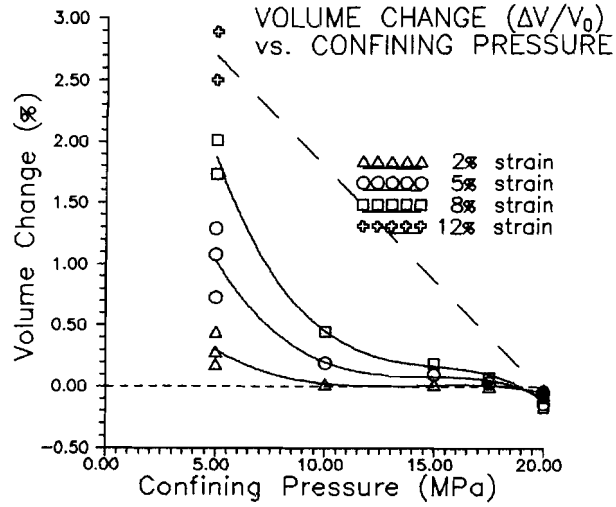

Figure 4.3. Volume change versus confining pressure data, at constant strains, for all tests performed on synthetic, fine-grained halite. The transition from dilatant (positive volume change) to non-dilatant behaviour at ~ 18 MPa is clearly visible.

Table 4.2. Permeability development with volume change and strain for synthetic pure halite samples deformed at ~ 4 x $10^{-5}s^{-1}$ under a confining pressure of 5 MPa.

Specimen Number	Strain	Volume Change %	Permeability m^2
P40T24	1.45	0.26	1.83 x 10^{-17} d
P40T24	2.91	0.59	5.47 x 10^{-17} s
P40T24	3.92	0.84	9.98 x 10^{-17} d
P40T24	5.01	1.10	1.43 x 10^{-16} s
P40T24	5.79	1.29	1.41 x 10^{-16} d
P40T24	7.11	1.52	1.43 x 10^{-16} s
P40T24	7.54	1.62	1.44 x 10^{-16} d
P40T24	9.19	1.95	1.39 x 10^{-16} s
P40T24	9.70	2.12	1.31 x 10^{-16} d
P40T24	11.83	2.48	1.15 x 10^{-16} s
P40T24	11.83	2.48	*1.65 x 10^{-16} s
P40T24	11.83	2.48	*1.70 x 10^{-16} s
P40T48	0.73	0.09	2.48 x 10^{-19} s
P40T48	1.15	0.23	1.55 x 10^{-17} d
P40T48	1.55	0.32	2.24 x 10^{-17} s
P40T48	2.40	0.54	1.08 x 10^{-16} d
P40T48	3.27	0.80	2.77 x 10^{-16} s
P40T48	3.65	0.90	3.09 x 10^{-16} d
P40T48	4.70	1.21	3.86 x 10^{-16} d
P40T48	5.70	1.48	4.03 x 10^{-16} s
P40T48	6.06	1.58	3.96 x 10^{-16} d
P40T48	7.27	1.87	3.75 x 10^{-16} d
P40T48	8.56	2.15	3.39 x 10^{-16} d
P40T48	9.84	2.43	2.99 x 10^{-16} d
P40T48	10.20	2.50	2.93 x 10^{-16} s
P40T48	10.66	2.63	2.76 x 10^{-16} d
P40T48	11.69	2.85	2.49 x 10^{-16} d
P40T48	12.66	3.03	2.23 x 10^{-16} d
P40T48	13.04	3.09	2.17 x 10^{-16} s
P40T48	13.04	3.09	*3.26 x 10^{-16} s
P40T11	1.62	0.21	6.32 x 10^{-17} d
P40T11	5.26	0.84	2.81 x 10^{-16} d
P40T11	6.68	1.09	2.80 x 10^{-16} s
P40T11	6.69	1.10	3.98 x 10^{-16} s
P40T11	6.69	1.10	4.01 x 10^{-16} s
P40T11	6.69	1.10	*4.10 x 10^{-16} s

s = static determination
d = dynamic determination
* = axially unloaded

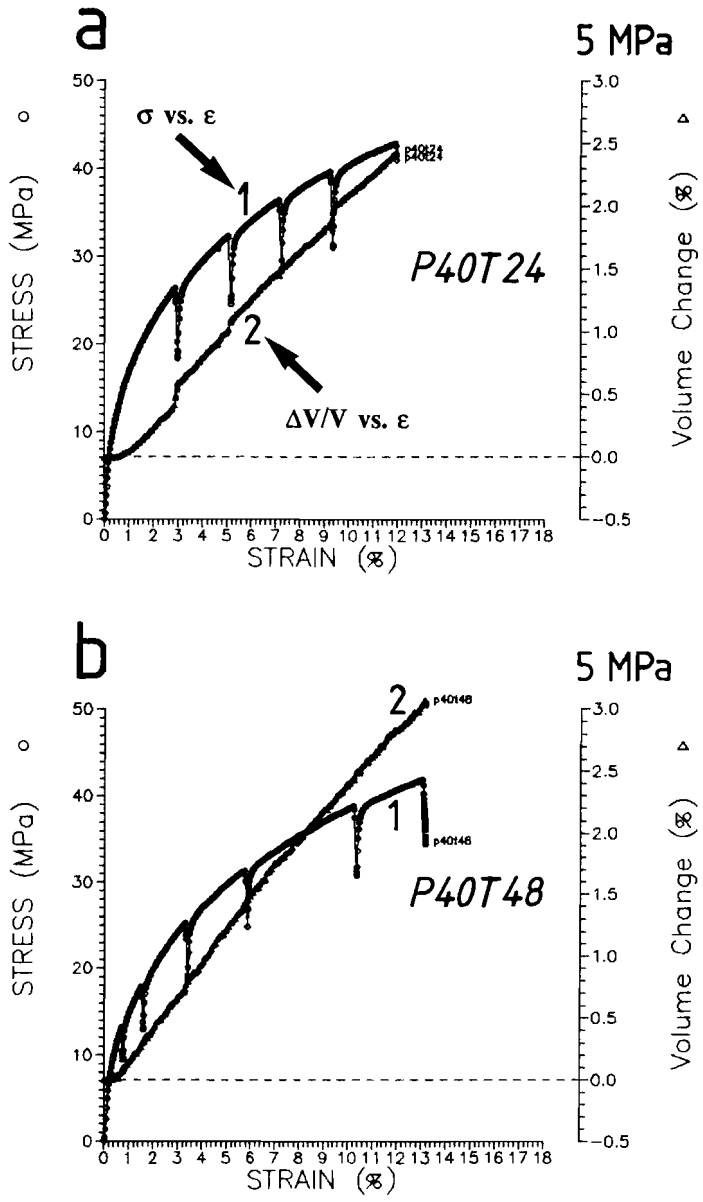

Figure 4.4a, b. Stress vs. strain and volume change vs. strain data for the two incremental deformation tests (P40T24 and P40T48) performed on the synthetic salt at 5 MPa confining pressure (see Table 4.1). Permeability was determined at and between each increment of strain.

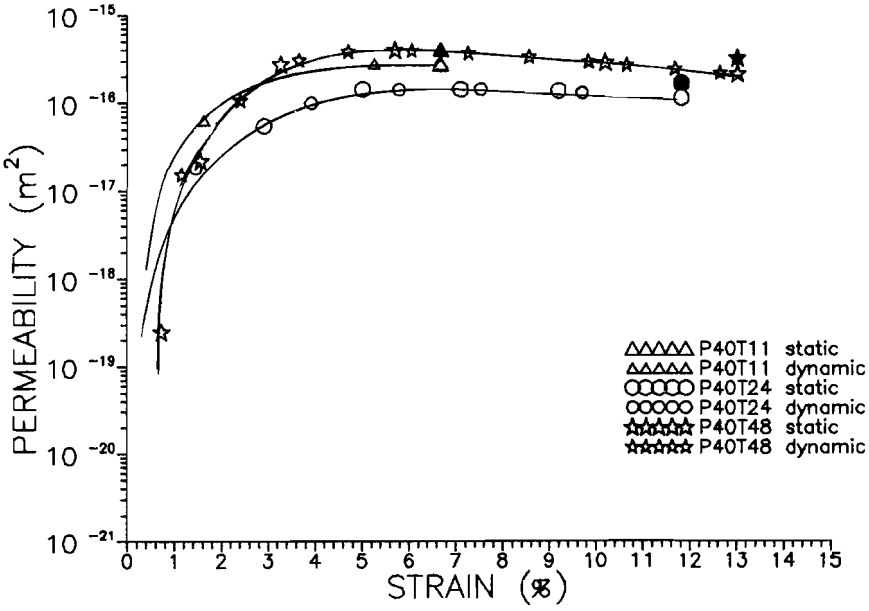

Figure 4.5. Data on the development of permeability with progressive strain obtained for the synthetic salt samples tested at 5 MPa confining pressure (P40T11, 24, 48). Large symbols represent determinations of permeability made under static conditions, i.e. between strain increments. Smaller symbols represent dynamic determinations made during deformation. Solid symbols are determinations made after the final axial load was removed.

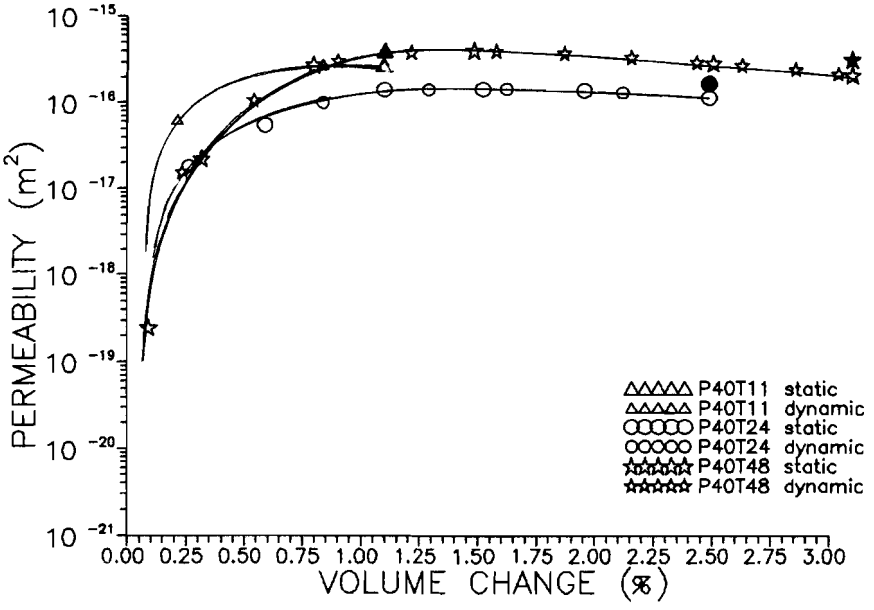

Figure 4.6. The development of permeability with progressive dilatant volume change in the samples tested at 5 MPa confining pressure (P40T11, 24, 48). Symbols follow the convention of Figure 4.5.

4.4. Microstructural observations and interpretations

4.4.1. Undeformed synthetic salt rock

Optical examination of sections of the annealed synthetic starting material, using both transmission and reflection microscopy, revealed an entirely recrystallized microstructure in which the original (cubic) grains of the powder were completely reworked. The grain texture was near polygonal (foam texture) with fluid inclusions (some containing gas) delineating the grain boundaries, triple points and junctions (see Figures 4.7a and b). The grainsize distribution appeared to have narrowed compared to the original powder, with most of the grains in the range 300 - 350 μm (c.f. 200 - 400 μm in the original powder). Polished and etched surfaces (prepared following Spiers et al., 1986) revealed the material to be free from plastic deformation features and dislocation substructure (Figure 4.7b). Microcracks and fractures were also absent.

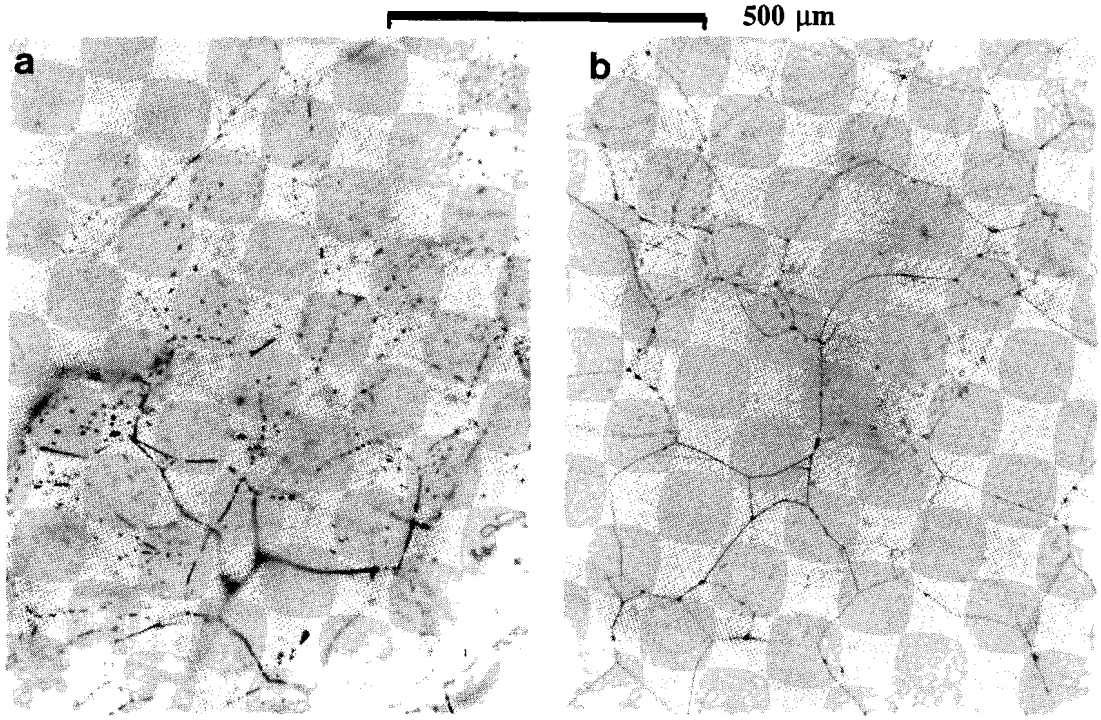

Figure 4.7a, b. (a) Transmission optical micrograph of the transparent fine-grained synthetic halite starting material. The annealed polygonal microstructure is visible in depth as lines of dark gas-filled fluid inclusions along grain edges and across some grain faces. In (b), grain boundaries and triple junctions are clearly visible on the etched surface, using reflected light. Note the absence of dislocation substructure.

4.4.2. Deformed material

Externally, the deformed samples all exhibited very little barrelling, even after 15% strain.

The microstructure of sectioned, highly dilated material (5 MPa confining pressure) showed intergranular microcracks to be widespread but with no evidence whatsoever of transgranular cracking. The intergranular microcracks were made easily visible by the impregnation method mentioned previously. The network of grain boundary microfractures is illustrated in Figures 4.8a-d. The crack spacing was clearly controlled by the grainsize, and cracks parallel to the specimen axis (shortening direction) were visibly wider. Nearly all grain boundaries were at least partly open and the grains showed a general compression-parallel flattening fabric. Polished and etched thin sections showed clear evidence of intergranular plasticity such as intense slip bands and other dislocation etch features not present in the starting material (see Figure 4.8e).

The non-dilated material deformed at 20 MPa confining pressure showed extensive recrystallization to have taken place, with exaggerated grain growth to diameters upto ~ 5 mm. Earlier grains were traceable inside the large recrystallized grains by the presence of fluid inclusions arranged in polygonal networks similar to the polygonal texture of the undeformed samples (see Figure 4.9a). The recrystallized grains themselves were free from plastic deformation features normally revealed by etching of the polished section. Their boundaries generally contained numerous worm- and tube-like fluid inclusions. While the bulk of the microstructure was dominated by these large recrystallized grains, some smaller (300 μm) grains were observed near the outer surfaces of the samples. These showed heavy dislocation damage and appear to be remnants of the initial microstructure overprinted with the plastic deformation features incurred during mechanical testing. The microstructure of these remnant regions closely resembles that seen in heavily dilated material, except that the intergranular microcracking is absent. Figure 4.9b shows such a region where small plastically deformed grains have clearly been consumed (i.e. overgrown) by recrystallization. Putting all this information together, it is inferred that the samples developed a plastically deformed crack-free microstructure during testing, which then recrystallized statically during the 2 - 3 month period that the samples were stored (at room T) prior to sectioning.

An examination of the entire suite of samples showed that all subjected to confining pressures greater than or equal to 15 MPa (i.e. developing little or no dilatancy, $\leq$ 0.25%) had substantially recrystallized, while those deformed at pressures below 10

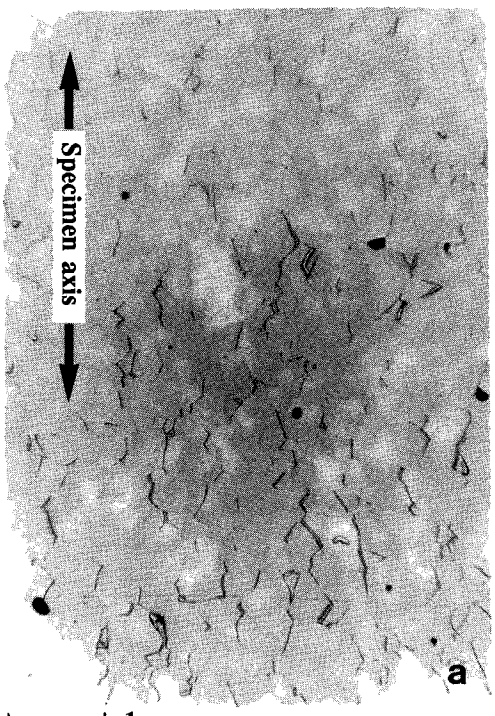
Specimen axis
a
1 mm

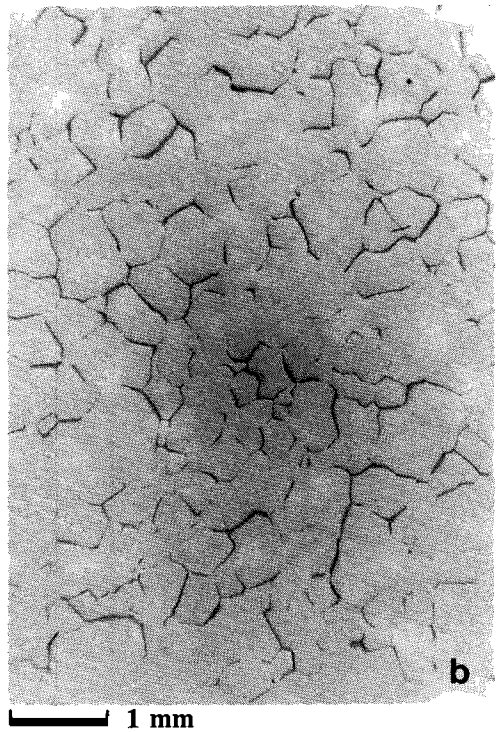
b
1 mm

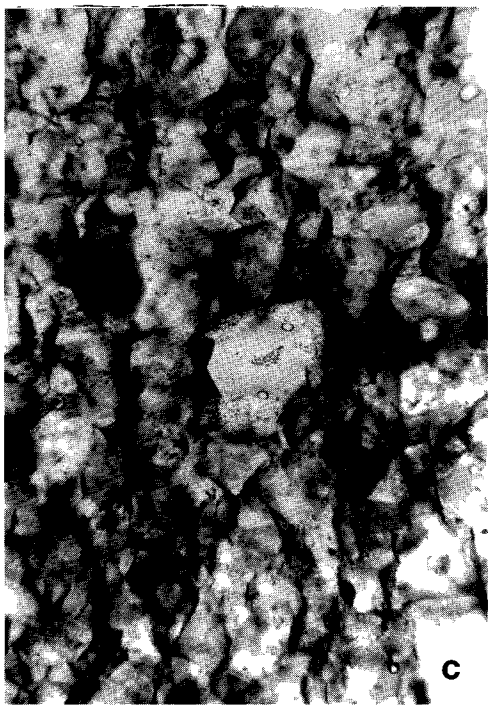
c
1 mm

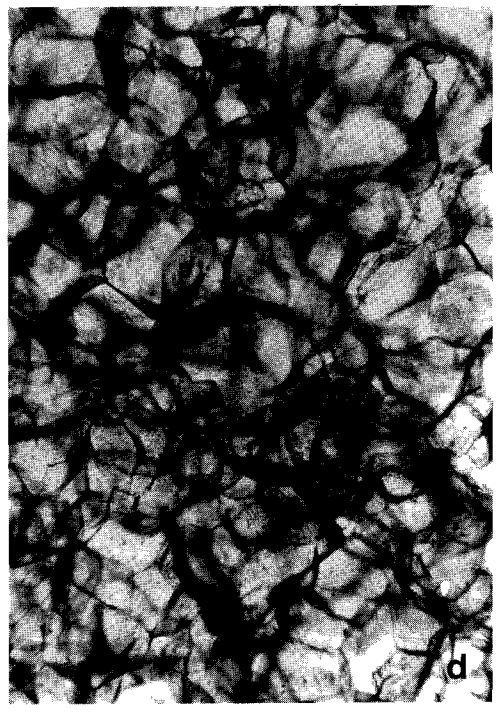
d
1 mm

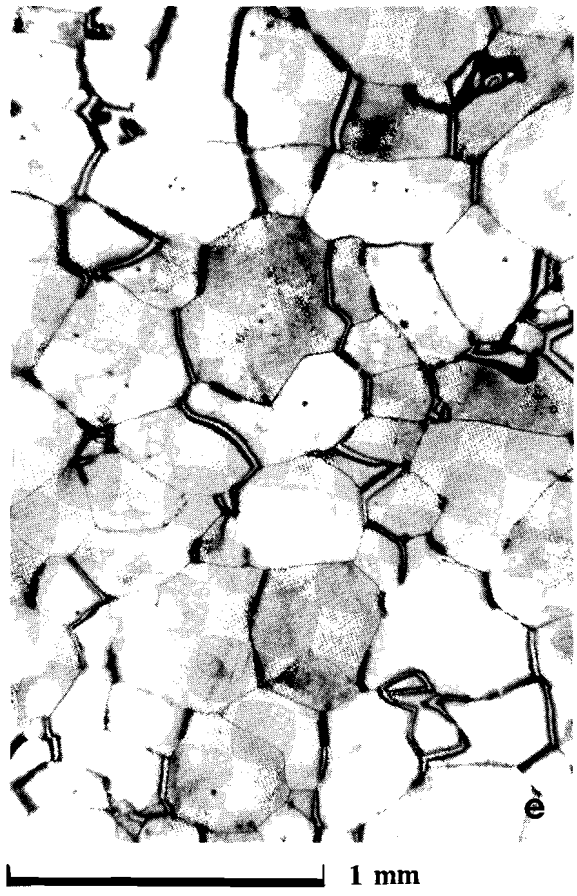

Figure 4.8a-e. Dilated fine-grained synthetic halite material deformed under 5 MPa confining pressure (Sample No. P40T11, ~ 1% dilatation). (a) - Reflection optical micrograph showing zig-zag microcracks following grain boundaries and terminating in tapered segments. These axial microcracks are oriented parallel to the maximum principal stress direction. (b) - Reflection optical micrograph showing the more isotropic distribution of grain boundary microcracks perpendicular to the specimen shortening axis. (c) - Transmission optical micrograph of axial section showing the dark resin-filled, dilated grain boundary microcrack network in depth. (d) - Similar to (c) but oriented as for (b). (e) - Reflection optical micrograph of etched surface showing intragranular crystal plastic deformation features, revealed by dislocation etching, in addition to intergranular microcracking.

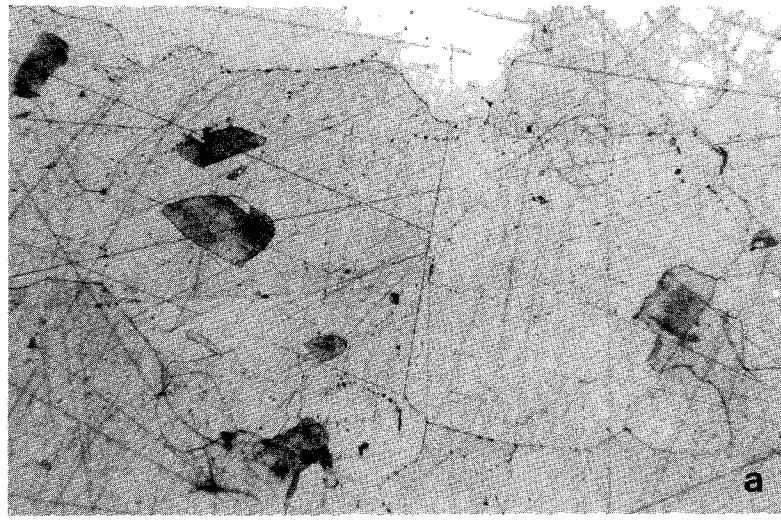

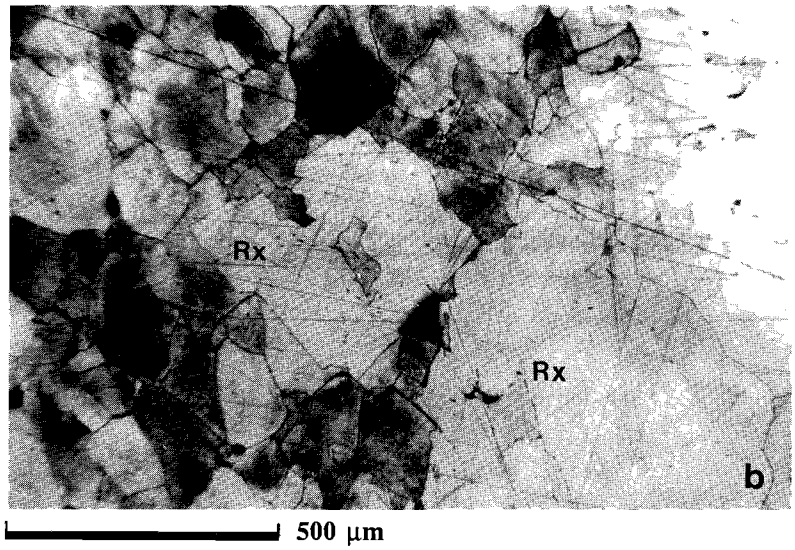

Figure 4.9a, b. Sample P40T25 (deformed under 20 MPa confining pressure).

a) Reflected light micrograph of recrystallized non-dilated synthetic halite showing remnants of earlier grains traceable by fluid inclusion arrays.

b) Reflected light micrograph of region near specimen outer surface showing plastically deformed, heavily etched, grains partially consumed by larger recrystallized damage free grains (marked Rx) typical of the specimen centre.

MPa (i.e. in the dilatant field) showed no recrystallization. All recrystallized samples showed some non-recrystallized areas near their surfaces. These clearly preserved the plastically deformed microstructure seen in the entirely non-recrystallized samples (though microcracking was absent). One sample (P40T23) deformed at 17.5 MPa confining pressure showed a cluster of cubic halite crystals, up to 1 cm across, growing outwards from the specimen centre (Figure 4.10). The grain boundaries between these crystals were inferred to contain brine films, since they were easily disturbed during section preparation (see Spiers et al., 1986). This made the boundaries suddenly visible as thermomechanical distortion caused them to open and lose optical continuity, thus reflecting instead of refracting the incident light. On this basis it is concluded that the mechanism of post-deformational recrystallization was a fluid-assisted one of the type reported by Spiers et al. (1986) and Urai et al. (1986). Clearly, this mechanism seems to be suppressed in material deformed under low pressure (strongly dilatant) conditions.

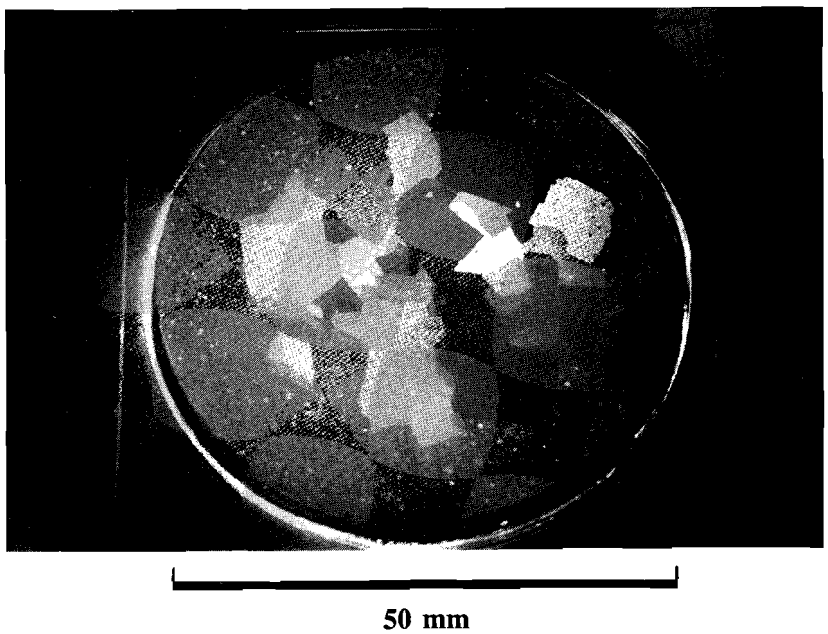

Figure 4.10. Photomicrograph of a large cluster of recrystallized halite grains in specimen P40T23 (deformed under 17.5 MPa confining pressure to 9.2% strain, and stored, at room temperature).

4.5. Discussion

4.5.1. Effects of confining pressure on mechanical behaviour and dilatancy

The present experiments performed on synthetic fine-grained salt at different confining pressures have clearly shown an effect of pressure on dilatancy and on mechanical behaviour, i.e. resistance to deformation.

First referring to Figure 4.3, the significant dilatancy developed at low pressures clearly falls towards zero at confining pressures in excess of 18 MPa, for the range of strains covered in the present experiments. A "dilatancy transition" for these conditions and low strains ($\leq$ 15%) can therefore be placed at ~ 18 MPa.

Referring now to strength aspects, it has been shown that the stress supported at constant strain gradually increases with increasing confining pressure, see Figure 4.2. In seeking to explain this effect, it is important to consider the possible "strength" contribution of the work done by the dilating samples as they expanded against the confining pressure (see Edmond and Paterson, 1972). Following Edmond and Paterson, this "strength" contribution can be corrected for, to yield the intrinsic material flow stress/strength ($\sigma_{corrected}$) using the equation

$$\sigma_{corrected} = \sigma_{measured} - P\,(d\varepsilon_v / d\varepsilon_1) \qquad (4.1)$$

Here, $Pd\varepsilon_v$ is the work done by the specimen in expanding by a volumetric strain $d\varepsilon_v$, against the confining pressure P, whilst shortening by a strain of $d\varepsilon_1$. (N.B. $d\varepsilon_v$ and $d\varepsilon_1$ are taken positive for dilatation and axial shortening respectively).

This equation has been applied to "correct" the stress vs. pressure data of Figure 4.2 for the volumetric work effect in question. The results are plotted in Figure 4.11, which barely differs from Figure 4.2. Clearly then, the effect is very small (< 1%) and cannot explain the observed increase in measured flow stress with increasing confining pressure. This must therefore represent a true increase in strength. Discounting the effect of pressure on dislocation mobility, known to produce a weakening effect at high pressures (.1 - 1 GPa, see Auten et al., 1973), the observed strengthening of the synthetic salt rock material towards high pressures can only be attributed to the accompanying decrease in damage by dilatant microcracking activity. Alternatively stated, the test material was weaker at low pressures due to the decreased traction-bearing capacity of (microcracked) grain boundaries.

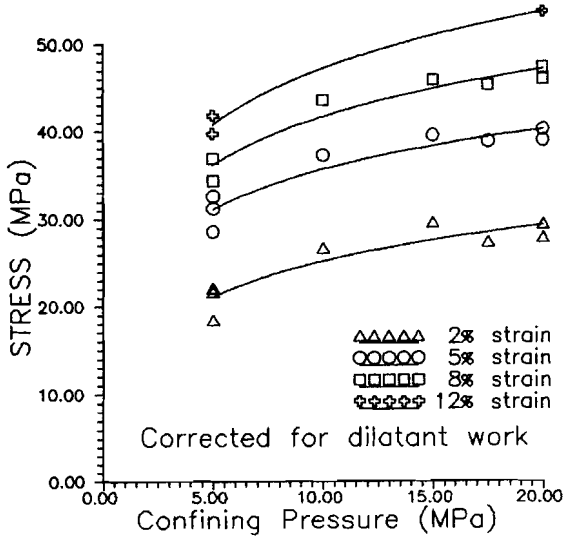

Figure 4.11. Intrinsic flow stresses (i.e. corrected for volumetric work according to Equation 4.1) plotted against confining pressure, at the fixed strains indicated.

4.5.2. Permeability development versus strain and dilatancy

The experiments designed to follow the development of permeability with deformation in the dilatant field (at 5 MPa) showed an extremely rapid rise of permeability followed by saturation (Figures 4.5 and 4.6). Taking microstructural observations into account, this rapid appearance of permeability with strain, and especially with dilatant volume change, suggests the sudden or critical establishment of a conductive (i.e. percolating) network of grain boundary microfractures (Englman et al., 1983; Charlaix et al., 1987 and Gueguen and Dienes, 1989). If established in the present tests, the observed saturation behaviour implies that such a network would have to maintain roughly constant fluid conductivity despite an on-going increase in the conduit volume of the network as dilatancy proceeds. This might be possible if the network conductivity at high strains were controlled by grain boundary fractures oriented sub-perpendicular to the maximum principal stress, these being forced to remain almost closed under axial load. Such an explanation is supported by the increase in permeability recorded when the axial load was removed from the samples at the end of the deformation tests (see Figures 4.5 and 4.6, solid symbols).

In summary, the observed critical development of permeability is far too rapid to explain using simple porosity/permeability models such as the Carman-Kozeny type (Dullien, 1979) which predict gradual permeability increase. Instead a percolation model which includes the development of connectivity as well as porosity is required. Such a model is developed in Chapter 6 and applied to the present data with considerable success.

4.5.3. Comparison with natural material and effects of grainsize and microstructure

The mechanical behaviour and volumetric behaviour of the synthetic salt rock is qualitatively similar to that of the coarser grained natural Asse Speisesalz tested under similar conditions (see Chapter 3 and Spiers et al., 1986). Both materials deformed by crystal plastic mechanisms (glide) coupled with dilatancy at lower confining pressure, and undergo a transition to non-dilatant behaviour at effective pressures greater than 15 - 18 MPa.

In the fully dilatant field, the fine-grained material tends to be weaker and more dilatant than the Asse salt. For example, at ~ 5 MPa and 10% strain, the fine-grained salt is ~ 10% weaker and a factor of 3 more dilatant (c.f. Figures 4.4 and 3.11-15). Now the microcracking is confined to grain boundaries in the finer material and, as in the case of the Asse salt, can be attributed to the existence of insufficient (< 5) easy slip systems to allow intergranular strain compatibility. The relative weakness and enhanced dilatancy of the fine salt is probably related, via grainsize, to the greater frequency of grain boundary microcracks in the finer material. The absence of transgranular cracking in the synthetic salt is thought to reflect the more equant (i.e. polygonal) grain shapes in this material compared to the interlocked grain structure of the Asse Speisesalz which exhibits inter- and intragranular cracking.

Let us now consider the non-dilatant field (confining pressure > 18 MPa). A comparison of the flow strength of the fine material in this field (i.e. at 20 MPa), with the results of experiments performed on natural Asse salt under similar conditions (see Spiers et al., 1986, p. 63), shows the finer synthetic material to now be stronger (by 5% at 10% strain). This is broadly consistent with expectations based on dislocation interaction models for the work hardening effect of grain boundaries (or neighbouring grains) on the intracrystalline plastic flow strength of polycrystals. Such models include the Hall-Petch grain boundary hardening model (see Reed-Hill, 1973, p. 228) as well as the similar boundary compatibility model of

Ashby (1970). In essence, these predict linear relations between σ and $d^{-1/2}$, where σ = plastic flow (or yield) stress and d = grainsize. In both cases the grain boundaries are considered to form barriers to dislocation glide, causing pile-ups and flow resistance which increases with closer barrier spacing. The σ vs. d data available from the tests on the fine-grained salt and the coarse Asse material, in the non-dilatant field, are insufficient to quantitatively test the applicability of these models. Nonetheless, a grain boundary hardening effect seems by far the most likely reason for the relatively high strength of the finer salt under non-dilatant conditions.

Aside from the mechanical behaviour, the rapid development of permeability with strain and dilatant volume change seen in the synthetic material is very similar to the behaviour exhibited by the coarser Asse material (c.f. Figures 4.5 and 4.6 with 3.16 and 3.17). Both seem to show a critical development followed by a saturation to comparable values of permeability with increasing strain and dilatancy. The critical threshold appears to occur a little earlier with respect to both linear and volumetric strain in the finer synthetic material. In conclusion, it can be stated that the grainsize and microstructure of the salt rocks studied do not strongly influence the development of dilatancy and permeability during plastic deformation in the dilatant field, though dilatancy is slightly enhanced in the fine material.

4.6. Summary / conclusions

Combined deformation plus permeametry experiments have been performed to investigate the influence of intracrystalline plastic deformation processes on dilatancy and permeability development in pure, fine-grained, synthetic salt rock. The experiments were carried out at room temperature, at confining pressures in the range 5 - 20 MPa, and at strain rates of ~ $10^{-5}s^{-1}$. The principal results and conclusions are summarized below.

Firstly, the results obtained showed a transition from dilatant to non-dilatant behaviour at confining pressures > 18 MPa (effective pressures > 16.5 MPa). In the dilatant field (comparable with gallery wall conditions in a salt mine), the fine-grained synthetic salt rock developed more dilatancy (3 vol% developed at 5 MPa, 10% strain) and was weaker than the coarser natural Asse salt rock of Chapter 3, deformed under identical conditions. The more equant polygonal texture of the finer grained synthetic material produced only grain boundary cracks, as a result of intergranular strain compatibility problems. In the Asse material, transgranular cracking also developed as a response to heterogeneity in deformation at the grain

scale between its coarser more irregular and interlocked crystals. The lower flow strength of the synthetic material and the enhanced dilatancy can be attributed to the far greater density of grain boundary microcracking resulting from the finer grainsize. At pressures above the dilatancy transition, the finer grained synthetic material showed a transition to a higher flow strength than the coarser Asse material, this being consistent with grain boundary hardening and related theories such as the Hall-Petch model.

The permeability development for the synthetic material was found to be very similar to that for Asse salt under dilatant conditions. Very rapid initial permeability development (from 10^{-21} to $10^{-17}m^2$) occurred with small amounts of volumetric strain (0.2%), suggesting critical behaviour. This critical permeability development is thought to result from linkage of grain boundary microcracks and is further discussed in terms of percolation theory in Chapter 6. The permeability of the fine salt, once developed, soon achieved saturation values (at ~ $10^{-16}m^2$) with increasing strain and dilatant volume change. This is thought to reflect limits imposed by the available population of grain boundaries suitably oriented for dilatation. The saturation permeability may have been controlled by the poor conductivity of narrow, unfavourably oriented grain boundary microcracks (those sub-perpendicular to the maximum principal stress) linked in series with the wider, axially oriented microcracks, as observed in the microstructure.

Post-deformational, fluid-assisted recrystallization was observed extensively in the fine salt specimens deformed at or above 15 MPa (final dilatancies < 0.25%). This occurred at room temperature over the period of 2 - 3 months between testing and sectioning of the samples. Although this recrystallization played no role in the present rapid experiments, similar experiments performed on time scales of 2 - 3 months (i.e. at strain rates < $10^{-8}s^{-1}$) at pressures ≥ 15 MPa can be expected to exhibit dynamic recrystallization possibly reducing flow strength (Spiers et al., 1989), as well as affecting dilatancy and/or permeability development. Nonetheless, if small dilatant volume changes, ~ 0.2 - 0.3 vol%, are able to occur by grain boundary dilatation or microfracture in salt or other similarly textured rock materials, then permeability is likely to develop rapidly in a similar (critical) manner to that shown by the present experiments.

CHAPTER 5

Experiments on Synthetic Salt/Anydrite Rock: Effect of Anhydrite as a Rigid Second Phase

5.1. Introduction

In the preceeding chapters (Chapters 3 & 4), it was shown that plastic deformation of halite rock can lead to very large increases in permeability when accompanied by minor dilatancy ($\leq$ 0.2 vol%). This effect was seen both in natural salt rock (Chapter 3) and in fine-grained synthetic material (Chapter 4), and was attributed to microcracking caused by grain-to-grain strain compatibility problems.

It was also pointed out in Chapter 4 that the addition of a rigid second phase (such as anhydrite) to pure polycrystalline salt can be expected to produce additional strain compatibility problems, possibly enhancing dilatancy and permeability development during plastic deformation and thus extending the dilatant field to higher pressures. Comparable effects, causing strength changes and void formation, are known to occur during the plastic deformation of metals containing a rigid phase (see Kelly & Nicholson, 1971). For example, intra- and intergranular rigid precipitates in plastically deformable alloys form barriers to dislocation motion, thus increasing flow stresses and work hardening rates (e.g. Ashby, 1966, 1970). At the same time, the stress and deformation fields generated around such precipitates can give rise to substantial stress enhancement effects leading to cavitation at particle/matrix interfaces, to fracture of the particles, to steep gradients in dislocation activity and density in surrounding grains, and conceivably to dilatancy in the matrix (refer Eshelby, 1957; Ashby, 1966, 1970; Tanaka et al., 1970).

Clearly, the above effects could have important implications for the development of dilatancy and permeability during plastic deformation of salt rocks containing typical (rigid) impurities such as anhydrite. Areas of relevance here include the behaviour of salt/anhydrite rock

a) in the radioactive waste disposal environment, and
b) as an analogue for polyphase silicate rocks containing "rigid" porphyroclasts (e.g. quartz/feldspar and olivine/pyroxene rocks where both fluid and melt transport might be strongly influenced by deformation).

To date, the mechanical behaviour of only a few geologically relevant composite materials have been investigated experimentally (see Jordan, 1986, 1987 for calcite in halite; see also Price, 1982 and Ross et al., 1987 for anhydrite in halite). No data seem to be available on the influence of plastic deformation on dilatancy and permeability in salt/anhydrite composites or similar materials. Chapter 4 of this thesis was concerned with the influence of plastic deformation on pure synthetic salt rock. Here, this work is extended to systematically investigate the effect of anhydrite added as a second phase.

5.2. Experimental approach, material and methods

5.2.1. Approach

The present experiments consisted of combined triaxial deformation plus permeametry tests performed on synthetic salt rock samples identical to those used in Chapter 4 but containing anhydrite as a second phase. The experiments were carried out just within the non-dilatant field for the pure synthetic material, i.e. at room temperature, a strain rate of ~ 4 x $10^{-5}s^{-1}$ and a confining pressure of 20 MPa (see Chapter 4). In order to determine the effect of the added anhydrite as fully as possible, both the anhydrite content (volume fraction) and particle size were independently varied from sample to sample. The anhydrite content was varied in the range 5 - 35 vol%, using mean particle sizes of roughly 10 times, 1 times and 0.1 times the grainsize of the halite matrix (~ 300 μm).

5.2.2. Sample preparation

The samples were prepared by cold pressing and annealing appropriate mixtures of granular salt plus particulate anhydrite. The procedure followed was essentially identical to that described in Chapter 4 for pure salt samples.

Starting Materials - Unsieved analytical grade sodium chloride powder (Merck, grainsize 200 - 400 μm) was used for the halite "matrix" material. Particulate anhydrite was prepared by crushing and sieving anhydrite rock taken from the Upper Triassic of the Swiss Jura (Belchen Tunnel locality, see Laubscher, 1984). This consisted predominantly of fine-grained anhydrite (coarsest crystals ≤ 200 μm) plus occasional small rhombs of dolomite (≤ 300 μm). Thermo-gravimetric analysis (TGA) showed the anhydrite content to be > 95% with the carbonate content < 3.5% and gypsum ($CaSO_4.2H_2O$) ≤ 0.3%, by weight. Triaxial experiments

performed on this rock showed it to exhibit elastic-brittle behaviour under the conditions of present interest, with very high compressive strength (e.g. ~ 145 MPa at 10 MPa confining pressure - see tests by Peach in Spiers et al., 1989). The initial permeability of the material was also determined and found to be $< 10^{-19} m^2$. To prepare the required particulate anhydrite, the anhydrite rock was crushed and sieved to make three grainsize fractions, namely a "coarse" (4.8 - 8.0 mm), a "medium" (300 - 600 μm) and a "fine" (37 - 75 μm) fraction. The fine fraction was washed with acetone to remove the very fine dust that was not removed by sieving. The medium and coarse fractions were tumble ground to round the fragments to relatively smooth sub-ellipsoidal particles with low shape factors (mostly in the range 1 - 2.5).

Mixing, Pressing and Annealing - The granular salt and particulate anhydrite materials were mixed appropriately to produce composite batches containing 5, 10, 20, 25, 30 and 35 vol% of each of the three anhydrite fractions (coarse, medium and fine particles). To ensure good mixing, each batch was prepared and mixed in ten equal lots. The lots were tipped into the pre-lubricated cold pressing (piston-and-cylinder) apparatus described in Chapter 4 in a rapid manner intended to avoid unmixing. The samples were then pressed at 200 MPa for 20 minutes following the procedure outlined in Section 4.2.1. The pressed billets were subsequently removed from the pressing vessel, machined to correct dimensions, and annealed hydrostatically at 100 MPa / 150°C in viton jackets for one week (for details, refer Section 4.2.1). During cooling, the hydrostatic pressure was maintained to minimize any microcrack damage due to the different thermal expansion coefficients of the anhydrite and halite. When room temperature was reached, the pressure was removed gradually, also to avoid cracking the specimens. The 125 mm by 50 mm diameter cylindrical samples thus obtained were stored in a dry room (RH < 15%) until required for testing.

5.2.3. Microstructure of samples prior to deformation

The above procedure yielded 3 sets of samples respectively containing coarse, medium and fine anhydrite particles in volume fractions of around 5, 10, 15, 20, 25 and/or 35%. These sets will be referred to henceforth as the coarse, medium and fine suites of samples. Their microstructure was investigated optically using polished and etched sections prepared following Spiers et al. (1986).

Coarse and Medium Suites - These samples exhibited a closely similar microstructure consisting of polycrystalline anhydrite particles embedded in a dense, recrystallized halite matrix (Figures 5.1a, b). In both suites, the anhydrite particles showed a conspicuous alignment of long axes normal to the cylindrical axis of the samples. This is illustrated for coarse material in the axial ratio vs. fluctuation diagram of Figure 5.2. In both coarse and medium samples, the mean axial ratio of the anhydrite particles was not significantly different from the shape factor before pressing. In addition, the particles showed little or no evidence of internal deformation or microcracking. The observed fabric is therefore inferred to have formed by rigid rotation of the anhydrite particles during the cold pressing stage of sample preparation. It may also be partly inherited from deposition of the granular salt / anhydrite mix into the pressing vessel.

The halite matrix surrounding the anhydrite in both coarse and medium samples was characterized by a more or less polygonal recrystallized microstructure similar to that seen in the pure halite starting material described in Chapter 4 (see Figures 5.3a, b). As in the pure material, most grain boundaries and triple junctions contained arrays of fine-scale fluid inclusions mostly containing gas. These appeared to be isolated. In the coarse suite, the average grainsize of the halite matrix was around 250 - 300 μm (Figure 5.3a). In the medium suite, however, the matrix grainsize tended to be slightly finer, i.e. around 100 - 200 μm (Figure 5.3b), and fluid inclusions seemed to be more abundant. Examination of etched sections in reflected light revealed the matrix halite grains to be apparently free of plastic deformation features and dislocation substructure in both suites of samples (Figures 5.3a, b).

Fine Suite - The samples containing fine-grained anhydrite displayed a somewhat different microstructure, particularly at higher anhydrite contents. Firstly, the samples possessed no visible shape fabric in the anhydrites. Rather, the fine anhydrite grains (mostly single crystals) were more or less exclusively located at halite grain boundaries. At anhydrite contents $\geq$ 10%, the fine-grained anhydrite formed an essentially continuous network surrounding individual salt grains or clusters of salt grains (Figures 5.1c and 5.3c). These grains and grain clusters tended to show the initial size and cubic shape characteristic of the starting salt powder, with some evidence for flattening parallel to the cold pressing direction (i.e. sample axis) - see Figures 5.1c and 5.3c. Examination of etched sections showed no evidence for dislocation substructures characteristic of plastic deformation in the halite. Indeed, all of the original halite grains (from the starting powder) seemed to have recrystallized either into single new grains or, more

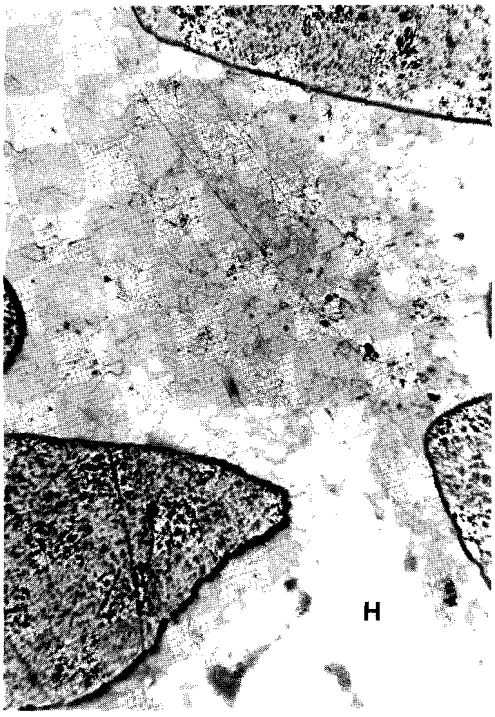

a) Coarse

b) Medium

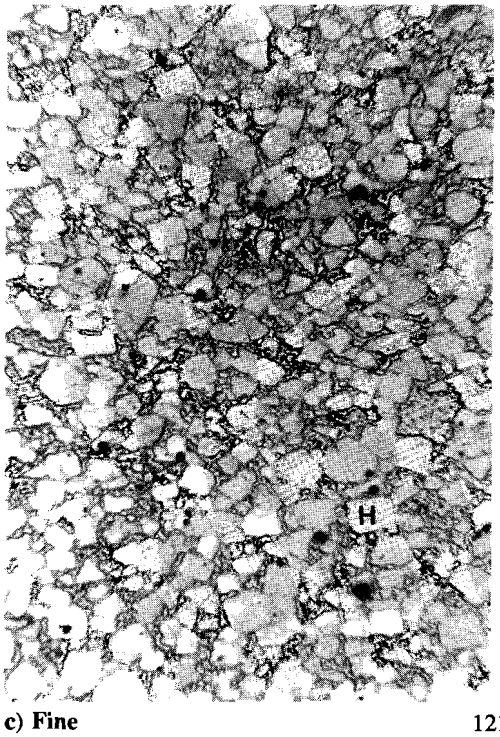

c) Fine

2 mm

Specimen axis

Figure 5.1a,b,c. The general microstructure of the coarse (a), medium (b) and fine (c) suites of salt/anhydrite composite materials prior to deformation. Reflected light micrographs of polished sections. Anhydrite content is ~ 20% in all cases shown. All micrographs at same scale (H = halite).

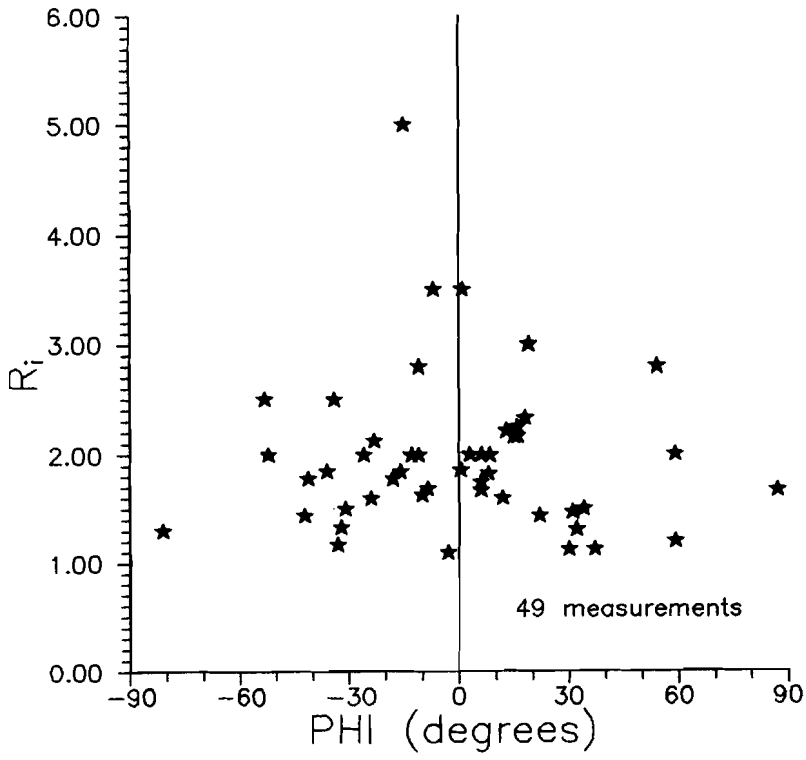

Figure 5.2. Axial ratio (R_i) vs. fluctuation (ϕ) diagram showing shape fabric of anhydrite clasts in an undeformed coarse composite sample containing ~ 20% anhydrite. Fluctuation ϕ represents angular deviation of clast long axes from a plane oriented normal to the cylindrical sample axis.

a) Coarse

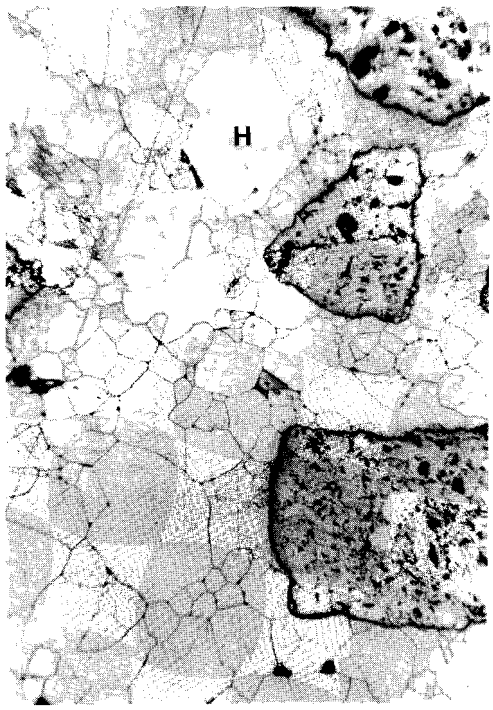

b) Medium

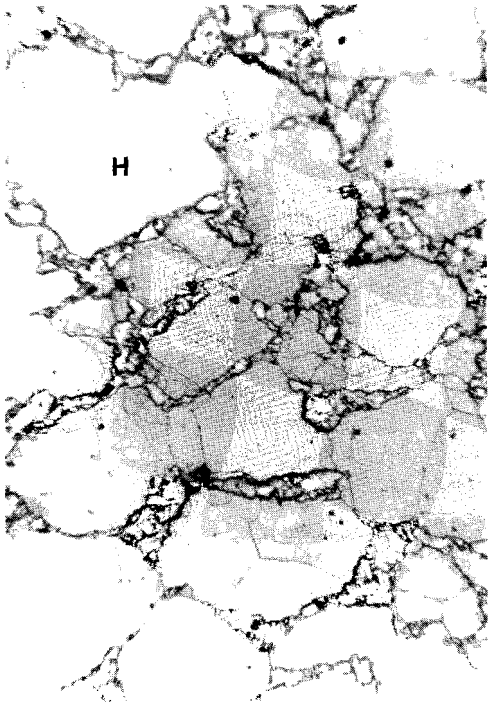

c) Fine

500 μm

Figure 5.3a,b,c. Detailed microstructure of the coarse (a), medium (b) and fine (c) suites of salt/anhydrite composites (~ 20% anhydrite) prior to deformation. Reflected light micrographs of polished and etched sections showing the recrystallized microstructure of the halite. All micrographs are reproduced at the same scale (H = halite). Specimen axis vertical in all cases. Note the difference in grain size of the halite matrix between a) and b). Note that in c) the fine-grained anhydrite forms a network surrounding recrystallized salt grains inherited from the original powder (see text).

commonly, into the above mentioned clusters of semi-polygonal new grains (see Figures 5.1c and 5.3c).

Lastly, vacuum impregnation of blue-dyed epoxy resin into the samples containing fine anhydrite revealed that the grain boundary networks of anhydrite retained a small amount of connected porosity. No such porosity was seen in the coarse and medium suites of samples, except for minor amounts developed at the surface of the anhydrite particles in the medium suite.

5.2.4. Experimental apparatus and conditions

The three suites of samples containing coarse, medium and fine fractions of anhydrite were all deformed under identical conditions using the Heard triaxial/dilatometric apparatus described in Chapter 2. Argon gas permeametry was performed before, during and after deformation using the system and transient step method also described in Chapter 2. In addition to the measurements performed under the conditions of the deformation tests (20 MPa), the permeability of all samples was measured before and after deformation (i.e. initially and finally) at a reference confining pressure of 5 MPa. All permeametry was conducted at a mean argon pressure of 1.5 MPa with a 0.2 MPa step. The detailed experimental procedures employed were the same as those mentioned in Chapters 2, 3 and 4. Computer-reduced stress, strain and volume change data were obtained from automatically logged signals as described in Section 4.2.2.

As mentioned previously, the deformation conditions for the present tests were chosen, following the investigations of the previous chapter, such that pure synthetic salt rock (i.e. the pure halite end-member) would be non-dilatant. All samples were therefore deformed at a confining pressure of 20 MPa, with 1.5 MPa argon gas (pore fluid) pressure, to total strains of ~ 15% at a constant strain rate of ~ 4 x $10^{-5}s^{-1}$ and at room temperature. In all cases, deformation to ~ 15% strain was carried out in a single step.

5.3. Results: Mechanical data

The three suites of samples tested are listed in Tables 5.1a and b along with their initial porosities and permeabilities, the applied strains and final permeabilities.

Table 5.1a. Initial porosities and permeabilities for the 3 suites of salt/anhydrite samples tested. Porosity was calculated from annealed sample density and volume of the component solids (pure anhydrite, $CaSO_4$, was assumed).
Permeabilities were determined at an initial reference confining pressure of 5 MPa and a mean argon gas pressure of 1.5 MPa, using a transient step magnitude of 0.2 MPa. A second initial permeability determination was made at 20 MPa. Permeability determinations marked "*" were inferred from measurements made under lower confining pressure.

Sample	Anhydrite Content Vol%	Initial Porosity %	Initial Permeability (1) at 5 MPa m^2	Initial Permeability (2) at 20 MPa m^2
COARSE				
P40T30	5	0.34	$< 10^{-21}$	$* < 10^{-21}$
P40T26	10	0.39	$< 10^{-21}$	$* < 10^{-21}$
P40T28	10	0.58	$< 10^{-21}$	$* < 10^{-21}$
P40T41	15	0.19	1.02×10^{-21}	$* < 10^{-21}$
P40T27	20	0.57	$< 10^{-21}$	$* < 10^{-21}$
P40T22	25	0.86	1.41×10^{-21}	$< 10^{-21}$
P40T29	35	0.78	$< 10^{-21}$	$* < 10^{-21}$
MEDIUM				
P40T36	5	0.52	1.72×10^{-21}	
P40T32	10	0.51	$< 10^{-21}$	$* < 10^{-21}$
P40T35	10	0.34	$< 10^{-21}$	$* < 10^{-21}$
P40T40	15	0.42	$< 10^{-21}$	$* < 10^{-21}$
P40T34	18.1	0.28	2.25×10^{-21}	
P40T38	20	0.69	$< 10^{-21}$	$* < 10^{-21}$
P40T37	25	0.52	1.01×10^{-20}	
P40T39	35	2.85	1.62×10^{-18}	5.99×10^{-19}
FINE				
P40T42	5	0.38	1.06×10^{-21}	
P40T31	10	0.50	$< 10^{-21}$	$* < 10^{-21}$
P40T43	10	0.13	1.79×10^{-21}	
P40T44	15	0.78	4.08×10^{-21}	
P40T33	20	1.19	$< 10^{-21}$	$* < 10^{-21}$
P40T45	20	1.15	1.93×10^{-19}	2.37×10^{-19}
P40T46	25	0.89	3.37×10^{-19}	2.96×10^{-19}
P40T49	30	2.11	1.95×10^{-18}	1.83×10^{-18}

Table 5.1b. Applied strains and final permeabilities for the 3 suites of salt/anhydrite samples tested. Permeabilities were determined using a mean argon gas pressure of 1.5 MPa, using a transient step magnitude of 0.2 MPa. Permeability determinations marked "*" were inferred from measurements made under lower confining pressure and identical strain.

		Permeabilities after deformation (at final strain)		
Sample	Final Strain %	(3) Permeability at 20 MPa, sample loaded axially m^2	(4) Permeability at 20 MPa, load removed m^2	(5) Permeability at 5 MPa, axial load removed m^2
COARSE				
P40T30	16.16			1.809×10^{-20}
P40T26	14.56			8.54×10^{-21}
P40T28	9.78	$* < 10^{-21}$	$* < 10^{-21}$	$< 10^{-21}$
P40T41	15.8			1.20×10^{-20}
P40T27	15.55	$< 10^{-21}$	$* < 10^{-21}$	$< 10^{-21}$
P40T22	15.96		7.15×10^{-20}	1.99×10^{-19}
P40T29	16.01	3.43×10^{-18}	4.11×10^{-18}	1.58×10^{-17}
MEDIUM				
P40T36	16.21			1.41×10^{-21}
P40T32	15.84	$* < 10^{-21}$	$* < 10^{-21}$	$< 10^{-21}$
P40T35	15.99	$* < 10^{-21}$	$* < 10^{-21}$	$< 10^{-21}$
P40T40	15.54	$* < 10^{-21}$	$* < 10^{-21}$	$< 10^{-21}$
P40T34	16.38			1.11×10^{-19}
P40T38	15.79		2.14×10^{-19}	7.92×10^{-20}
P40T37	15.35	1.3×10^{-18}	1.41×10^{-18}	2.11×10^{-18}
P40T39	15.48	9.43×10^{-18}	1.36×10^{-17}	2.34×10^{-17}
FINE				
P40T42	16.18		$* < 10^{-21}$	$< 10^{-21}$
P40T31	15.82		$* < 10^{-21}$	$< 10^{-21}$
P40T43	15.98		$* < 10^{-21}$	$< 10^{-21}$
P40T44	15.46		4.78×10^{-19}	
P40T33	16.24		1.11×10^{-18}	1.35×10^{-18}
P40T45	16.26	1.24×10^{-18}	2.21×10^{-18}	4.67×10^{-18}
P40T46	16.02	3.92×10^{-18}	4.81×10^{-18}	9.52×10^{-18}
P40T49	15.42	8.10×10^{-18}	1.17×10^{-17}	2.34×10^{-17}

5.3.1. Stress and volume change versus strain data

The stress vs. strain and volume change vs. strain data obtained for the three anhydrite grainsize suites are presented in order of ascending volume fraction of anhydrite in Figures 5.4 to 5.6. For comparison, Figure 5.4a shows data reported in Chapter 4 for the pure halite end-member deformed under identical conditions to the present experiments. Figures 5.4b to h correspond to the coarse-grained suite. Figures 5.5a-h and Figures 5.6a-h represent the medium and fine groups respectively. Notably, all samples containing > 5% anhydrite show dilatation. It is also clear from the data that the flow strength and dilatational volume change increase with increasing anhydrite content for all grain size groups. The various trends in the data are detailed below.

5.3.2. Effect of anhydrite content and particle size on flow strength

The basic data from Figures 5.4, 5.5 and 5.6 are replotted in Figures 5.7a, b and c respectively to show the effect of anhydrite particle content upon the flow stress supported at fixed strains. All three grainsize groups show a steady increase in flow strength with anhydrite particle content, at all strains. The effect of anhydrite particle size upon the flow stress at constant composition, and at strains of 2% and 10% shortening, is illustrated in Figures 5.8a and b respectively. Clearly, the sample flow stress also tends to increase with decreasing particle size.

5.3.3. Effect of anhydrite content and particle size on volume change

Sample volume change versus anhydrite volume fraction data obtained from Figures 5.4, 5.5 and 5.6 are presented for the three sample suites tested in Figures 5.9a (coarse), b (medium) and c (fine). At strains above 2%, the sample volume changes (referred to the initial volume at room conditions) show a progressive, non-linear increase with anhydrite particle content for all three particle size groups. At strains < 1-2%, the samples show a small amount of compaction.

Plots of volume change versus anhydrite particle size at constant anhydrite content, and at 2% and 10% strain are plotted in Figures 5.10a and 5.10b respectively. The trend lines are simple linear regression best fits through the data at constant anhydrite volume fraction. There does not appear to be a clear dependence of volume change upon particle size at either strain.

Figure 5.4a-h. Stress vs. strain and volume change vs. strain data obtained for the **coarse** anhydrite suite. Plots are presented in order of ascending volume fraction of anhydrite. N.B. Figure 5.4a shows data reported in Chapter 4 for the pure halite end-member. Volume changes are referred to the initial sample volume under ambient conditions.

Figure 5.5a-h. Stress vs. strain and volume change vs. strain data obtained for the **medium** anhydrite suite. Plots are presented in order of ascending volume fraction of anhydrite. Volume changes are referred to the initial sample volume under ambient conditions. (See page 130).

Figure 5.6a-h. Stress vs. strain and volume change vs. strain data obtained for the **fine** anhydrite suite. Plots are presented in order of ascending volume fraction of anhydrite. Volume changes are referred to the initial sample volume under ambient conditions. (See page 131).

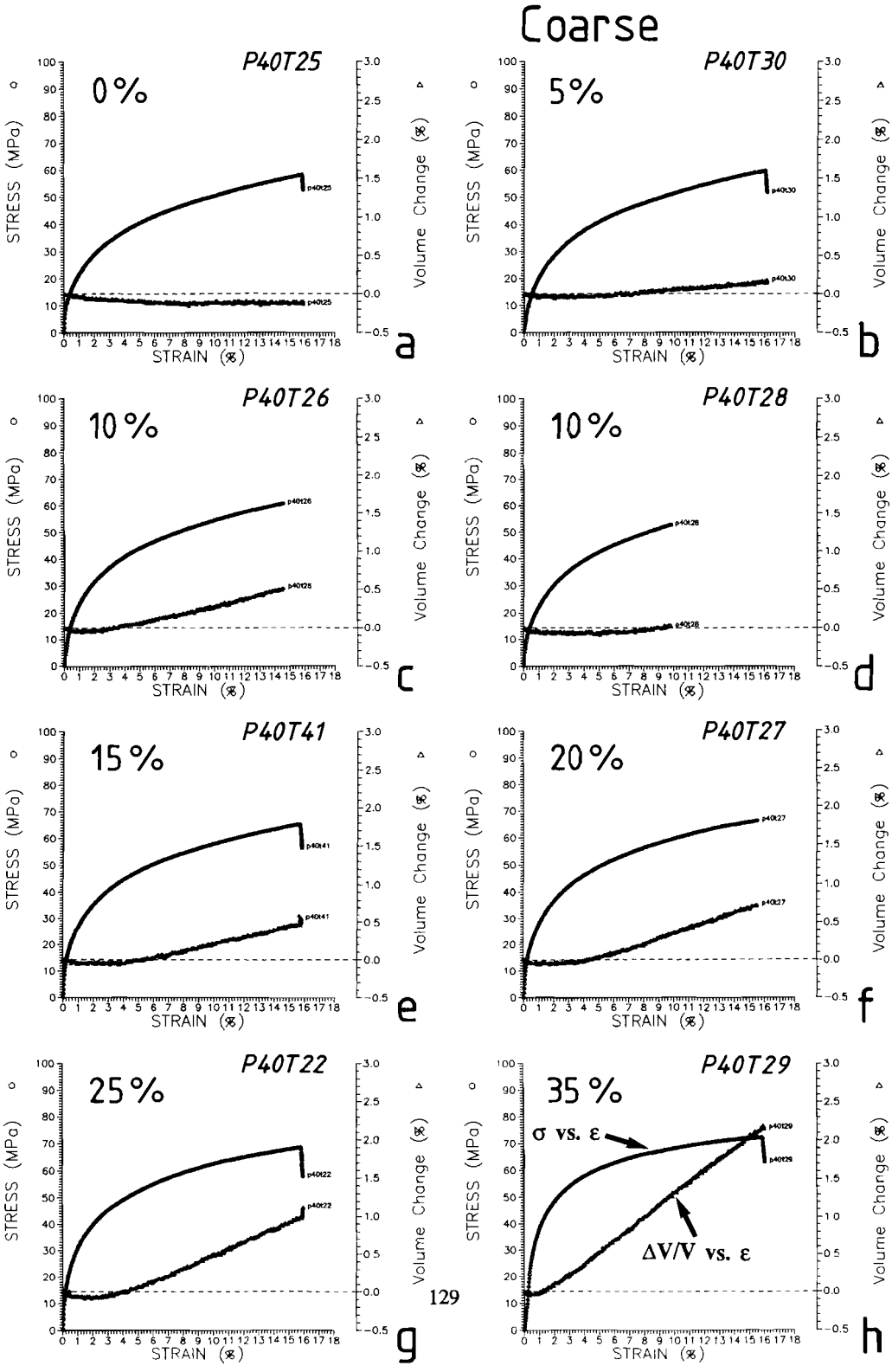
Coarse
P40T25
0%
a
P40T30
5%
b
P40T26
10%
c
P40T28
10%
d
P40T41
15%
e
P40T27
20%
f
P40T22
25%
g
P40T29
35%
σ vs. ε
ΔV/V vs. ε
h
STRESS (MPa)
Volume Change (%)
STRAIN (%)

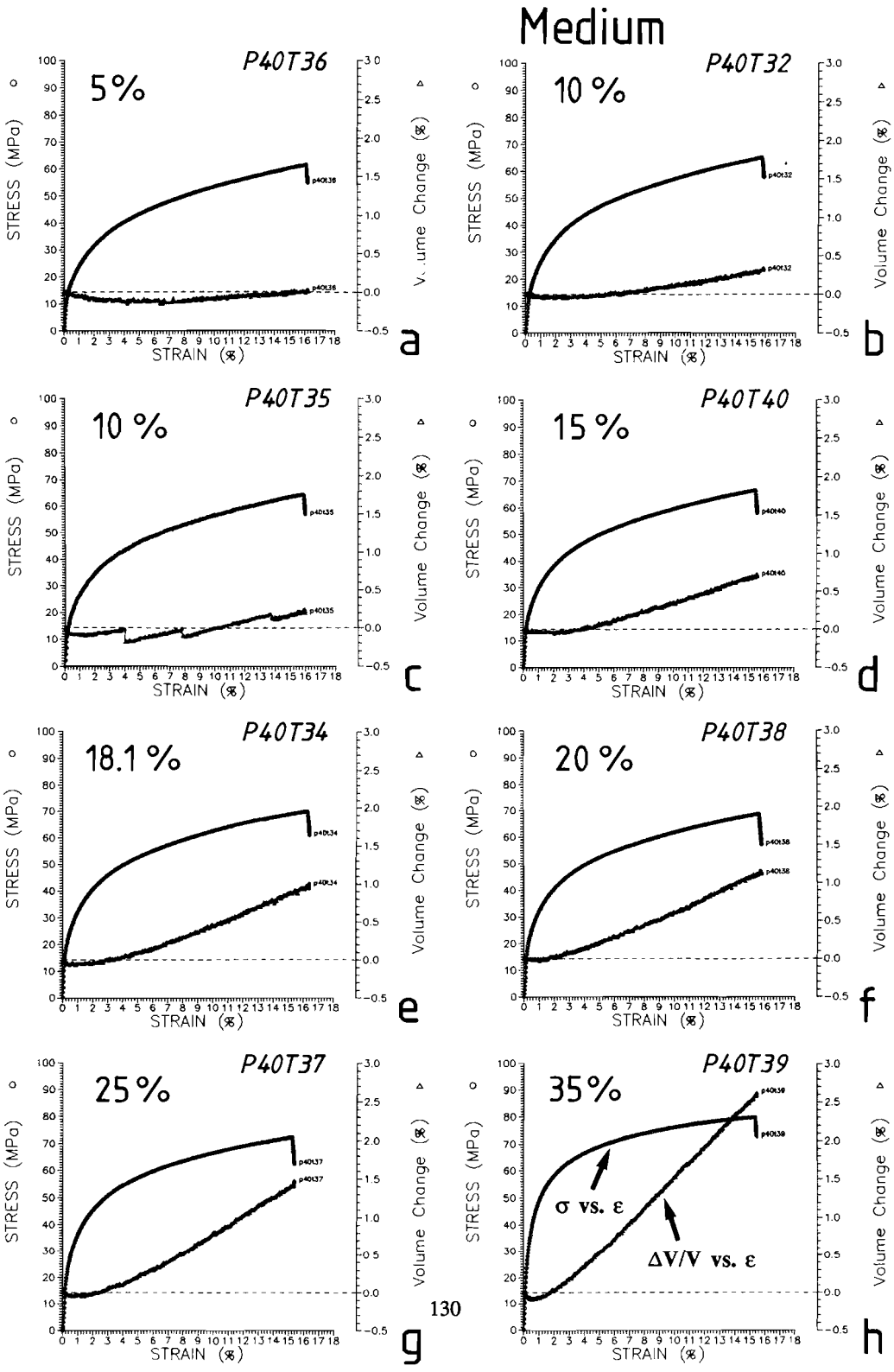
Medium
P40T36
5%
a
P40T32
10 %
b
P40T35
10 %
c
P40T40
15 %
d
P40T34
18.1 %
e
P40T38
20 %
f
P40T37
25%
g
P40T39
35%
σ vs. ε
ΔV/V vs. ε
h
STRESS (MPa)
STRAIN (%)
Volume Change (%)

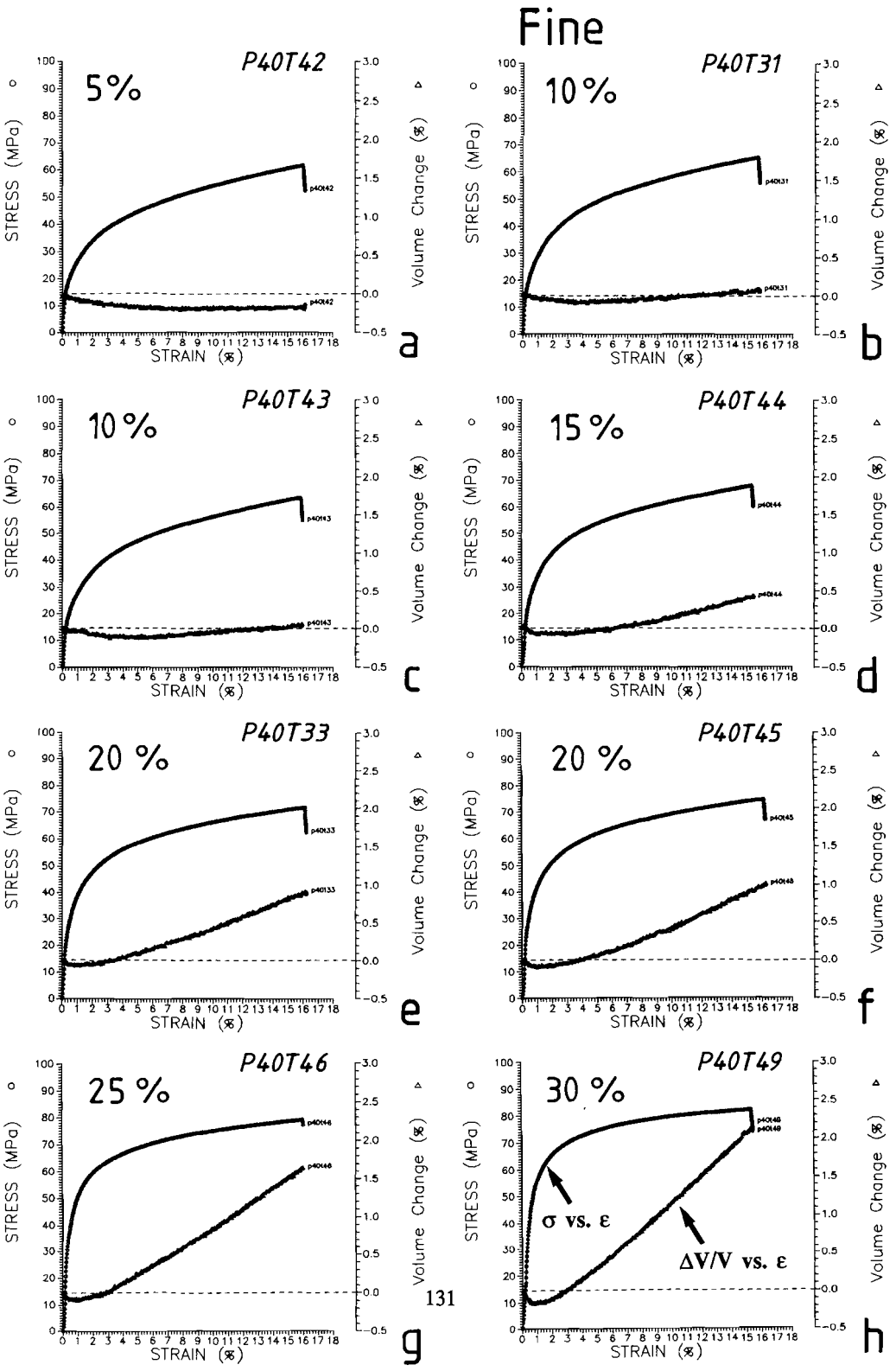
Fine
P40T42
5%
a
P40T31
10%
b
P40T43
10%
c
P40T44
15%
d
P40T33
20%
e
P40T45
20%
f
P40T46
25%
g
P40T49
30%
h
σ vs. ε
ΔV/V vs. ε
STRESS (MPa)
Volume Change (%)
STRAIN (%)

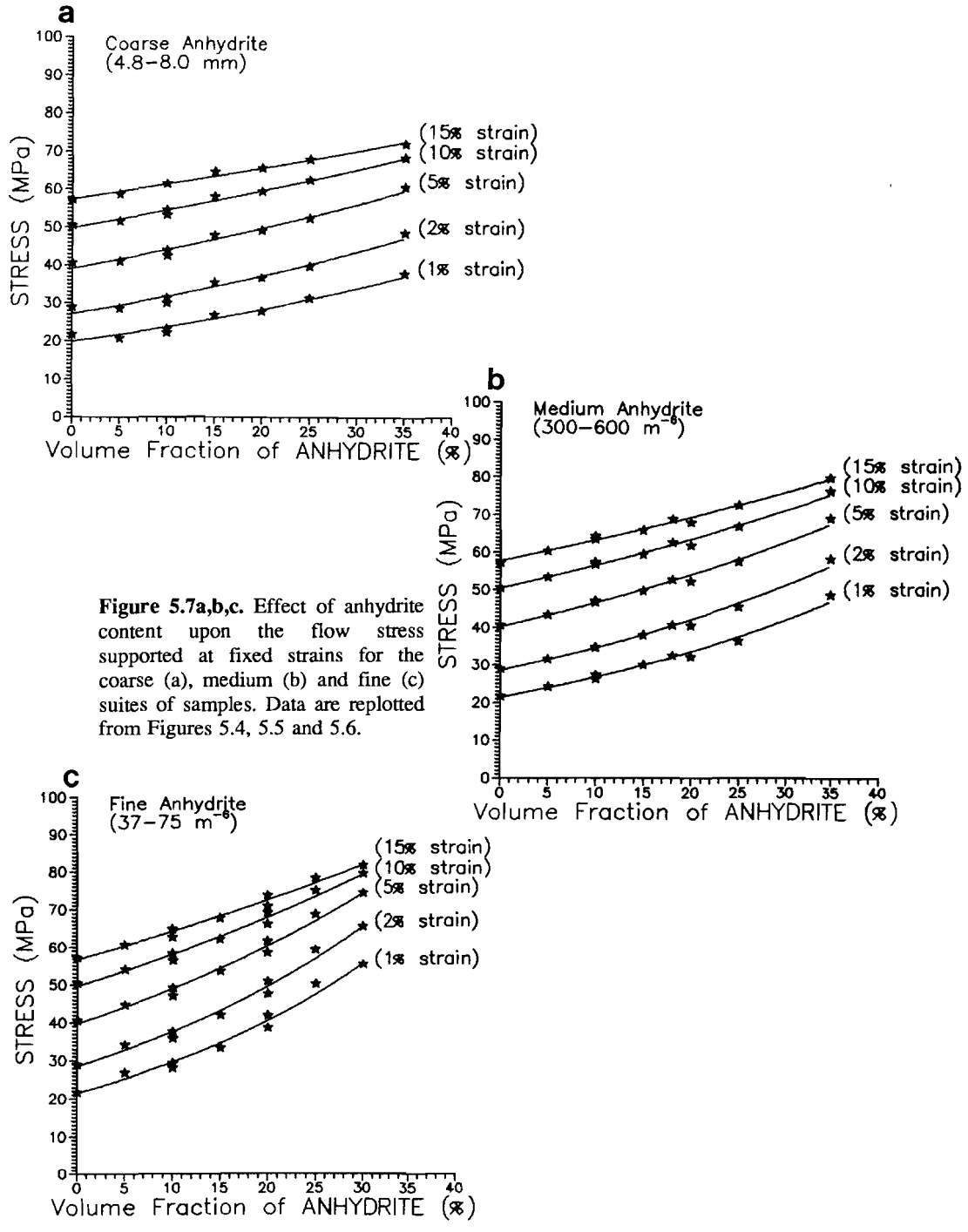

Figure 5.7a,b,c. Effect of anhydrite content upon the flow stress supported at fixed strains for the coarse (a), medium (b) and fine (c) suites of samples. Data are replotted from Figures 5.4, 5.5 and 5.6.

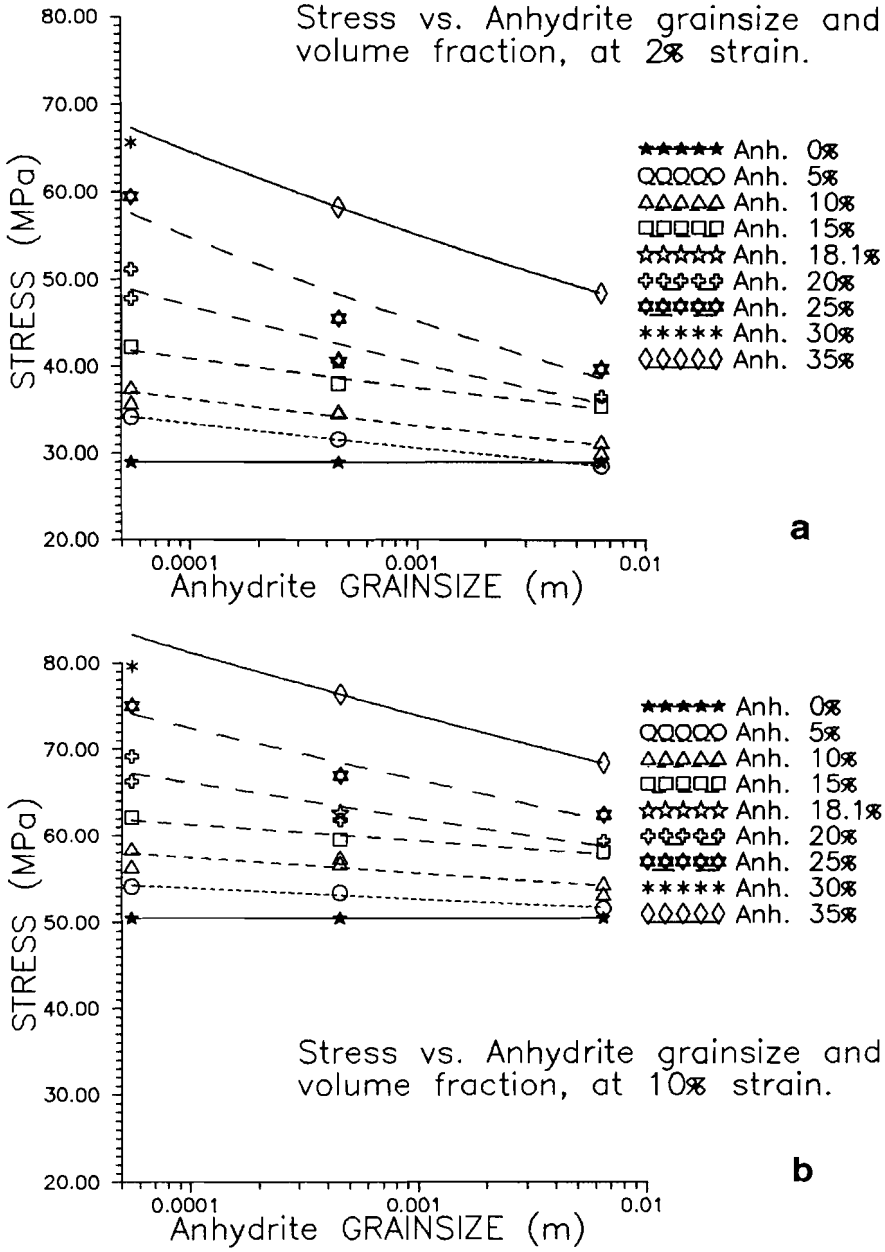

Figure 5.8a, b. Effect of anhydrite particle size upon the flow stress taken at constant composition and at strains of (a) 2% shortening and (b) 10% shortening.

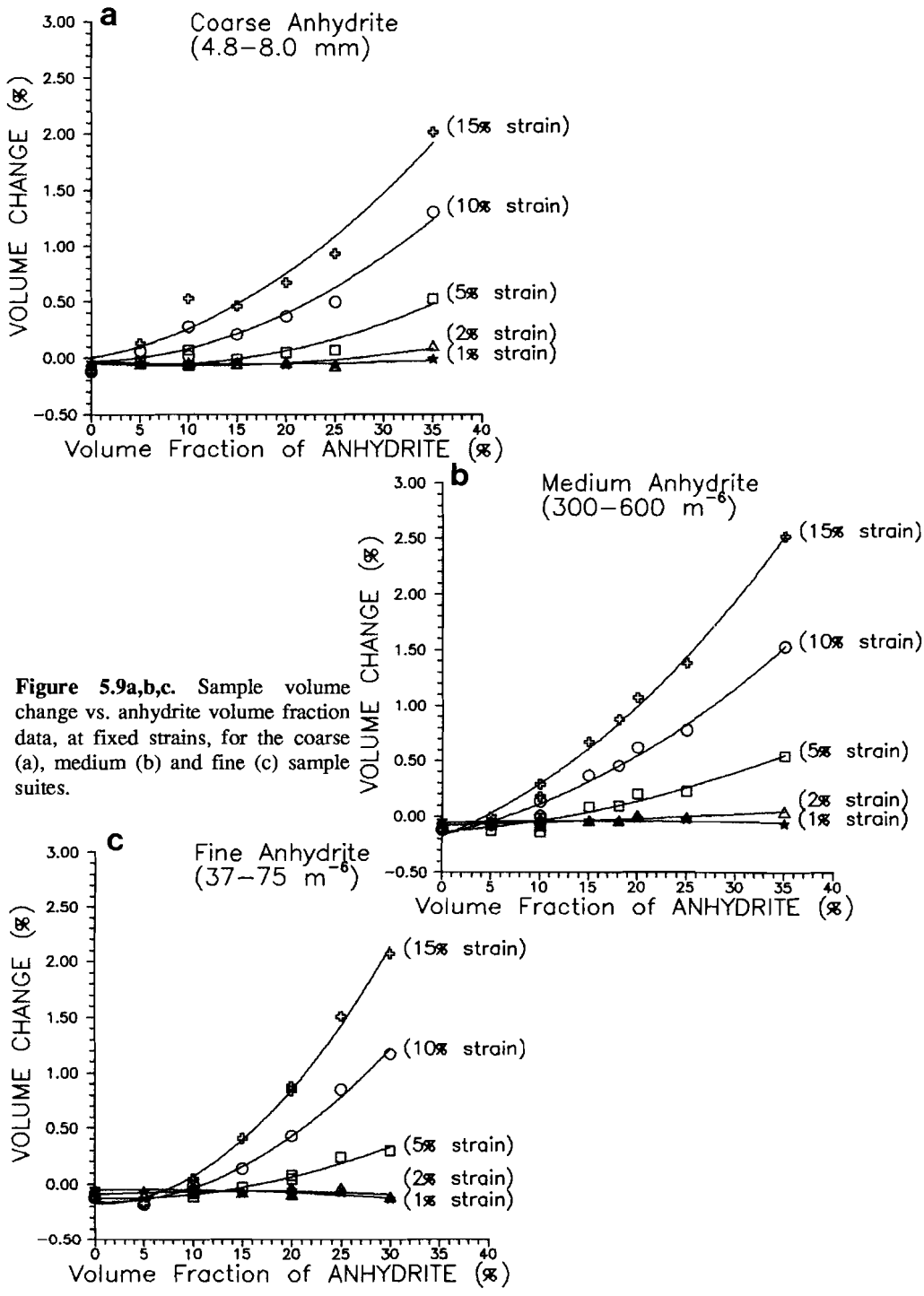

Figure 5.9a,b,c. Sample volume change vs. anhydrite volume fraction data, at fixed strains, for the coarse (a), medium (b) and fine (c) sample suites.

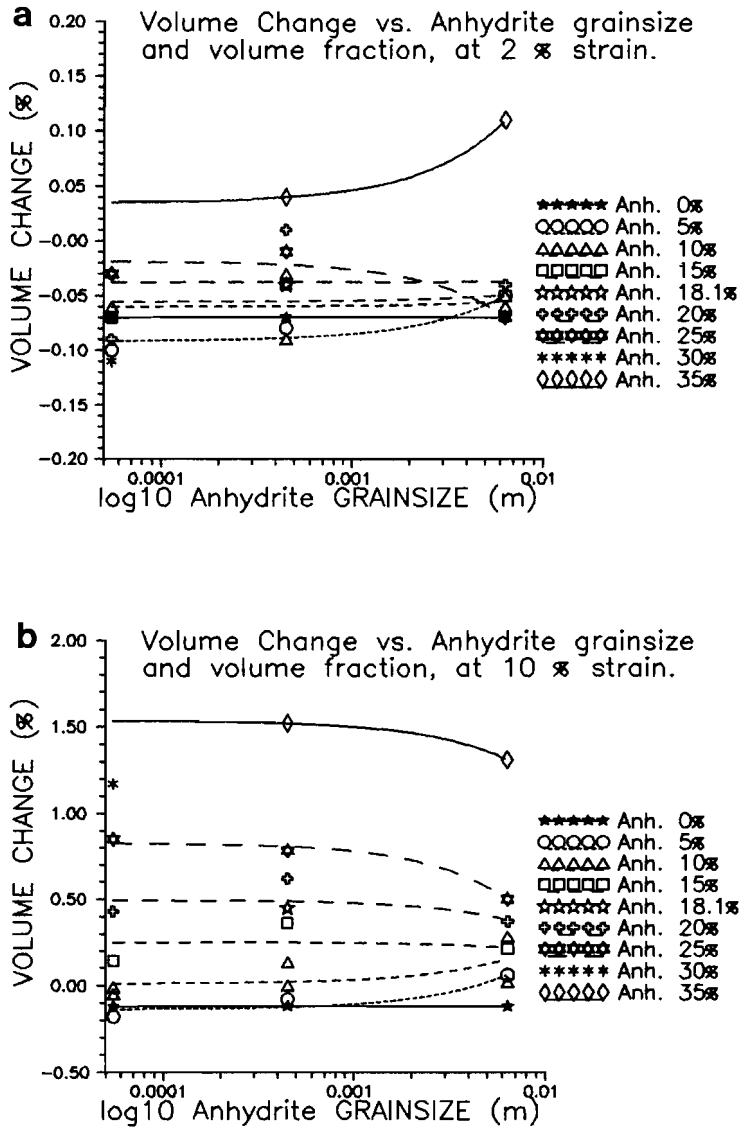

Figure 5.10a, b. Volume change vs. anhydrite particle size, at constant anhydrite content and at (a) 2% and (b) 10% strain. The trend lines are simple linear fits to the linear volume change vs. particle size data.

5.4. Results: Permeability data

5.4.1. Initial and final permeabilities

The complete set of initial and final (post-deformational) permeability data obtained for the three suites of samples tested is listed in Tables 5.1a and b. Note that the permeability data fall into 5 categories (labelled 1 to 5 in Table 5.1). These data are graphed against sample anhydrite content in the linear-linear plots presented in Figures 5.11a, b, and c, drawn for the coarse, medium and fine samples respectively. The same data are graphed in the corresponding log-linear plots given in Figures 5.12a, b and c.

From inspection of Figures 5.11a and 5.12a it is apparent that the initial permeability of the coarse samples, measured at 5 and 20 MPa, was around $10^{-21}m^2$ or less for all anhydrite contents. The initial permeability of the medium suite lies at around $10^{-21}m^2$ or less up to anhydrite contents of 15-20%, reaching $10^{-18}m^2$ at 35% (Figure 5.11b, 5.12b). The initial permeabilities of the fine material increased significantly above $10^{-21}m^2$ at anhydrite contents > 10-15% (Figure 5.12c).

The final permeabilities of the coarse, medium and fine samples show a relatively sharp increase towards higher anhydrite contents - see Figures 5.11 and 5.12. In the coarse suite, final permeabilities are $< \sim 10^{-20}m^2$ at anhydrite contents below 20-25%, but then rise dramatically to reach $\sim 2 \times 10^{-17}m^2$ by 35%. Similar trends in final permeability are seen for the medium and fine suites. In these cases, however, the dramatic rise occurs above anhydrite contents of 15-20% and 10-15% respectively. Note that in all three suites, the post-deformational permeability tended to increase on removal of axial load from the samples, and on lowering the confining pressure from 20 to 50 MPa after removal of the load (c.f. curves 3, 4, 5 in Figures 5.11 and 5.12).

Lastly, the effect of particle size on initial and final permeabilities can also be seen by comparing a, b and c in Figures 5.11 and 5.12. There is clearly no significant effect of particle size at anhydrite contents < 15-20%. At higher contents, however, initial and final permeabilities tend to increase with decreasing particle size. In this region (> 20%), the most significant difference is seen in the initial permeability of the coarse samples ($\leq 10^{-21}$) relative to the medium and fine suites.

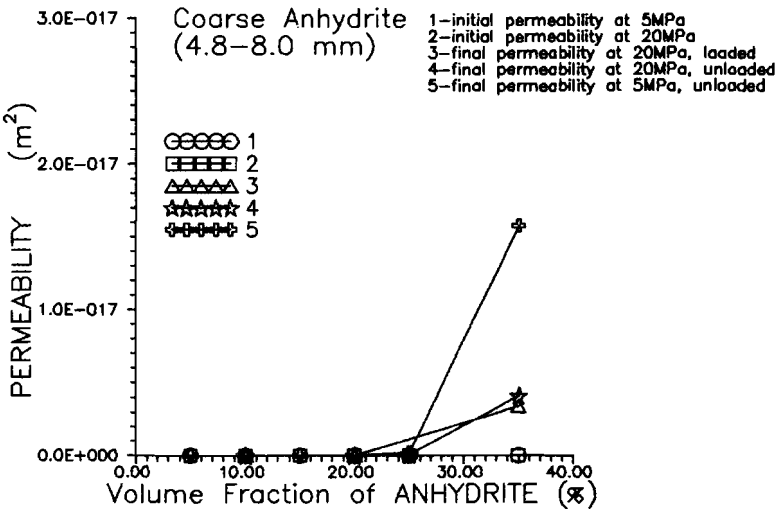

Figure 5.11a. Linear-linear plot of initial and final permeability vs. volume fraction of **coarse** anhydrite, for the conditions (1-5) and anhydrite particle sizes shown. (Data taken from Table 5.1a, b).

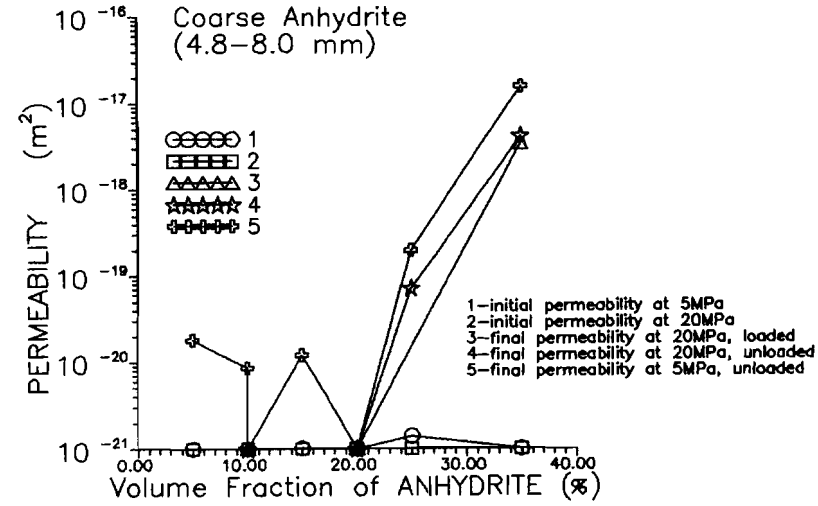

Figure 5.12a. Log_{10}-linear plot of initial and final permeability vs. volume fraction of **coarse** anhydrite for the conditions (1-5) and anhydrite particle sizes shown. All points plotted exactly on the abscissa, at $10^{-21}m^2$, represent permeability values $\leq 10^{-21}m^2$ (refer to Table 5.1a, b).

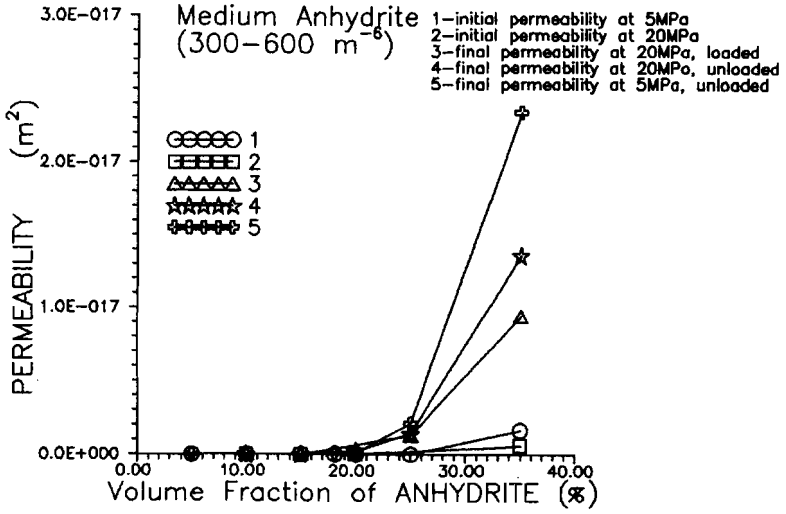

Figure 5.11b. Linear-linear plot of initial and final permeability vs. volume fraction of **medium** anhydrite, for the conditions (1-5) and anhydrite particle sizes shown. (Data taken from Table 5.1a, b).

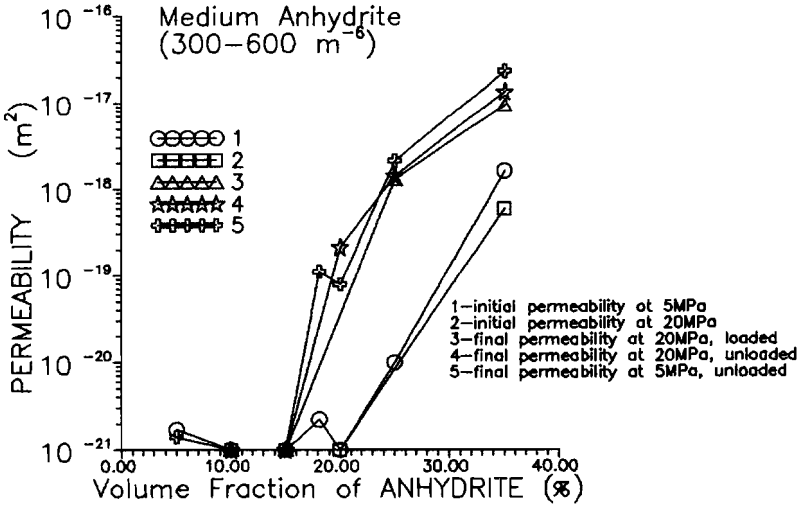

Figure 5.12b. Log_{10}-linear plot of initial and final permeability vs. volume fraction of **medium** anhydrite for the conditions (1-5) and anhydrite particle sizes shown. All points plotted exactly on the abscissa, at $10^{-21}m^2$, represent permeability values $\leq 10^{-21}m^2$ (refer to Table 5.1a, b).

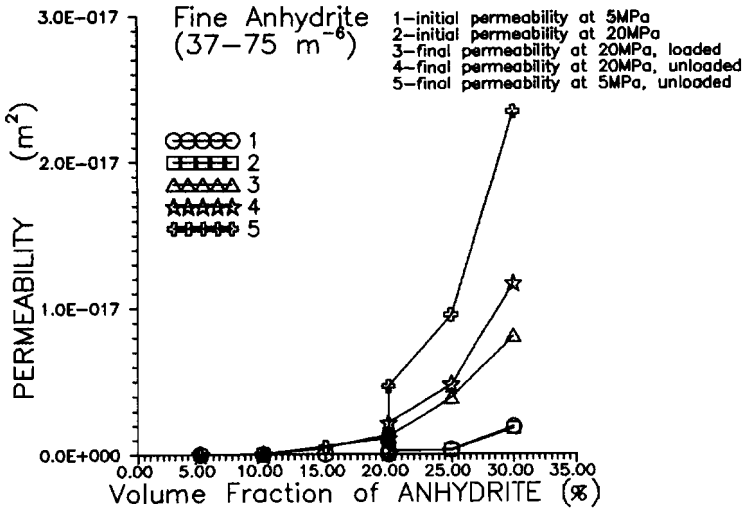

Figure 5.11c. Linear-linear plot of initial and final permeability vs. volume fraction of **fine** anhydrite, for the conditions (1-5) and anhydrite particle sizes shown. (Data taken from Table 5.1a, b).

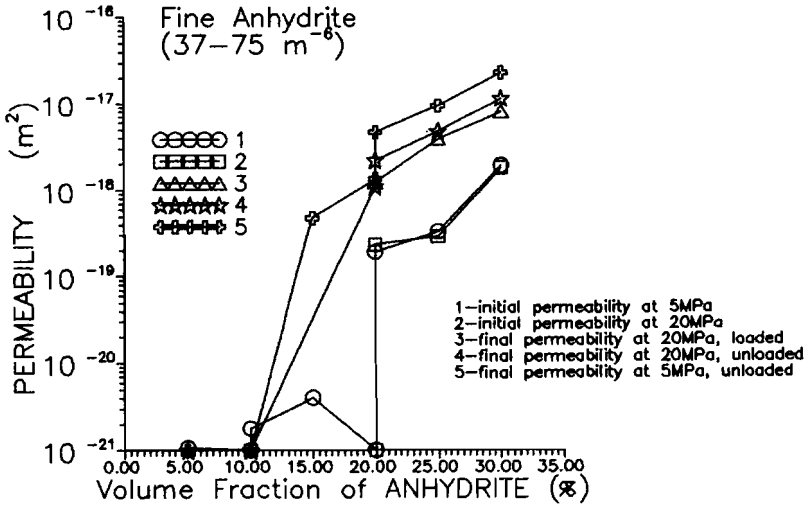

Figure 5.12c. Log_{10}-linear plot of initial and final permeability vs. volume fraction of **fine** anhydrite for the conditions (1-5) and anhydrite particle sizes shown. All points plotted exactly on the abscissa, at $10^{-21}m^2$, represent permeability values $\leq 10^{-21}m^2$ (refer to Table 5.1a, b).

5.4.2. Permeability development with strain and dilatancy

Aside from changes in initial to final permeabilities, data on the permeability development during deformation (i.e. at the deformation test confining pressure of 20 MPa) will now be presented. Such data could be obtained only for samples where the permeability test duration was very much less than the duration of the deformation test, and where the transient step method was not upset by non-uniformly developing dilatancy (N.B. such effects produced negative permeabilities).

The permeability vs. strain data obtained for the coarse, medium and fine samples during deformation are presented in Figures 5.13a, b and c. The permeability vs. volume change data are similarly presented in Figures 5.14a, b and c. These two permeability relationships will be considered in parallel.

The data for the coarse suite (see Figures 5.13a and 5.14a) show that for anhydrite contents < 10 vol% no significant permeability develops. At anhydrite contents ≥ 20-25 vol%, an approximately 2 orders of magnitude increase to ~ $10^{-19}m^2$ occurs in the first 3-5% strain, then saturating at levels of the order of $10^{-18}m^2$ (Figure 5.13a). In the corresponding permeability vs. volume change plot (Figure 5.14a), this increase to $10^{-19}m^2$ is seen to occur extremely rapidly in only the first 0.1 - 0.2% dilatancy. At intermediate anhydrite contents (10-20 vol%) transitional behaviour occurs, consisting of temporary or late appearance of permeability in the range 10^{-20} to $10^{-19}m^2$ (see Figures 5.13a and 5.14a).

In the case of the medium suite (Figures 5.13b and 5.14b), no significant permeability development occurs with strain or volume change when the anhydrite content is ≤ 10 vol%. At ~ 15 vol% anhydrite, there is a transient appearance of permeability in the first few percent of strain (see Figure 5.13b) and first 0.3% dilatancy (see Figure 5.14b). In the range 18-25% anhydrite content, permeabilities initially at ≤ $10^{-20}m^2$ increase rapidly by 1-2 orders of magnitude in the first 3% strain and only 0.1% dilatancy, settling out at ~ $10^{-19}m^2$. At the highest anhydrite contents investigated (35 vol%), the starting permeability of ~ $10^{-18}m^2$ shows a factor of 3 decrease in the first 2-3% strain (0.1% dilatancy) followed by a gradual increase reaching $10^{-17}m^2$ at 15% strain (~ 3% dilatancy).

The fine group of samples (see Figures 5.13c and 5.14c) show no significant permeability development at anhydrite contents of 5 vol% (i.e. remain ≤ $10^{-21}m^2$). At contents in the range 20-30 vol%, the initially high values between 2 x 10^{-19} and

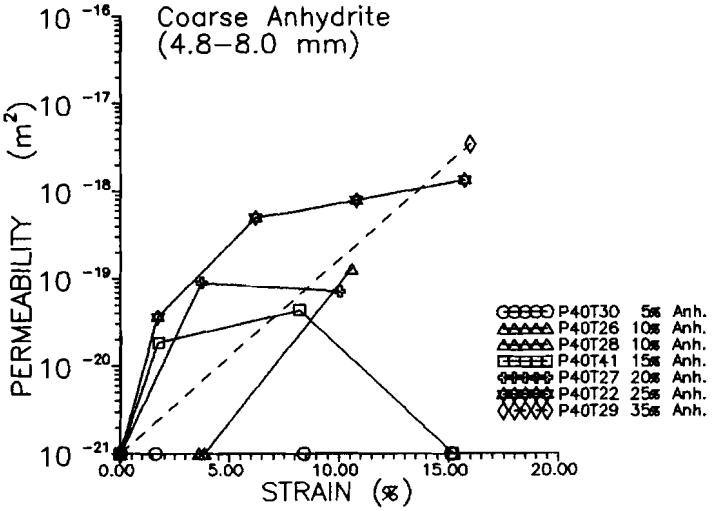

Figure 5.13a. Permeability vs. strain data obtained for the **coarse** suite of anhydrite-bearing salt samples. All points plotted exactly on the abscissa at $10^{-21}m^2$ represent permeability values $\leq 10^{-21}m^2$.

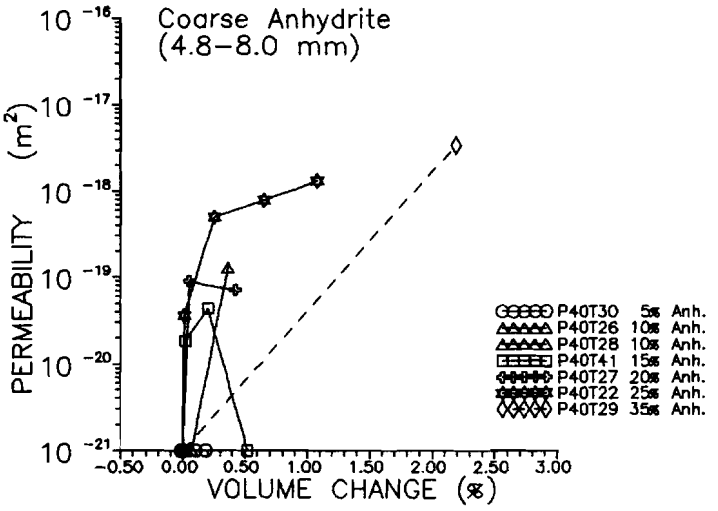

Figure 5.14a. Permeability vs. volume change data obtained for the **coarse** suite of anhydrite-bearing salt samples (dilatant volume changes are taken to be positive). All points plotted exactly on the abscissa at $10^{-21}m^2$ represent permeability values $\leq 10^{-21}m^2$.

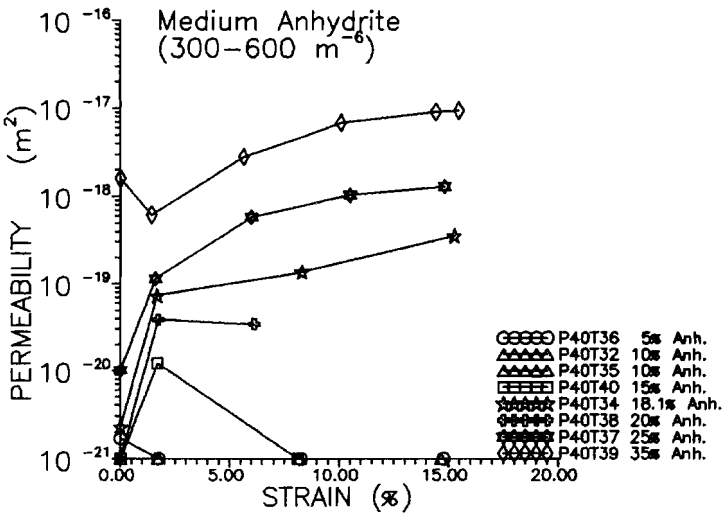

Figure 5.13b. Permeability vs. strain data obtained for the **medium** suite of anhydrite-bearing salt samples. All points plotted exactly on the abscissa at $10^{-21}m^2$ represent permeability values $\leq 10^{-21}m^2$.

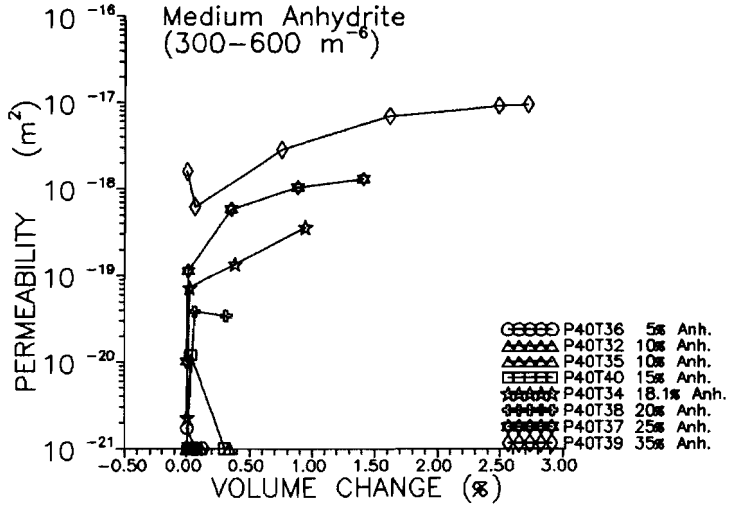

Figure 5.14b. Permeability vs. volume change data obtained for the **medium** suite of anhydrite-bearing salt samples (dilatant volume changes are taken to be positive). All points plotted exactly on the abscissa at $10^{-21}m^2$ represent permeability values $\leq 10^{-21}m^2$.

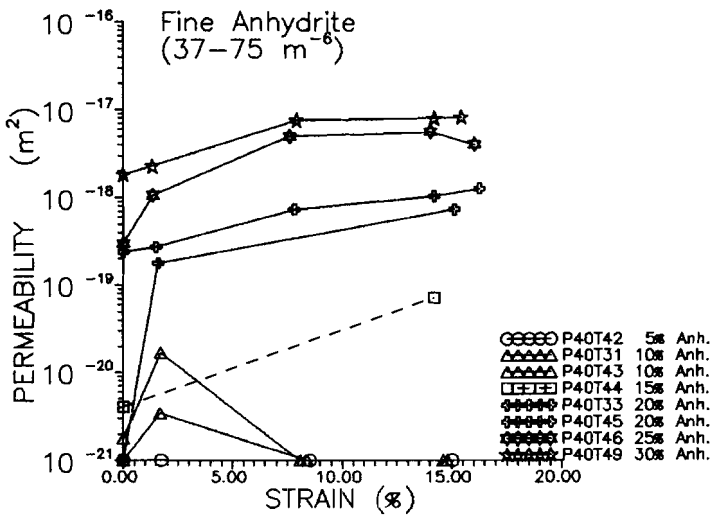

Figure 5.13c. Permeability vs. strain data obtained for the **fine** suite of anhydrite-bearing salt samples. All points plotted exactly on the abscissa at $10^{-21}m^2$ represent permeability values $\leq 10^{-21}m^2$.

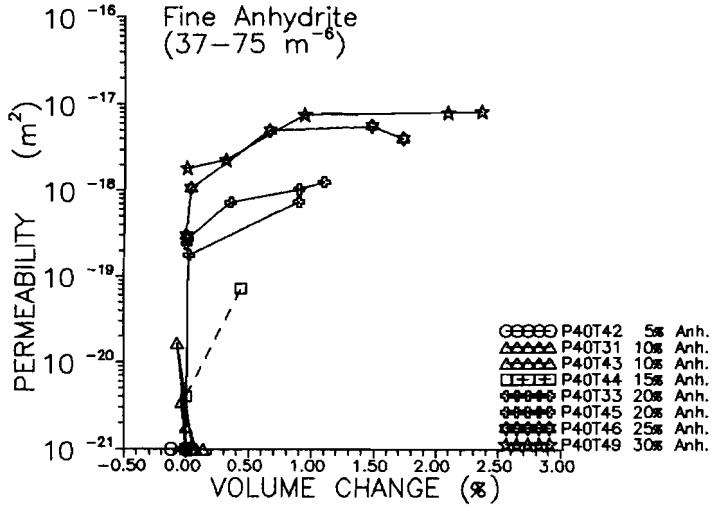

Figure 5.14c. Permeability vs. volume change data obtained for the **fine** suite of anhydrite-bearing salt samples (dilatant volume changes are taken to be positive). All points plotted exactly on the abscissa at $10^{-21}m^2$ represent permeability values $\leq 10^{-21}m^2$.

2 x $10^{-18}m^2$ show only a slight increase during deformation. Samples with intermediate contents (10-20 vol%) show

i) a transient/minor appearance of permeability at anhydrite contents of 10-15%, or
ii) a rapid transition, at 20 vol% anhydrite, from values of $\leq 10^{-21}m^2$ to saturate at ~ $10^{-19}m^2$ after only 2% strain and 0.1% dilatancy (see Figures 5.13c and 5.14c).

From the three sets of data presented above it is apparent that significant syn-deformational permeabilities could develop and/or persist only at anhydrite contents exceeding thresholds of 20-25% for the coarse, 15-20% for the medium and ~ 15% for the fine material (in good agreement with the threshold characteristics seen in the final permeability data). An additional difference related to particle size may be seen at high anhydrite contents. Here the medium and fine samples possess significant initial permeability (~ $10^{-18}m^2$) which shows only minor growth with strain and dilatancy. In contrast the initial permeability of the coarse suite was always $\leq 10^{-21}m^2$ and always showed dramatic growth at high anhydrite contents.

5.5. Post-deformational microstructures

After deformation, all samples retained a right cylindrical form showing very little "barrelling", despite the rather large strains imposed (15%). They were cut and sectioned using the methods described previously in Chapters 3 and 4, and connected porosity and microcrack damage were revealed by vacuum impregnation of the free face of the sections obtained using a blue-dyed epoxy resin. The impregnated sections were then polished and etched, using the methods of Spiers et al. (1986) and Urai et al. (1987) and the microstructure was examined using both transmission and reflection optical methods.

5.5.1. Coarse suite

These samples showed clear microstructural modification compared with the undeformed material. Firstly, the initial shape preferred orientation of the anhydrite particles was significantly enhanced, with the anhydrite "clasts" showing numerous discrete cracks (Mode I type) running parallel to the compression direction, plus extension normal to compression (Figure 5.15a). Cavitation of the anhydrite/halite interface was also observed at the tips of many of the elongate anhydrite clasts (see

Figure 5.15b, c). The clasts did not show evidence for intracrystalline plastic strain parallel to the compression direction, but some internal deformation by cataclasis was visible in the tip regions, accompanied by minor localized flattening. The enhanced shape fabric of the anhydrite particles is illustrated in the axial ratio (R_f) vs. fluctuation (ϕ) diagram of Figure 5.16 (c.f. Figure 5.2). Application of the automated unstraining method of Peach and Lisle (1979), to this data, yielded a bulk strain ellipse ratio (R_s) of 1.7 $\pm$ 0.05 compared with ~ 1.26 for the deformation actually imposed. Presumably this reflects the dilatant and heterogenous aspects of the deformation.

The halite matrix grains surrounding the clasts in the coarse samples showed a clear flattening fabric with widespread evidence for intracrystalline plastic deformation such as slip bands and high dislocation densities revealed by etching (see Figures 5.15a and b). Extreme flattening and intense plastic deformation features were locally observed in regions of salt constricted between closely separated anhydrite clasts (see Figure 5.15d). Frequently, such regions showed extensive recrystallization into arrays of substructure-free grains (Figures 5.15a and 5.15d) presumably developed after deformation. Pervasive microcracking was not seen in the salt matrix, though intergranular cracks were locally developed in the salt matrix situated in the "pressure shadow" regions between the tips of immediately adjacent clasts (Figure 5.15b). Such regions sometimes showed networks of grain boundary microcracks linking the clast tips, as well as showing cavitation of the salt/anhydrite interfaces (Figure 5.15b). In dilated regions of this type, recrystallization of the salt was conspicuously absent.

Broadly speaking, the microstructures described above were characteristic for the entire suite of coarse samples. However, the recrystallization and dilatancy features developed between neighbouring clasts were widespread only in samples with high anhydrite content (> 15 vol%), presumably because of increased clast proximity. In all samples, the dilatancy (as revealed by impregnation with blue-dyed resin) was clearly concentrated in the anhydrite. Linkage via microcracks in the salt matrix was only observed between clast tips (i.e. in the flattening plane) at the higher anhydrite contents. No evidence was found for clast linkage via the salt in an axial direction.

5.5.2. Medium suite

These samples exhibited a similar microstructure and anhydrite clast fabric to the coarse suite (see Figure 5.17a). However, the anhydrite in the medium suite showed more pervasively developed axial microcracking (Figure 5.17a). As in the coarse

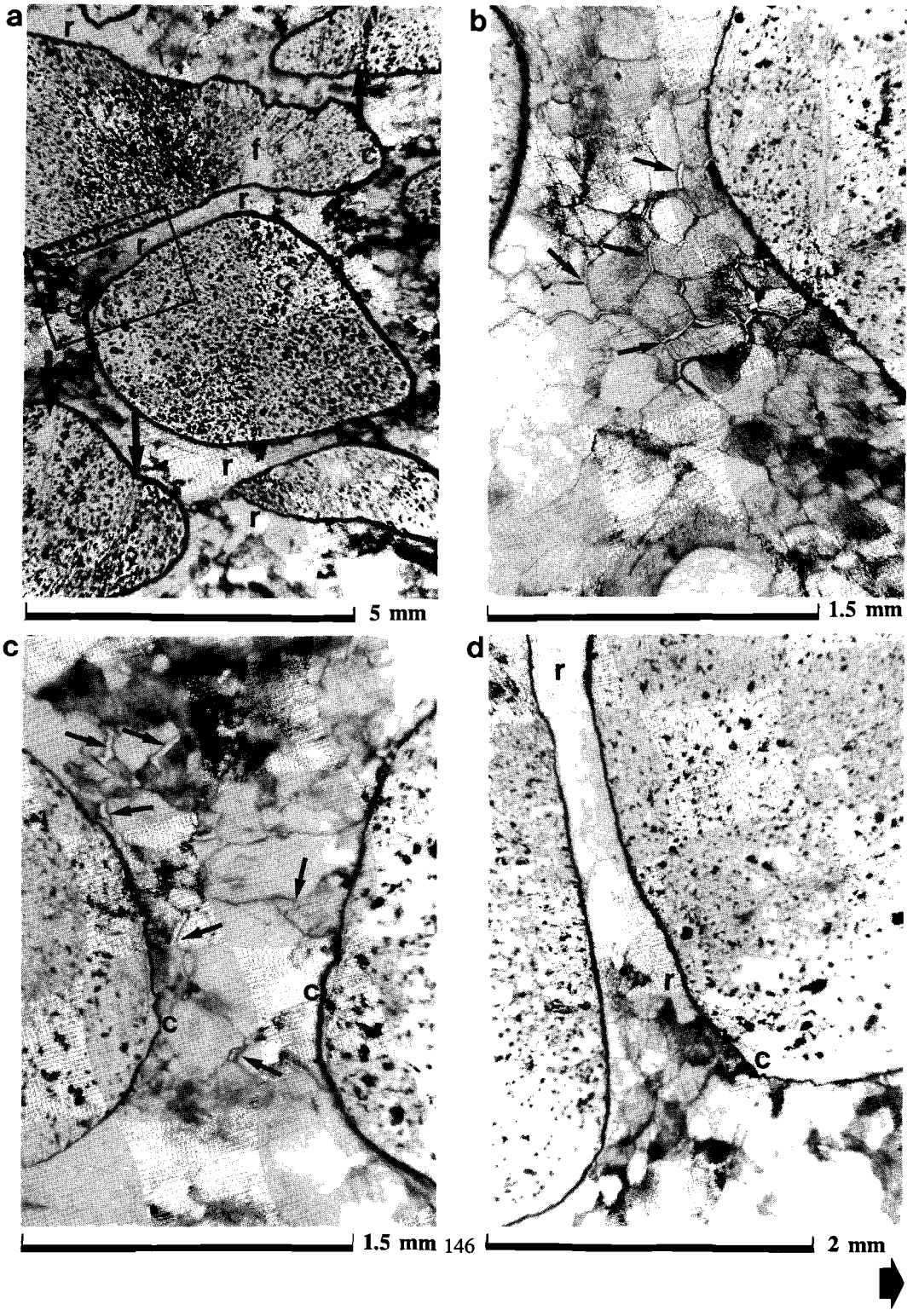
a
r
f
c
r
r
c
r
r
5 mm
b
1.5 mm
c
c
c
1.5 mm
d
r
r
c
2 mm

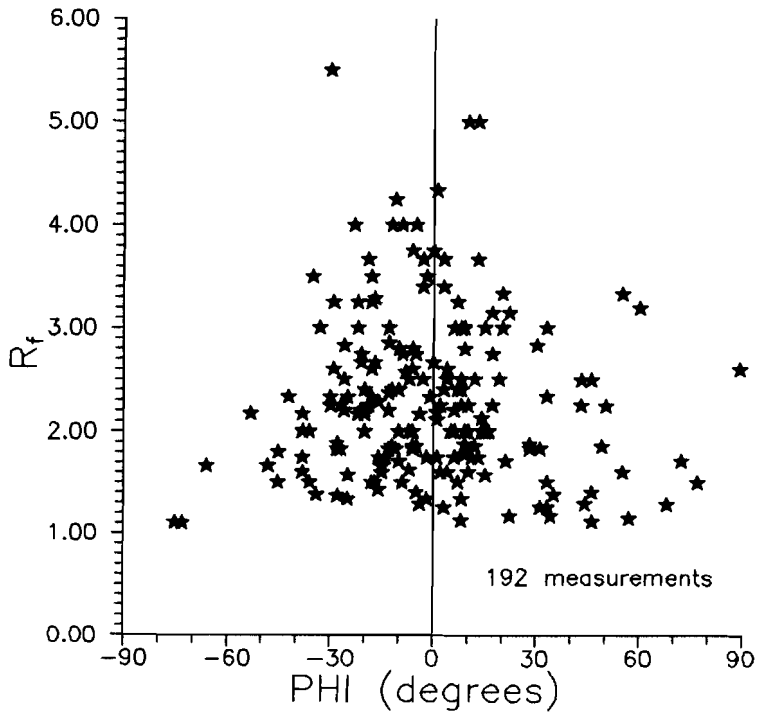

Figure 5.16. Axial ratio (R_f) of anhydrite clasts vs. orientation fluctuation (Phi), for deformed coarse sample P40T29 (35 vol% anhydrite, 16% strain). Diagram shows the enhanced shape fabric due to clast alignment and elongation in the flattening plane (Phi = 0^o).

Figure 5.15.a-d. Reflection optical micrographs illustrating the post-deformational microstructure of the coarse suite of salt/anhydrite samples. All micrographs from Sample P40T29 (35 vol% anhydrite, 16% strain).

a) Low magnification view showing the shape fabric of the anhydrite clasts and discrete cracks (arrowed) running parallel to the compression direction. Note extensive cataclasis in region "f". Note also the distribution of recrystallized halite regions "r" located vertically above and below clasts and the dilated non-recrystallized regions with clast/matrix cavitation "c" distributed horizontally around clasts (Rectangle = Figure 5.15d).

b), c) Region between tips of two elongate clasts. Note the cavitation "c" at the anhydrite/halite interface, the intergranular cracking (arrowed) in the halite matrix and the dislocation etch features in the deformed halite grains.

d) Region of salt matrix constricted between two anhydrite clasts. Note the extensive recrystallization "r" of the salt into arrays of substructure free grains. Neighbouring non-recrystallized matrix shows heavy dislocation etch features. This micrograph represents a magnified portion of (a).

material, the halite matrix showed flattened grains with slip bands and dislocation etch features. Once again, no microcrack dilatancy was developed in the matrix except in the "pressure shadow" regions between anhydrites (Figures 5.17a, b), and no microcrack linkage of clasts was observed axially. Recrystallization of the salt was somewhat more widespread than in the coarse samples (particularly at low anhydrite contents) but again did not occur in the dilated "pressure shadow" regions (Figures 5.17a, b).

5.5.3. Fine suite

As in the undeformed state, these samples showed a microstructure characterized by flattened halite grains and grain clusters surrounded by a network of fine-grained anhydrite particles. In contrast to the undeformed material, however, the deformed samples showed a stronger flattening fabric (Figures 5.18a, b). This was particularly apparent in samples with high anhydrite content (> 15 vol%). Here the flattened "cubic" outlines of the halites inherited from the starting salt powder were clearly visible (Figures 5.18a, b). Internally, the halite grains showed strongly developed slip lines, kink domain structures and dislocation etch patterns, providing clear evidence for dislocation plastic deformation (Figures 5.18a, b). Some grains also showed internal growth of idiomorphic recrystallized grains free of visible dislocation substructures (Figures 5.18a, b - grains marked "R"). The grain boundary anhydrites exhibited extensive dilatancy (revealed by the blue resin) and formed a fully connected dilated network at the higher anhydrite contents (≥ 10-15 vol%; see Figure 5.18, anhydrite content ~ 30 vol%).

5.6. Discussion

The data reported for the present deformation experiments on synthetic salt rock containing coarse, medium and fine anhydrite particles show the following main trends:

1. a steady increase in flow stress with increasing anhydrite content and decreasing particle size;
2. a non-linear increase in dilatancy with anhydrite content at strains > 2%, with little effect of particle size;
3. an increase in post-deformational permeability with anhydrite content, seen at contents exceeding threshold values of 20-25 vol% for coarse, 15-20 vol% for medium and ~ 15 vol% for fine.

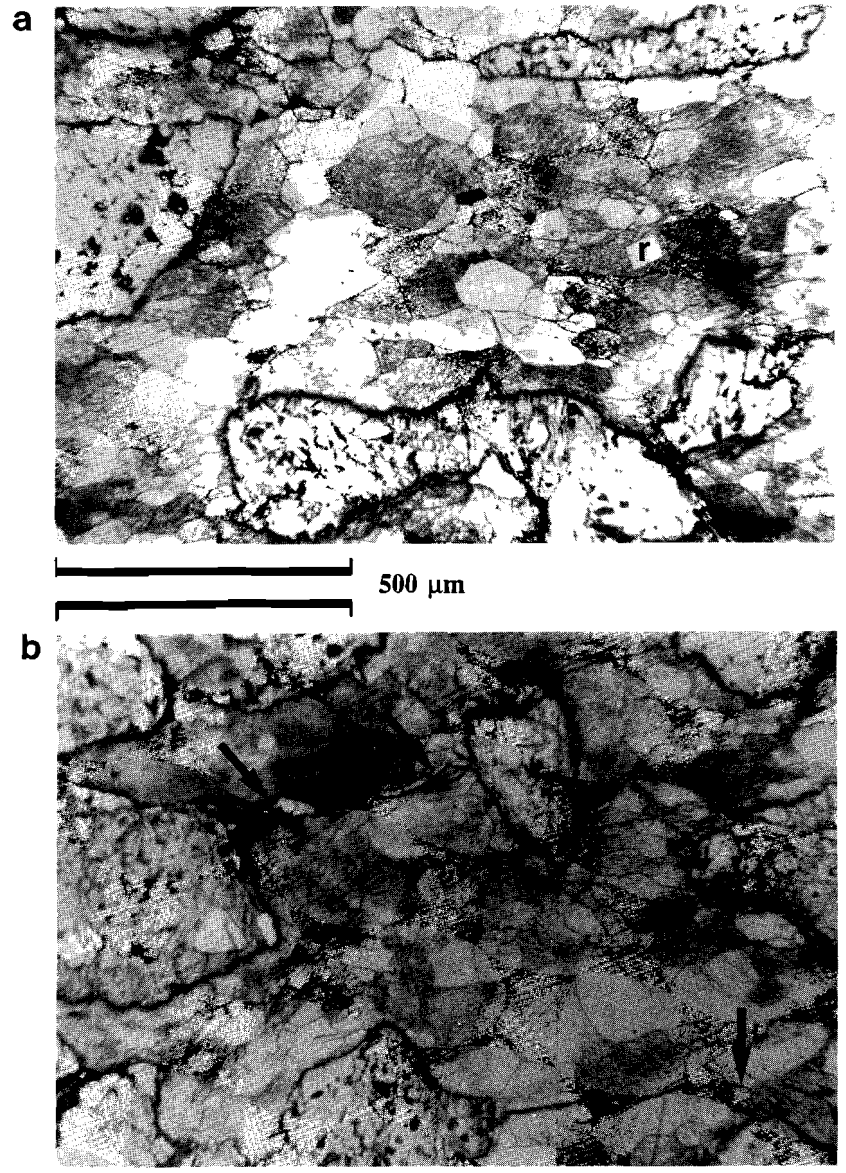

Figure 5.17a, b. Reflection optical micrograph of polished and etched sections showing the post-deformational microstructures of the medium suite. All micrographs from Sample P40T39 (35 vol% anhydrite, 15.5% strain).

a) Dilated and extended anhydrite clasts showing pervasive axial microcracking. The flattened halite grains of the matrix exhibit intense etching of dislocation features in contrast to the occasional (post-deformational) euhedral recrystallized grains marked "r".

b) Similar micrograph showing a dilatant region of heavily deformed and etched halite between anhydrite clasts. The wide horizontal cross-cutting cracks (arrowed) are features produced by unloading.

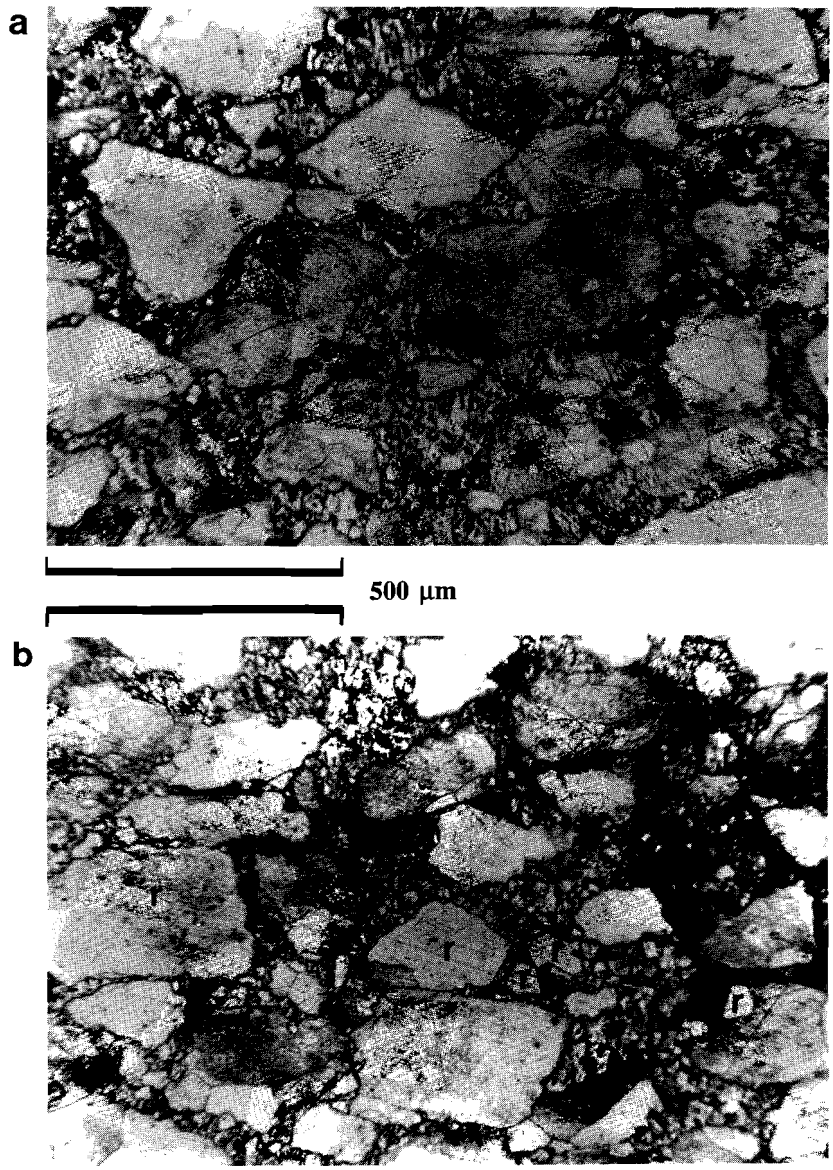

Figure 5.18a, b. Reflection optical micrographs illustrating the post-deformational microstructure of the fine suite of salt/anhydrite samples. All micrographs from Sample P40T49 (30 vol% anhydrite, 15.4% strain).

a) Flattened halite grains and grain clusters with distorted cubic outlines and dislocation etch features indicative of plastic deformation. The halite grains are surrounded by strongly dilated anhydrite which has been pervasively microfractured. The anhydrite clearly forms a continuous permeable network.

b) Similar view showing post-deformational recrystallization of some heavily deformed halite hosts. Non-etched idiomorphic recrystallized grains "r" stand out in contrast to their, heavily etched, deformed halite hosts.

In addition to these trends, microstructural analysis showed that while the salt deformed by intracrystalline plastic mechanisms (glide field - refer Figure 1.2; also Frost and Ashby, 1982) the anhydrite was relatively rigid and brittle and accommodated almost all dilatancy developed during deformation. At the same time, a variety of microstructures (grain flattening, dislocation substructures, recrystallization, grain boundary dilatancy in pressure shadows) provided evidence for steep gradients in the deformation (and presumably stress) field around isolated anhydrite clasts, such as seen in the coarse and medium suites.

In the present section, an attempt is made to explain the above mentioned trends, taking the microstructural observations into account.

5.6.1. Effect of anhydrite content and particle size on flow strength

As mentioned in the introduction to this chapter, it is well established in the materials literature that the addition of rigid particles to a plastically deformable alloy generally leads to an increase in flow strength (Kelly and Nicholson, 1971). Such effects are caused by the strain compatibility problems, and associated resistance to dislocation motion, introduced by the rigid second phase (Ashby, 1966, 1970). Hardening effects of this type are expected to increase with second phase content (Ashby, 1966; Ebeling and Ashby, 1966) and with decreasing particle size, since both lead to an increase in the average density of piled-up (or geometrically necessary) dislocations required to accommodate misfit of the rigid particles (Ashby, 1970). Though most microphysical models for this type of hardening have been developed for single crystals (Ashby, 1970, 1971), similar effects are implied for polycrystalline systems.

Further to these hardening effects, the presence of the relatively rigid and brittle anhydrite particles in the samples studied here can be expected to produce a number of additional strength effects. First, the induced dilatancy requires work to be done in fracturing the anhydrite and in increasing the sample volume against the confining pressure (see Chapter 4, and Edmond and Paterson, 1972). Also, the volumetric influence of the relatively rigid anhydrite implies that for given strains and strain rates imposed on the samples, the average strain and average strain rate in the plastically deforming, work hardening, salt matrix will be accordingly enhanced. In addition, at anhydrite contents where a mechanically continuous network of anhydrite is developed, the anhydrite framework can be expected to become load supporting (Handy, 1990). All of these various effects can be expected

to produce an increase in strength with anhydrite content, and their possible contribution to the measured flow stress will now be assessed.

First, consider the strength effect of the "PΔV" term associated with the work done against the confining pressure during dilatation of the samples (i.e. principally of the anhydrite). As discussed in Chapter 4 and given by Edmond and Paterson (1972), the flow stress contribution ($\delta\sigma$) produced by this effect can be written

$$\delta\sigma = P d\varepsilon_v/d\varepsilon \qquad (5.1)$$

where P is confining pressure (20 MPa in all tests) and $d\varepsilon_v/d\varepsilon$ is the rate of change of volumetric strain with respect to axial strain. From the stress and volume change vs. strain data presented in Figures 5.4 - 5.6, the maximum value of $\delta\sigma$ term was ~ 4 MPa, at an anhydrite content of 35% (P40T39), a volume change of ~ 2.5% and 15% strain (Figure 5.5h). This yields a maximum value for $\delta\sigma$ of about 4% of the measured flow stress. Since the observed increases in flow stress at high anhydrite contents were 20-150% with respect to anhydrite-free material (refer Figure 5.7), it is clear that work done in dilating the samples (i.e. the anhydrite) cannot account for the observed dependence of flow strength on anhydrite content. Further since dilatancy was found to be roughly independent of particle size (refer Figure 5.10), the volumetric work effect cannot account for the observed dependence of flow strength on particle size either. Notably, the work done in creating the observed density of fracture surfaces within the dilated anhydrite is easily shown to be negligible for typical surface energies of 0.1 - 1 J/m^2.

Secondly, let us consider the volumetric effect of the added (relatively rigid) anhydrite on the average matrix strain and strain rate, hence flow stress. It is easily shown that the maximum enhancement of average matrix strain and strain rate can be expressed in the form

$$\langle E_h \rangle \approx \langle E_b \rangle / (1 - f) \qquad (5.2)$$

where $\langle E_h \rangle$ represents the average strain $\langle \varepsilon_h \rangle$ or strain rate $\langle \dot{\varepsilon}_h \rangle$ in the matrix halite, $\langle E_b \rangle$ represents the imposed bulk strain or strain rate, and f is the volume fraction of anhydrite (assumed perfectly rigid). In addition it is well established, from the very large body of experimental data on creep effects in salt, that the dependence of creep rate ($\dot{\varepsilon}$) on applied differential stress (σ) under the present conditions can be empirically described by power laws of the form $\dot{\varepsilon} \propto \sigma^n$ where n > 6 (see Heard, 1972; Carter and Hansen, 1983; Wawersik and Zeuch, 1986). Thus

the mean matrix stress developed in the present experiments (at fixed strain) can be written

$$<\sigma_h> \propto <\dot{\varepsilon}_h>^{1/n} = c\ \{<\dot{\varepsilon}_b> / (1 - f)\}^{1/n} \qquad (5.3)$$

where $n > 6$ and c is a constant. Using these relations, the average increase in matrix strain rate due to the addition of the maximum of 35 vol% anhydrite would be from $4 \times 10^{-5}s^{-1}$ to $6.15 \times 10^{-5}s^{-1}$, a factor of 1.54 increase. Therefore the change in flow stress is expected to be by a factor of $< (\sqrt[6]{1.54}) = 1.07$. The implied strengthening of 7% is much smaller than the observed stress increases of 20-150% after the addition of 30-35 vol% anhydrite (see Figure 5.7).

Using similar reasoning, the volumetric effect of the anhydrite on the average matrix strain and strain hardening (strain partitioning effect) can be estimated from the stress-strain curve for the pure salt (Figure 5.4a). This curve can be accurately approximated by a fourth order polynomial as shown in Figure 5.19. Coupling Equation 5.2 with this polynomial enables the average enhanced matrix stress $<\sigma_h>$ to be calculated as a function of anhydrite content and applied strain, for all samples tested. The results are compared with the measured flow stresses (σ) in Figure 5.20a, b and c, where the ratio $R = <\sigma_h>/\sigma$ is plotted versus anhydrite content at applied strains of 1, 5 and 15%. Figure 5.20 demonstrates that the matrix strain/stress enhancement effect accounts for more than half but not all of the observed strengthening with anhydrite content (represented in Figure 5.7). In the coarse suite, this strain partitioning effect accounts for 80-90% of the strengthening observed at high strains ($\geq$ 5%) and high anhydrite contents. However, the contribution of this effect becomes progressively less significant in the finer material, reaching about 70-80% in the medium and 60-70% in the fine, at similar strains and anhydrite contents. Since the strain and strain rate partitioning/enhancement effects described by Equation 5.2 depend only on anhydrite content, these effects cannot explain the observed dependence of the flow stress on particle size.

Thirdly, the possibility of strengthening due to the establishment of a load supporting framework of anhydrite is considered. Notably, the experimental data, particularly for coarse and medium samples (Figures 5.4, 5.5 and 5.7a and b), show an increase in flow strength at anhydrite contents well below those required for significant load-bearing interaction of the clasts (~ 60 vol% - Arzi, 1978; Handy, 1990). While there may be some effect in the fine suite (where all the anhydrite is located at grain boundaries), the framework effect is thus unable to explain the experimental data.

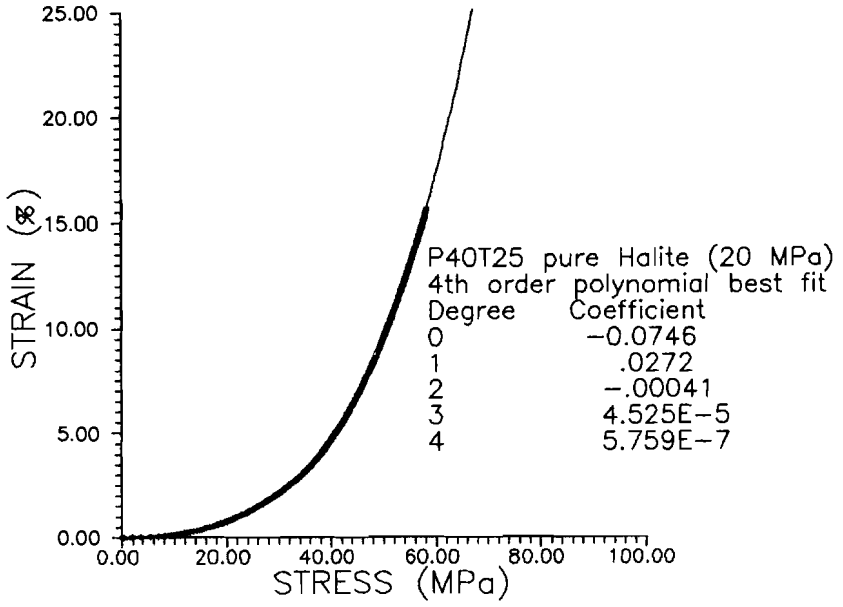

Figure 5.19. Fourth order polynomial best fit to the stress-strain data for the pure halite sample P40T25. The stress-strain data (asterisks) form the heavy curve. The best fit polynomial is the thinner curve passing through the data. Note excellent fit to data.

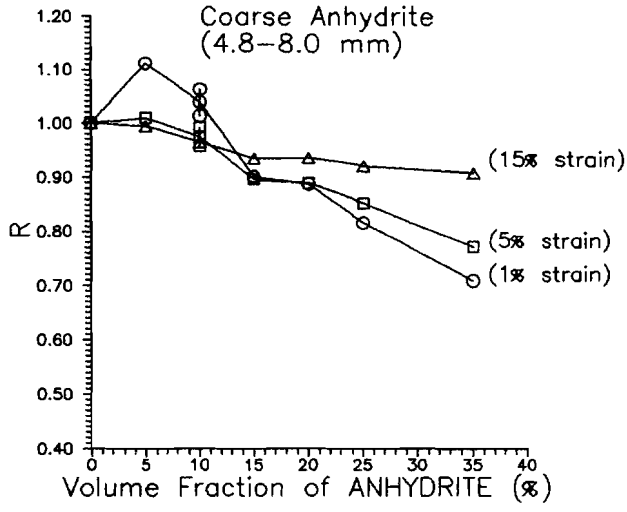

Figure 5.20a-c. Ratio (R) between the enhanced matrix stress (estimated from the work hardened flow stress of pure halite, at the enhanced matrix strain calculated from Equation 5.2) and the measured flow stress for given values of bulk strain, plotted as a function of anhydrite content for the coarse (a), medium (b) and fine (c) anhydrite/halite suites.

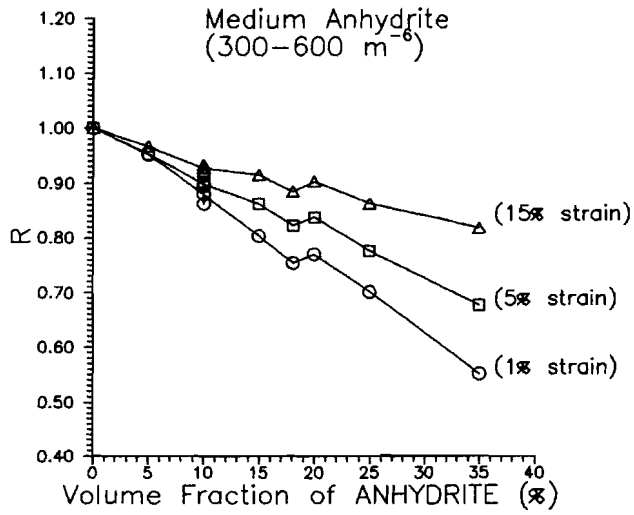

Figure 5.20b.

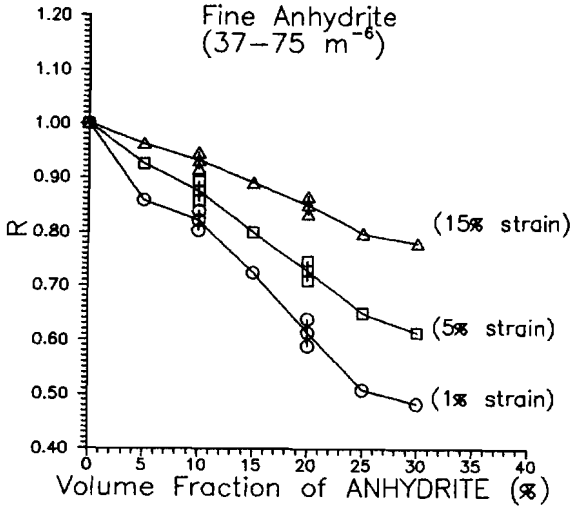

Figure 5.20c.

Lastly, attention is focussed on hardening effects related to the dislocation barrier and associated strain incompatibility effects considered by Ashby (1970), for example. Ashby's model for the hardening of plastically deformable single crystals by widely dispersed intragranular particles is written

$$\tau = \tau_0 + 2CG\sqrt{(f/r)b\gamma} \qquad (5.4)$$

where γ is shear strain, τ and τ_0 are shear flow stresses in the particle-hardened and particle-free conditions respectively, G is the shear modulus of the host material, b is the Burgers vector for the active dislocation slip system and C is a constant (~ 3; Ashby, 1970). The "wavelength" of the stress and deformation field around the particles is determined by the average slip distance of the geometrically necessary dislocations and is proportional to f/r, where f is the volume fraction of the rigid particle phase and r is the particle radius. This expression (Equation 5.4) was derived for intracrystalline precipitates on a scale similar to the slip distances of the dislocations themselves. However, it seems reasonable to assume that a similar but longer-range influence of the stress fields around the present anhydrite inclusions would produce gradients in strain with a wavelength possibly reaching up to several halite grain diameters, thus generating geometrically necessary dislocations in the halite in much the same manner.

Clearly, the above model needs to be extended to the polycrystalline case for an adequate quantitative comparison with the present experimental data on the coarse and medium samples. Ashby's conceptually similar hardening model for single phase polycrystals, based on grain boundary misfit (Ashby, 1970; Equation 3.5) and written

$$\tau = \tau_0 + C^*G\sqrt{b\varepsilon/D} \qquad (5.5)$$

where ε is the imposed strain and D is the grainsize, may be more applicable to the fine samples, but insufficient data exists to test this. Nonetheless, the existing models do serve to illustrate that particle content and size should influence flow strength in a manner consistent with findings reported here for the salt/anhydrite composites.

On the basis of the preceeding arguments, it is inferred that the increase in flow strength with anhydrite content seen in the coarse, medium and fine suites is mostly due to enhanced strain and thus enhanced strain hardening in the salt matrix. At strains $\geq$ 5%, this typically accounts for at least 80% of the hardening in the coarse, 70% in the medium and 60% in the fine. The remaining hardening can be best

explained in terms of a strain incompatibility/dispersion hardening mechanism which becomes increasingly important with decreasing particle size, in agreement with existing models.

5.6.2. Effect of anhydrite content and particle size on dilatancy

The present experiments were conducted under conditions falling just within the non-dilatant crystal plastic deformation field for pure halite end-member material (see Chapter 4). However, the results obtained clearly show that the addition of just a few percent of anhydrite particles (> 5-10%) forces significant dilatancy to develop under these conditions, provided strains exceed ~ 5% (Figure 5.9). On the basis of microstructure, most of this dilatancy is related to axial cracking within the anhydrite particles, with the halite deforming plastically and showing very little microcracking (as expected from the pure end-member).

Consider now the non-linear dependence of dilatant volume change on anhydrite content reported for the coarse, medium and fine sample suites in Figure 5.9. These data show that while dilatation is known to be concentrated in the anhydrite, dilatant volume change at constant strain is not simply proportional to anhydrite content. This is clearly apparent from Figures 5.21a-c where sample volume change, normalized to anhydrite content, is plotted against anhydrite content. This confirms that the volumetric strain occurring in (and locally around) the added anhydrite increases with the amount of anhydrite present in all three suites (Figures 5.21a-c). The most likely explanation is that the extent of microcracking increases towards higher anhydrite contents as a result of the corresponding increases in flow stress caused by the strain partitioning and dispersion hardening effects discussed in the previous section. Although the effect of particle size on dilatancy is relatively small (Figure 5.10), it is clear from Figure 5.21 that the volumetric strain normalized to anhydrite content tends to reach higher values in the medium and fine material than in the coarse. In accordance with the conclusions drawn regarding flow strength, this is thought to reflect the higher stresses developed in the medium and fine samples as a result of the increased component of dispersion hardening (hence increased particle interaction).

5.6.3. Permeability development

The present permeability data for both undeformed and deformed samples are clearly characterized by some kind of threshold behaviour in which permeability

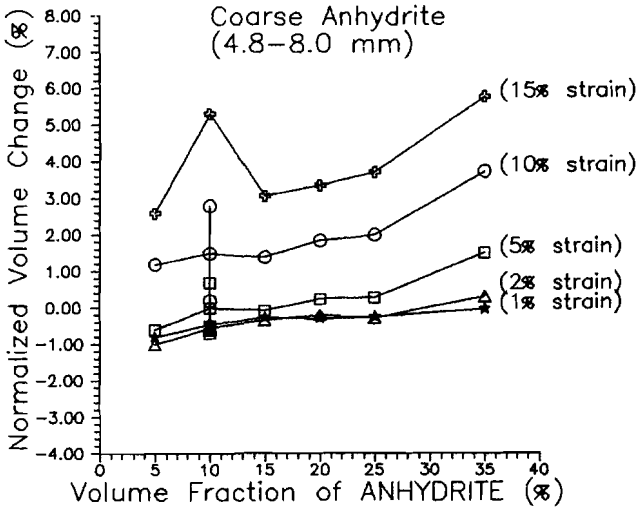

Figure 5.21a.

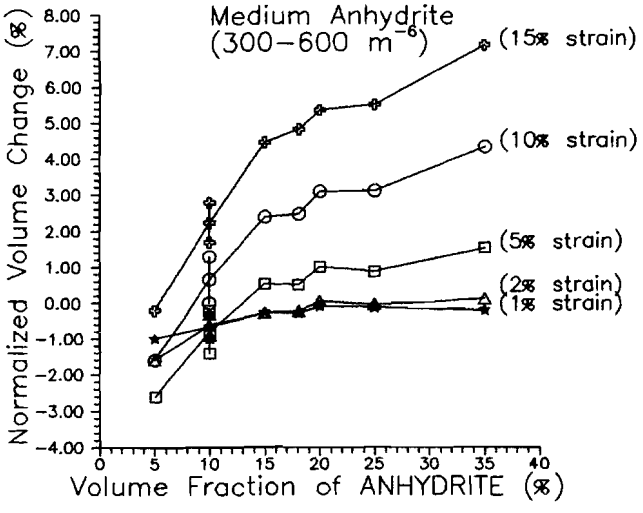

Figure 5.21b.

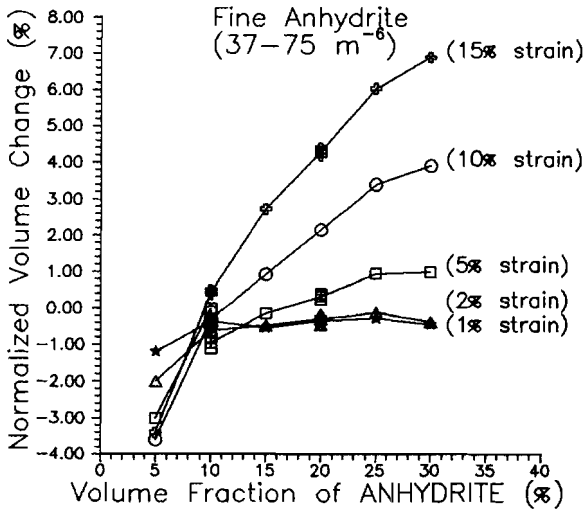

Figure 5.21a-c. Plots of sample volume change (normalized to anhydrite content) versus anhydrite content at given strains, for the coarse (a), medium (b) and fine (c) anhydrite/halite composite suites.

increases strongly with anhydrite content, at contents above some critical value. The initial permeability of the coarse suite of samples was essentially too low to measure in reasonable times and therefore showed no threshold behaviour. This is entirely consistent with the observed microstructure (Figure 5.1) of intact anhydrite clasts encapsulated in the dense salt matrix. However, thresholds are apparent in the initial permeability data for the medium and fine composites, namely at 15-20 vol% and 10-15 vol% respectively (Figures 5.11 and 5.12). In the fine suite, the onset of permeability clearly corresponds to the establishment of a connected network of permeable anhydrite clusters around the halite grains, as evidenced by microstructural observations. In the case of the medium suite, the initial microstructure is similar to that of the coarse material. In contrast to the coarse clasts, however, the medium clasts did show some surface porosity. On this basis, it is proposed that the appearance of permeability at 15-20 vol% in the medium material may be related to the onset of direct interaction between the permeable surfaces of the clasts.

Consider now the permeabilities measured in the deformed samples (i.e. the final permeabilities represented in Figures 5.11 and 5.12). Firstly, it is interesting to note that most samples showing a significant increase in permeability as a result of deformation also showed an increase in final permeability when the axial load was

removed and when the confining pressure was reduced from 20 to 5 MPa. This is inferred to be due to the elastic relief (opening) of deformation-induced microcracks. Secondly, the deformed medium and fine sample suites showed essentially the same threshold-type behaviour as that seen in their undeformed equivalents, though the permeabilities attained in the deformed material are significantly higher (refer to Figures 5.11 and 5.12). This threshold behaviour presumably reflects the same microscale transport mechanisms inferred for the undeformed material, with the deformation-enhanced permeability resulting from the extensive dilatation and microcracking observed in the anhydrite. Thirdly, in contrast to the undeformed coarse samples (where the anhydrite clasts were intact), the deformed coarse material showed similar threshold behaviour to that seen in the medium and fine suites, with substantial permeability developing at anhydrite contents above ~ 20%. By comparison with the medium material, this behaviour may be due to the onset of direct "conductive" interaction between the heavily cracked clasts seen in the deformed state.

Having focussed on the various threshold effects, the observed increase in final permeability with anhydrite content, seen in the coarse, medium and fine samples above the corresponding threshold value, is now addressed. This must reflect increased "conductivity" related directly to increased anhydrite content. It must also reflect the increased dilatancy found to occur within the anhydrite at high anhydrite contents (see Section 5.6.2).

Finally, let us consider the data obtained on permeability development during deformation, rather than simply before and after (see Figures 5.13, 5.14). With regard to this data, all 3 suites of samples showed elements of common behaviour. Firstly, samples with anhydrite contents well below the appropriate threshold value (< 20% for coarse, < 15% for medium, < 10-15% for fine) showed no significant permeability development during any stage of deformation. Samples with anhydrite contents well above their threshold did show enhancement of permeability by deformation. In the fine suite, this effect was steady and was presumably associated with simple growth or dilatation of the existing pore network within the grain boundary anhydrite arrays. In the coarse and medium samples, however, the deformation-enhancement effect was often large and rapid, with permeabilities increasing by 2-3 orders of magnitude within the first 0.2% of bulk dilatation. This is similar to the behaviour seen in the natural and synthetic salt materials investigated in Chapters 3 and 4, and likewise suggests a critical phenomenon involving the establishment of pore connectivity. Interestingly, most samples with anhydrite contents in the neighbourhood of the observed threshold contents (coarse 20%, medium ~ 15%, fine 10-15%) exhibited some kind of transitional permeability

development behaviour during deformation. In particular, many such samples showed a transient appearance of permeability. This is believed to be due to the development of only transient connectivity between dilating anhydrite particles during deformation.

From the above it seems that critical connectivity phenomena played an important role in determining the threshold behaviour and development of permeability in the present deformation experiments on salt/anhydrite composites. This question will be further addressed in Chapter 6, in the proper framework of percolation theory.

5.7. Summary and conclusions

Experiments have been performed on synthetic salt/anhydrite rock in order to investigate the influence of macroscopically ductile (plastic) deformation on dilatancy and permeability development. The experiments represent an extension of similar work on pure synthetic salt reported in Chapter 4, and were intended to systematically investigate the effect of anhydrite as a rigid second phase.

The experiments consisted of triaxial deformation/permeametry tests carried out under conditions where pure salt is non-dilatant, namely at room temperature, a confining pressure of 20 MPa, and a constant strain rate of $\sim 4 \times 10^{-5} s^{-1}$. The experiments were carried out using synthetically prepared samples in which anhydrite content was independently varied in the range 5-35 vol%, using particle sizes of $\sim 10^{1}$, 10^{0} and 10^{-1} times the grainsize of the halite "matrix". The coarse and medium suites of samples consisted of anhydrite clasts surrounded by a dense halite matrix, while in the fine suite, the anhydrite accummulated in networks at halite grain boundaries.

The results of the experiments showed all samples to deform by work hardening flow, with almost all developing significant dilatancy ($\leq$ 3%) by 15% strain. The stress-strain data obtained from the tests showed that the flow strength of the samples, at fixed strain, increased with increasing anhydrite content and with decreasing anhydrite particle size. The extent of dilatancy also increased with anhydrite content. The effect of increasing anhydrite content on flow stress was shown to be largely due to the enhancement of strain and thus strain hardening in the halite, by the presence of the "rigid" anhydrite. The effect of decreasing particle size on flow strength was inferred to be due to a strain-incompatibility hardening effect similar to dispersion hardening. The increase in dilatation with anhydrite

content was shown to reflect an increase in volume-specific dilatation occurring within the anhydrite at the higher contents and correspondingly higher flow stresses.

In addition to the effects of deformation on dilatation described above, the permeability of the samples (to gas) also increased with deformation, but only in samples with anhydrite contents above certain critical threshold values, namely 20-25% in coarse samples, 15-20% in medium samples, and 10-15% in the fine samples. Samples with very low initial permeability ($< 10^{-21}m^2$), and with high anhydrite content showed critical permeability growth effects with the permeability rising by 2-3 orders of magnitude in the first 0.2% of dilatation. It was proposed that the observed threshold and critical growth behaviour were controlled by the establishment of conducting connectivity between dilated anhydrite regions in the sample. This question will be addressed in detail in Chapter 6 using percolation theory.

The present results are of direct relevance to the behaviour of salt/anhydrite rock in radwaste repositories and storage caverns sited in salt. Viewing the salt/anhydrite system as a rock analogue, the results also provide useful insight into the influence of deformation on the development of dilatancy and permeability in plastically deformable rocks containing a rigid/brittle second phase. These aspects are treated in detail in Chapter 7.

CHAPTER 6

Experimental Results versus Theoretical Models

6.1. Introduction

The results from the previous chapters have shown that during (macroscopically) plastic deformation of salt rocks and salt/anhydrite composites, the development of very small amounts of dilatancy caused initially very rapid and large changes in permeability which subsequently reached saturation. Qualitatively speaking, extremely rapid jumps of this type, from essentially zero permeability to a finite value, are not consistent with behaviour predicted by classical models relating permeability to connected porosity (Carman, 1937; see Dullien, 1979).

As mentioned in previous chapters, this raises the question as to whether the observed rise followed by saturation behaviour can be better interpreted as a connectivity development phenomenon of a type similar to that which produces the sudden or "critical" onset of electrical conductivity in insulating polymers that contain conductive particles (Deutscher et al., 1983(I); Nangrani and Gerteisen, 1985). Phenomena of this type are known as "percolation phenomena". In recent years many such phenomena have been recognized in diverse branches of science, and a great deal of attention has been paid to the development of an appropriate theoretical framework in which to treat them (Flory, 1941; Broadbent and Hammersley, 1957; Shante and Kirkpatrick, 1971; Essam, 1980; Stauffer, 1979 and 1985; Balberg, 1987). This theory is known as "percolation theory" and has been widely applied in materials physics (Kirkpatrick, 1973; Deutscher et al., 1983(II); Stauffer, 1985; Guyon et al., 1989). Recently, models based on percolation theory have been developed to describe permeability in fractured rocks containing macroscale networks of cracks (Dienes, 1982; Englman et al., 1983; Long and Witherspoon, 1985; Wilke et al., 1985; Gueguen and Dienes, 1989; Hestir and Long, 1990).

In the present chapter, classical models relating permeability to already connected porosity are reviewed and are shown, by means of order-of-magnitude calculations, to be inapplicable to the experimental results reported in this thesis (Chapters 3-5). General aspects of percolation theory are then reviewed and the theory is used to develop a microcrack linkage model appropriate for comparison with the present

experimental data for natural and pure synthetic salt. Comparison of the results for these materials, and for the salt/anhydrite composites, with various aspects of percolation theory leads to the conclusion that the observed permeability "jumps" do represent critical percolation phenomena. The controlling factor here is the connectivity of the available porosity, this being determined either by microcrack linkage in the pure salts or by chained contact between permeable second phase regions in the salt/anhydrite composites.

6.2. Models relating permeability to connected porosity

6.2.1. Formulation

Models for fluid flow through media pervaded by connected porosity (see Carman, 1937; Dullien, 1979) are typically constructed by in some way averaging the microscale interstitial flow velocities v_i, associated with the microscale pressure gradients $(\Delta P/L_c)_i$, across an assemblage of idealized elementary pores such as cylindrical pipes, prismatic pores or penny-shaped cracks of characteristic length $(L_c)_i$. Flow through these elements is described by the appropriate, geometrically scaleable hydraulic formula, such as the Hagen-Poiseuille equation

$$v_i = - (D_c^2/32\mu)_i \, (\Delta P/L_c)_i \tag{6.1}$$

for laminar flow in cylindrical channels, where D_c is the (effective) channel diameter and μ is the fluid viscosity. Expressions for the average interstitial velocity $\langle v_i \rangle$ and hence macroscopic velocity v can be obtained in a number of ways, the most simple being to assume that all conduits are identical and arranged in a simple network (see Turcotte and Schubert, 1982, section 9.3). Alternatively, more sophisticated averaging techniques can be used, taking into account the statistically distributed nature of micro-variables such as pore or crack aperture, length and orientation (Gray and O'Neill, 1976; Dullien, 1979 and references therein; Lehner, 1979; Dienes, 1982; Englman et al., 1983; Hassanizadeh, 1986). For one-dimensional flow, the resulting expressions for flow velocity generally take the form

$$v = K(\Delta P_m/L) \tag{6.2}$$

where K is a constant reflecting pore structure and $\Delta P_m/L$ is the macroscopic pressure gradient. By comparison with Darcy's law written

$$v = - (\kappa/\mu) \, (\Delta P_m/L) \tag{6.3}$$

a final expression for macroscopic permeability (κ) can be obtained.

Probably, the best-known model for flow in a porous medium with connected porosity is that due to Carman and Kozeny (Kozeny, 1927; Carman, 1937). This approach can be seen as equivalent to assuming Hagen-Poiseuille flow through a network of tubular pores. Carman and Kozeny obtained an expression for average interstitial flow velocity $\langle v_i \rangle$ by rewriting the Hagen-Poiseuille equation (Equation 6.1) in macroscopic average form as

$$\langle v_i \rangle = -(D_H^2/16\theta^*\mu).(\Delta P_m/L_e) \tag{6.4}$$

where θ^* is a geometric shape factor, $(\Delta P_m/L_e)$ represents the macroscopic pressure gradient with respect to average network length (L_e), and where D_H is an average channel diameter (hydraulic diameter - see Dullien, 1979, p. 170). The relationship between the macroscopic velocity (v) and the average interstitial velocity $\langle v_i \rangle$ is then specified using assumptions such as the Dupoit-Forcheimer assumption (Dullien, 1979) written

$$\langle v_i \rangle = (v/\phi)\,(L_e/L) \tag{6.5}$$

where ϕ represents porosity. This introduces the tortuosity (L_e/L) which expresses the more tortuous microscale path distance, L_e, covered by a fluid molecule relative to the direct macroscopic distance, L, covered in the same time. Finally an expression for permeability, κ, is obtained by inserting v from Equation 6.5 into Darcy's law for macroscopic flow, given by Equation 6.3. The result (Dullien, 1979) is

$$\kappa = \phi D_H^2 / (16\ \theta^*\ (L_e / L)^2) \tag{6.6}$$

Similar results for the permeability (κ) are obtained more or less regardless of averaging method used. Thus, the above type of expression forms the basis for practically all widely used models, differing mainly in the physical significance and values of the terms D_H^2 and $\theta^*(L_e/L)^2$ which depend upon pore geometry. In Carman and Kozeny's approach for granular aggregates, D_H was taken from hydraulic practice as

$$D_H \approx 4\phi/S_o\,(1 - \phi) \tag{6.7}$$

where ϕ is (connected) porosity and S_o is specific pore surface area based on the solid's volume (Dullien, 1979). The corresponding permeability vs. porosity

equation following from Equation 6.5 is known as the Carman-Kozeny equation and is written

$$\kappa_{CK} = \phi^3/[\theta^*(L_e/L)^2(1 - \phi)^2 S_o^2] \tag{6.8}$$

where the subscript CK denotes the Carman-Kozeny permeability.

As a second example of the above type of permeability versus connected porosity model, consider the case of a network of fully linked penny-shaped cracks as analyzed by Dienes (1982) and used later in this chapter. Using a continuum averaging technique applied to cracks with statistically distributed width, orientation, radius and spacing, Gueguen and Dienes (1989) showed that

$$\kappa = \frac{2}{15} \langle w \rangle^2 \phi.\theta^{**} \tag{6.9}$$

where ϕ is fully connected microcrack porosity or dilated volume change, θ^{**} is a constant incorporating tortuosity, and $\langle w \rangle$ is the mean crack half-width (c.f. Equation 6.6). For a fixed population of cracks which simply widen during dilatancy, we must then have $\phi \propto \langle w \rangle$ and hence $\kappa \propto \phi^3$, which resembles the Carman-Kozeny Equation (6.8) when ϕ is small.

6.2.2. Model validity and limitations: The problem of connectivity

The various κ vs. ϕ models described above have gained experimental support for a wide range of porous media with well-connected, intergranular pore networks. For example, in experiments on artificial sandstones made from fused glass spheres, Wong et al. (1984) showed that the Carman-Kozeny relation holds true for porosities ranging from $\phi = 0.6$ down to $\phi = 0.03$. Deviation at lower porosity was seen to correspond to the appearance of occluded pores plus a significant departure from the simple intergranular pore/conduit geometry seen in the range $0.03 \leq \phi \leq 0.6$. Notably, numerical models for the consolidation of 3-D arrays of interpenetrable spheres also indicate a breakdown in connectivity below a critical porosity of ~ 0.03 (Roberts and Schwartz, 1985).

Experimental support for κ vs. ϕ models derived for connected planar crack porosity is less direct. Permeability changes, induced by elastic closure of cracks during changes in effective stress, provide some support for parallel plate, Poiseuille flow models in fractured rocks (Bernabe, 1986) and single fractures (Kranz et al., 1979; Trimmer et al., 1980; Walsh, 1981). All these experiments showed $\kappa \propto$ (crack

aperture)^3, in agreement with the parallel plate model (c.f. Equation 6.9). For single fractures, Nolte et al. (1989) found much higher exponents with $\kappa \propto$ (crack aperture)$^{\sim 8}$. These high exponents were explained as reflecting a dependence of crack contact area and tortuosity on crack aperture (c.f. Equation 6.9, taking θ^{**} to be variable).

In summary, the available evidence indicates that the permeability vs. porosity models discussed above appear to work for intergranular porosities between 3 and 60%. Extrapolation to lower porosity presents problems because:

a. the structure will not scale with porosity due to changes in pore geometry;
b. there may be a breakdown in connectivity of pores or cracks caused by either purely geometric or surface tension (healing) effects (von Bargen and Waff, 1986).

6.2.3. Theory vs. experimental data on salt

An attempt is now made to assess the applicability of the above type of connected porosity models to the permeability behaviour seen in the experiments on salt rock reported in Chapters 3 and 4.

In the Asse salt rock investigated in Chapter 3, most of the initial porosity (~ 0.2% - Spiers et al., 1986) occurs in planar arrays of apparently isolated grain boundary inclusions. Examination of the pure synthetic salt, investigated in Chapter 4, showed the initial porosity (< 1%) also to be apparently disconnected and confined to grain boundary inclusions and tubes at triple junctions. So, connected porosity models are unlikely to be applicable to these materials in the undeformed condition.

Simple calculations of the permeability expected for the initial porosity (~ 0.2%) of the Asse salt material using a fully connected grain boundary facet flow model, analogous to Equation 6.9 (Dienes, 1982; Gueguen and Dienes, 1989), gave values of ~ 10^{-15}m^2. This is five orders of magnitude greater than the initial permeability actually observed. Similar calculations for an assumed network of triple junction tubes (taking maximum porosity = 1%) for the synthetic salt material, using a fully connected pipe flow model (Gueguen and Dienes, 1989), gave permeabilities of ~ 1 x 10^{-16}m^2. Again this is far in excess of the observed initial values of $\leq 10^{-21}$m^2. However, the calculated values for the Asse and synthetic salt correspond quite well

with the saturation values of ~ $10^{-16}m^2$ measured after just ~ 0.02% of deformation induced dilatancy (porosity increase).

Clearly simple, scaleable-geometry, permeability vs. porosity models which ignore the connectivity aspect of the flow network are inadequate to describe the initial permeability of the Asse and synthetic pure salts, investigated in Chapters 3 and 4, or to describe the rapid "growth" behaviour observed to occur with minor dilatancy. They may, however, explain the saturation behaviour seen towards higher dilatancies. Identical conclusions apply to the salt/anhydrite samples investigated in Chapter 5, in cases where these show sudden appearance of permeability with dilatancy.

6.3. Introduction to percolation theory

The above discussion confirms that the extremely rapid (critical) development of permeability, seen in the experiments of Chapters 3 to 5, requires a model that allows the growth of pore or crack connectivity to be considered. As mentioned already, so-called percolation theory provides the necessary theoretical framework for this. In recent years, percolation theory has been widely applied in the physical sciences to treat many similar critical "connectivity" phenomena. Examples include phase transitions, polymer gelation, dilute magnetization (Ising spin models), thermal and electrical conduction in insulator/conductor mixtures (amorphous semi-conductors and discontinuous metal films), stochastic star formation in spiral galaxies, and the propagation of forest fires or disease epidemics (see Deutscher et al., 1983(I); Stauffer, 1985, for these and many other examples).

Here the basic concepts of percolation theory are introduced. This is done as a pre-requisite to the description of percolation models suitable for comparison with the experimental results.

6.3.1. Basic concepts and terminology

The classic paper of Broadbent and Hammersley (1957) introduced percolation theory in terms of the random penetration of a "fluid" into a medium. Though the problem of water permeation was cited as an example, it was not until the 1980's that percolation theory was seriously used in this context (Dienes, 1982; Englman et al., 1983; Charlaix et al., 1984; Wilke et al., 1985; Gueguen et al., 1986; Gueguen and Dienes, 1989).

The theory of percolation focusses on the statistical study of connectivity between randomly placed elements in a medium. It began with probabilistic studies of direct connection developed between discretely occupied sites (site percolation), or developed via bonds between sites (bond percolation), in rigidly defined lattices. More recently, percolation theory has evolved towards continuum descriptions of connectivity in 3-D disordered media, i.e. with non-uniform distributions of site location, bond lengths and strengths, without the underlying regularity of a lattice geometry (see Balberg, 1987). Figures 6.1a to f show the concepts of site, bond and continuum percolation. The reader is referred to Shante and Kirkpatrick (1971), Kirkpatrick (1973), Essam (1980), Deutscher et al. (1983(I)), Stauffer (1985) and Balberg (1987) for review articles.

6.3.2. Lattice percolation models

The main principles of percolation theory are best understood from a consideration of bond and site percolation models referred to a rigid lattice (Stauffer, 1985). The sites in Figure 6.1a all have an equal probability (^{s}p) of being filled (●) and a probability ($1 - {}^{s}p$) of being empty (o). If ^{s}p is very low, then few sites will be occupied and clusters of sites consisting of two or more occupied neighbours will be very few. Increasing ^{s}p will produce higher densities of occupied sites and hence more clusters. At a critical threshold probability ($^{s}p_c$), a cluster large enough to span the whole lattice will be produced and the lattice will through-connect or "percolate". At this point through-going connectivity is established in the form of an infinite "percolation cluster" independently of the size of the lattice (Stauffer, 1979). Further increases in ^{s}p will add sites to clusters and clusters to the main "percolating cluster", thus increasing the size of the percolating cluster until, as $^{s}p \rightarrow 1$, all the sites become filled and involved in percolation.

The above process is essentially the same for bonds between lattice sites, with ^{b}p representing the probability of existence of bonds in a given lattice, and ($1 - {}^{b}p$) the probability of absence (see Figure 6.1b). Increasing ^{b}p from initially low values essentially causes bond networks to form and, at a critical threshold ($^{b}p_c$), an infinite network will become established that spans the whole lattice, independently of the lattice size. Applying these ideas to fluid transport, a fluid entering a bond percolation cluster will be able to traverse the lattice via a percolation path, i.e. the lattice will have become permeable. In this case, the sites and bonds can be respectively seen as valves at joints (sites) and valves in pipes (bonds) in a simple plumbing model, see Figures 6.1c and d.

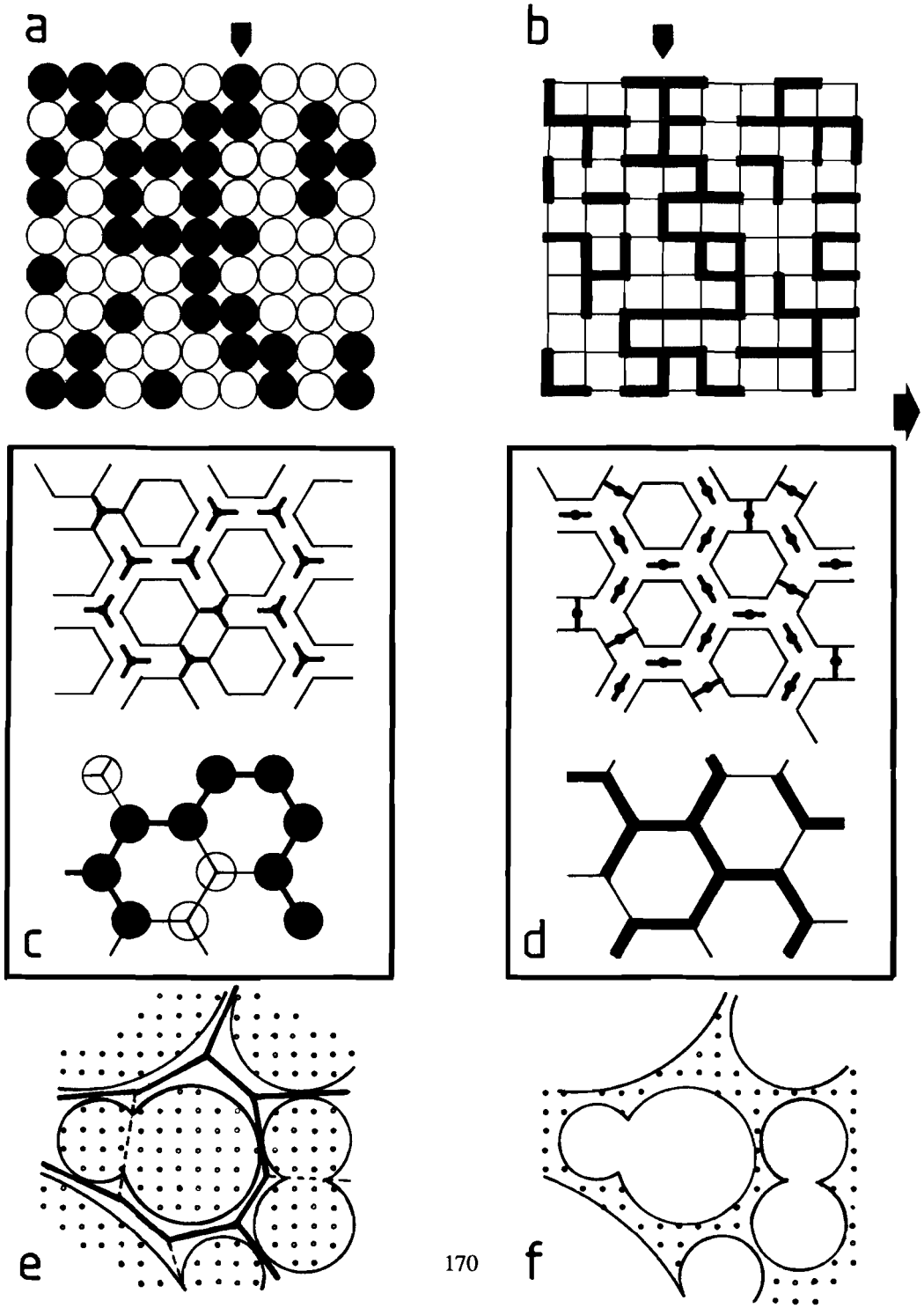
a
b
c
d
e
f

The critical threshold probabilities ${}^{s}p_c$ and ${}^{b}p_c$, referred to above, are called percolation thresholds. These take different values depending on the dimensionality and geometry of the lattice. For example in the case of a 2-D square lattice, ${}^{s}p_c$ and ${}^{b}p_c$ are 0.59275 and 1/2 respectively, while for a 2-D triangular lattice ${}^{s}p_c = 1/2$ and ${}^{b}p_c = 0.34729$, and for a 3-D simple cubic lattice ${}^{s}p_c = 0.3117$ and ${}^{b}p_c = 0.2492$ (Stauffer, 1985; Frisch et al., 1962). Now, the probability that a bond or site belongs to the percolation cluster is usually written as ${}^{i}P$, i = s, b (site or bond). Below the percolation threshold, i.e. when ${}^{i}p < {}^{i}p_c$ (i = s, b), ${}^{i}P = 0$ and no percolation cluster exists. However, when ${}^{i}p$ just exceeds ${}^{i}p_c$, the percolation probability ${}^{i}P$ has been shown by application of scaling theory (Stauffer, 1979), with verification by computer simulation "experiments" using Monte Carlo methods and renormalization techniques (see Essam, 1980; Stauffer, 1979 and 1985), to grow

---

Figure 6.1a-f. Percolation types (after Stauffer, 1985; Deutscher et al., 1983(I); Halperin et al., 1985):

a) Site percolation on a square lattice. Occupied sites are black, unoccupied sites are white. Lattice spanning, site percolation cluster shown by arrow.
b) Bond percolation on a square lattice. Active bonds are shown as thick lines, inactive bonds are shown as thin lines. Lattice spanning bond percolation cluster is shown by arrow.
c) Plumbing analogy of site percolation. Sites are represented by valves at joints in a hexagonal network of pipes. The hexagonal lattice is redrawn below to show the occupied sites (open valves) in black and the unoccupied sites (closed valves) in white.
d) Plumbing analogy of bond percolation. Bonds are represented by valves in the pipes in a hexagonal network of pipes. The hexagonal lattice is redrawn below to show the active bonds (open valves) as thick lines and inactive bonds (closed valves) as thin lines.
e) The "Swiss cheese" continuum percolation model. Shaded regions represent "bubbles" of non-conducting material. A bond percolation network is drawn as thick black lines in the conducting region between the "bubbles". To illustrate the link with lattice models, intersecting "bubbles" may be viewed as missing or inactive bonds and bond-nodes may be interpreted as sites. As the non-conducting regions progressively occupy more space (c.f. a compacting sandstone with pore space reduction), then the conducting regions become pinched out so that percolation and macroscale conductivity (permeability) will cease.
f) The "blue cheese" continuum percolation model. Shaded regions represent non-conducting material as for e) but here the bulk of the material shown as "bubbles" is conducting. Percolation of the space occupied by non-conducting material causes isolation of the conducting regions and macroscopic breakdown of conductivity.

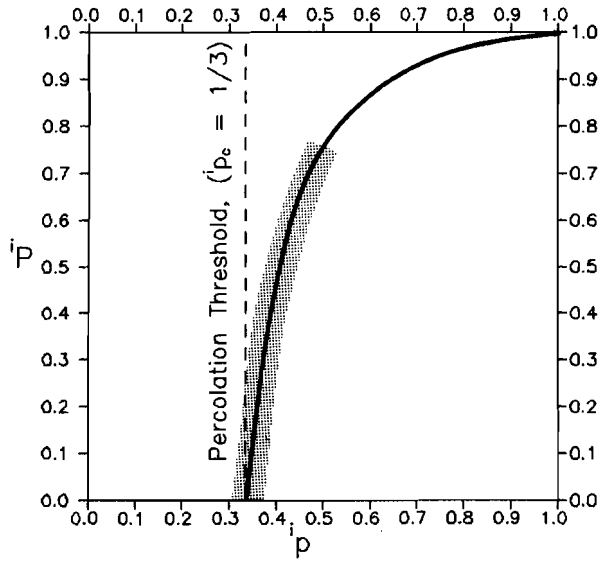

Figure 6.2. Schematic diagram showing the typical growth form of the percolation cluster size ${}^{i}P$ as a function of site or bond occupation probability ${}^{i}p$. The critical growth of ${}^{i}P$ just above the percolation threshold (${}^{i}p_c = 1/3$ in this case) follows a power law ${}^{i}P \propto ({}^{i}p - {}^{i}p_c)^{\beta}$ where in this case $\beta < 1$. This is only true for the critical growth region immediately above the percolation threshold (shaded). Above this region, the growth rate of ${}^{i}P$ decreases, so that ${}^{i}P = 1$ at ${}^{i}p = 1$, where all bonds percolate. Below the critical percolation threshold no bonds are expected to percolate and ${}^{i}P = 0$.

---

rapidly in a manner approximated by a power function of the form

$$ {}^{i}P \propto ({}^{i}p - {}^{i}p_c)^{\beta} \tag{6.10} $$

where, typically ß increases with the dimensionality of the system from ~ 0.14, for 2-D; ~ 0.4, for 3-D to a maximum of 1, for ∞-D - Bethe lattices (Essam, 1980; Stauffer, 1985). However, as ${}^{i}p$ increases and approaches unity, then Equation 6.10 no longer provides a good approximation, since ${}^{i}P \rightarrow 1$ as ${}^{i}p \rightarrow 1$. This is illustrated in Figure 6.2. As ${}^{i}p \rightarrow 1$, ${}^{i}P$ can be calculated either by analytical methods (Stauffer, 1979; Essam, 1980) or by Monte Carlo simulation (Frisch et al., 1962; Stauffer, 1979).

6.3.3. Continuum percolation models

In continuum percolation models, sites and bonds are considered to be spatially distributed and not tied to fixed lattice positions. Also (as in some lattice models), the site size and bond length can be assigned continuously distributed finite magnitudes. These features can drastically change percolation thresholds in comparison with simple lattice models. However, provided the site size and location are not too widely distributed, percolation thresholds in continuum site models tend to occur at the same critical occupied volume fraction (3-D) / areal fraction (2-D) as obtained in lattice site models with finite site size (Balberg and Binnenbaum, 1987(I); Balberg, 1985). This view is based on the finding that volumetric and areal percolation thresholds in this type of lattice model are independent of lattice type (Scher and Zallen, 1970).

Because of the absence of a rigid lattice, continuum percolation descriptions more closely resemble real physical systems (see Balberg, 1987 for recent review). Continuum approaches include the so-called "Swiss cheese" model (Halperin et al., 1985 and Feng et al., 1987), and the "blue cheese" model (Sornette, 1988 and Gilabert et al., 1990), see Figures 6.1e and f. In both of these models, the growth and deterioration of connectivity near the percolation threshold, has been shown to follow a similar power law to growth in lattice models (Equation 6.10), see Halperin et al. (1985).

The "Swiss cheese" model is illustrated in Figure 6.1e. Here, regions of "non-conducting" material are represented by either hard or interpenetrating (soft) spheres (or "bubbles") in the conducting matrix, depending upon the application. (N.B. the percolation properties depend on interpenetrability; see Bug et al., 1985 and 1986; Balberg and Binnenbaum, 1987II). The intersection of the spheres causes the disappearance of conducting links, similar to the loss of bonds in lattice models. Exceeding a critical volume fraction of spherical insulators thus causes the continuum to stop percolating. The critical volume fraction of spheres is very high (~ 97%) and has been used to explain the very low porosities to which electrical conductivity persists in wet sedimentary rocks (see Roberts and Schwartz, 1985). The Swiss cheese model has clear applications with respect to modelling the pore structure and permeability of sandstones (see Wong et al., 1984, and Wong, 1988 for review article).

The "blue cheese" model is the antithesis of the "Swiss cheese" model (see Figure 6.1f). The bulk of the medium is conducting, unlike the insulating spheres that form the bulk in the "Swiss cheese" model. The blue cheese model has been used to

calculate the effect of dispersed non-conducting regions, such as cracks or slots in a conducting medium (Sornette, 1988 and Gilabert et al., 1990). The model could also be used to treat the effect of impermeable barrier networks upon fluid flow in reservoir rocks, and in damage theory (Gilabert et al., 1990).

6.3.4. Structure and growth of the percolating cluster: Transport properties

Recent advances in percolation theory have concentrated upon aspects of scale invariance and growth behaviour of the percolating cluster near the percolation threshold. These aspects are expected to exhibit essentially the same characteristics in both lattice and continuum models. With regard to scale invariance, it has been established (Gefen et al., 1981 and Aharony et al., 1985 following Stanley, 1977) that the percolation cluster at the threshold is a fractal of size or mass M which varies with length scale (L) as $M \propto L^D$, where D is the fractal dimension (Feder, 1988). For 2-D (Euclidean 2-space) site percolation, the value of D is given as $D = 91/48 \approx 1.9$ (Stauffer, 1985; Aharony, 1986). In the 3-D (Euclidean 3-space) case, $D \approx 2.5$ (Stauffer, 1985). This has led to research on fluid flow through fractal networks as models of the percolating cluster - see Adler and Jaquin (1987), Jaquin and Adler (1987), Adler (1988) and Lemaitre and Adler (1990).

Regarding critical behaviour near the percolation threshold, much effort has been directed towards evaluating the growth of transport properties, e.g. conductivity (fluid and electrical), see Kirkpatrick (1973), Halperin et al. (1985), Feng et al. (1987) and Halperin (1989). For simple, relatively direct percolation networks, very near the percolation threshold, the bulk transport properties could be assumed to scale linearly with the probability ${}^iP$ of a bond or site belonging to the percolation cluster, so that from Equation 6.10

$$T \propto {}^iP \propto ({}^ip - {}^ip_c)^\beta \qquad (6.11)$$

where T is the transport property of interest. However recent work on both lattice and continuum models, has shown that transport properties do not necessarily scale in this way with the geometrical growth of the percolation cluster as defined by ${}^iP$ (Last and Thouless, 1971; Kirkpatrick, 1971; Pike and Seager, 1974; Webman et al., 1977; Straley, 1981; Ben-Mizrahi and Bergman, 1981; Feng et al., 1987; Halperin, 1989). This is because the transport flux is carried by a subset of the percolation cluster (called the backbone cluster), with "dangling" or "dead end" subsets not contributing to transport, see Figure 6.3 (Stanley, 1977; Pike and Stanley, 1981; Stanley and Coniglio, 1984). Furthermore, the backbone will generally contain

parallel site/bond clusters ("blobs") whose "conductivity" is insensitive to the addition of further sites/bonds (Figure 6.3). Thus with reference to Figure 6.3, bulk transport properties will be determined primarily by the density of serial "links" in the backbone, secondarily by the density of "blobs", with the "dangling clusters" playing no role. Notably near the percolation threshold a single missing link will strongly impair transport (Stanley and Coniglio, 1984).

This difficulty of relating bulk transport properties and their growth to the percolation probability ${}^{i}P$ is the subject of continuing research (Straley, 1982; Stanley and Coniglio, 1984; Halperin, 1989). Results obtained to date using Monte Carlo simulations (Stauffer, 1979) and analytical methods (Straley, 1982) show that, while ${}^{i}P \propto ({}^{i}p - {}^{i}p_c)^{\beta}$, the growth of transport properties can be approximated by power laws of the form

$$T \propto ({}^{i}p - {}^{i}p_c)^{\mu} \tag{6.12}$$

where $\mu > \beta$ and varies widely, depending on the nature of the system (Halperin, 1989; Stauffer, 1985 - equation 64).

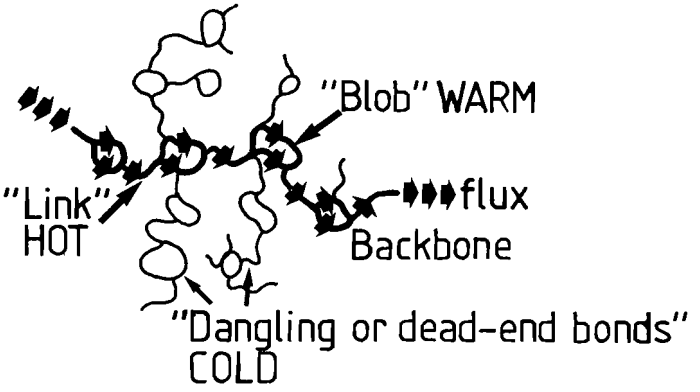

Figure 6.3. Schematic (topological) representation of part of a percolation cluster. Transport flux is carried by the "backbone" shown as thick lines whereas the side chains, which constitute "dead ends" or "dangling bonds", do not contribute. The conducting backbone may be subdivided into regions connected in parallel ("blobs") and sections which are serially connected by single bonds ("links"). The links are the most important conductivity-controlling components since one missing link will terminate flow. By using an electrical conduction analogy (all bonds having resistance, R), then all of the current (I) must pass through the "links" hence they may be called "hot" bonds (I^2R, heating effect). The "blobs" therefore represent "warm bonds" which share the current and the "dangling bonds" remain "cold".

Finally, the more general problem of bond or site percolation where the bond strengths are continuously distributed, instead of single valued, is also an important ongoing area of study w.r.t. transport properties (see Kogut and Straley, 1979; Lubensky and Tremblay, 1986; Tremblay and Machta, 1989; Tyč and Halperin, 1989). Figure 6.4 after Pike and Seager (1974) shows the effect of widening the range of bond strengths upon electrical conductivity development in a lattice bond-percolation model. The broader distributions produce a more rapid increase in conductivity just above the percolation threshold (Seager and Pike, 1974).

Charlaix et al. (1987), using the method of Ambegaokar et al. (1971), investigated the permeability of networks composed of cracks with widely varying apertures (i.e. bond strengths). They conclude that the fluid transport is controlled by a sub-distribution of narrower cracks having relatively low conductance. These cracks play a crucial role similar to the singly connected "links" in the percolation backbone. The effect of high-conductance, wider cracks is masked by these less conductive crucial cracks. The narrowest cracks are unimportant since they effectively become shorted out by other (wider) cracks in the network.

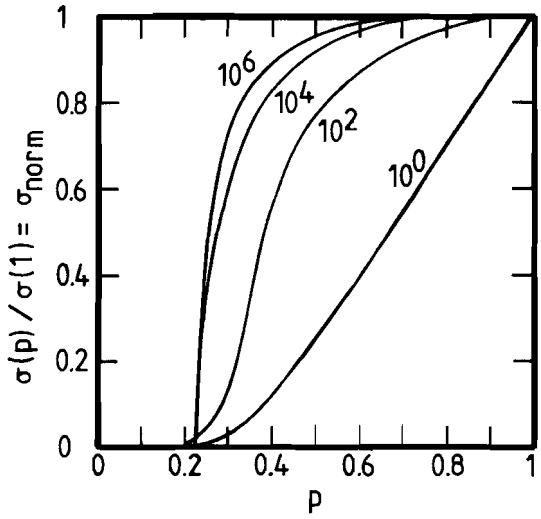

Figure 6.4. Growth of electrical conductivity in networks composed of a range of bond strengths. Conductivity is normalized to the fully percolating, resistive bond, network at ${}^{b}P = 1$, and plotted against bond occupancy fraction (probability) ${}^{b}p$. The curves are annotated with the range (10^{A}) of conductances (G_{ij}) allocated to the bonds according to the distribution $-A \leq \log_{10}G_{ij} \leq +A$. The curve 10^{o} represents networks composed of bonds with a single strength (conductance). Note that conductivity rises much faster, above the percolation threshold (${}^{b}p_{c} \approx 0.25$ for this simple cubic lattice), in networks composed of bonds with a progressively wider range of bond strengths then $A \rightarrow 6$. The curves were generated using Monte Carlo computer simulations by Seager and Pike (1974).

6.4. A percolation model based on microcrack linkage

6.4.1. Approach

Dienes (1982) presented a model relating rock permeability to (micro)crack distribution using a continuum averaging method to sum crack scale flow, plus percolation theory to specify crack linkage. Here, this model has been adapted, following the approach of Gueguen and Dienes (1989), to describe the critical development of permeability with progressive dilatancy. In the model, randomly oriented and positioned, "penny shaped", cracks are allowed to intersect and form permeable pathways. These pathways are local in extent at low crack number densities but, at a critical density, percolation is produced. This results in the appearance of macroscopic permeability which rapidly develops with further increase in crack density.

The starting point of the model consists of a description of the fluid flow properties of an isotropic assemblage of connected cracks in terms of their average dimensions and number density. The degree of active (i.e. conducting) connection between cracks is then addressed using lattice-type bond percolation theory. The results are used to describe a critical threshold of percolation and the development of conducting connectivity immediately above this threshold. This approach leads to a model relating permeability to crack number density and hence dilatancy. The symbols used in the analysis are defined in Table 6.1 and Figures 6.5a, b.

6.4.2. Permeability of a connected microcrack network

Dienes (1982, equation 12) showed, using Poiseuille's law for laminar flow between parallel plates, that, for an isotropic distribution of intersecting penny-shaped cracks, the permeability tensor is also isotropic and may be expressed as

$$\kappa_{11} = \kappa_{22} = \kappa_{33} = (8/15)\pi^2\theta\langle A\rangle^3\{N_o\langle c^5\rangle\} \qquad (6.13)$$

where the various terms appearing are defined in Table 6.1. Now the quantity $2\pi N_o$ is the crack number density of the entire sub-population of active, flow-carrying, fully through-connected cracks. With reference to Table 6.1 it can therefore be written

$$2\pi N_o = P^*.N = P^*/\langle l\rangle^3 \qquad (6.14)$$

Table 6.1. List of terms used in the microcrack linkage model. (Refer also to Figures 6.5a and b).

n_i	=	unit vector normal to i'th crack.
h_i	=	maximum thickness of crack i (m).
w_i	=	$h_i/2$ (m).
c_i	=	radius of crack i.
$l_{i,j}$	=	crack spacing centre of crack i to centre of crack j (m).
$\langle w \rangle$	=	mean crack half width (m).
$\langle c \rangle$	=	mean crack radius (m).
$\langle l \rangle$	=	mean crack spacing (m).
$\langle A \rangle$	=	$\langle w \rangle / \langle c \rangle$ = mean aspect ratio. Assumed to be constant in the model.
N	=	crack number density of the total population of cracks in all orientations, not necessarily connected (cracks per unit volume).
N	=	$1/\langle l \rangle^3$ for an isotropic distribution.
N_c	=	critical crack number density at percolation threshold (cracks per unit volume).
N_f	=	final crack number density, after deformation (m^{-3}).
N_o	=	crack number density of all connected cracks that form the flux carrying network averaged over all orientations (per unit volume and spherical angle, i.e. per steradian). Does not include disconnected or "dead end" cracks.
$2\pi N_o$	=	crack number density of all connected cracks that form the flux carrying network, per unit volume (m^{-3}). Does not include disconnected or "dead end" cracks.
π	=	3.14159....
p	=	probability of crack intersection.
q	=	(1 - p).
z	=	coordination number of the lattice, i.e. possible bonds per site (here z = 4 for the chosen Bethe lattice).
P_c	=	critical probability of crack intersection at the percolation threshold.
q_c	=	$(1 - p_c)$.
B	=	average number of active bonds per site (≡ percolation density of Scher and Zallen, 1970).
B_c	=	average number of active bonds per site at the percolation threshold.
$\langle V \rangle$	=	average excluded volume (m^3).
$\langle V_{ex} \rangle$	=	total excluded volume = $N_c \langle V \rangle$ (dimensionless).
r	=	intersecting disc radius (m). Used in excluded volume calculation (≡ crack radius).
P^*	=	fraction of intersecting cracks (bonds) belonging to the conducting (i.e. flow carrying) part of a percolating network. P^* is also the probability that a crack is not isolated and at least two infinite paths leading to and from the crack, exist (c f. P which is the fraction of bonds belonging to the total percolation cluster including "dangling bonds"). $P^* \subseteq P$ and excludes dangling or isolated bonds.

Q = probability that a path from a crack through an adjacent crack is finite (i.e. does not reach infinity - a requirement of percolation). Referring to Figure 6.6b, then a path from crack (1) is finite either because it is not connected to (2) or, if connected because the z-1 paths from (2) are finite.

κ_{ij} = permeability tensor.

θ = hydraulic aperture shape and drag factor describing the deviation of the flow from an ideal parallel-sided channel (Poiseuille flow model). Values of $\theta = 0.5$ or less are most likely since real cracks are generally tapered and rough sided.

D = dilatation defined as $\Delta V/V_s$ where ΔV is the volume change due to microcracking and V_s is the initial volume of the rock sample.

α = volumetric shape factor giving the deviation in volume from the ideal penny shaped crack, defined as (real crack volume)/(ideal penny shaped crack volume).

ϕ = porosity.

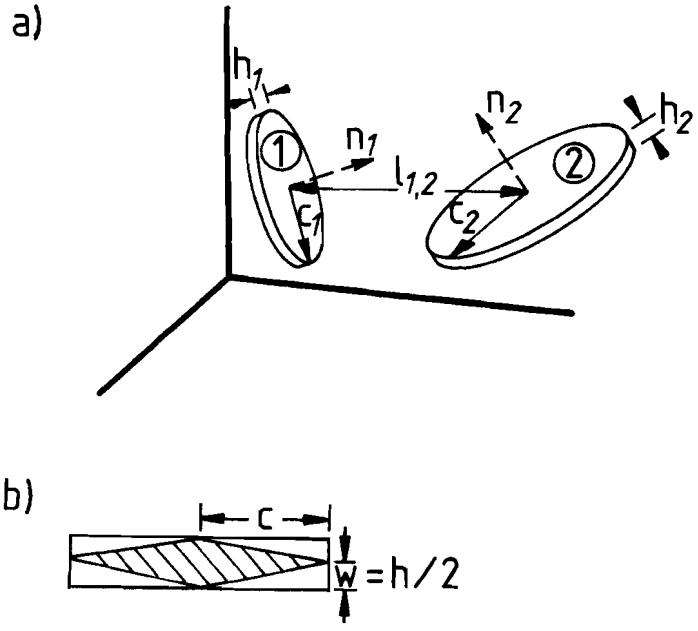

Figure 6.5a, b. Elements of the microcrack geometry and definitions of the microvariables used in the present microcrack linkage model.

a) Spacial relationships between penny shaped cracks (see Table 6.1 for explanation of terms).

b) Cross section of an ideal penny shaped crack. The shaded part represents a more realistic tapered profile, here $\alpha = 2/3$ (see Table 6.1 for explanation of terms).

Equation (6.13) thus modifies to

$$\kappa = (8/15)\pi^2\theta\langle A\rangle^3(\langle c^5\rangle/2\pi)\, P^*/\langle l\rangle^3 \qquad (6.15)$$

Assuming single or narrowly distributed crack size(s) with isotropic orientation distribution, the approximation $\langle c^5\rangle \approx \langle c\rangle^5$ holds, thus yielding

$$\kappa = (4/15)\pi\theta\langle w\rangle^3\langle c\rangle^2\, P^*/\langle l\rangle^3 \qquad (6.16)$$

6.4.3. Introduction of dilatation term

Equation (6.16) is now rewritten in terms of dilatation $D = \Delta V/V_s$ (see Table 6.1), assuming all microcracks are dilatancy-induced. To do this, D must first be expressed in terms of the crack dimension micro-variables $\langle c\rangle$, $\langle l\rangle$, $\langle w\rangle$ taking into account a shape deviation factor α defined

α = (real crack volume) / (ideal penny- shaped crack volume)

Writing the dilatant volume change as

$$\Delta V = (2\pi.\langle c\rangle^2.\langle w\rangle.\alpha) \times (N.V_s) \qquad (6.17)$$

and since $N = 1/\langle l\rangle^3$, for an isotropic distribution, then

$$D = \frac{\Delta V}{V_s} = 2\pi\langle c\rangle^2\langle w\rangle\alpha/\langle l\rangle^3 \qquad (6.18)$$

A similar result was derived for porosity (ϕ) by Gueguen and Dienes (1989) but neglecting crack shape deviation, i.e. assuming $\alpha = 1$. For the simple case of a linearly tapered crack like that shown in cross section in Figure 6.5b, then $\alpha = 2/3$. Since real cracks are tapered, this seems more likely for real cracks than $\alpha = 1$. Finally, combining Equations (6.16) and (6.18) gives permeability in terms of dilatancy and P^*, that is

$$\kappa = (2/15)\langle w\rangle^2\theta.\alpha.D.P^* \qquad (6.19)$$

6.4.4. Evaluation of the active crack connectivity (P^*) using bond percolation theory

It is now necessary to obtain an expression for the non-isolated and active (i.e. flow-carrying) fraction of the total crack population P^* (see Table 6.1). This is done following Dienes (1982) who assumed an isotropic distribution of cracks which intersect forming a regular branching network, described by a Bethe lattice (or Cayley tree - see Stauffer, 1985) of coordination number 4. This approach has the advantage of allowing a precise description of the percolation process albeit less general than a continuum model. The restriction on the crack intersection distribution is not ideal but probably quite realistic for the case of grain boundary controlled cracks to which this model is later applied. The nature of the Bethe lattice crack network is illustrated in Figure 6.6a which shows a group of intersecting cracks where the maximum allowed number of intersections (4 per crack) has been achieved. The crack intersections form bonds between sites represented by the crack centres. This network of sites and bonds is represented in Figure 6.6b, illustrating the branching tree form of the Bethe lattice.

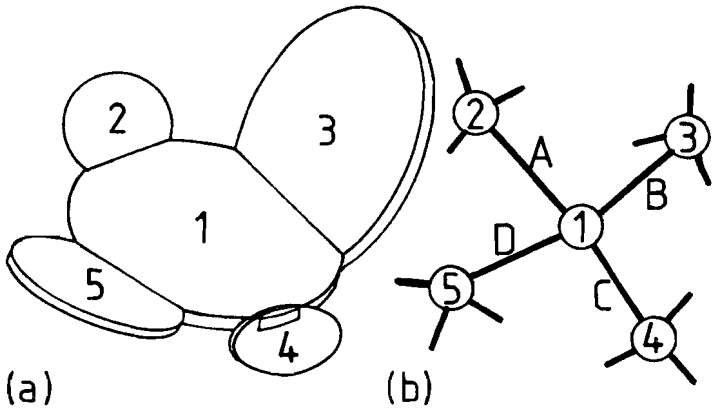

Figure 6.6a, b. Bethe lattice structure used in the present model.

a) Group of four cracks numbered (2, 3, 4 and 5) which intersect with a central crack (1). The intersections A, B, C, D are equivalent to bonds.

b) Crack intersections in a site/bond percolation-theory diagram, where the sites (crack centres) are numbered and bonds (crack intersections) are lettered in accordance with the crack diagram (a). The maximum number of possible intersections (bonds) per crack (site) has been chosen to be 4 to correspond with a Bethe lattice also of coordination number (z) = 4.

The bond percolation model is now defined as follows. First all bonds have an equal probability (p) of existence (i.e. all cracks have an equal probability of intersection). Therefore the probability of non-existence is q = (1 - p). Let Q be defined as the probability that a path from a crack (site) to an adjacent crack (site) is finite, i.e. that such a path does not form part of an infinite, and therefore percolating, network. Referring to Figure 6.6b, the path from crack site 1 to crack site 2 may be finite either when bond A does not exist or, if the bond A does exist, when all of the three paths from the adjacent crack (crack 2) are finite. Using Boolean logic, Q can thus be written

$$Q = q \text{ OR } [\text{NOT } (q) \text{ AND } Q \text{ AND } Q \text{ AND } Q], \text{ i.e.}$$

$$Q = q + (1 - q)\, Q^3 \tag{6.20}$$

The roots of this equation for the probability Q are

$$Q = 1, \text{ or } (1/(1 - q) - 3/4)^{1/2} - 1/2,$$

subject to the constraint $0 \leq Q \leq 1$. The second of these roots exceeds 1 when $q > 2/3$, and $q = 2/3$ therefore marks a critical point from where the first root ($Q = 1$) becomes appropriate and the paths in the network are certain to be finite, i.e. no percolating cluster exists (see Dienes, 1982). When $q < 2/3$, $Q < 1$ so that an infinite (i.e. percolating) path may exist.

An expression for probability P^* of a crack belonging to the flow carrying part of an infinite network (percolation cluster) is now sought. A crack may be considered to be inactive (i.e. not flow carrying) if it is entirely unconnected to other cracks, if it is part of a finite (non-percolating) network, or if it lies within a "dangling cluster" (see Section 6.3.4). This implies that, the probability $(1 - P^*)$ of a crack being isolated from (i.e. not actively participating in) the flow carrying part of an infinite percolating network is the probability that either all 4 paths from the crack are finite (each with probability Q) or that any path which links with a neighbour must have all 3 paths leading from that neighbour set as finite (Dienes, 1982). Expressed in Boolean logic, this is written

$$\text{NOT } (P^*) = [Q \text{ AND } Q \text{ AND } Q \text{ AND } Q] \text{ OR } 4[\text{NOT } (Q) \text{ AND } Q \text{ AND } Q \text{ AND } Q]$$

so that

$$(1 - P^*) = Q^4 + 4(1 - Q)Q^3 = 4Q^3 - 3Q^4 \tag{6.20}$$

Therefore

$$P^* = 1 - 4Q^3 + 3Q^4 \tag{6.21}$$

Coupling this with the relation p = (1 - q) for the probability of crack intersection (bond existence) and with the expression for the second root of Q (valid when $q \leq 2/3$) now yields

$$P^* = 1 - 4[(1/p - 3/4)^{1/2} - 1/2]^3 + 3[(1/p - 3/4)^{1/2} - 1/2]^4 \tag{6.22}$$

with the percolation threshold occurring at $p_c = 1 - q_c = 1/3$. Hence when the probability p of crack intersection (bond existence) exceeds $p_c = 1/3$, then the crack intersection network described here will percolate and be permeable via the flux-carrying part of a network-spanning cluster of intersecting cracks.

6.4.5. Expression for crack intersection probability (p)

The probability of crack intersection (p) may be obtained in terms of the crack dimensions and their distribution by the method of Charlaix et al. (1984). These authors used the concept of average excluded volume <V> (Onsager, 1949), defined as the average, over all orientations, of the volume around an object within which another object must have its centre in order for the two objects to intersect. The total excluded volume $\langle V_{ex} \rangle$ was found by Balberg et al. (1984) to be a quasi-invariant, at the percolation threshold, using the already recognized invariance of the average number of bonds per site, B_c (Scher and Zallen, 1970). This invariance result yields the useful equivalence relation

$$B_c \equiv \langle V_{ex} \rangle = N_c \langle V \rangle \tag{6.23}$$

where <V> is the average excluded volume of a given pair of discs (cracks) and N_c is the number of disc (crack) centres per unit volume at the percolation threshold (Balberg et al., 1984).

Now, the average excluded volume <V> of a pair of identical intersecting discs of radius r was shown by De Gennes (1976) to be $\langle V \rangle = \pi^2 r^3$. Substituting the average crack radius <c> for r then gives

$$\langle V_{ex} \rangle = N\langle V \rangle = N\pi^2 \langle c \rangle^3 \tag{6.24}$$

which at onset of percolation yields

$$B_c = N_c \pi^2 \langle c \rangle^3 \tag{6.25}$$

The approximately invariant relationship $B_c = zp_c$ (Pike and Seager, 1974) may now be applied, where z is the coordination number of bonds per site (4 in the present Bethe lattice), so that at the percolation threshold,

$$N_c \pi^2 \langle c \rangle^3 = 4p_c \tag{6.26}$$

Following Charlaix et al. (1984), provided that the distribution of crack spacing, size and orientation are not too wide, this relation (Equation 6.26) implies that the average number of intersections per crack can be written $B = 4p = N\pi^2 \langle c \rangle^3$. This leads to the result

$$p \approx N\pi^2 \langle c \rangle^3 / 4 \tag{6.27}$$

in agreement with that obtained by Dienes and co-workers (Dienes, 1978; Gueguen and Dienes, 1989) using a mean free path method.

6.4.6. Final assembly of the permeability vs. dilatancy model

The above expression for the crack intersection probability p (Equation 6.27) may be substituted into Equation 6.22 and the resulting expression for P^* inserted into Equation 6.19 to obtain a relationship between permeability and crack geometry and number density, N. The result is

$$\kappa = (2/15)\theta\alpha D \langle w \rangle^2 \left[1 - 4\left((4/(\pi^2 \langle c \rangle^3 N) - 3/4)^{1/2} - 1/2\right)^3 + 3\left((4/(\pi^2 \langle c \rangle^3 N) - 3/4)^{1/2} - 1/2\right)^4\right] \tag{6.28}$$

Further substitution for N making use of the relations $N = 1/\langle l \rangle^3$, $A = \langle w \rangle / \langle c \rangle$ and Equation 6.18 then gives the final desired expression relating permeability to dilatancy and crack geometry.

$$\kappa = (2/15)\theta\alpha D \langle w \rangle^2 \left[1 - 4\left((8A\alpha/\pi D - 3/4)^{1/2} - 1/2\right)^3 + 3\left((8A\alpha/\pi D - 3/4)^{1/2} - 1/2\right)^4\right] \tag{6.29}$$

6.4.7. Characteristics and applicability of the model

Equations 6.18 (D vs. microvariables) and Equation 6.27 (p vs. microvariables) may be combined to give

$$p = \frac{8A\alpha}{\pi D}, \quad [0 \leq p \leq 1] \tag{6.30}$$

This expression of the crack connection probability p may be used in Equation 6.22 (P^* vs. p) to specify the relationship between P^* vs. D and κ vs. D since $\kappa \propto P^*$ via Equation 6.19. Similarly, curves of absolute permeability vs. dilatancy may be generated via Equation 6.29 for various values of the microvariables <c>, <w> and <*l*>, and suitably set values of θ and α. This system of relationships forms the basis of a numerical algorithm which provides a useful method of assessing the properties of the present model and of drawing comparisons with experimental data.

The most important characteristic of the model (see Equations 6.19 and 6.22) is that permeability will appear at the percolation threshold $p = p_c = 1/3$. From equation 6.30 this corresponds to a critical dilatation, D_c, of $8A\alpha/(3\pi)$. With continued dilatancy, Equations 6.22 and 6.30 imply that growth of the percolating cluster and hence P^* will remain in operation until a dilatation of $8A\alpha/\pi$, at which point P^* and p reach unity and all cracks are linked. This behaviour is summarized in the P^* vs. D plot of Figure 6.7, generated numerically from Equations 6.22 and 6.30 assuming that dilatancy produces cracks of fixed average dimensions, i.e. cracks once formed, do not grow.

Near the percolation threshold, most percolation models predict that conductivity grows in a manner which can be approximated by $\sigma \propto (p - p_c)^n$ (see Section 6.3.2. and Stauffer, 1979). The Dienes type model used here is characterized by $P^* \propto (p-p_c)^2$ (see Figure 6.8). Equation 6.16 thus predicts $\kappa \propto (p - p_c)^2$ near the threshold. In formulations which take tortuous path-length and the non-conducting nature of dangling bonds into account, n = 3 (Straley, 1982). This discrepancy is due to the fact that, in the Dienes-type model, only dangling bonds are accounted for. Numerically, however, the discrepancy will be insignificant. In the Bethe lattice parallel regions or "blobs" do not exist (Straley, 1982) and therefore have no effect. However, since the present Dienes-type model assumes that <u>all</u> non-dangling bonds connected to the percolating cluster contribute to <u>forward</u> flow, the model must slightly overestimate the rate of development of κ with $(p - p_c)$ and with dilatation, near the percolation threshold. In addition, it must slightly overestimate κ at all values of $P^* < 1$. Nonetheless, these overestimates for the Bethe lattice model will

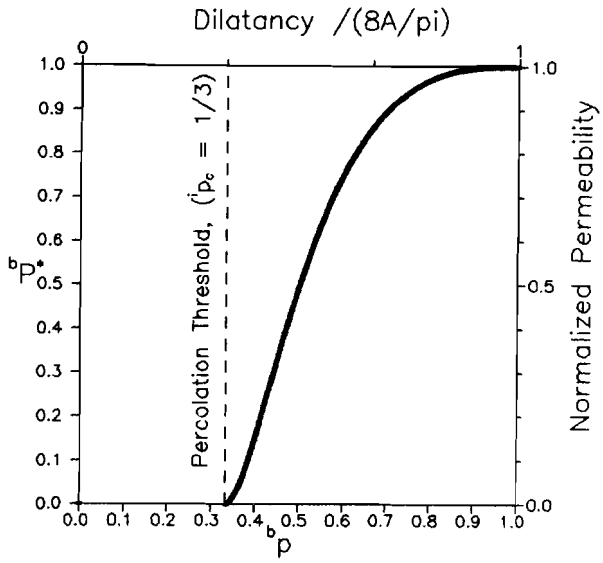

Figure 6.7. Critical growth of the probability P^* and permeability κ^* versus probability p and dilatation, as predicted by the present crack linkage percolation model, i.e. Equations 6.22 and 6.30 (for definition of terms, see Table 6.1). Here, permeability is normalized to that of the fully connected network. Note that all cracks are assumed to remain constant in size after nucleation. Dilatancy is associated with growth in crack population, towards a fully connected network of cracks. This final state corresponds to a maximum crack density determined by the assumed crack geometry.

Figure 6.8.

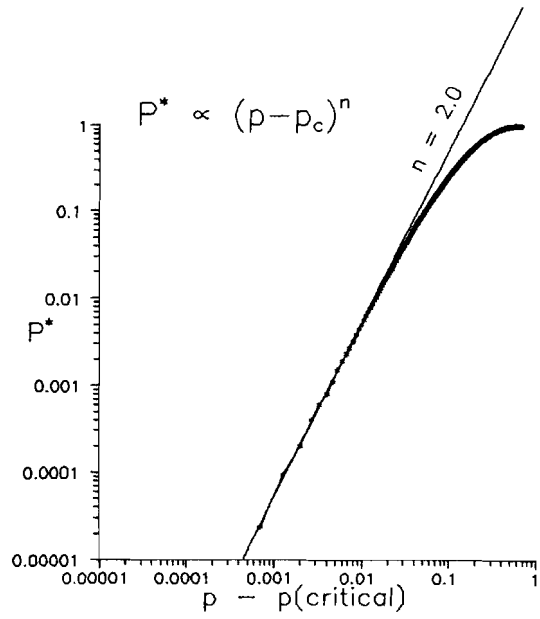

be small, with the error in κ approaching zero as both p and $P^* \rightarrow 1$. By this point (i.e. at $p = P^* = 1$) all possible bonds are fully connected.

Aside from the minor internal weaknesses of the present model, referred to above, its applicability to the critical development of permeability in real microcracked systems depends on the applicability of the following underlying assumptions:

a) that the growing crack network can be represented by the Bethe lattice (probably reasonable for grain boundary microcrack arrays - see Section 6.4.4);
b) that all dilatation is converted into microcrack porosity, with no pre-existing microcracks;
c) that the crack width and radius distributions are narrow;
d) that the crack orientation distribution is isotropic;
e) that all crack microvariables are isotropically correlated in space.

The effect of a broad distribution of crack widths and hence a broad range of bond conductivities was addressed in Section 6.3.4, and can be expected to lead to significantly lower permeabilities in the range $p_c \leq p \leq 1$ than predicted by the present model. The presence of non-uniform spatial or anisotropic orientational correlations with crack width distribution will be bound to affect the direct applicability of the model.

6.4.8. Permeability development beyond the critical region

The development of permeability beyond the critical region ($P^* < 1$) described by the above percolation model depends whether the total crack number density remains equal to the value achieved at $P^* = p = 1$, or whether the population grows with progressive dilatancy. Two extremes can thus be envisaged, namely

a) one involving growth in number density at constant average crack dimensions after $P^* = 1$, and
b) one of constant maximum population (N_{max}) which accommodates dilatancy by crack widening (or growth) after $P^* = 1$.

Figure 6.8. Growth of the conductive percolation probability P^* with $(p - p_c)$ as predicted by the present Dienes-type model. Note that near the percolation threshold ($P_c = 1/3$), $P^* \propto (p - p_c)^2$ to a close approximation. Curve generated numerically from Equation 6.29. Terms defined in Table 6.1.

These two extreme types of post-critical permeability development are represented as follows:

Case a

$$\kappa = (2/15)\langle w\rangle^2\theta\alpha D \qquad (6.31)$$

This is identical to Equation 6.19 but, in the post critical region, crack width and radius depend on dilatancy according to Equation 6.19 with P^* arrested at 1.

Case b

$$\kappa = \theta D^3\pi^2\langle c\rangle^2/(480.\alpha) \qquad (6.32)$$

This is essentially Equation 6.19 with P^* arrested at 1 (Equation 6.31),but with $\langle w\rangle$ no longer constant and expressed in terms of dilatancy at constant crack number density (making use of Equations 6.18 and $D_{p=1} = 8\langle w\rangle\alpha/\pi\langle c\rangle$ from Equation 6.30 - see previous Section).

Computer generated curves based on the critical percolation model (Equation 6.29) and the above equations are used in the following sections for comparison with the experiments on salt.

6.5. The percolation model vs. results on pure synthetic salt

The permeability versus dilatancy data reported for fine-grained,synthetic salt rock in Chapter 4 will now be compared with the crack linkage percolation model. The pure synthetic material had a more homogeneous microstructure than the Asse material and should therefore be easier to interpret in terms of the percolation model.

6.5.1. Microstructural constraints on crack microvariables

The microstructure of the pure salt samples for which permeability development could be monitored during deformation at 5 MPa is now recalled and analyzed further (Chapter 4, samples P40T24, 48, 11). Notably the orientation distributions of the cracks were isotropic in basal section (see Figure 4.8b) and anisotropic in (axial) sections parallel to the compression and the permeability measurement directions

(see Figure 4.8a). Crack geometry and distribution were strongly controlled by grain structure and almost all cracks were intergranular, possessing the appearance of grain boundary facets (see Figure 4.8). Transgranular cracks were not observed. The mean crack spacing <*l*> was therefore approximately equal to the average grain diameter of 300 - 400 μm. Axially oriented cracks tended to be widest and consisted of parallel sided intergranular segments chained across several grain diameters ending in tapered cracks of vanishing crack-width (see Figure 4.8a). Non-axial cracks were narrow and tapered. Individual intergranular crack "lengths" or segment diameters <2c> were slightly less than the average grainsize diameter, i.e. ~ 200 - 400 μm. The distribution of final crack widths (h = 2w) was measured from micrographs of axial sections of samples. This was found to be quite broad for both the parallel-sided and tapered crack populations, with a strong skew towards narrow crack widths (see Figure 6.9a). Tapered cracks were assumed triangular in cross section and their average width was taken as half their maximum width. Since the measurements of crack width were taken from 2-D sections, they must represent overestimates of the true crack widths due to orientation errors. In practice this error is less than a factor of 2 since very oblique cracks were not observable. Expressing the class intervals of measured crack widths (h = 2w) as an equivalent conductance $\kappa_{eq} = h^3$ (i.e. using Poiseuille's law for fluid flow between parallel plates) shows the conductance distributions for both parallel sided and tapered cracks to be heavily skewed towards lower values (see Figure 6.9b) and approximately log-normal in form (see Figure 6.9c). The mode (in this case ≈ geometrical mean) of the combined conductance for both crack distribution types gave an equivalent "average" crack width of $\langle h \rangle \approx 1 \times 10^{-5}$m. The arithmetic mean of the combined crack width distributions (Figure 6.9a) was $\langle h \rangle \approx 1.6 \times 10^{-5}$m. Using equations 6.17 and 6.18, these final crack width values imply an average final crack density (N_f) of ~ 2.7×10^{10} cracks per m^3 to satisfy the ~ 3% dilatant volume change accumulated by the specimens. Note that all of the above quantities refer to the final deformed state and may have taken different values during deformation.

6.5.2. Permeability development

The permeability development during dilatancy results for the fine-grained pure salt experiments at 5 MPa confining pressure are drawn against a background of computer generated curves in Figures 6.10 and 6.11. These curves are of two types. The heavy curves (* symbols) are generated using the crack linkage model with constant crack dimensions (<c>, <h>) and growing crack number (N) in the post critical region (i.e. using Equations 6.29, and 6.31 when $P^* = 1$), taking $\langle c \rangle = 2 \times 10^{-4}$m (as observed) and the values of <h>, θ and α shown (Figures 6.10, 6.11).

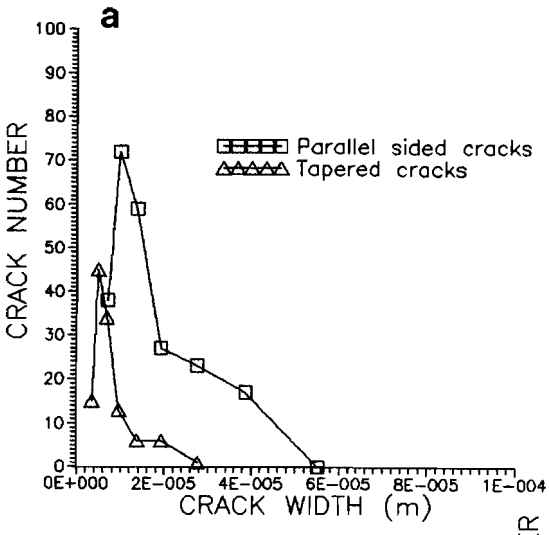

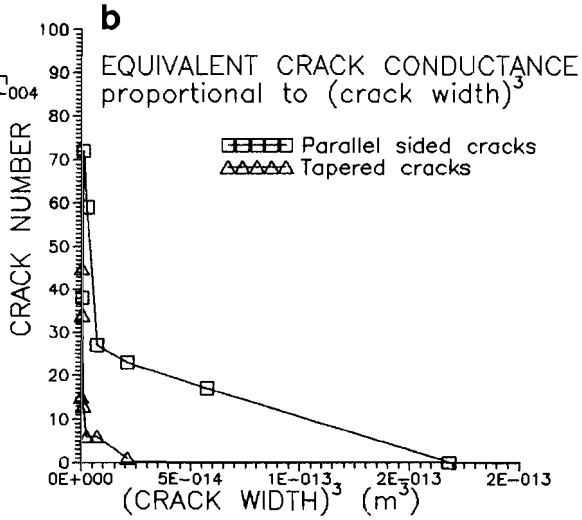

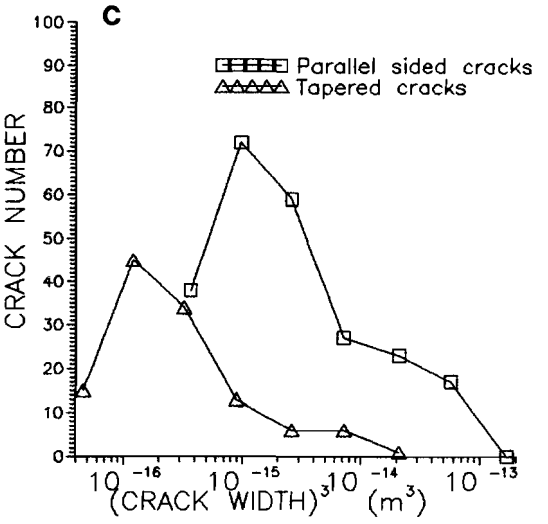

Figure 6.9. Crack width and equivalent conductance statistics for fine-grained halite deformed and dilated to 1.1 vol% (sample number P40T11, Chapter 4).

a) Histogram showing measured crack numbers versus measured crack width, i.e. versus class interval mean, <h>. Tapered cracks are assumed to be linearly tapered so that average width = 1/2 maximum width.

b) Equivalent hydraulic conductance distribution based on a $\kappa \propto$ (crack width, $<h>)^3$ relation, showing a strong skew towards low conductances.

c) Logarithmically plotted version of Figure 6.9b, showing the approximately "log-normal" distribution of equivalent conductances.

The chosen values for θ and α are upper and lower bounds (see Table 6.1 and Section 6.4.3). The continuous curves labelled "N_{max} limit" are generated using Equation 6.32, taking $P^* = 1$ and the values of θ, α and N_{max} shown (see Figures 6.10 and 6.11). The continuous curves represent the locus of $P^* = 1$, and show the post-critical development of permeability (κ) with dilatant volume change (D), associated with an increasing crack width <h> (constrained via Equation 6.18) at constant crack number ($N = N_{max}$, achieved at $P^* = 1$) and constant radius <c> $\approx 2 \times 10^{-4}$m (observed). The points at which the two families of curves intersect (arrows in Figures 6.10 and 6.11) represent the points on the critical development (heavy) curves where P^* attains unity. Beyond such points, the N_{max} branch shows the upper extreme for post-critical permeability development ($N = N_{max}$, growing crack width, spacing = l_{max}), while the lower branch shows the lower extreme (constant crack dimensions, increasing crack number).

From Figures 6.10 and 6.11, it is clear that the experimental data are characterized by a rapid growth in permeability which reaches saturation after a small (0.75%) dilatant volume change. The data at low volume change appear consistent with a low percolation threshold (< 0.1% volume change) and rapid conductive network formation with cracks around 1×10^{-6}m in width (or a little less). The percolation process appears to be complete by 0.75% volume change, since the permeability and hence crack network appear to have fully stabilized above this (i.e. no further growth). The agreement with the simple crack linkage model therefore only extends to the point of full network establishment, where $P^* \rightarrow 1$ and the fixed maximum number of cracks (N_{max}) are fully connected (see arrow labelled X on the heavy curves with h = 1 μm).

Beyond this point (X), the constant crack dimensions plus growing crack number curves, drawn for $h = 1 \times 10^{-6}$m (lower branch, heavy curves), cannot be valid despite the superficial agreement with the experimental data trend, because

a) the observed mean crack width is about 10 x 1 μm, and
b) the microstructurally constrained crack number density (N_f) after 3% dilatant volume change is about 10 x lower than the value implicitly predicted by the model.

The alternative extreme behaviour beyond point X (Figures 6.10 and 6.11), that is the constant crack number (N_{max} limit) curve with growth in width, is now considered (upper branch from X). This model predicts a crack width, at 3% dilatant volume change, of 4.7×10^{-6}m for <c> $= 2 \times 10^{-4}$m, $\theta = 1$, and $\alpha = 1$ (Figure 6.11), which is close to the mean observed value of 1.6×10^{-5}m. The model

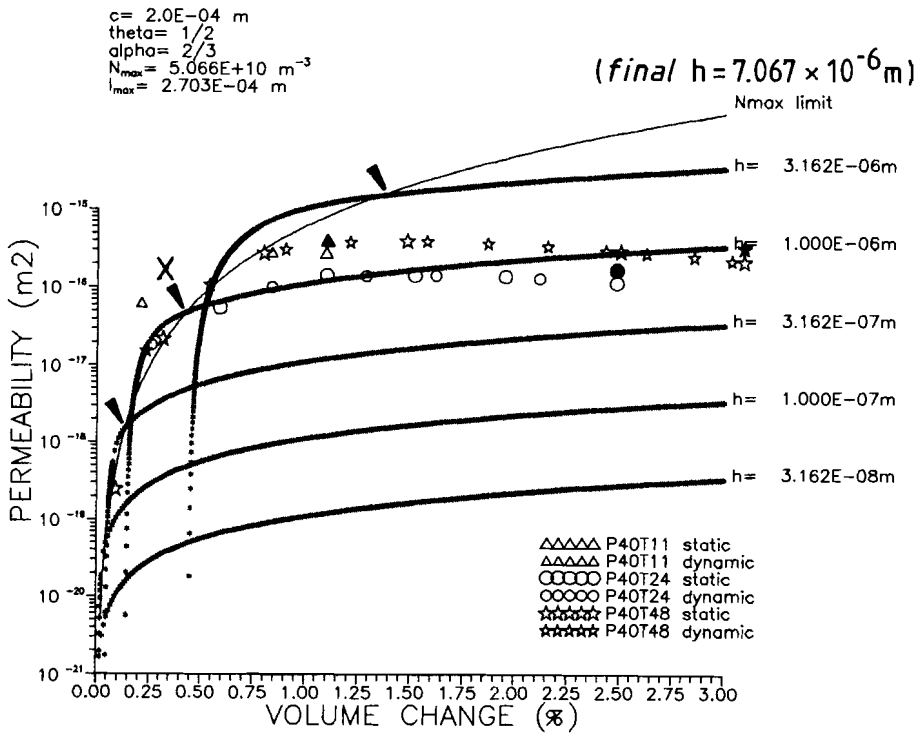

Figure 6.10. Computer generated permeability versus dilatancy curves based on the crack linkage model (Equation 6.29). Actual data from the synthetic halite experiments are overlain for comparison. The (heavy) curves composed of small asterisks were drawn for a crack radius, c, of 2 x 10^{-4}m and parameters indicated, for a set of constant crack width values, h. The intersection of these curves with a constant population crack-widening model (thin continuous curve marked N_{max} limit) are shown by arrows. These points mark the limit of the percolation control part of the crack linkage model, where $P^* = 1$. The final value of h, calculated for the constant population (N_{max} limit) model, corresponding to 3% dilatational volume change is shown above the "N_{max} limit" legend. The arrowed point marking $P^* = 1$ for the h = 1 x 10^{-6}m constant crack width curve is additionally marked with an "X". See text for details.

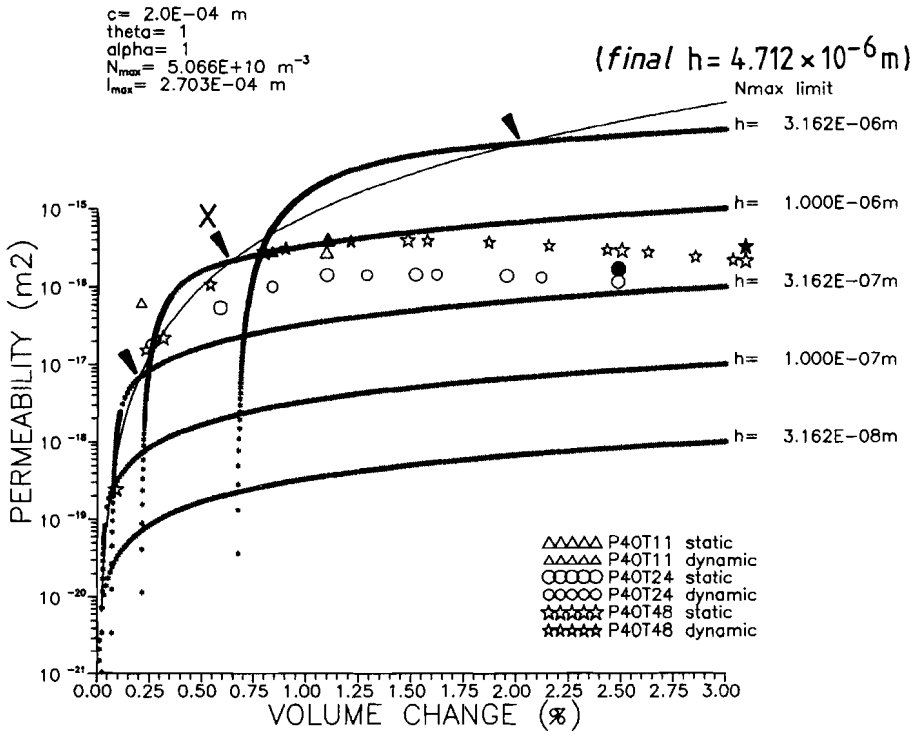

Figure 6.11. Same as for the previous Figure (6.10) but with the parameters theta and alpha (related to the crack cross sectional characteristics) set to unity. Note the minor shift in the plots with respect to the previous figure where theta = 1/2 and alpha = 2/3.

therefore seems consistent with the microstructure, including the observation that the available grain boundaries constrain the maximum crack number. However, the problem of the permeability data not following this "N_{max} limit" curve remains to be explained.

In seeking an explanation for the above discrepancies between the models and the experimentally observed permeability saturation behaviour and microstructural constraints, attention is now focussed on the crack distribution. The wide distribution of crack widths and the serial chaining observed in axial sections are not ideally consistent with the assumptions for the percolation and growth models (see Section 6.4.7). Following the arguments, set out in Section 6.3.4, covering wide distributions of bond strengths, the permeability saturation behaviour may be controlled by the narrower cracks especially where serially connected. Since most of the observed (wider) axial cracks and their chains terminate via or are cross-linked by tapered cracks of vanishing width, these narrow (tapered) cracks would certainly limit the flow and cause post-critical permeability saturation at a lower value than predicted by the present models when applied for the observed mean crack width of order 10 μm (see Figures 6.10 and 6.11).

In conclusion then, the data for the fine synthetic salt rock appears consistent with a percolation-controlled development of permeability involving grain boundary governed crack geometry (i.e. intergranular cracks of initial width ~ 1 μm) and a percolation threshold of < 0.1 % dilatant volume change. The total population of cracks was limited by the available number of grain boundaries, particularly the axial ones. Apparently after percolation was established, and the number of grain boundary cracks could no longer grow dramatically ($p \rightarrow 1$), a wide distribution of crack widths developed with progressive dilatancy, largely as a result of axial crack opening. As a result of this, permeability saturated after the initial percolating breakthrough, under the control of the narrower tapered and, non-axial, cross-linking cracks.

6.6. Percolation model vs. results on Asse salt

6.6.1. Microstructural constraints

It was shown in Chapter 3 that deformation of Asse speisesalz under dilatant conditions produced rapid growth of permeability with dilatant volume change. This growth saturated by 0.5 volume % to values around $10^{-16}m^2$, in a manner very similar to the synthetic material. The microstructural data were summarized in

Chapter 3, notably Table 3.4. Once again, the average crack spacing $<l>$ was very similar to the average grainsize, this time ~ 1.5 - 4.5 mm. Crack widths covered a broad range up to 0.2 mm. Cracks differed from the synthetic material in that many were transgranular and grain boundary cracks were more irregular in profile, following the more irregular grain shapes. The average final crack density (N_f) calculated from the microstructural data was between 1 x 10^7 and 1 x 10^8 per m^3. This requires average (penny-shaped) crack widths of between 2 x 10^{-6} and 3 x 10^{-5} m to produce the measured dilatancy.

6.6.2. Permeability development

The permeability development versus dilatancy results from the Asse salt experiments, deformed under similar conditions to the synthetic material, are drawn against the computer generated curves for the correspondingly larger crack radii, in Figures 6.12 and 6.13. A picture of permeability development can be seen which is very similar to the synthetic material behaviour. A very low percolation threshold occurs at dilatant volume changes < 0.05%, followed by rapid permeability growth, apparently following cracks of less than 10^{-6}m mean width, until the permeability saturated at ~ 0.2 vol%.

Since the mean measured crack widths in the Asse material are >> 10^{-6}m, and since the observed crack number density is 10x lower than implied by the model, the simple crack linkage model can only apply to the Asse salt during the initial percolation (network forming) stage. This stage corresponds to a very small initial dilatant volume change (< 0.1 vol%) and from Figures 6.12 and 6.13 must involve very narrow cracks (< 10^{-6}m). Once again, the crack widening model, for behaviour following the initial percolation stage, predicts reasonable final crack widths (~ 30 μm) and thus appears to offer the best explanation of the observed microstructure. However, it does not explain the post-critical permeability development (N_{max} curves, Figures 6.12 and 6.13). As for the synthetic material, it is inferred that after the critical appearance of permeability in the Asse salt (via very fine grain scale cracks), axially oriented cracks widened preferentially. However, post-critical growth of the permeability seems to have been limited by fine or tapered cross-linking cracks.

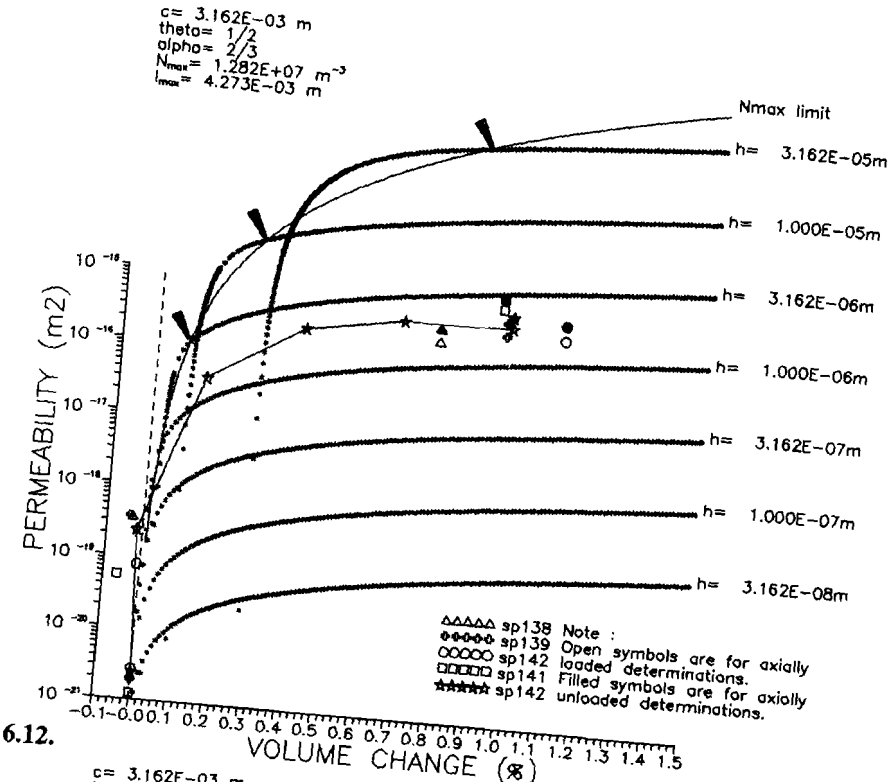

Figure 6.12.

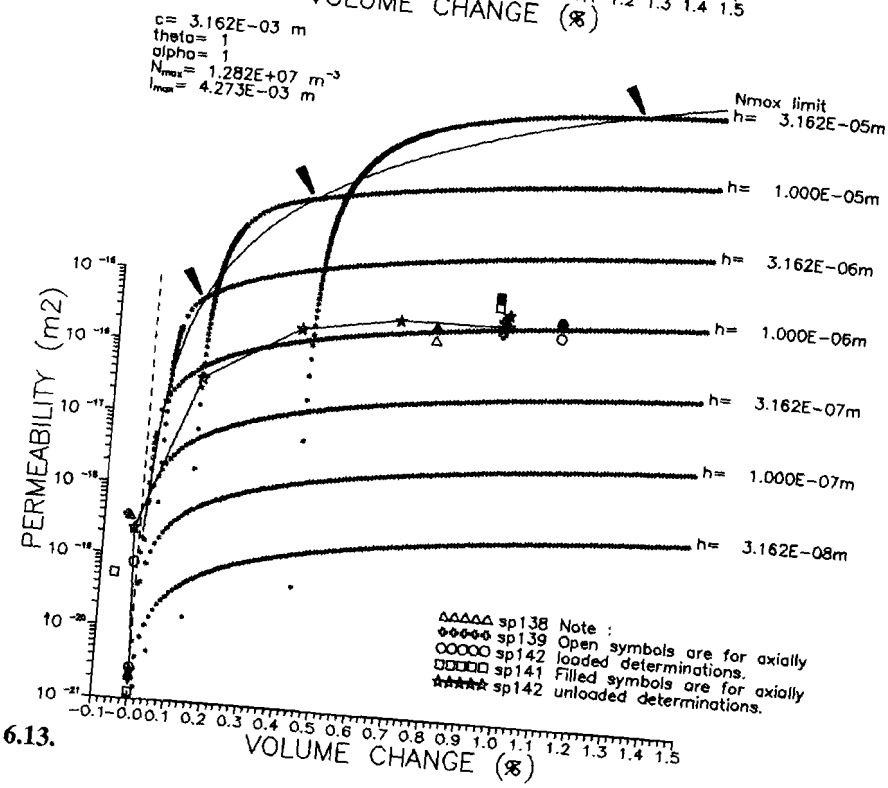

Figure 6.13.

Figure 6.12. Computer generated permeability versus dilatancy curves based on the crack linkage model (Equation 6.29). Actual data for the natural Asse speisesalz halite experiments (Chapter 3) are overlain for comparison. The (heavy) computer generated curves composed of small asterisks were drawn for the crack radius of 3.16 x 10^{-3}m and parameters indicated, for a set of constant crack width values (h). The intersection of these curves with a constant population crack-widening model (N_{max} limit) are shown by arrows. These points mark the limit of the percolation control part of the crack linkage model, where $P^* = 1$.

Figure 6.13. Same as Figure (6.12) but with the parameters theta and alpha (related to the crack cross sectional characteristics) set to unity. Note the minor shift in the plots with respect to the previous figure where theta = 1/2 and alpha = 2/3.

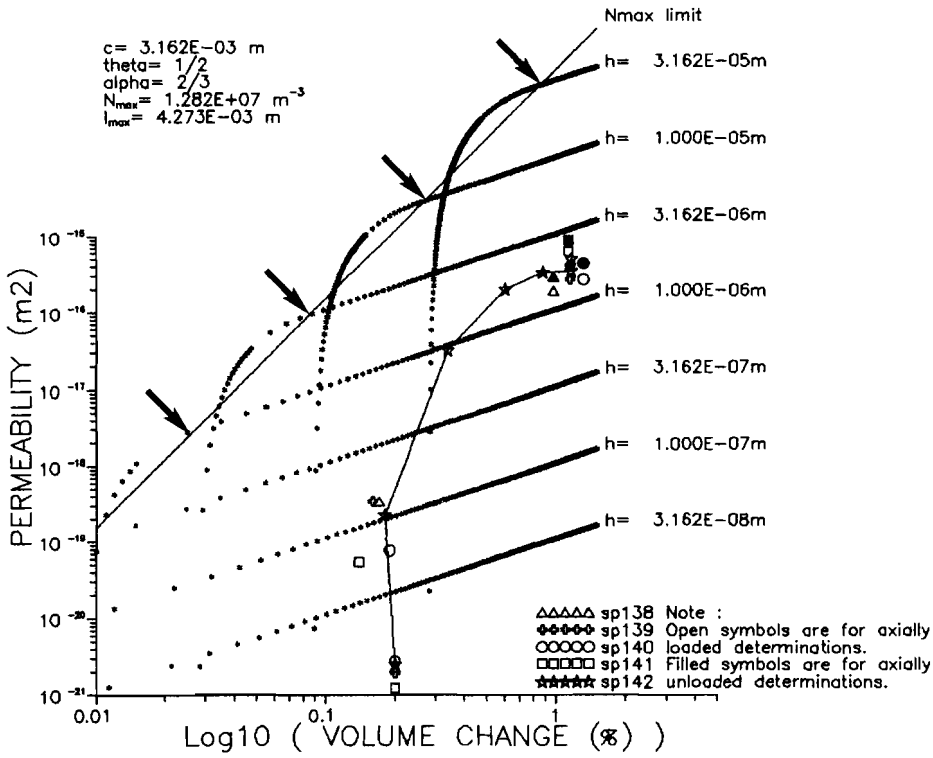

Figure 6.14. The computer generated information of Figure 6.12 plotted on logarithmic axes. The experimental data is plotted with a volume change offset of 0.2 vol% to indicate the effect of a partially connected network related to initial sample porosity. The critical behaviour is clear and suggests a percolation threshold directly at ~ 0.2 vol%. Arrows on each reference set mark $P^* = 1$ as for Figure 6.12.

6.6.3. Role of initial porosity

Unlike the synthetic material the contribution of the initial porosity may not be completely ignored in the case of the Asse salt. This is due to the microstructural arrangement of the porosity in planar arrays of tabular/spherical grain boundary inclusions, loosely comparable in form to the deformation-induced grain boundary cracks. The maximum grain boundary porosity of the Asse salt was about 0.2% and assuming this to be in planar inclusions, it could act as a partially connected network shifting the permeability development curves by this amount relative to the measured dilatancy. Such a shift has been applied to the Asse data and is shown in Figure 6.14 as a $\log_{10}\kappa$ vs. $\log_{10}$(volume change) plot. Here volume change is represented w.r.t. fully dense material and thus equals total porosity. The data imply a percolation threshold at ~ 0.2% volume change, following the critical growth form predicted by the percolation model for a crack width of ~ 3 x 10^{-5}m. It is possible then that the grain boundary inclusion structure of the Asse salt may have enhanced the critical onset of permeability, but this does not alter the conclusion that the saturation value was determined by resistive, non-axial cross link cracks.

6.7. Percolation behaviour of the salt/anhydrite composites

Chapter 5 reported data on permeability development for three suites of experiments carried out on Coarse, Medium and Fine anhydrite in salt composites under conditions where pure synthetic halite would be non-dilatant. The results will now be recalled and discussed in terms of the various percolation models introduced in Section 6.3.

6.7.1. Coarse composites

Initial permeability measurements made on the coarse sample suite showed values < $10^{-21}m^2$, similar to the pure synthetic material. The initial porosity reached values upto 0.86%. Impregnation with blue-dyed resin revealed minor porosity at clast/matrix interfaces. However, neither the salt matrix nor anhydrite clasts showed any real evidence for connected porosity or cracks (see Section 5.2.3).

The deformed samples developed significant dilatancy at all anhydrite contents, and this dilatancy increased with anhydrite content. The onset of significant deformation-induced permeability did not occur until 20-25% volume fraction of anhydrite was present. Examination of the microstructure coupled with impregnation

showed the bulk of the dilatancy to be represented by numerous axial microcracks in the anhydrite clasts (see Section 5.5). Cavitation sometimes occurred at clast/matrix interfaces which were parallel to the compression direction, and was locally accompanied by intergranular cracking in the matrix causing short range cross-linkage between clasts (see Figures 5.15b and c). This local dilatancy in the salt matrix was highly heterogeneously distributed, preventing meaningful application of the crack linkage model at the specimen scale. The fact that dilatancy and therefore fluid conductivity was concentrated in the anhydrite clasts suggests that a continuum site percolation model for packs of hard conducting spheres might be more applicable (c.f. electrical conduction in glass and metal sphere assemblages). Simple models of this type require ~ 16 vol% of conducting regions (sites) to achieve 3-D percolation, following the Scher and Zallen criterion derived from amorphous semi-conductor studies (Scher and Zallen, 1970; Zallen and Scher, 1971, see also Balberg and Binnenbaum, 1987I). Since dilatant matrix "haloes" around the anhydrite clasts are of negligible volume, this value is roughly consistent with the observed clast content of ~ 20% associated with the appearance of permeability (see Figure 5.12a). Because of uncertainties in the manner of intersection between clasts, such as clast/clast contact areas and their connectivity, no statement can be made about the magnitude of the permeability to be expected. However, since conductivity is concentrated in the anhydrite "blobs" linked more or less serially with other blobs, in the percolation backbone structure, then the permeability can be expected to saturate, with progressive dilatancy, due to limiting control at the serial connections. This behaviour was indeed observed in the more dilatant samples (see Figures 5.13a and 5.14a).

6.7.2. Medium composites

The undeformed medium composite material showed higher permeability and porosity than the synthetic pure salt material (see Section 5.4). Initial permeabilities increased significantly at ~ 15-20% anhydrite clast content (see Figures 5.11b and 5.12b). Samples with anhydrite contents > 25% had substantially higher porosity (upto 2%) observable in the salt matrix. However, optical examination and resin impregnation indicated that this was not significantly connected (see Section 5.2.3). The anhydrite clasts again appeared free from fractures, but resin did impregnate some of the clast surfaces, perhaps because of surficial damage during clast preparation. The initial permeability take off point of 15-20 volume percent anhydrite falls in the range for a hard sphere, Scher - Zallen type of continuum site-percolation model. Taking into account the apparently permeable clast surfaces, this

would appear to explain the observed compositional threshold for initial permeability.

As in the coarse suite of samples, the medium composites showed dilatancy during deformation (see Figure 5.9b). Significant deformation-induced permeability increases occurred at volume fractions greater than 10% (see Figure 5.11b). As for the coarse suite, microstructural examination showed the bulk of dilatancy to have occurred in the anhydrite clasts, though dilatant haloes were somewhat more widespread. This would suggest that superimposed on top of the hard sphere, (clast) site-percolation type of behaviour are elements of crack-linkage and growth in the salt matrix, with dilatant haloes effectively extending the clast site radius. The broad effect of this would be to lower the bulk percolation threshold from ~ 16% anhydrite content towards the values observed (~ 10%).

6.7.3. Fine composites

The undeformed fine anhydrite/halite composites exhibited higher initial permeability and porosities than the pure material (see Section 5.4). Significantly higher permeabilities were measured in samples with more than 10-15 vol% of anhydrite (see Figures 5.11c and 5.12c). Microstructural examination of material with 5-10% anhydrite showed isolated clusters of fine anhydrite particles scattered around halite grain boundaries. In contrast material with > 10% anhydrite showed a pre-existing network of clustered anhydrite particles coating the salt grains (see Figure 5.3c). In all samples, clustered anhydrite accepted an impregnating resin and was pervaded by connected interparticulate porosity.

The low anhydrite volume fraction responsible for the take off in initial permeability seen in the fine suite is somewhat lower than expected for a Scher - Zallen hard sphere continuum percolation model. This is not surprising in view of the microstructure. In particular, at the low anhydrite contents ($\leq$ 10%) the distribution of the porous clusters of anhydrite particles over the 2-D surfaces of the halite grains suggests a bulk behaviour possibly influenced by 2-D percolation via the grain boundary arrays of anhydrite clusters. The Scher - Zallen criterion for 2-D continuum site percolation is ~ 50% areal fraction of conductive relative to non-conductive material. At the low anhydrite contents, it is reasonable to assume the anhydrite clusters on grain boundaries to be ~ 1 particle diameter in thickness. Then, taking the anhydrite grainsize to be d and the halite grainsize to be S, and assuming cubic halite grains, it is easily shown that the required volume fraction of anhydrite for 2-D percolation is $[(S + \phi_c.d)^3 - S^3]/S^3$, where ϕ_c is the 2-D areal

percolation threshold (~ 0.5) and for the realistic ratio d = S/10, a volume fraction for percolation of 15.8% is thus implied. However, this is an upper bound since not all of the 2-D arrays of anhydrite clusters have to be connected to achieve bulk conductivity. Bulk conductivity will be governed by an additional percolation threshold, at a higher structural level. This percolation threshold will be similar to the (grain boundary) crack linkage threshold and thus around 1/3. Therefore the anhydrite networks may be expected to percolate and become permeable at anhydrite contents between 15.8/3 and 15.8 vol%. The 2-level percolation model therefore appears to give a reasonable explanation for the observed development of initial permeability with anhydrite content in the fine composites. The unknown conductivity of the anhydrite particle clusters (sites) prevents any permeability magnitude estimates.

Finally, the fine suite of composite samples showed little increase in permeability with deformation-induced dilatancy, except at anhydrite contents between 10-20% (see Section 5.4.2). This presumably reflects that the percolation threshold was already well exceeded even at anhydrite contents ≥ 20% in the undeformed state. At higher anhydrite contents, permeability enhancement related to dilatancy accumulating in the anhydrite networks may also have been offset by deformation-related disruption of the anhydrite network.

6.8. Conclusions

Permeability versus porosity models based on a pre-established flow network of self similar geometry are inadequate to describe the critical permeability versus dilatancy (crack porosity) relationships seen in the experiments on pure halite, both natural and synthetic (see Chapters 3 and 4). A crack-linkage/bond-percolation model successfully describes the experimental observations of rapid permeability growth to saturation after small dilatant volume changes due to grain boundary microcracking. In the post critical region, the observed crack microstructure suggests a fixed crack population with progressively widening aperture. However, due to the broadness of the actual crack width distributions and orientational correlation (preferential opening of axial cracks), the crack widening model (case b, Equation 6.32) fails quantitatively to predict the permeability development in the post-critical region. In terms of dilatant volume change, the percolation threshold for this predominantly grain boundary controlled crack linkage process in the two salts tested is very low, < 0.05 vol%. The permeable network is established before cracks have grown wider than ~ 1 μm. Beyond this the main dilatative process seems to be one of opening axial grain boundary cracks.

A continuum site-percolation model assuming random volumetric packing of impenetrable spherical objects adequately explains the threshold behaviour seen in the salt/anhydrite composite materials with respect to permeability versus volume fraction of anhydrite, when the anhydrite particles are much coarser than the halite grainsize. This applies both before and after deformation. When the anhydrite was much finer than the halite grainsize, then a combination of 2-D site-percolation along anhydrite lined grain boundaries, and 3-D bond-percolation linking these boundaries gives a reasonable, semi-quantitative, explanation of the critical dependence of starting permeabilities on anhydrite content and the subsequent development of permeability with deformation. As a general conclusion a second rigid/brittle phase present in a plastically deformable material, as in these salt/anhydrite composites, can become strongly dilated and if present in amounts > 10-15% can lead to large increases in permeability even if the matrix remains impermeable.

CHAPTER 7

Implications for Natural Rock Systems and Suggestions for Further Work

7.1. General aspects

Despite considerable microstructural evidence to the contrary, it is frequently assumed that crystal plastic deformation processes in natural rock systems generally procede in the absence of brittle processes, like microfracture, with deformation occuring to the exclusion of dilatancy and permeability development. However, the very small dilatancies seen in the present experiments on salt rocks may be quite easily achievable during natural deformation at low effective confining pressures, such as produced in the presence of a high pressure pore fluid.

The possibility of dilatancy occurring in the "fully ductile" field in materials other than salt, under laboratory conditions, is a real one. This was demonstrated almost ten years ago in the room temperature experiments of Edmond and Paterson (1972). Until now, such small dilatancies have been rarely measured in high temperature experiments in the ductile field (an exception being Fischer and Paterson, 1989) since they are beyond the resolution of most high temperature equipment. However, it is argued here that the possibility of small dilatancies and hence large increases in fluid transport capability in natural ductile deformation cannot be excluded and is even likely (see also Carter et al., 1990). This would be particularly so when one considers strain compatibility problems associated with the heterogeneous nature of geological structures, such as non-planar anastomosing shear zones (in the crust or upper mantle), where fluid (melt, H_2O, CO_2, etc.) pressures might be maintained relatively high.

Under conditions where mass transport in the fluid phase is significant, it seems likely that permeability production during dilatation will be simultaneously inhibited by crack healing effects. Whether or not this is the case will essentially be determined by the relative rates of crack production and healing/densification (see Atkinson and Meredith, 1987). This implies the existence of a field of conditions within which permeability development during ductile deformation (in the presence of a chemically active fluid phase) is feasible, and a second field (healing

dominated) in which deformation proceeds without permeability development. Clearly, in the field where dilatancy is possible a wide range of additional effects (both transient and steady state) would be brought about, e.g. dilatancy → permeability increase → aqueous fluid transport → water weakening → enhanced ductile deformation → compaction and permeability reduction → fluid pressure increase → dilatancy, and so on. Such a process may, as suggested by Brodie and Rutter (1985) and Carter et al. (1990), become self regulating and achieve a dynamic equilibrium leading to steady state deformation.

On the basis of the above arguments and speculations, it is possible to identify a number of medium and large scale deformation phenomena where creep induced dilatancy and permeability may play an important role. Three such phenomena of particular interest in the applied and pure Earth sciences are i) creep deformation in radioactive waste repositories and storage sites in salt formations, ii) the migration of partial melt in tectonically active regions of the mantle, and iii) deformation in large-scale shear zones in the lower crust and upper mantle. These will now be discussed in further detail. The present results on salt rocks are of direct relevance to the questions of waste disposal and storage in salt formations. Viewing salt as a rock analogue, the results are also relevant to other plastically deforming rock systems in the crust or upper mantle. The important analogy here is essentially a geometric one. It is that any material undergoing plastic deformation with small amounts of microcrack dilatancy will, on the basis of percolation theory, show very large increases in permeability similar to those reported here for salt rocks.

7.2. Implications for waste disposal and storage in salt formations

7.2.1. Recap of the problem

As outlined in the Introduction (Chapter 1), salt rock is widely considered as a favourable medium for the geological disposal of high-level radioactive waste. This is chiefly because of its ductility, high thermal conductivity, low permeability and self-healing capacity.

Current "radwaste" disposal concepts (for the Netherlands, see OPLA-Eindrapport Fase 1, 1989) focus on boreholes in a salt dome, operated from a conventional mine (see Figure 1.1a). Boreholes and caverns in layered salt formations are also considered as suitable sites (see Matalucci and Hunter, 1981, for the U.S. WIPP site). The principal aim for all proposed disposal concepts is to achieve long-term integrity of the seal between the waste and the hydrosphere (hence biosphere). The

fluid transport properties of the disposal formations are therefore of primary importance. Accordingly, the influence of mechanical stresses and plastic deformation produced

a) by the creation of mine galleries and boreholes, and
b) by thermal stressing caused by heat-emitting high level waste

upon host salt formations, and their fluid transport potential, forms a topic of major research effort (see Hardy and Langer, 1984, 1988 and references therein).

In addition, the influence of stress and deformation on the fluid transport properties of salt rocks is directly relevant to modelling studies in the following areas of growing activity, namely

i) the (strategic) storage of oil and gas in solution-mined caverns in salt formations, and
ii) disposal of chemical waste in solution-mined cavities.

(see Hardy and Langer, 1984, 1988 and references therein).

In this section, applied aspects relating to the way in which the permeability of salt and salt/anhydrite rocks can be influenced by deformation will be considered, making use of the experimental results described earlier. Discussion will be focussed on "radwaste" disposal in domal salt, although essentially similar arguments apply to disposal in layered salt. The implications of the present work will be considered for the so-called "normal evolution scenario" (which involves undisturbed creep closure of galleries and boreholes under essentially dry conditions, i.e. with natural brine inclusion migration only) and for the "altered evolution scenario" (which involves brine intrusion into the repository area, by one mechanism or another, followed by brine expulsion) - see Spiers et al. (1986, 1989). Finally, the implications of the present work will be briefly considered as regards the storage of fluids in solution-mined cavities.

7.2.2. Radwaste disposal: Normal evolution scenario

Permeability development around openings - The experimental results reported in this thesis are relevant to worst case repository conditions of high deviatoric stresses and strain rates, plus low hydrostatic stress. In the normal evolution scenario, such conditions are only expected to occur in the wall regions of freshly excavated or converging galleries and boreholes, with more favourable conditions pertaining in the relatively high temperature near field regions and in the far field. This has been demonstrated by Prij (1983; Prij and Vons, 1984) who carried out finite element modelling of transient and (pseudo)-steady state creep effects (including stress

deviations from the primitive hydrostatic state) produced by mining and boring, and by introduction of heat emitting waste. This modelling was carried out at several scales, namely the salt dome, gallery, and borehole scales.

Prij (1983) and Prij and Vons (1984) used creep laws for salt appropriate for low temperature dislocation glide/creep mechanisms. His results for the stress evolution around a converging gallery (at 900 m depth) have been used here to show, in equivalent stress vs. mean stress space, the stress path followed by natural, plastically deforming salt at various depths into the gallery wall. These data are plotted on a diagram taken from Spiers et al. (1989) showing the dilatancy transition for the Asse and other natural salts (see Figure 7.1). The trend of the dilatancy transition obtained from the present experiments on synthetic fine-grained halite (Chapter 4) is also presented in this figure. The stress evolution paths are drawn for three locations corresponding to depths into the gallery wall of 2.25 m, 4.3 m and 7.9 m (finite element nodes 83, 56 and 40 of Prij, 1983). Clearly the stress evolution path at 2.25 m depth enters or approaches the indicated dilatancy transition after about 100-1000 days (Figure 7.1). The deeper locations stay well within the non-dilatant field. This is consistent with observations on the starting permeabilities of natural (Asse) wall-rock material reported in Chapter 3 (see Figure 3.4), where material deeper than 3 m (from the 800 m gallery wall) appeared non-dilated and impermeable ($\kappa < 10^{-20}m^2$) while shallower material exhibited significant permeability ($\sim 10^{-17}m^2$ when measured in the laboratory in a direction perpendicular to the gallery wall; note that permeabilities may be higher in

---

Figure 7.1. Stress evolution paths (arrowed lines) predicted by finite element analyses (Prij, 1983; Prij and Vons, 1984) for a gallery wall ([40], [56], [83]) and a borehole containing heat emitting waste ([100]). The numbers denoted [X] are nodes from the analysis of Prij (1983) and Prij and Vons (1984). Nodes [40], [56] and [83] are 21, 10 and 3 metres respectively into the wall of a gallery of 3 metre radius situated at a depth of 900 m. Node [100] is 0.5 m into the wall of a vertical borehole containing heat emitting waste at a depth of 988.5 m (see inset). The stress evolution paths are plotted against a background dilatancy map for salt rock (from Spiers et al., 1989), to which the present synthetic halite data (P40T series, see Chapter 4) have been added. Note that the dilatant/non-dilatant field boundaries for natural and synthetic salt almost exactly coincide. The shaded area represents the minimum extent of the dilatant/permeable field for the anhydrite/salt composites (data from Chapter 5). Clearly, the stress evolution paths predicted for material at a depth of 3 m (node [83]) inside the gallery wall approach the dilatant field, probably entering it, after 100-1000 years. Equivalent stress is defined here as $\sigma_{eq} = (3/2\ \sigma_{ij}^{*}\sigma_{ij}^{*})^{1/2}$ and mean stress is defined $\sigma_{mean} = \sigma_{ii}/3$ where σ_{ij}^{*} is the deviatoric stress tensor and σ_{ij} is the total stress tensor.

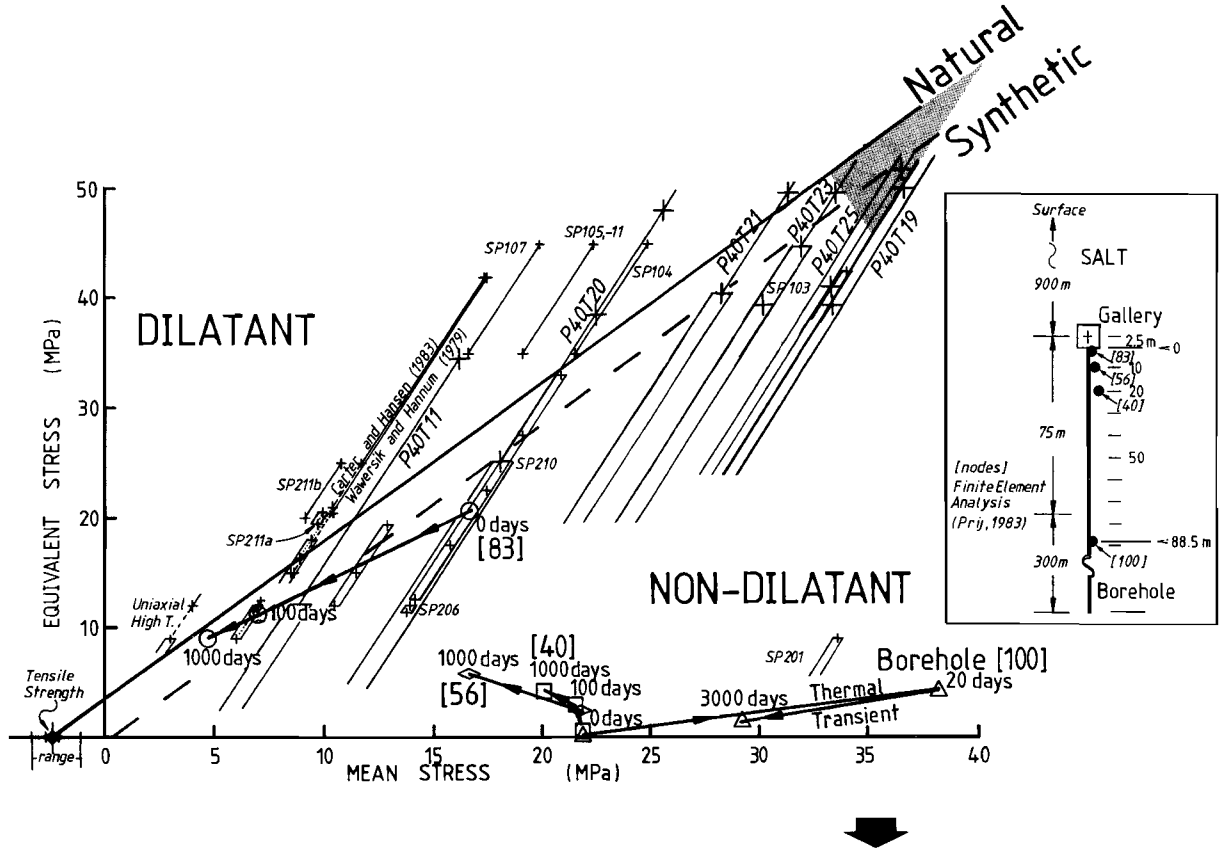
Natural
Synthetic
DILATANT
NON-DILATANT
EQUIVALENT STRESS (MPa)
MEAN STRESS (MPa)
Tensile Strength
range
Uniaxial High T.
1000 days
100 days
0 days
[83]
[56]
[40]
SP107
SP105-11
SP104
SP103
SP211b
SP211a
SP210
SP206
SP201
P40T11
P40T20
P40T21
P40T23
P40T25
P40T19
Calder and Hansen (1983)
Wawersik and Hannum (1979)
Borehole [100]
Thermal Transient
3000 days
20 days
Surface
SALT
900 m
Gallery
75 m
[nodes] Finite Element Analysis (Prij, 1983)
300 m
Borehole
[100]
≈88.5 m

directions parallel to the wall due to "exfoliation fracturing"). It therefore appears that a permeable, dilated zone about 3 m thick, containing well-connected networks of microcracks, will occur around galleries at typical repository depths of say 900 m from the surface. This conclusion is supported by the additional modelling work of Hambley (1990) - see also Mraz and Dusseault (1986). From the results on halite rock reported in Chapters 3 and 4, and from the corresponding interpretation in terms of microcrack percolation theory, it is clear that practically any dilatation in gallery wall material will exceed the percolation threshold and produce permeabilities approaching $10^{-17}m^2$ (refer Figures 6.12, 6.13).

The stress evolution around deep boreholes in salt rock containing hot waste cannisters was also analyzed by Prij (1983) and Prij and Vons (1984). The mean (hydrostatic) stress close to the borehole was found to rise rapidly, due to thermally induced stresses, and to effectively confine the cannisters, and it is easily shown using Figure 7.1 that the deviatoric stresses generated would be insufficient to cause dilatation in the salt. The evolution of the thermal stresses at a distance of 0.5 m from such a borehole, at a point remote (88.5 m) from the overlying gallery, are indicated in Figure 7.1 using Prij's finite element results (node [100]).

Effect of anhydrite - The effect of anhydrite impurities often present in salt rock is now assessed in the above framework, using the data from the experiments on salt/anhydrite composites reported in Chapter 5. In the composite experiments, the effect of anhydrite on the mechanical properties was quite large, and considerable dilatancy and permeability were developed under high pressure conditions (20 MPa) where pure salt is non-dilatant. In the case of the coarse (~ 5 mm) and medium (~ 0.5 mm) anhydrite clasts, the effect was significant for anhydrite contents greater than the site-interaction percolation limits of ~ 20 vol% and ~ 15 vol% respectively (see Section 6.7). In the case of the fine anhydrite distributed at grain boundaries, dilatancy and permeability became important (the latter even before deformation) at a compound percolation threshold of 10-15% anhydrite (see Section 6.7). The minimum extension of the dilatant field associated with the addition of these quantities of anhydrite is illustrated in Figure 7.1 (shaded area).

In the case of a gallery cut in salt containing amounts of anhydrite in excess of the above-mentioned thresholds, the presence of the anhydrite would clearly have the effect of extending the dilated/permeable zone around the gallery, presumably increasing its permeability to post-percolation values (10^{-18} to $10^{-17}m^2$, see Figs. 5.13, Fig. 7.1). More detailed quantitative statements cannot presently be made regarding this, except to say that salt containing more than 10-15% anhydrite (particularly fine grainboundary anhydrite) will be stronger, more dilatant, and will

show a wider permeable zone in gallery and borehole walls than purer salt. Clearly then, anhydrite-rich salt (> 10-15 vol%) should preferably be avoided as host material for critical regions of a radwaste repository.

Transport potential of converging backfilled galleries - In a converging backfilled gallery in anhydrite-poor salt, the permeability and transport potential of the salt backfill itself will be much higher than the dilated gallery rim, that is until the porosity of the convergence-compacted backfill falls to a few percent (see Spiers et al., 1989). This can be viewed as the long-term state of the gallery, reached after 50-100 years if backfill properties are optimal (at a depth of say 800 m - Spiers et al., 1989). From that point on, the entire system can be treated together as having a permeability less than $10^{-16}m^2$, with an increase in the cross sectional area for hydraulic flow to include the dilated ~ 3 m annulus around the gallery wall. The permeability vs. porosity relation for salt backfill at these low porosities was determined by Spiers et al. (1989) to be $\kappa \approx (2.55 \times 10^{-11})\phi^{2.57}$ for $\kappa > 10^{-17}m^2$. This is very similar to the relation governing strongly dilated salt rock (Peach et al., 1987) and can therefore be used to estimate the bulk permeability of the gallery system at long-term porosities of 2-5%. If even lower porosities are eventually reached (< 1-3% say), the backfill and wall-rock will presumably become completely impermeable as they pass through a percolation threshold similar to that seen in the natural and synthetic deformed materials (Figures 6.10 - 6.13). Notably, the presence of a small amount of brine in the backfill will enhance compaction creep and hence gallery convergence or "sealing" rates. In addition, surface energy effects in wet backfill will lead to porosity occlusion and an even faster reduction in connectivity and permeability than otherwise expected (Spiers et al., 1989).

7.2.3. Radwaste disposal: Altered evolution scenarios

Water Intrusion - In the altered evolution "worst-case scenario" involving influx of brine and repository flooding, the transport potential of galleries will again be primarily controlled by the permeability of the salt backfill, until its porosity is reduced to a few percent. At this point, the dilated gallery walls will also contribute comparable permeability and, to a first approximation, the influx/transport problem can be treated following the preceding section. Should intrusion occur, the presence of brine within galleries, is expected to enhance compaction creep in the backfill and hence convergence of the gallery (Spiers et al., 1989). Thus, the brine will ultimately be expelled by gallery closure (with or without contaminants, depending on the integrity of the wasteform). While the gallery backfill is still highly porous, this process will be controlled by the rate of gallery convergence. However, as the

gallery converges and the backfill densifies to low porosities (~ 5%), the long-term expulsion/convergence process will become controlled by the bulk permeability of the backfill/wall-rock system. Upper bounds can be placed on the long term permeability of this system in the manner outlined in the last section. However, permeabilities in a brine-flooded system may very well be lower due to pore-occlusion and crack-healing/anti-percolation effects caused by surface energy driven mass transfer through the liquid phase (see Spiers et al., 1990). In the very long term, a wet backfill/gallery system can be expected to assume the microstructure and properties of natural salt, with some fluid presumably remaining trapped (see Spiers et al., 1989). The presence of high concentrations of anhydrite above the quoted percolation thresholds could possibly inhibit this final healing process, reinforcing the idea that anhydrite-rich (> 10-15%) salt should be avoided for critical regions of a repository. Notably, anhydrite is stable, i.e. does not convert to gypsum in the presence of saturated brine at the expected repository conditions (MacDonald, 1953; see also experiments by Peach in Spiers et al., 1989).

Shear zone formation - Results of modelling the evolution of the global stress and displacement fields, in repository-bearing salt formations (see Prij, 1983; Prij and Vons, 1984, and references in Hardy and Langer, 1984, 1988), put the stress conditions well inside the non-dilatant field of Figure 7.1. However, it is conceivable that where high and sustainable pore fluid pressures are present (e.g. near a large gas/brine body in the salt, or at the contact with the cover rocks) then deformation could become locally concentrated in a dilatant shear zone progressively penetrated by fluid. In such cases, the maximum displacement would generally be limited to that provided by the global thermal expansion caused by the hot waste, and would therefore be insignificant on the scale of the salt body. However, if this deformation were to take place in a narrow shear zone, then strains of the order seen in the present experiments might be produced within the zone and dilatancy may occur giving super-percolative permeabilities up to $10^{-16}m^2$ (see Figure 6.12, 6.13). Such a zone could conceivably propagate downwards from surface faults, or outwards from gas/brine bodies, to produce a relatively rapidly creeping, wet dilatant shear zone, water-weakened by processes such as fluid-assisted diffusional creep and recrystallization (Spiers et al., 1989, 1990). The long term permeability and fluid transport/expulsion behaviour of any zone of this type will be determined by self-regulating competition (Brodie and Rutter, 1985) between hydraulically assisted dilatation and crack healing. No further quantitative statement can presently be made here, particularly if the possible effects of anhydrite content are also considered. Nonetheless, the worst case effects of such a zone can easily be incorporated into safety analysis by allowing for the existence of a generic permeable zone. This has been taken into account in recent work by Prij

and co-workers (OPLA-Eindrapport Fase 1, 1989, and safety studies referred to therein) and was shown to have no significant effect on safety considerations.

7.2.4. Storage of oil and gas

In the last 20 years, solution mined caverns in salt formations have been increasingly used both for commercial and strategic storage of oil and natural gas (Bérest and Minh, D.N., 1981; Hardy and Langer, 1984, 1988, and references therein). Such caverns are now also receiving attention as possible sites for disposal of fluid chemical wastes. Clearly, the stability and deformation behaviour of these caverns is of great importance in their design and operation. Above all there is the question, particularly for gas storage, of the ability of such caverns to hold pressure. This is determined by the fluid transport properties of the salt wall-rock which usually undergoes some convergent creep. The data reported in this thesis (Chapters 3 and 4) provide some insight into the magnitude of permeabilities which can be expected to occur in the dilatant deformation field for salt rock shown in Figure 7.1. Essentially, whenever dilatancy occurs, post-critical permeabilities of 10^{-17} to $10^{-16}m^2$ can be expected to develop (see Figures 6.12 and 6.13). This should provide a useful constraint in numerical modelling studies. The results for salt/anhydrite composites reported in Chapter 5 clearly suggest that salt rock with a grain boundary anhydrite content > 10-15% is unlikely to be a very suitable host for volatile fluid storage caverns.

7.3. Implications for dilatancy induced transport of partial melt

Partially molten regions of the Earth's mantle in tectonically active regions may be subject to transient creep effects (Carter and Kirby, 1978), and under low effective stress, where $P_{melt} \rightarrow P_{rock}$, this may lead to hydraulic fracture (Nicolas and Jackson, 1982 and Wilshire and Kirby, 1989). Under such conditions dilatation may occur, thus producing melt-carrying, non-equilibrium, grain boundary network configurations. Rates of deformation would have to be relatively high for this dilatancy to be sustained against the effects of surface energy driving forces tending to restore equilibrium, thus causing diffusive mass transport and crack healing. Sufficient fluid would also have to be available to rapidly fill the dilatant regions. Volatile fluids with higher compressibilities would be most efficient here (Wilshire and Kirby, 1989) and may very well be the path finding agents for major melt migration.

In partially molten systems, dilatant grain parting or intergranular cracking would produce similar network geometries to those seen in the pure salt experiments. Since only very small dilatant volume changes (< 0.2%) are required for percolative connectivity, permeability could presumably be established with very minor fluid input. Experimental deformation of spinel lherzolite in the presence of partial melt (Green and Borch, 1990) has already shown that steady state creep can occur together with dynamic recrystallization and dynamically stable grain boundary melt films. In nature, such networks could easily be permeable.

However, it is likely that in many partially molten systems surface tension healing effects and near equilibrium spatial distributions of fluid would dominate under hydrostatic conditions, and the expulsion of melt would be controlled by thermodynamically stable channels along grain edges and junctions (Bulau et al., 1979; Waff and Bulau, 1979; von Bargen and Waff, 1986). A multiphase grain control model of percolation, following such melt channel geometries, has been proposed by Nakano and Fujii (1989). The model was used to show that only 0.8 vol% of melt was required for macroscopic connectivity in ol/cpx/opx peridotite with at least 63% olivine. Dilatancy related to transient or steady state deformation would obviously enhance these melt transport properties.

Considerable evidence is growing for the presence of partial melt in the upper mantle to explain geophysical anomalies such as seismic low velocity and high electrical conductivity. A variety of melt filled void shapes and sizes are required to explain the observed anomalies (Shankland et al., 1981). In future, this may shed light on mechanisms of melt migration. Interestingly, local grain-scale melt flow has been proposed to explain transient displacements following earthquakes (Mavko and Nur, 1975).

7.4. Implications for deformation in the lower crust and upper mantle

It is widely believed that deformation in the tectono-metamorphic environments of the lower crust and upper mantle involve largely ductile deformation processes (intra-crystalline plasticity, diffusional flow and super plasticity) and that dilatancy is relatively unimportant. While pervasive deformation certainly occurs in such environments, e.g. the Pan African mobile belts (Coward, 1980a) and Proterozoic shear belts of Greenland (Grocott and Watterson, 1980), there is growing recognition that most of the extensional and compressional displacements in such environments tend to be accommodated in localized shear zones (Coward, 1980a, b; Brodie and Rutter, 1987). Indeed, there is a great deal of geological evidence for

crustal scale failure where extensional shear zones, thrust zones and transcurrent shear zones may penetrate through the crust and into the upper mantle (Coward, 1980a, b). Many such mylonitic shear zones are often associated with evidence of fluid movement, made apparent by mineralization, retrograde metamorphism and other geochemical changes (Beach, 1980; Brodie, 1980; Cox et al., 1986; Kerrich, 1986; Sinha et al., 1986, Sibson et al., 1988). Many steep fault zones of this type appear to be extremely long lived and frequently reactivated, hence the expression "fundamental faults" (Obee and White, 1986). Their role as a soft zone is frequently related to diffusive mass transport in the presence of fluids (White et al., 1986). Macroscopic evidence for association between fluids and large scale mylonitic shear zones in the lower crust and mantle thus raises the question of the fluid transport properties and dilatancy versus permeability relations in such ductile zones.

With regard to the mylonitic shear zones developed in quartzo-feldspathic rocks in the middle and lower crust, there is abundant meso- and micro-scale evidence for dilatancy and fluid movement. In particular, feldspars present in quartz mylonites frequently show clear evidence of brittle deformation, i.e. cracks, crack-seal and augen pull aparts. Augen overgrowths and mineral segregation by diffusive mass transfer, with isotopic redistribution affecting age determination (Ploegsma, 1989), all form geochemical evidence of fluid transport. The brittle phases are often volumetrically less important than the ductile quartz matrix but, as in the case of the results for salt-anhydrite aggregates, could be very significant with regard to permeability considerations.

Consider now the case of mylonitic shear zones developed at the base of the crust and penetrating through into the upper mantle, such as those reported in the extensional tectonic environments associated with ocean opening - see Brodie and Rutter (1987), Drury et al. (1990), Hoogerduijn Strating (1990). These authors infer that the ocean opening process involves lithospheric thinning by extensional faulting and exposure of the upper mantle material, predominantly by asymmetric detachment along low angle shear zones transecting the lithosphere (Wernicke, 1984). Microstructural evidence from many of the associated peridotite tectonites shows micro-fracture of rigid orthopyroxenes, development of amphiboles, and anastomosing zones of extremely fine-grained recrystallized olivine plus amphibole (Hoogerduijn Strating, 1990). While the mechanism of grainsize reduction is perhaps unclear (cataclasis versus metamorphic reactions), the available evidence strongly suggests the occurrence of dilatancy and fluid infiltrations during shear deformation under upper mantle conditions of 800 - 925°C, and 600 - 800 MPa for the spinel-edenite (amphibole) peridotites of Drury et al. (1990). These authors also note that syntectonic hydration may have had an important effect on the strength of

the lithosphere. The geometry and similarity between these opx/ol mylonite microstructures and the experimentally deformed halite-anhydrite aggregates would suggest that at orthopyroxene contents > 15 vol%, permeabilities could be expected to be similarly enhanced, reaching ~ $10^{-16}m^2$ if the associated dilatancy (0.2 vol% maximum) were to be achieved through microfracture.

Aside from the above-mentioned geological and microstructural evidence, several workers have suggested that deep seismic reflectors could be explained by low angle shear zones and juxtaposition of compositional variations in upper mantle material (Brodie and Rutter, 1987; Blundell, 1990). The presence of hydrous fluids (H_2O, CO_2, etc.) in such shear zones has been suggested to explain the high electrical conductivity inferred for these depths. However, it is important to note that the presence of hydrous fluids alone is not enough to explain the seismic reflection contrast (Warner, 1990a & b), despite the growing claims for the influence of arrays of fluid inclusions (from healed cracks) on seismic shear wave anisotropy at higher crustal levels (Lovell et al., 1990).

On the basis of the above considerations, it seems reasonable to conclude that, when fluid pressures are high, dilatancy can dominate over healing even under lower crustal and upper mantle conditions. By comparison with the halite/anhydrite experimental results and percolation theory, it can be expected that permeabilities above the threshold could be as high as $10^{-16}m^2$ at least transiently. Permeability values of this order would allow very rapid transport rates. In quartzo-feldspathic systems in the crust, access of fluid via such permeability, either from above or below, could lead to water weakening phenomena (inter- or intragranular) strongly decreasing the strength of the continental lower crust. Seismic pumping and mechanisms of downward fluid migration are described by Sibson et al. (1988), Sibson (1990) and Oliver et al. (1990). Similarly, access of fluid from the crust, into extensional shear zones in the upper mantle during ocean opening, could also lead to grainsize reduction plus inter-/intragranular water weakening effects coupled with downward propagation of shear even further into the upper mantle. Such effects could dramatically reduce the strength of the lithosphere and aid continental parting.

7.5. Suggestions for further work

The experiments reported in this thesis have shown that plastic deformation of salt and salt/anhydrite rocks (containing up to 30% of rigid/brittle anhydrite) can lead to dramatic increases in permeability when accompanied by minor dilatation (< 0.2

vol% for pure salt). The development of the permeability with dilatancy has been interpreted in the framework of bond percolation models (pure salt) and site percolation models (salt/anhydrite rocks). However, it will be apparent to the reader that a number of questions remain unanswered or only partly answered, and that some new questions are raised. This prompts the following suggestions for further work.

1) In Chapter 3 measurements of permeability in natural salt from gallery walls in the Asse Mine were reported. These were made in a direction parallel to the core length, i.e. normal to the gallery wall. Future laboratory measurements of permeability in gallery wall material should attempt to determine the anisotropy of permeability (i.e. the full permeability tensor), see Section 7.2.

2) Data have been reported on the time dependent decay of permeability in dilated natural salt under wet and dry, hydrostatically confined conditions (Chapter 3). However, the extrapolation of this laboratory data to predict long-term decay characteristics proved problematic due to the lack of a theoretical model. A microphysical permeability decay model is needed which relates both mechanical (creep) closure of cracks and crack healing/occlusion to environmental variables such as hydrostatic stress, pore fluid pressure and composition, brine flow rate and temperature.

3) Deformation experiments performed on fine-grained synthetic salt (Chapter 4), at room temperature and under essentially non-dilatant conditions produced samples which underwent extensive post-deformational fluid-assisted recrystallization. This occurred during the 2-3 months period of storage (at room temperature) which followed testing and resulted in growth of grains up to ~ 1 cm diameter. Such recrystallization may very well occur during long-term, low strain rate deformation under similar conditions. This should be investigated further since it may influence both creep behaviour and dilatancy/permeability development at room temperature both in experiments and in salt mines.

4) In Chapter 5, the effect of anhydrite as a rigid second phase was shown to be quite large in enhancing deformation-induced dilatancy and permeability. Further experiments of this type are needed to delineate the range of conditions and anhydrite contents under which dilatancy occurs. (Perhaps an upper confining pressure limit of 100 MPa can be placed on this, following the work of Handin and Hager (1957) and Müller and Siemes (1974) on the brittle-ductile transition of pure anhydrite at room temperature). In the present experiments, the anhydrite was disseminated or concentrated at grain boundaries. Therefore the results

obtained cannot be expected to apply to salt rock containing layered anhydrite impurities, nor do they provide information relevant to compositionally banded silicate rocks. Deformation induced permeability developed in such systems is likely to be highly anisotropic. Further experiments would be needed to gain insight into the behaviour of such systems.

5) The simple bond percolation model used in this thesis (Chapter 6) to explain the development of permeability with dilatancy, in the deformation experiments on pure salt, requires a number of refinements. In particular, the model needs to be extended to systems with widely distributed crack conductivities to quantitatively account for the saturation behaviour of the type seen in the present experiments. Anisotropic crack orientation distributions should also be taken into account. To test the applicability of this generalized theory to deformation-dilated materials it would be necessary to determine the evolution of the complete permeability tensor during deformation experiments. Deformation experiments employing non-coaxial strain paths would be of interest here, e.g. in comparing permeability development in simple shear with axial compression.

6) The present results imply that minor amounts of dilatancy occurring in natural rock systems undergoing plastic deformation can lead to large increases in permeability provided that crack healing does not predominate. In order to fully assess the implications for natural rocks it is necessary to develop bond and site percolation models which relate permeability development to the competing effects of deformation-induced dilatancy and crack closure/healing processes. Such models would enable permeability to be mapped as a function of deformation conditions (and rock composition). In principle they could be extended to include thermodynamic effects such as dihedral angle considerations and the development of non-equilibrium fluid films within grain boundaries, as recently observed in experimentally deformed rock/fluid systems (Urai et al., 1983, 1986; Green and Borch, 1990; Spiers and Schutjens, 1990; Spiers et al., 1990). Non-equilibrium effects such as these may enhance permeability as dramatically as microcracking, since they can lead to the sudden establishment of connectivity.

7) Lastly, there is a clear need for combined deformation/permeametry experiments on silicate rocks under H.P.T. conditions favouring intracrystalline plastic deformation and diffusional flow mechanisms. It would therefore be necessary to develop apparatus to measure dilatancy and permeability at these extremely difficult conditions. This has already begun in the H.P.T. Laboratory at Utrecht,

by applying the sinusoidal permeameter method (Fischer, 1987; Kranz et al., 1990; Fischer and Paterson, 1991 - in prep.). To date there is considerable disagreement over the correct analysis behind this method, but the method provides a promising means of determining the internally connected porosity and permeability continuously during deformation under high pressure-temperature conditions. The method also has the advantage of producing minimal flow-through of fluid, thus reducing sample scale mass transport effects.

REFERENCES

Adler, P.M. and Jaquin, C.G., 1987. Fractal porous media I: Longitudinal Stokes flow in random carpets. Transport in Porous Media, Vol. 2, pp. 553-569.

Adler, P.M., 1988. Fractal porous media III: Transversal Stokes flow through random and Sierpinski carpets. Transport in Porous Media, Vol. 3, pp. 185-198.

Aharony, A., Gefen, Y., Kapitulnik, A. and Murat, M., 1985. Fractal eigen-dimensionalities for percolation clusters. Phys. Rev. B, Vol. 31, pp. 4721-4722.

Aharony, A., 1986. Percolation. In: Directions in Condensed Matter Physics. Grinstein, G. and Mazenko, G. (Eds.). World Scientific, Singapore, pp. 1-50.

Aharony, A. and Feder, J. (Eds.), 1990. Fractals in physics: Essays in honour of Benoit B. Mandelbrot. North Holland, ISBN-0-444-88646-X.

Ambegaokar, V., Halperin, B.I. and Langer, J.S., 1971. Hopping conductivity in disordered systems. Phys. Rev. B, Vol. 4, No. 8, pp. 2612-2620.

American Petroleum Institute RP27, 1956. Recommended practice for determining permeability of porous media. Third edition, September 1952. Reissued August 1956.

Arzi, A.A., 1978. Critical phenomena in the rheology of partially melted rocks. Tectonophysics, Vol. 44, pp. 173-184.

Ashby, M.F., 1966. Work hardening of dispersion-hardened crystals. Phil. Mag., Vol. 14, pp. 1157-1178.

Ashby, M.F., 1970. The deformation of plastically non-homogeneous materials. Phil. Mag., Vol. 21, pp. 399-424.

Ashby, M.F., 1971. The deformation of plastically non-homogeneous alloys. In: Kelly and Nicholson, 1971, Chapter 3: Materials Science Series Applied Science, Publishers Ltd. London, ISBN 0-444-20105-Xm.

Atkinson, B.K. and Meredith, P., 1987. The theory of subcritical crack growth with applications to minerals and rocks (Chapter 4). In: Fracture Mechanics of Rock, B.K. Atkinson (Ed.). ISBN 0-12-066265-5. Academic Press London.

Auten, T.A., Davis, L.A. and Gordon, R.B., 1973. Hydrostatic pressure and the mechanical properties of NaCl polycrystals. Phil. Mag., Vol. 28, pp. 335-341.

Balberg, I., Anderson, C.H., Alexander, S. and Wagner, N., 1984. Excluded volume and its relation to the onset of percolation. Phys. Rev. B, Vol. 30, No. 7, pp. 3933-3943.

Balberg, I., 1985. "Universal" percolation-threshold limits in the continuum. Phys. Rev. B, Vol. 31, No. 6, pp. 4053-4055.

Balberg, I., 1987. Recent developments in continuum percolation. Phil. Mag. B, Vol. 56, No. 6, pp. 991-1003.

Balberg, I. and Binnenbaum, N., 1987(I). Scher and Zallen criterion: Applicability to composite systems. Phys. Rev. B, Vol. 35, No. 16, pp. 8749-8752.

Balberg, I. and Binnenbaum, N., 1987(II). Invariant properties of the percolation thresholds in the soft-core / hard-core transition. Phys. Rev. A, Vol. 35, No. 12, pp. 5174-5177.

Baes, C.F., Jr., Gilpatrick, L.O., Kitts, F.G., Bronstein, H.R. and Shor, A.J., 1983. The effect of water in salt repositories. (Final Report) ORNL-5950. Oak Ridge National Laboratory Nuclear Fuels and Waste Programs. (Union Carbide) Oak Ridge Tennesee 37830.

Beach, A., 1980. Retrogressive metamorphic processes in shear zones with special reference to the Lewisian Complex. J. Struct. Geol., Vol. 2, No. 1/2, pp. 257-263.

Ben-Mizrahi, A. and Bergman, D.J., 1981. Non-universal critical behaviour of random resistor networks with a singular distribution of conductances. J. Phys. C: Solid State Phys., Vol. 14, pp. 909-922.

Bérest, P. and Minh, D.N., 1981. Deep underground storage cavities in rocksalt: Interpretation of in-situ data from French and foreign sites. In: The Mechanical Behaviour of Salt. Proceedings of the First Conference; Hardy, H.R. Jr. and Langer, M. (Eds.). Transtech Publications 1984, IsBN 0-87849-045-0.

Bérest, P. and Ghoreychi, M., 1988. Rocksalt solution and nuclear waste disposal; The concept of overburden. In: Mechanical Behaviour of Salt II. Proc. of the Second Conference, Hannover, FRG; Hardy, H.R., Jr. and Langer, M. (Eds.). Transtech Publications 1988, ISBN 0-87849-071-X, pp. 661-674.

Bernabe, Y., 1986. The effective pressure law for permeability in Chelmsford granite and Barre granite. Int. J. Rock Mech. Min. Sci. and Geomech. Abstr., Vol. 23, No. 3, pp. 267-275.

Bernabe, Y., 1987. A wide range permeameter for use in rock physics. Int. J. Rock Mech. Min. Sci. and Geomech. Abstracts, Vol. 24, No. 5, pp. 309-315.

Blundell, D.J., 1990. Seismic images of the continental lithosphere. J. Geol. Soc. London, Vol. 147, pp. 895-913.

Bockris, J. O'M. and Reddy, A.K.N., 1970. Modern electrochemistry. Vols. 1 and 2. Plenum, New York, ISBN 0-3066-25001-2 (v.1).

Brace, W.F., Walsh, J.B. and Frangos, W.T., 1968. Permeability of granite under high pressure. J. of Geophys. Res., Vol. 73, No. 6, pp. 2225-2236.

Brace, W.F., 1972. Pore pressure in geophysics. Geophys. Monograph, Vol. 16, pp. 265-273. Am. Geophys. Union, Washington.

Brace, W.F., 1978. A note on permeability changes in geologic material due to stress. Pageoph., Vol. 116, pp. 627-633.

Brace, W.F., 1980. Permeability of crystalline and argillaceous rocks. Int. J. Rock Mech. Min. Sci. and Geomech. Abstr., Vol. 17, pp. 241-251.

Broadbent, S.E. and Hammersley, J.M., 1957. Percolation processes. I. Crystals and Mazes. Proc. Cambridge Philos. Soc., Vol. 63, pp. 629-641.

Brodie, K.H., 1980. Variations in mineral chemistry across a shear zone in phlogopite peridotite. J. Struct. Geol., Vol. 2, No. 1/2, pp. 265-272.

Brodie, K.H., 1981. Variation in amphibole and plagioclase composition with deformation. Tectonophysics, Vol. 78, pp. 385-402.

Brodie, K.H. and Rutter, E.H., 1985. On the relationship between deformation and metamorphism with special reference to the behaviour of basic rocks. In: Metamorphic Reactions: Kinetics, Textures and Deformation; Thompson, A.B. and Rubie, D.C. (Eds.). Springer, New York, pp. 138-179.

Brodie, K.H. and Rutter, E.H., 1987. Deep crustal extensional faulting in the Ivrea Zone of northern Italy. Tectonophysics, Vol. 140, pp. 193-212.

Brown, S.R., 1987. Fluid flow through rock joints: The effect of surface roughness. J. Geophys. Res., Vol. 92, No. B2, pp. 1337-1347.

Bug, A.L.R., Safran, S.A., Grest, G.S. and Webman, I., 1985. Do interactions raise or lower a percolation threshold? Phys. Rev. Lett., Vol. 55, No. 18, pp. 1896-1899.

Bug, A.L.R., Safran, S.A. and Webman, I., 1986. Continuum percolation of permeable objects. Phys. Rev. B, Vol. 33, No. 7, pp. 4716-4724.

Bulau, J.R., Waff, H.S. and Tyburczy, J.A., 1979. Mechanical and thermodynamic constraints on fluid distribution in partial melts. J. Geophys. Res., Vol. 84, No. B11, pp. 6102-6108.

Carman, P.C., 1937. Trans. Inst. Chem. Eng. London, Vol. 15, pp. 150.

Carter, N.L. and Kirby, S.H., 1978. Transient creep and semi-brittle behaviour of crystalline rocks. Pageoph., Vol. 116, pp. 807-839.

Carter, N.L. and Hansen, F.D., 1983. Creep of rocksalt. Tectonophysics, Vol. 92, pp. 275-233.

Carter, N.L., Kronenberg, A.K., Ross, J.V. and Wiltschko, D.V., 1990. Control of fluids on deformation of rocks. In: Deformation Mechanisms, Rheology and Tectonics. Knipe, R.J. and Rutter, E.H. (Eds.). Geol. Soc. London Special Publication No. 54, pp. 1-13.

Chandler, R., 1981. Transient streaming potential measurements on fluid-saturated porous structures: An experimental verification of Biot's slow wave in the quasi-static limit. J. Acoustical Soc. America, Vol. 70, No. 1, pp. 116-121.

Charlaix, E., Guyon, E. and Rivier, N., 1984. A criterion for percolation threshold in a random array of plates. Solid State Communications, Vol. 50, No. 11, pp. 999-1002.

Charlaix, E., Guyon, E. and Roux, S., 1987. Permeability of a random array of fractures of widely varying apertures. Transport in Porous Media, Vol. 2, pp. 31-43.

Charlaix, E., Kushnick, A.P. and Stokes, J.P., 1988. Experimental study of dynamic permeability in porous media. Phys. Rev. Lett., Vol. 61, No. 14, pp. 1595-1598.

Cook, G.A. (Ed.), 1961. Argon helium and the rare gases. Vol. 1, History occurrence and properties. Interscience Publishers.

Coward, M.P., 1980a. Shear zones in the Precambrian crust of southern Africa. J. Struct. Geol., Vol. 2, No. 1/2, pp. 19-27.

Coward, M.P., 1980b. The Caledonian thrust and shear zones of N.W. Scotland. J. Struct. Geol., Vol. 2, No. 1/2, pp. 11-17.

Cox, S.F., Etheridge, M.A. and Wall, V.J., 1986. The role of fluids in syntectonic mass transport, and the localization of metamorphic vein-type ore deposits. Ore Geology Reviews, Vol. 2, pp. 65-86.

Darcy, H., 1856. Les fontaines publiques de Dijon (Dalmont, Paris).

De Gennes, P.G., 1976. The physics of liquid crystals. Oxford University Press.

Deutscher, G., Zallen, R. and Adler, J., 1983(I). Percolation structures and processes. Annals of the Israel Physical Society. (ISSN 0309-8710 v.5). Adam Hilger Ltd. ISBN 0-85274-477-3.

Deutscher, G., Kapitulnik, A. and Rappaport, M., 1983(II). Percolation in metal-insulator systems. In: Percolation Structures and Processes; Deutscher, G., Zallen, R. and Adler, J. (Eds.). Annals of the Israel Physical Society, Vol. 5, pp. 207-228.

Dienes, J.K., 1978. A statistical theory of fragmentation. In: Proceedings of the 19th U.S. Symposium on Rock Mechanics. Kim, Y.S. (Ed), pp. 51-55.

Dienes, J.K., 1979. On the inference of crack statistics from observations on an outcropping. In: Proceedings of the 20th US Symposium on Rock Mechanics, Austin, Texas; Gray, K.E. (Chairman).

Dienes, J.K., 1982. Permeability, percolation and statistical crack mechanics. In: Issues in Rock Mechanics; Goodman, R.E. and Heuze, F.E. (Eds.); American Institute of Mining, Metallurgical and Petroleum Eng. New York.

Drury, M.R., Hoogerduijn Strating, E.H. and Vissers, R.L.M., 1990. Shear zone structures and microstructures in mantle peridotites from the Voltri Massif, Ligurian Alps, NW Italy. Geologie en Mijnbouw, Vol. 69, pp. 3-17.

Duba, A.G., Durham, W.B., Handin, J.W. and Wang, H.F. (Eds.) 1990. The brittle-ductile transition in rocks, "The Heard Volume". Geophys. Monogr., Vol. 56, American Geophysical Union.

Dullien, F.A.L., 1979. Porous media - fluid transport and pore structure. Academic Press. Inc., New York, London. ISBN 0-12-223650-5.

Ebeling, R. and Ashby, M.F., 1966. Dispersion hardening of copper single crystals. Phil. Mag., Vol. 13, pp. 805.

Edmond, J.M. and Paterson, M.S., 1972. Volume changes during the deformation of rocks at high pressures. Int. J. Rock Mech. Min. Sci. and Geomech. Abstr., Vol. 9, pp. 161-182.

Englman, R., Gur, Y. and Jaeger, Z., 1983. Fluid flow through a crack network in rocks. J. of Appl. Mech., Vol. 50, pp. 707-711.

Eshelby, J.D., 1957. The determination of the elastic field of an ellipsoidal inclusion, and related problems. Proc. R. Soc. London, A241, pp. 376-396.

Essam, J.W., 1980. Percolation theory. Rep. Prog. Phys., Vol. 43, pp. 833-912.

Evans, B., Fredrich, J. and Wong, T.F., 1990. The brittle-ductile transition in rocks: Recent experimental and theoretical program. In: The brittle-ductile transiton in rocks; Duba, A., Durham, W., Handin, J. and Wang, H.F. (Eds.). Geophys. Monogr., Vol. 56, American Geophysical Union.

Feder, J., 1988. Fractals. Plenum Press, New York. ISBN 0-306-42851-2.

Feng, S., Halperin, B.I. and Sen, P.N., 1987. Transport properties of continuum systems near the percolation threshold. Phys. Rev. B, Vol. 35, No. 1, pp. 197-214.

Fischer, G.J., 1987. Dilatancy and permeability in rock deformation. Unpublished Ph.D. thesis, Australian National University.

Fischer, G.J. and Paterson, M.S., 1989. Dilatancy during rock deformation at high temperatures and pressures. J. Geophys. Res., Vol. 94, No. B12, pp. 17607-17617.

Fischer, G.J. and Paterson, M.S., 1991 (in prep.). Measurement of permeability and storage capacity in rocks during deformation at high temperature and pressure. Submitted for publication "Brace Symposium Volume". Wong, F.F. and Evans, B. (Eds.). Academic Press?

Flory, P.J., 1941. J. Am. Chem. Soc., Vol. 63, pp. 3091.

Frisch, H.L., Hammersley, J.M. and Welsh, D.J.A., 1962. Monte Carlo estimates of percolation probabilities for various lattices. Phys. Rev., Vol. 136, No. 3, pp. 949-951.

Frost, H.J. and Ashby, M.F., 1982. Deformation Mechanism Maps. Pergamon Press Ltd. ISBN-0-08-029337-9 (pbk).

Gandhi, C. and Ashby, M.F., 1979. Fracture mechanism maps for materials which cleave: FCC, BCC and HCP metals and ceramics. Acta Metallurgica, Vol. 27, pp. 1565-1602.

Gangi, A.F., 1985. Permeability of unconsolidated sands and porous rocks. J. Geophys. Res., Vol. 90, No. B4, pp. 3099-3104.

Gefen, Y., Aharony, A., Mandelbrot, B.B. and Kirkpatrick, S., 1981. Solvable fractal family, and its possible relation to the backbone at percolation. Phys. Rev. Lett., Vol. 47, No. 25, pp. 1771-1774.

Gevantman, L.H. (Ed.), 1981. Physical properties data for rocksalt. U.S. Department of Commerce. Nat. Bureau of Standards, Mon. 167.

Gilabert, A., Benayad, M., Sornette, A., Sornette, D. and Vanneste, C., 1990. Conductivity and rupture in crack-deteriorated systems. J. Phys. France, Vol. 51, pp. 247-257.

Gloyna, E.F. and Reynolds, T.D., 1961. Permeability measurements of rocksalt. J. Geophys. Res., Vol. 66, No. 11, pp. 3913-3921.

Gray, W.G. and O'Neill, K., 1976. On the general equations for flow in porous media and their reduction to Darcy's law. Water Resources Research, Vol. 12, No. 2, pp. 148-154.

Green II, H.W., and Borch, R.S., 1990. The rheology and microstructure of partially molten lherzolite experimentally deformed under upper mantle pressures and temperatures. Terra Abstracts, Vol. 2, No. 2, p. 8.

Grocott, J. and Watterson, J., 1980. Strain profile of a boundary within a large ductile shear zone. J. Struct. Geol., Vol. 2, No. 1/2, pp. 111-117.

Gueguen, Y., David, C. and Darot, M., 1986. Models and time constants for permeability evolution. Geoph. Res. Lett., Vol. 13, No. 5, pp. 460-463.

Gueguen, Y., Dienes, J., 1989. Transport properties of rocks from statistics and percolation. Mathematical Geology, Vol. 21, No. 1, pp. 1-13.

Guyon, E., Mitescu, C.D., Hulin, J.-P, and Roux, S., 1989. Fractals and percolation in porous media and flows? Physica D, Vol. 38, pp. 172-178.

Halperin, B.I., Feng, S. and Sen, P.N., 1985. Differences between lattice and continuum percolation transport exponents. Phys. Rev. Lett., Vol. 54, No. 22, pp. 2391-2394.

Halperin, B.I., 1989. Remarks on percolation and transport in networks with a wide range of bond strengths. In: Fractals in Physics, Essays in Honour of Benoit B. Mandelbrot, Aharony, A. and Feder, J. (Eds.). Physica D, Vol. 38, pp. 179-183.

Hambley, D.F., 1990. Steady-state stress distribution around mined openings in salt rock. Int. J. Rock Mech. Min. Sci. and Geomech. Abstr., Vol. 27, No. 1, pp. 15-22.

Handin, J. and Hager, R.V., Jr., 1957. Experimental deformation of sedimentary rocks under confining pressure: Tests at room temperature on dry samples. Bull. Amer. Assoc. Petr. Geol., Vol. 41, pp. 1-50.

Handy, M.R., 1990. The solid-state flow of polymineralic rocks. J. Geoph. Res., Vol. 95, No. B6, pp. 8647-8661.

Hardy, H.R., Jr. and Langer, M. (Eds.), 1984. The mechanical behaviour of salt I. Proceedings of the First Conference. Transtech Publications. ISBN 0-87849-045-0.

Hardy, H.R., Jr. and Langer, M. (Eds.), 1988. The mechanical behaviour of salt II. Proceedings of the Second Conference. Transtech Publications. ISBN 0-87849-071-X.

Hassanizadeh, S.M., 1986. Derivation of basic equations of mass transport in porous media. Part. 1: Macroscopic balance laws; Part 2: Generalized Darcy's and Fick's laws. Adv. Water Resources, Vol. 9, pp. 196-222.

Heard, H.C., 1972. Steady-state flow in polycrystalline halite at pressure of 2 kilobars. In: Flow and Fracture of Rocks. Am. Geoph. Union Monograph, No. 16, pp. 191-209.

Hestir, K. and Long, J.C.S., 1990. Analytical expressions for the permeability of random two-dimensional Poisson fracture networks based on regular lattice percolation and equivalent media theories. J. Geophys. Res., Vol., 95, No. B13, pp. 21565-21581.

Hoogerduijn Strating, E.H. 1991 . The evolution of the Piemonte-Ligurian ocean. A structural study of ophiolite complexes in Liguria (NW Italy). Ph.D. thesis, University of Utrecht, Geologica Ultraiectina, No. 74.

Hsieh, P.A., Tracy, J.V., Neuzil, C.E., Bredehoeft, J.D. and Silliman, S.E., 1981. A transient laboratory method for determining the hydraulic properties of 'tight' rocks - I. Theory. Int. J. Rock Mech. Min. Sci. and Geomech. Abstracts, Vol. 18, pp. 245-252.

Jaquin, C.G. and Adler, P.M., 1987. Fractal porous media II: Geometry of porous geological structures. Transport in Porous Media, Vol. 2, pp. 571-596.

Johnson, D.L., Koplik, J. and Dashen, R., 1987. Theory of dynamic permeability and tortuosity in fluid saturated porous media. J. Fluid Mechanics, Vol. 176, pp. 379-402.

Jordan, P.G., 1986. Gefüge-entwicklung und mechanische Eigenschaften von zwei-Phasen-Aggregaten (Kalk-Halit) bei experimenteller Deformation. Ph.D. Thesis, ETH Zürich, No. 8059.

Jordan, P.G., 1987. The deformation behaviour of bimineralic limestone halite aggregates. Tectonophysics, Vol. 135, pp. 185-197.

Katz, A.J. and Thompson, A.H., 1986. Quantitative prediction of permeability in porous rock. Phys. Rev. B, Vol. 34, No. 11, pp. 8179-8181.

Kelly, A. and Nicholson, R.B. (Eds.), 1971. Strengthening methods in crystals. Materials Science Series, Applied Science Publishers Ltd. London. ISBN 0-444-20105-Xm.

Kerrich, R., 1986. Fluid transport in lineaments. Phil. Trans. Roy. Soc. London, A.317, pp. 219-251.

Kirkpatrick, S., 1971. Classical transport in disordered media: Scaling and effective medium theories. Phys. Rev. Lett., Vol. 27, No. 25, pp. 1722-1725.

Kirkpatrick, S., 1973. Percolation and conduction. Reviews of Modern Physics, Vol. 45, No. 4, pp. 574-588.

Klinkenberg, L.J., 1941. The permeability of porous media to liquids and gases. Drilling and Production Practice, pp. 200-213.

Kogut, P.M. and Straley, J.P., 1979. Distribution-induced non-universality of the percolation conductivity exponents. J. Phys. C: Solid State Phys., Vol. 12, pp. 2151-2159.

Kozeny, J., 1927. Royal Academy of Science, Vienna. Proc. Class I, Vol. 136, p. 271.

Kranz, R.L., Frankel, A.D., Engelder, T. and Scholz, C.H., 1979. The permeability of whole and jointed Barre granite. Int. J. Rock Mech. Min. Sci. and Geomech. Abstr., Vol. 16, pp. 225-234.

Kranz, R.L., Saltzman, J.S. and Blacic, J.D., 1990. Hydraulic diffusivity measurements on laboratory rock samples using an oscillating pore pressure method. Int. J. Rock Mech. Min. Sci. and Geomech. Abstr., Vol. 27, No. 5, pp. 345-352.

Kronenberg, A.K., Segall, P. and Wolf, G.H., 1990. Hydrolytic weakening and penetrative deformation within a natural shear zone. In: The brittle-ductile transition in rocks, "The Heard Volume"; Duba, A.G., Durham, W.B., Handin, J.W. and Wang, H.F. (Eds.). Geophys. Monogr., Vol. 56, pp. 21-36.

Langer, M., 1984. The rheological behaviour of rocksalt. In: The Mechanical Behaviour of Salt; Proceedings of the First Conference; Hardy, H.R., Jr. and Langer, M. (Eds.). Transtech Publications, pp. 201-240.

Last, B.J. and Thouless, D.J., 1971. Percolation theory and electrical conductivity. Physical Review Letters, Vol. 27, No. 25, pp. 1719-1721.

Laubscher, H.P., 1984. Sulfate deformation in the upper Triassic of the Belchen tunnel (Jura Mountains, Switzerland). Eclogae Geol. Helv., Vol. 77, No. 2, pp. 249-259.

Lehner, F.K., 1979. A derivation of the field equations for slow viscous flow through a porous medium. Ind. Eng. Chem. Fundam., Vol. 18, No. 1, pp. 41-45.

Lemaitre, R. and Adler, P.M., 1990. Fractal porous media IV: Three-dimensional Stokes flow through random media and regular fractals. Transport in Porous Media, Vol. 5, pp. 325-340.

Lin, W., 1982. Parametric analyses of the transient method of measuring permeability. J. Geophys. Res., Vol. 87, No. B2, pp. 1055-1060.

Long, J.C.S. and Witherspoon, P.A., 1985. The relationship of the degree of interconnection to permeability in fracture networks. J. Geophys. Res., Vol. 90, No. 84, pp. 3087-3098.

Lovell, J.H., Crampin, S. and Shepherd, T.J., 1990. Stress in the Earth's crust: The link between crustal fluids and extensive-dilatancy anisotropy. J. Geol. Soc. London, Vol. 147, pp. 971-978.

Lubensky, T.C. and Tremblay, A.M.S., 1986. Expansion for transport exponents of continuum percolating systems. Phys. Rev. B, Vol. 34, No. 5, pp. 3408-7895.

MacDonald, G.J.F., 1953. Anhydrite-gypsum equilibrium relations. American Journal of Science, Vol. 251, pp. 884-898.

Matalucci, R.V. and Hunter, T.O., 1981. Geomechanical applications for the Waste Isolation Pilot Plant (WIPP) project. In: The Mechanical Behaviour of Salt; Proceedings of the First Conference. Hardy, H.R., Jr. and Langer, M. (Eds.). Transtech Publications, 1984, ISBN 0-87849-045-0, pp. 791-812.

McCaig, A.M. and Knipe, R.J., 1990. Mass-transport mechanisms in deforming rocks: Recognition using microstructural and microchemical criteria. Geology, Vol. 18, pp. 824-827.

Mavko, G. and Nur, A., 1975. Melt squirt in the asthenosphere. J. Geophys. Res., Vol. 80, No. 11, pp. 1444-1448.

Mraz, D.Z. and Dusseault, M.B., 1986. Effects of geometry on the bearing capacity of pillars in salt rock. Presented at Can. Inst. of Min., RMSCC Workshop, Saskatoon, Canada.

Müller, P. and Siemes, H., 1974. Festigkeit, Verformbarkeit und Gefügeregelung von Anhydrit - Experimentelle Stauchverformung unter Manteldrucken bis 5 kbar bei Temperaturen bis 300°C. Tectonophysics, Vol. 23, pp. 105-127.

Nakano, T. and Fujii, N., 1989. The multiphase grain control percolation: Its implication for a partially molten rock. J. Geophys. Res., Vol. 94, No. B11, pp. 15653-15661.

Nangrani, K. and Gerteisen, S., 1985. Conductive composites blunt E.M.I. effects. Res. Dev., July, pp. 60-63.

National Academy of Sciences, U.S., 1957. The disposal of radioactive waste on land. National Research Council, Report of the Committee on Waste Disposal of the Division of Earth Sciences, April 1957.

Neuzil, C.E., Cooley, C., Silliman, S.E., Bredehoeft, J.D. and Hsieh, P.A., 1981. A transient laboratory method for determining the hydraulic properties of 'tight' rocks - II. Application. Int. J. Rock Mech. Min. Sci. and Geomech. Abstr., Vol. 18, pp. 253-258.

Nicolas, A. and Poirier, J.P., 1976. Crystalline plasticity and solid state flow in metamorphic rocks. John Wiley & Sons Ltd., London. ISBN 0-471-63791-2.

Nicolas, A. and Jackson, M., 1982. High temperature dikes in peridotites: Origin by hydraulic fracturing. J. Petrology, Vol. 23, Part 4, pp. 568-582.

Nolte, D.D., Pyrak-Nolte, L.J. and Cook, N.G.W., 1989. The fractal geometry of flow paths in natural fractures in rock and the approach to percolation. Pageoph., Vol. 131, Nos. 1/2, pp. 111-138.

Nur, A. and Byerlee, J.D., 1971. An exact effective stress law for elastic deformation of rock with fluids. J. Geophys. Res., Vol. 76, No. 26, pp. 6414-6419.

Obee, H.K. and White, S.H., 1986. Microstructural and fabric heterogeneities in fault rocks associated with a fundamental fault. Phil. Trans. Royal Soc. London, A317, pp. 99-109.

Oliver, N.H.S., Valenta, R.K. and Wall, V.J., 1990. The effect of heterogeneous stress and strain on metamorphic fluid flow, Mary Kathleen, Australia, and a model for large scale fluid circulation. J. Metamorphic Geol., Vol. 8, pp. 311-331.

Onsager, L., 1949. Ann. N.Y. Acad. Sci., Vol. 51, p. 627.

OPLA - Eindrapport Fase 1, 1989. Onderzoek naar geologische opberging van radioactief afval in Nederland. Commissie Opberging te Land (OPLA). Eindrapport Fase 1, mei 1989. Ministerie van Economische Zaken, Den Haag. 130 pp met 2 bijlagen.

Paterson, M.S., 1969. Ductility of rocks. In: Physics of Strength and Plasticity. Argon, A.S. (Ed.). M.I.T. Press, Cambridge, Mass., pp. 377-392.

Paterson, M.S., 1978. Experimental rock deformation: The brittle field. Springer-Verlag Berlin, ISBN 3-540-08835-0, New York, ISBN 0-387-08835-0.

Peach, C.J. and Lisle, R.J., 1979. A Fortran IV program for the analysis of tectonic strain using deformed elliptical markers. Computers and Geosciences, Vol. 5, pp. 325-334.

Peach, C.J., Spiers, C.J., Tankink, A.J. and Zwart, H.J., 1987. Fluid and ionic transport properties of deformed salt rock. European Communities - Commission, Nuclear Science and Technology Series EUR-10926, ISBN 92-825-6921-7.

Pike, G.E. and Seager, C.H., 1974. Percolation and conductivity; a computer study. Phys. Rev. B, Vol. 10, No. 4, pp. 1421-1447.

Pike, R. and Stanley, H.E., 1981. Order propagation near the percolation threshold. J. Phys. A: Math. Gen., Vol. 14, L169-L177.

Ploegsma, M., 1989. Shear zones in the west Uusimaa area, SW Finland. Ph.D. Thesis, Vrije Universiteit te Amsterdam.

Price, R.H., 1982. Effects of anhydrite and pressure on the mechanical behaviour of synthetic rocksalt. Geophys. Res. Lett., Vol. 9, No. 9, pp. 1029-1032.

Prij, J., 1983. Creep behaviour of a salt dome with a repository. Stichting Energieonderzoek Centrum Nederland, Petten, april 1983, ECN 83-063.

Prij, J. and Vons, L.H., 1984. Numerical and experimental investigations on the time dependent behaviour of a salt dome with a high-level waste repository. In: Scientific Basis for Nuclear Waste Management VII. McVay, G.L. (Ed.). Materials Research Society Symposia Proceedings, Vol. 26, pp. 1-9.

Pudewills, A., 1988. Thermomechanical calculations for a HLW borehole. In: Mechanical Behaviour of Salt II; Proceedings of the Second Conference; Hardy, R.H., Jr. and Langer, M. (Eds.). Transtech Publications, ISBN 0-87849-071-X.

Reed-Hill, R.E., 1973. Physical metallurgy principles (2nd edition). Van Nostrand-Reinhold. ISBN 0-442-26868-8.

Roberts, J.N. and Schwartz, L.M., 1985. Grain consolidation and electrical conductivity in porous media. Phys. Rev. B, Vol. 31, No. 9, pp. 5990-5997.

Robin, P.F., 1973. Note on effective pressure. J. Geophys. Res., Vol. 78, No. 14, pp. 2434-2437.

Rolnik, H.I.A., 1988. High-level waste repository in rock salt: Suitable rheological forms. In: Mechanical Behaviour of Salt II; Proceedings of the Second Conference. Hardy, H.R., Jr. and Langer, M. (Eds.). Transtech Publications, 1988, ISBN 0-87849-071-X, pp. 625-643.

Ross, J.V., Bauer, S.J. and Hansen, F.D., 1987. Textural evolution of synthetic anhydrite-halite mylonites. Tectonophysics, Vol. 140, pp. 307-326.

Rubie, D.C., 1990. Reaction-enhanced deformability. In: Deformation processes in minerals, ceramics and rocks; Barber, D.J. and Meredith, P.G. (Eds.); Miner. Soc. London, Unwin Hyman London, ISBN 0-04-445508-5, pp. 262-292.

Rutter, E.H. and Brodie, K.H., 1985. The permeation of water into hydrating shear zones. In: Advances in Physical Geochemistry; Thompson, A.B. and Rubie, D.C. (Eds.). Springer, Berlin, pp. 242-250.

Rutter, E.H., 1986. On the nomenclature of mode of failure transitions in rocks. Tectonophysics, Vol. 122, pp. 381-387.

Sanyal, S.K., Pirnie III, R.M., Chen, R.O. and Marsden, S.S., Jr., 1972. A novel liquid permeameter for measuring very low permeability. Soc. of Petr. Eng. J., pp. 206-209.

Scher, H. and Zallen, R., 1970. Critical density in percolation processes. J. Chem. Phys., Vol. 53, pp. 3759-3761.

Seager, C.H. and Pike, G.E., 1974. Percolation and conductivity; A computer study II. Phys. Rev. B., Vol. 10, No. 4, pp. 1421-1447.

Shankland, T.J., O'Connell, R.J. and Waff, H.S., 1981. Geophysical constraints on partial melt in the upper mantle. Reviews of Geophysics and Space Physics, Vol. 19, No. 3, pp. 394-406.

Shante, V.K.S. and Kirkpatrick, S., 1971. An introduction to percolation theory. Adv. in Physics, Vol. 20, Nos. 83-88, pp. 325-357.

Sheng, P. and Zhou, M.Y., 1988. Dynamic permeability in porous media. Phys. Rev. Lett., Vol. 61, No. 14, pp. 1591-1594.

Sibson, R.H., Robert, F. and Poulsen, K.H., 1988. High-angle reverse faults, fluid pressure cycling, and mesothermal gold-quartz deposits. Geology, Vol. 16, pp. 551-555.

Sibson, R.H., 1990. Conditions for fault-valve behaviour. In: Deformation Mechanisms, Rheology and Tectonics; Knipe, R.J. and Rutter, E.H. (Eds.). Geol. Soc. London Special Publication, No. 54, pp. 15-28.

Sinha, A.K., Hewitt, D.A. and Rimstidt, J.D., 1986. Fluid interaction and element mobility in the development of mylonites. Geology, Vol. 14, pp. 883-886.

Skrotzki, W. and Haasen, P., 1988. The role of cross slip in the steady state creep of salt. In: The Mechanical Behaviour of Salt II; Proceedings of the Second Conference; Hardy, H.R., Jr. and Langer, M. (Eds.). Transtech Publications, ISBN 0-87849-071-X.

Sornette, D., 1988. Critical transport and failure in continuum crack percolation. J. Phys. France, Vol. 49, pp. 1365-1377.

Spiers, C.J., Urai, J.L., Lister, G.S., Boland, J.N. and Zwart, H.J., 1986. The influence of fluid-rock interaction on the rheology of salt rock. European Communities - Commission, Nuclear Science and Technology Series. EUR-10399. ISBN 92-825-6214-X.

Spiers, C.J., Urai, J.L. and Lister, G.S., 1988. The effect of brine (inherent or added) on rheology and deformation mechanisms in salt rock. In: The Mechanical Behaviour of Salt II; Proceedings of the Second Conference; Hardy, H.R., Jr. and Langer, M. (Eds.). Transtech Publications, ISBN 0-87849-071-X.

Spiers, C.J., Peach, C.J., Brzesowsky, R.H., Schutjens, P.M.T.M., Liezenberg, J.L. and Zwart, H.J., 1989. Long-term rheological and transport properties of dry and wet salt rocks. European Communities - Commission, Nuclear Science and Technology Series. EUR 11848. ISBN 92-825-9191-3.

Spiers, C.J. and Schutjens, P.M.T.M., 1990. Densification of crystalline aggregates by fluid-phase diffusional creep. In: Deformation Processes in Mineral Ceramics and Rocks; Barber, D.J. and Meredith, P.G. (Eds.). Miner. Soc. London. Unwin Hyman London. ISBN 0-04-445088-5.

Spiers, C.J., Schutjens, P.M.T.M., Brzesowsky, R.H., Peach, C.J., Liezenberg, J.L. and Zwart, H.J., 1990. Experimental determination of constitutive parameters governing creep of rocksalt by pressure solution. In: Deformation Mechanisms, Rheology and Tectonics. Knipe, R.J. and Rutter, E.H. (Eds.). Geol. Soc. London, Special Publication, No. 54, pp. 215-227.

Stanley, H.E., 1977. Cluster shapes at the percolation threshold: An effective cluster dimensionality and its connection with the critical-point exponents. J. Phys. A: Math. Gen., Vol. 10, No. 11, L211-L220.

Stanley, H.E. and Coniglio, A., 1984. Flow in porous media: The "backbone" fractal at the percolation threshold. Phys. Rev. B, Vol. 29, No. 1, pp. 522-524.

Stauffer, D., 1979. Scaling theory of percolation clusters. Physics Reports, Vol. 54, No. 1, pp. 1-74.

Stauffer, D., 1985. Introduction to percolation theory. Taylor and Francis London. ISBN 0-85066-315-6.

Straley, J.P., 1981. Threshold behaviour of random resistor networks: a synthesis of theoretical approaches. J. Phys. C: Solid State Physics, Vol. 15, pp. 2333-2341.

Straley, J.P., 1982. Threshold behaviour of random resistor networks: a synthesis of theoretical approaches. J. Phys. C: Solid State Physics, Vol. 15, pp. 2333-2341.

Sutherland, H.J. and Cave, S.P., 1980. Argon gas permeability of New Mexico rock salt under hydrostatic compression. Int. J. Rock Mech. Min. Sci. and Geomech., Abstr., Vol. 17, pp. 281-288.

Tanaka, K., Mori, T. and Nakamura, T., 1970. Cavity formation at the interface of a spherical inclusion in a plastically deformed matrix. Phil. Mag., Vol. 21, pp. 267-279.

Touret, J.L.R., 1986. Fluid inclusions in rocks from the lower continental crust. In: The Nature of the Lower Continental Crust; Dawson, J.B., Carswell, P.A., Hall, J. and Wedepohl, J.H. (Eds.). Special Publ. Geol. Soc. London, Vol. 24, pp. 1661-172.

Tremblay, A.-M.S., Machta, J., 1989. Finite-size effects in continuum percolation. Phys. Rev. B, Vol. 40, No. 7, pp. 5131-5139.

Trimmer, D., Bonner, B., Heard, H.C. and Duba, A., 1980. Effect of pressure and stress on water transport in intact and fractured gabbro and granite. J. Geophys. Res., Vol. 85, No. B12, pp. 7059-7071.

Trimmer, D., 1982. Laboratory measurements of ultra low permeability of geologic materials. Rev. Sci. Instrum., Vol. 53, No. 8, pp. 1246-1254.

Turcotte, D.L. and Schubert, G., 1982. Geodynamics: Applications of continuum physics to geological problems. John Wiley & Sons, New York.

Tyč, S. and Halperin, B.I., 1989. Random resistor network with an exponentially wide distribution of bond conductances. Phys. Rev. B., Vol. 39, No. 1, pp. 877-880.

Urai, J.L., 1983. Water-assisted dynamic recrystallization and weakening in polycrystalline bischofite. Tectonophysics, Vol. 96, pp. 125-157.

Urai, J.L., Spiers, C.J., Zwart, H.J. and Lister, G.S., 1986. Weakening of rocksalt by water during long-term creep. Nature, Vol. 324, No. 6097, pp. 554-557.

Urai, J.L., Spiers, C.J., Peach, C.J., Franssen, R.C.M.W. and Liezenberg, J.L., 1987. Deformation mechanisms operating in naturally deformed halite rocks as deduced from microstructural investigations. Geol. Mijnbouw, Vol. 66, pp. 165-176.

Verruijt, A., 1982. Groundwater flow (2nd edition). Macmillan Press London. ISBN 0-333-32959-7 (pbk).

Von Bargen, N. and Waff, H.S., 1986. Permeabilities, interfacial areas and curvatures of partially molten systems: Results of numerical computations of equilibrium microstructures. J. Geophys. Res., Vol. 91, No. B9, pp. 9261-9276.

Waff, H.S. and Bulau, J.R., 1979. Equilibrium fluid distribution in an ultramafic partial melt under hydrostatic stress conditions. J. Geophys. Res., Vol. 84, No. B11, pp. 6109-6114.

Walder, J. and Nur, A., 1986. Permeability measurement by the pulse-decay method: Effects of poroelastic phenomena and non-linear pore pressure diffusion. Int. J. Rock Mech. Min. Sci. and Geomech. Abstr., Vol. 23, No. 3, pp. 225-232.

Walls, J.D., Nur, A.M. and Bourbie, T., 1982. Effects of pressure and partial water saturation on gas permeability in tight sands: Experimental results. J. of Petroleum Techn. (April 1982), No. 34, pp. 930-936.

Walsh, J.B. and Grosenbaugh, M.A., 1979. A new model for analyzing the effect of fractures on compressibility. J. Geophys. Res., Vol. 84, No. B7, pp. 3532-3536.

Walsh, J.B., 1981. Effect of pore pressure and confining pressure on fracture permeability. Int. J. Rock Mech. Min. Sci. and Geomech. Abstr., Vol. 18, pp. 429-435.

Warner, M.R., 1990a. Absolute reflection coefficients from deep seismic reflections. Tectonophysics, Vol. 173, pp. 15-23.

Warner, M.R., 1990b. Basalts, water or shear zones in the lower continental crust? Tectonophysics, Vol. 173, pp. 163-173.

Watson, E.B. and Brenan, J.M., 1987. Fluids in the lithosphere. 1. Experimentally-determined wetting characteristics of CO_2-H_2O fluids and their implications for fluid transport, host-rock physical properties, and fluid inclusion formation. Earth and Planet. Sci. Lett., Vol. 85, pp.497-515.

Wawersik, W.R. and Hannum, D.W., 1980. Mechanical behaviour of New Mexico rocksalt in triaxial compression up to 200°C. J. Geophys. Res., Vol. 85, No. B2, pp. 891-900.

Wawersik, W.R. and Zeuch, D.H., 1986. Modelling and mechanistic interpretation of creep of rocksalt below 200°C. Tectonophysics, Vol. 121, pp. 125-152.

Webman, I., Jortner, J. and Cohen, M.H., 1977. Critical exponents for percolation conductivity in resistor networks. Physical Review B., Vol. 16, No. 6, pp. 2593-2596.

Wernicke, B., 1984. Uniform-sense normal simple shear of the continental lithosphere. Can. J. Earth Sci., Vol. 22, pp. 108-125.

White, S.H. and Knipe R.J., 1978. Transformation- and reaction-enhanced ductility in rocks. J. Geol. Soc. London, Vol. 135, pp. 315-316.

White, S.H. and White, J.C., 1981. On the structure of grain boundaries in tectonites. Tectonophysics, Vol. 78, pp. 613-628.

White, S.H., Bretan, P.G. and Rutter, E.H., 1986. Fault-zone reactivation: kinematics and mechanisms. Phil. Trans. Royal Soc. London, A317, pp. 81-97.

Wilke, S., Guyon, E., de Marsily, G., 1985. Water penetration through fractured rocks: Test of a tridimensional percolation description. Mathem. Geol., Vol. 17, pp. 17-27.

Wilshire, H.G. and Kirby, S.H., 1989. Dikes, joints and faults in the upper mantle. Tectonophysics, Vol. 161, pp. 23-31.

Wong, P.Z., Koplik, J. and Tomanic, J.P., 1984. Conductivity and permeability of rocks. Phys. Rev. B, Vol. 30, No. 11, pp. 6606-6614.

Wong, P.Z., 1988. The statistical physics of sedimentary rock. Physics Today, Vol. 41, No. 12, pp. 24-32. (American Institute of Physics).

Yamamoto, T. and Turgut, A., 1988. Acoustic wave propagation through porous media with arbitrary pore size distributions. J. Acoustical Soc. America, Vol. 83, No. 5, pp. 1744-1751.

Zallen, R. and Scher, H., 1971. Percolation on a continuum and the localization-delocalization transition in amorphous semi-conductors. Phys. Rev. B, Vol. 4, No. 12, pp. 4471-4479.

Zoback, M.D. and Byerlee, J.D., 1975. The effect of microcrack dilatancy on the permeability of Westerly granite. J. Geophys. Res., Vol. 80, No. 5, pp. 752-755.

NEDERLANDSE SAMENVATTING

De vloeistoftransporteigenschappen van gesteenten zijn goed bekend onder hydrostatische omstandigheden, maar er is weinig bekend omtrent deze eigenschappen tijdens kristal-plastische deformatie. Dit soort gegevens zijn echter nodig als basis voor de kennisvorming inzake het opbergen van radioactief afval in zoutformaties. Zij zijn ook nodig voor een beter begrip van gesteentedeformatie, de ontwikkeling van schuifzones en de daarmee gepaard gaande beweging van vloeistoffen, èn metamorfose en verertsing, in de diepe korst en zelfs in de bovenmantel.

Dit onderzoek betreft de ontwikkeling van fundamenteel begrip inzake de invloed van kristal-plastische vervorming op dilatatie (volumevergroting) en de ontwikkeling van permeabiliteit in zout- en zout-anhydrietgesteenten. Het onderzoek is primair experimenteel gericht en tracht de invloed van vervorming op permeabiliteit te verklaren in termen van percolatie-theorie, zoals deze in de vaste stof fysica wordt gehanteerd. De resultaten hebben direct betrekking op het gedrag van zoutgesteenten in afvalopberg-systemen, èn door zout als een analoog materiaal te beschouwen, verschaffen zij tevens inzicht in de effecten van plastische vervorming op de vloeistoftransporteigenschappen van kristallijne gesteenten in het algemeen.

In **Hoofdstuk 1** worden de te onderzoeken vraagstellingen geintroduceerd. **Hoofdstuk 2** beschrijft de experimentele apparatuur en methoden, die werden gebruikt en ontwikkeld gedurende het onderzoek. Het in **Hoofdstuk 3** beschreven onderzoek is in hoofdzaak gericht op de invloed van kristal-plastische vervorming op dilatatie en de ontwikkeling van permeabiliteit in natuurlijke zoutgesteenten (Asse Speisesalz, Duitsland), onder voor opslag relevante omstandigheden. Het intacte uitgangsmateriaal heeft een extreem lage permeabiliteit ($< 10^{-21} m^2$). In gedeformeerd materiaal uit de wanden van mijn-gangen zijn waarden tot $10^{-16} m^2$ gemeten. In tri-axiale vervormingsexperimenten bij kamertemperatuur leidde geringe dilatatie (< 0.2 vol%) tijdens kristal-plastische deformatie tot extreem snelle initiële toename van permeabiliteit. Dit suggereert kritiek gedrag (plotseling ontstaan van permeabiliteit), zoals door percolatie-theorie beschreven. Microstructurele waarnemingen duiden erop dat dilatatie gepaard gaat met micro-barsten, zowel langs als door de korrels. Aanvullende hydrostatische experimenten, uitgevoerd met droog gedilateerd materiaal, laten zien dat de door vervorming geïnduceerde permeabiliteit afhangt van de druk, op een wijze die het best kan worden verklaard door een elastisch micro-barst sluitingsmodel. Soortgelijke hydrostatische experimenten met gedilateerd materiaal, zowel droog als nat, laten zien dat de permeabiliteit afneemt met de tijd. De

snelheid, waarmee permeabiliteit afneemt, is groter in nat materiaal, waarschijnlijk als gevolg van het dichttrekken van micro-barsten.

Hoofdstuk 4 beschrijft tri-axiale compressie-experimenten, ontworpen om de invloed te bepalen van plastische deformatie op zowel dilatatie als op de ontwikkeling van permeabiliteit in fijnkorrelige synthetische zoutgesteenten; bij kamertemperatuur, alzijdige drukken (P_c) in de orde van 5-20 MPa en vervormingssnelheden ($\dot{\varepsilon}$) van ~ 4 x $10^{-5}s^{-1}$ tot een totale vervorming van ~ 15%. De monsters vertonen mechanisch gedrag, vergelijkbaar met het Asse zout. Zij zijn echter enigszins zwakker en vertonen meer dilatatie (tot 3 vol%) in het dilatatie-bereik (P_c < 18 MPa), terwijl ze enigszins sterker zijn in het dilatatie-vrije bereik (P_c > 18 MPa). Microstructurele waarnemingen bevestigen dat vervorming plaatsvond door het glijden van dislocaties. In het dilatatie-bereik ging vervorming gepaard met de ontwikkeling van micro-barsten langs korrelgrenzen. Evenals tijdens de experimenten met het Asse materiaal produceert geringe dilatatie extreem snelle initiële toename in permeabiliteit ($\leq 10^{-21}m^2$ tot ~ 2 x $10^{-16}m^2$), wederom duidend op kritiek gedrag. De kleine verschillen, in mechanisch en dilatatie gedrag, die tussen synthetische en natuurlijke zouten zijn waargenomen, worden verklaard door verschillen in korrelgrootte.

Hoofdstuk 5 is een aanvulling op het werk aan synthetisch zout (Hoofdstuk 4) om systematisch de invloed van gecontroleerde toegevoegde hoeveelheden anhydriet, als een vaste tweede fase, te bepalen. Tri-axiale compressie-experimenten zijn uitgevoerd met monsters van synthetische zoutgesteenten met 0-35 vol% anhydriet in één van drie korrelgrootten; t.w. 10x, 1x of 0.1x de haliet matrix korrelgrootte van ~ 350 μm. Alle experimenten zijn uitgevoerd bij kamertemperatuur, $\dot{\varepsilon}$ = 4 x $10^{-5}s^{-1}$ en P_c = 20 MPa (d.w.z. binnen het dilatatie-vrije bereik voor zuiver synthetisch zout) tot totale vervormingen van ~ 15%. Alle monsters met $\geq$ 10 vol% anhydriet vertonen significante dilatatie (tot 2.5 vol%). Alle typen monsters vertonen bovendien een tendens tot toename van vloeispanning en dilatatie (bij constante vervorming) bij toenemend anhydrietgehalte. Zoals waargenomen bij de onderzochte zuivere zoutgesteenten, werd dilatatie in eerste instantie vergezeld door extreem snelle ontwikkeling van permeabiliteit (van $\leq 10^{-21}m^2$, bij laag anhydrietgehalte, tot ~ 3 x $10^{-17}m^2$ in de meeste gevallen) hetgeen in overeenstemming is met kritiek gedrag. Microstructurele studies geven aan dat de zoutmatrix van alle monsters vervormt door dislocatieglij-mechanismen met beperkte dilatatie langs de korrelgrenzen. Daarentegen vertoont de anhydriet altijd uitgebreide vorming van micro-barsten en/of dilatatie. De tendens tot toename van vloeispanningen met anhydrietgehalte wordt toegeschreven aan, met name, vervormingsconcentratie in het

zout en, in mindere mate, aan rigide deeltjes-verharding, zoals in sommige metalen wordt waargenomen.

In **Hoofdstuk 6** worden de experimentele resultaten vergeleken met microfysische modellen. In eerste instantie wordt een overzicht gegeven van klassieke Darciaanse vloeimodellen, die permeabiliteit in verband brengen met volledig onderling verbonden porositeit. Aangetoond wordt dat deze modellen niet toepasbaar zijn op de experimentele gegevens. Vervolgens worden de beginselen van moderne percolatie-theorie geintroduceerd en gebruikt om een micro-barst verbindingsmodel te ontwikkelen, dat de kritieke ontwikkeling (het plotselinge optreden) voorspelt van permeabiliteit met dilatatie tijdens vervorming. Als dit "binding percolatie" model wordt toegepast op de waargenomen barst-microstructuur verklaart het op succesvolle wijze initiële snelle toename van permeabiliteit in zowel het Asse als in het zuiver synthetisch zout. Door gedetaileerde vergelijking van het model met de resultaten van deze materialen wordt afgeleid dat ononderbroken verbinding van micro-barsten (de percolatie drempel) optreedt bij minieme dilatanties van < 0.05 vol% en geassocieerd wordt met zeer smalle (< 1 μm) micro-barsten langs korrelgrenzen. Verzadiging van permeabiliteit na de kritieke ontwikkelingsfase kan worden verklaard in termen van verbreding van de barstwijdte-verdeling, terwijl niet-axiale barsten smal blijven en de stroming beperken. Het "binding percolatie" model is niet geschikt om de ontwikkeling van permeabiliteit in zout-anhydrietgesteenten te verklaren, omdat dilatatie geconcentreerd is in de anhydriet-locaties. Daarom worden de experimentele gegevens vergeleken met verschillende "locatie (site) percolatie" modellen, die in wezen de initiële toename van permeabiliteit beschrijven in termen van het ontstaan van direct contact tussen de gedilateerde en permeabele anhydriet-locaties. Deze modellen blijken een bevredigende verklaring te geven voor de experimentele resultaten, met name ten aanzien van de invloed van anhydrietgehalte op kritiek gedrag.

Concluderend heeft het onderzoek aangetoond dat vrij geringe dilatatie bij plastische vervorming van zout en zout-anhydriet materiaal aanleiding kan geven tot een bijzondere grote toename in permeabiliteit. Het proefschrift eindigt met een bespreking, in **Hoofdstuk 7**, van de implicaties hiervan voor de vloeistoftransporteigenschappen van zoutgesteenten in afvalopbergplaatsen en voor de vloeistoftransporteigenschappen van delen van de aardkorst en de bovenmantel, die plastische vervorming ondergaan. Hierin zijn suggesties voor aanvullend onderzoek opgenomen.

ACKNOWLEDGEMENTS

The support of my promotor, Prof. H.J. Zwart, is greatly appreciated. I hope that his interest in the H.P.T. Laboratory activities will continue well into his retirement years.

My co-promotor and close colleague, Dr. Chris Spiers, is heartily thanked for help and guidance far beyond the call of duty. His enthusiasm for the exact, and relentless pursuit of the underlying maxim, whilst managing to maintain a clear overview, has proved invaluable in guiding me towards this long awaited goal.

My "paranimfen", Jaap Liezenberg and Rolf Brzesowsky, are thanked for their present support, and also, together with Chris and other co-workers from the earlier years of the "Salt Project", for doing their part to create the petrophysics group which currently flourishes in the H.P.T. Laboratory at Utrecht.

Experimental investigations, involving high pressure rock deformation machines with associated measurement and control equipment, require reliable technical support. I am happy to say that in the H.P.T. Laboratory we have an excellent team. Gert Kastelein and Eimert de Graaff are especially thanked for their help and co-operation in the early constructional, and later operational phases of the many items of equipment - particularly the Heard Apparatus, which was central to this thesis work. Peter van Krieken provided excellent back-up during the experimental programme, with sample preparation and thermal analyses. Ad Jongerius is remembered for constructing the gas permeametry apparatus.

The initial part of this experimental work and the majority of the equipment was funded through contract research for the Dutch Ministry of Economic Affairs and the Commission of the European Communities. Their financial support, together with that of the University, is gratefully acknowledged.

I wish to thank my colleagues (students and staff) in the faculteit Aardwetenschappen who have been of assistance. Hugo de Boorder, Cees Passchier and Rolf Brzesowsky are thanked for their help with "de Nederlandse vertaling". Reinoud Vissers and Eilard Hoogerduijn Strating both provided useful geological discussion.A special thank you to John Savage for pointing out a key article which opened my eyes to percolation theory.

Fred Quint and the A.V. Dienst department are thanked for their prompt help with illustrative matters.

This thesis would certainly not have been possible without the skills and patience of Magda Mathot-Martens who processed the text and made a huge effort to produce this fine result, of which I am proud. I will always be grateful for her assistance.

Finally to Hildemieke and to all those supporters who waited, I should like to say that ***as a team****, "WE SCORED!".*

CURRICULUM VITAE

Colin Jack Peach B.Sc. (Hon.); ARSM; FGS (London).

DATE OF BIRTH:	*3rd May 1954.*	
PLACE OF BIRTH:	*Staines, Middlesex, England, U.K.*	
HIGH SCHOOL EDUCATION:	*1965-1972:*	*Tudor Grammar School, Feltham, Middlesex.*
UNDERGRADUATE STUDIES:	*1972-1975:*	*Imperial College of Science and Technology, University of London.*
GRADUATED:	*1975:*	*B.Sc. (Honours) Geology.*
POSTGRADUATE EXPERIENCE:	*1975-1978:*	*Research Assistant, Geology Department, City of London Polytechnic.*
	1978-1983:	*Research Assistant Experimental Rock Deformation Laboratory / Geology Department, Imperial College, University of London.*
	1983-1988:	*Contract Researcher "Salt Project", HPT Laboratorium / vakgroep Geologie, Rijksuniversiteit Utrecht, Utrecht, NL.*
	1988-date:	*University Lecturer / Researcher, HPT Laboratorium, Instituut voor Aardwetenschappen, Rijksuniversiteit Utrecht, NL.*

A view into the infinite dimensional world of the Bethe lattice (Cayley tree), of co-ordination number 4.